Universidade Federal do Rio Grande do Sul
Escola de Engenharia
Programa de Pós-Graduação em Engenharia Civil

Response of Lightly Cemented Sand under Multiaxial Loading

Marina Bellaver Corte

Porto Alegre
2020

MARINA BELLAVER CORTE

RESPONSE OF LIGHTLY CEMENTED SAND UNDER MULTIAXIAL LOADING

Thesis presented to the Graduate Program in Civil Engineering of the Federal University of Rio Grande do Sul as part of the requirements of the Degree of Doctor in Engineering.

Porto Alegre
2020

CIP - Catalogação na Publicação

Corte, Marina Bellaver
Response of Lightly Cemented Sand under Multiaxial Loading / Marina Bellaver Corte. -- 2020.
260 f.
Orientador: Nilo Cesar Consoli.

Tese (Doutorado) -- Universidade Federal do Rio Grande do Sul, Escola de Engenharia, Programa de Pós-Graduação em Engenharia Civil, Porto Alegre, BR-RS, 2020.

1. Carregamento multiaxial. 2. Areia fracamente cimentada. 3. Ensaios de laboratório. 4. Anisotropia. I. Consoli, Nilo Cesar, orient. II. Título.

Elaborada pelo Sistema de Geração Automática de Ficha Catalográfica da UFRGS com os dados fornecidos pelo(a) autor(a).

MARINA BELLAVER CORTE

RESPONSE OF REINFORCED SAND UNDER MULTIAXIAL LOADING

This Doctoral Thesis was assessed by the Board of Examiners and was considered suitable for obtaining the title of DOCTOR IN ENGINEERING, in the field of Geotechnical Engineering. Its final version was approved by the supervising professor and the Graduate Program in Civil Engineering of the Federal University of Rio Grande do Sul.

Porto Alegre, 16th March 2020.

Prof. Nilo Cesar Consoli
PhD, Concordia University, Canada
Supervisor

Prof. Nilo Cesar Consoli
PPGEC/UFRGS Coordinator

BOARD OF EXAMINERS

Prof. Erdin Ibraim
University of Bristol
PhD, INSA/ENTPE Lyon, France

Prof. Pedro Domingos Marques Prietto
University of Passo Fundo
D. Eng. UFRGS, Brazil

Profª. Karla Salvagni Heineck
UFRGS
D. Eng. UFRGS, Brazil

Prof. Cesar Alberto Ruver
UFRGS
D. Eng. UFRGS, Brazil

To Pedro.

ACKNOWLEDGMENT

This thesis is the result of the contribution of many people. Some of them helped on the content of this volume, others assisted on my emotional support or even both.

Professor Nilo Cesar Consoli thanks for your guidance during my undergrad, master's and now PhD. You are an example of researcher and it has been a pleasure to be your student. I am sure this partnership with continue in the future.

Professor Erdin Ibraim, I would like to thank you for assisting me during my period in Bristol. For suggesting the use of the Hollow Cylinder, all the guidance and discussions, I am very thrilled.

I would like to acknowledge the support I received in the Geotechnical Laboratory in the University of Bristol, in special to the lab technician Gary Martin. Mair, Lawrence, Gary and Lucas our coffee lounge and Friday nights made these two-year fly.

To the Brazilian friends I made in Bristol, having you made me feel home. For the talks, drinks and food, Anderson, Fred, Luana, Olívia and Vincent, thank you so much. Thaís and Guilherme, thanks for bringing to Bristol a bit of Porto Alegre.

Dina and Leanne, having you in my life was a privilege. Thank you for sharing your home and your life with me. You made being away from home an easy task.

I cannot forget to thank all the friends I made in the LEGG family. João Victor, Pablo and Filipe, thanks for helping me with the results in my qualification, they are not included in the thesis, but they are definitely not forgotten. To the girls in the laboratory, thanks for bringing some girl's talk moments into the lab.

My friends, specially to Gabi, thanks for all the support when I just needed not talking about the PhD.

Lucas, meu gatinho, thanks for the advices, partnership and love. Your technical and emotional support were fundamental in this journey. Thanks for taking me with you to Bristol and for encouraging me to stay. I will always be thankful. "Não tem volta".

To my family, thank you for all the assistance, loving and understanding during my absence. Mom, thanks for being an example of resilience and insisting on an English course when I was younger. Camila, thanks for being always around when I needed.

Finally, I would like to express my gratefulness to CAPES and CNPq; without these governing institutions, this research would not have been possible.

Happiness can be found, even in the darkest of times,
if one only remembers to turn on the light.
Albus Dumbledore

Read the book.

Sebastião Maia

ABSTRACT

CORTE, M.B. **Response of cemented sand under multiaxial loading.** 2020. Doctoral Thesis (Doctor of Engineering) – Postgraduate Program in Civil Engineering, Federal University of Rio Grande do Sul, Porto Alegre.

The improvement of soil with the use of chemical agents is a common technique in geotechnical engineering. Although the use of cement is widely employed in the field, the behaviour of the mechanisms of soil response to multiple loadings is still not fully known. Previous studies have shown that even small amounts of cement add to the soil characteristics as strength, reduction to liquefaction potential, durability and lower deformability. This thesis presents experimental tests conducted on a lightly cemented sand on advanced soil apparatus. The laboratory study has been carried on an angular to sub-angular silica sand reinforced with Portland cement of high early strength. The study aims to investigate the behaviour of a cemented sand under multiaxial loading conditions. True triaxial tests on cemented sand were conducted in a Cubical Cell Apparatus and exploration of the material response including failure limits under different constant stress paths (θ = 0º, 30º, 60º, 90º, 120º, 150º, 180º) in the octahedral (π) plane were performed. The Hollow Cylinder Torsional Apparatus was used to vary the direction of the principal stresses during shearing (α = 0º, 15º, 30º, 45º, 60º, 75º, 90º). The Young's modulus and shear modulus were measured by the application of a series of small unload reload cycles at different stages along the stress paths. At these investigation points, additional series of unload-reload cycles of higher amplitudes were also applied and the stiffness moduli assessed. Non-contact high-resolution displacement transducers where used to measure the quasi-elastic properties of the material and their dependency on the stress state, density and cement content. Cubical samples were prepared to evaluate the stiffness evolution over time with bench bender elements. All tests performed were conducted with a dense lightly cemented sand and a loose lightly cemented sand, with the same porosity/volumetric cement content index (η/C_{iv}). Results showed that the cemented sand behaviour is entirely dependent on the direction of the principal loading. The intermediate principal stress directly effects on the behaviour of the cemented sand, as well as the direction of principal stress. Nevertheless, a reduction of the anisotropy of cemented specimens is observed through initial stiffness, as the cement hydration takes place.

Keywords: *multiaxial loading; lightly cemented sand; laboratory tests; anisotropy.*

RESUMO

CORTE, M.B. **Resposta de uma areia cimentada sob carregamentos multiaxiais.** 2020. Tese (Doutorado em Engenharia) – Programa de Pós-Graduação em Engenharia Civil, Universidade Federal do Rio Grande do Sul, Porto Alegre.

O melhoramento de solos através de agentes químicos é uma prática corrente na engenharia geotécnica. O uso de cimento para o reforço de solos tem sido amplamente empregado, todavia a resposta do solo cimentado a carregamentos multiaxiais ainda é desconhecida. Estudos anteriores mostraram que pequenas quantidades de cimento incorporadas ao solo são capazes de melhorar características como resistência, redução do potencial de liquefação e deformações e aumento da durabilidade. Esta tese apresenta uma série de resultados de ensaios laboratoriais realizados em uma areia fracamente cimentada. Os ensaios foram conduzidos em uma areia silicosa reforçada com cimento Portland de alta resistência inicial. A pesquisa investigou o comportamento da areia cimentada sob condições de carregamento multiaxiais. As amostras cimentadas foram conduzidas a uma célula triaxial cúbica onde o comportamento do material, até sua ruptura, foi verificado através de diferentes caminhos de tensões (θ = 0º, 30º, 60º, 90º, 120º, 150º, 180º) no plano octaédrico. Ensaios *hollow cylinder*, onde amostras em forma de cilindro vazado são ensaiadas através carregamentos axiais e torcionais, foram empregados para verificar o comportamento do material cimentado durante a rotação das tensões principados (α = 0º, 15º, 30º, 45º, 60º, 75º, 90º). Os módulos de Young e cisalhante foram medidos durante pequenos ciclos de carga e descarga em diferentes pontos durante o carregamento nos ensaios *hollow cylinder*, Amostras cúbicas foram preparadas para a avaliação da evolução da rigidez durante a cura através de *bender elements* inseridos nas seis faces das amostras. Os ensaios foram conduzidos em uma areia fracamente cimentada com uma composição densa e uma fofa, mantendo-se o mesmo índice porosidade/teor volumétrico de cimento (η/C_{iv}). Os resultados mostram que o comportamento da areia cimentada é dependente da direção principal de carregamento. A tensão principal intermediaria afetou o comportamento da areia cimentada, assim como a direção das tensões principais. Além disso, foi observada uma redução na anisotropia das amostras com a evolução da cimentação.

Palavras-chave: *carregamento multiaxial; areia fracamente cimentada; ensaios de laboratório; anisotropia.*

LIST OF FIGURES

Figure 2.1 – Typical shear modulus versus degree of cementation of cemented sands (CHANG & WOODS, 1992)..... 39

Figure 2.2 – Basic cementing phenomenon of stabilization (after CHANG &WOODS, 1992) 40

Figure 2.3 – Calcareous sand with 8% Portland cement (ISMAEL et al., 2002)..... 41

Figure 2.4 – Effect of cement content on strength for various soils stabilized with cement, cured for 7 days (INGLES & METCALF, 1972)..... 42

Figure 2.5 – Variation of unconfined compressive strength for two cemented soils with cement content (CONSOLI et al., 2012a) 43

Figure 2.6 – Effect of density on the strength of a clay stabilised with 10% cement (INGLES & METCALF, 1972) 44

Figure 2.7 – Variation of (a) cohesion intercept with relative density and (b) friction angle with the relative density for samples with 4% cement (CLOUGH et al, 1981)..... 44

Figure 2.8 – Variation of unconfined compression strength with porosity (CONSOLI et al., 2007)..... 44

Figure 2.9 – Effect of moulding moisture content on unconfined compression strength (CONSOLI et al., 2007) 45

Figure 2.10 – Effect of age on strength of various soils stabilized with 5% cement (INGLES & METCALF, 1972) 46

Figure 2.11 – Variation of unconfined compression strength with (a) cement content and (b) porosity for three curing times (after CONSOLI et al., 2011) 46

Figure 2.12 – Relationships between unconfined compressive strength and curing temperature (a) inorganic soils and (b) organic soil (note: 100 lb/in2 = 689.5 kPa) (CLARE & POLLARD, 1954) 47

Figure 2.13 – Effect of curing temperature on strength of stabilized clay (INGLES & METCALF, 1972) 48

Figure 2.14 – Idealized behaviour of cemented soil during shearing; (a) deviatoric stress versus mean effective stress and (b) normalized deviatoric stress versus axial strain (CUCCOVILO & COOP, 1999 after COOP & ATKINSON, 1993)..... 50

Figure 2.15 – Schematic diagram showing modes of shearing behaviour for the silica sandstone (a) deviatoric stress versus mean effective stress and (b) normalized deviatoric stress versus axial strain (CUCCOVILO & COOP, 1999)..... 51

Figure 2.16 -Relationship between unconfined compressive/tensile strength and void ratio with degree of cementation (LADE & TRADS, 2014, after HUANG & AIREY, 1998, and CONSOLI et al., 2007) 52

Figure 2.17 – Behaviour of weakly and strongly cemented sand under isotropic compression (CUCCOVILO & COOP, 1999) 53

Figure 2.18 – (a) variation of incremental yield stress with curing void ratio; (b) variation of primary yield stress with cement content (ROTTA et al., 2003) 54

Figure 2.19 – Results from CIU triaxial tests: (a) deviatoris stress and axial strain and (b) porepressure and axial strain (note: 1 ksf = 47.9 kN/m^2) (SAXENA & LASTRICO, 1978) 55

Figure 2.20 – Normalized undrained shear strength versus unconfined pressure (note: 1 ksf = 47.9 kN/m2) (SAXENA & LASTRICO, 1978) 56

Figure 2.21 – Typical stress-train curves for: (a) strongly cemented; (b) moderately cemented and (c) weakly cemented (after CLOUGH et al., 1981) 56

Figure 2.22 – Stress-strain curves for (a) 2% cement and (b) 4% cement (after CLOUGH et al., 1981) 57

Figure 2.23 – Stress-strain volumetric response for uncemented and cemented sandstone (SCHNAID et al., 2001) 58

Figure 2.24 – Variation of friction angle with b-value (after REDDY & SAXENA, 1993) ... 59

Figure 2.25 – Octahedral stress-strain contours for (a) uncemented and (b) cemented sand (REDDY & SAXENA, 1993) 60

Figure 2.26 – Rate volumetric strain at failure: (a) σ_{oct} = 138 kPa; (b) σ_{oct} = 276 kPa and; rate of volume change at failure under: (a) σ_{oct} = 138 kPa; (b) σ_{oct} = 276 kPa (REDDY & SAXENA, 1993) 60

Figure 2.27 – Simple stiffness parameters for non-linear soil (adapted from ATKINSON, 2000) 62

Figure 2.28 – Characteristic stiffness-strain behaviour of soil with typical strain ranges for laboratory tests and structures (ATKINSON, 2000 after ATKINSON & SALLDORS, 1991 and MAIR, 1993) 62

Figure 2.31 – Two different cementation-loading histories: (a) cementation before loading and (b) loading before cementation (RINALDI & SANTAMARINA, 2001 after FERNANDES & SANTAMARINA, 2008) 63

Figure 2.30 – Comparison between the two load-condition histories: micromechanical model (assuming a Poisson's ratio of 0.25) (FERNANDES & SANTAMARINA, 2001) 65

Figure 2.31 – Evolution of elastic modulus with increasing cementation and pressure (TRADS & LADE, 2014) 66

Figure 2.32 – Variation of G_{sec} with deviatoric strain amplitude for cemented samples (SHARMA & FAHEY, 2003) 66

Figure 2.33 – Closure of fissures results in initial lower Young's modulus in compression then in tension (TRADS & LADE, 2014, after LIAO et al., 1997) 67

Figure 2.34 – Soil behaviour within the strain-range dependency associated phenomena, theoretical models, and laboratory measurements (BORTOLOTTO, 2017 after ISHIHARA, 1996) 68

Figure 2.38 – Secant modulus for unload-reload loops against amplitude of deviatoric strain for cemented samples (SHARMA & FAHEY, 2003) 70

Figure 2.36 – Conceptual model for the tree-dimension conditions shown in triaxial plane (LADE & TRADS, 2014 after LADE & KIM, 1988) 71

Figure 2.37 – Conceptual model for stress-strain behaviour of cemented material in triaxial tests; (a) q versus p' (b) q versus ε (LADE & TRADS, 2014 after LADE & KIM, 1988) 72

Figure 2.38 – Three-dimensional failure surface produced from experimental evidence and viewed (a) from the side to show curved envelope in triaxial plane and biaxial planes and (b) from the end to show smoothly rounded triangular shape in octahedral plane (TRADS & LADE, 2014 after REDDY & SAXENA, 1988) 74

Figure 2.39 – Determination of a void/cement ratio to a q_u target (after FOPPA, 2005) 77

Figure 3.1 – Stress paths imposed in the cubical cell varying the principal stress direction (θ) 83

Figure 4.1 – Grain size distribution of Hostun Sand 87

Figure 4.2 – Cylindrical samples: (a) UCS testing; (b) Brazilian test; (c) Triaxial cell used for the unconfined tests; (d) detailed of the space for insertion of the bender elements 89

Figure 4.3 – (a) Mould for cubical samples and (b) sample prepared for the cubical cell apparatus 90

Figure 4.4 – (a) Sample inside the mould; (b) sample positioned in the cage; (c) sample with the bender elements inserted; (d) sample after testing; (e) sample connected to oscilloscope and PicoScope 91

Figure 4.5 – Hollow cylinder samples: (a) prepared mould; (b) base and top cap and inner membrane holder; (c) curvilinear compactor; (d) inner tube prepared; (e) top of specimen detail; (f) specimen ready for testing 92

Figure 4.6 – Position of loading in (a) unconfined compression strength and (b) unconfined tensile strength 94

Figure 4.7 – Triaxial frame used for the (a) and (b) split tensile strength; (c) unconfined compression strength 94

Figure 4.8 – Schematic view of BE in (a) cylindrical sample and (b) cubic sample 96

Figure 4.9 – Bender element movement diagram and model 97

Figure 4.10 – BE manufacture: (a) BE, (b) mould, (c and d) pairs prepared 98

Figure 4.11 – Screenshot of the program used for the seismic data acquisition in the time domain (PicoScope 6) 100

Figure 4.12 – Soil element under general stress state 102

Figure 4.13 – Representation of stress conditions on the octahedral plane (ISHIHARA & YAMADA, 1979) 105

Figure 4.14 – Stress representation on the octahedral plane (REDDY & SAXENA, 1993) .. 105

Figure 4.15 – Cubical cell schematic diagram and photograph of the frame (after SADEK, 2006) 107

Figure 4.16 – Pressure panel diagram and pictures (after FERREIRA, 2008) 108

Figure 4.17 – LVDT connections to the reading system 109

Figure 4.18 – General layout of the instrumentation components of the CCA testing system (after FERREIRA, 2008) 110

Figure 4.19 – Magnets to assure contact between cushion and LVDT 111

Figure 4.20 – Definition of forces and stresses in hollow cylinder specimen: (a) surface loads, (b) stress components and (c) main principal stresses on a representative element of the specimen's wall (MANDOLINI et al., 2018) 113

Figure 4.21 – Relationship between applied stresses and principal stresses using the Mohr circle 114

Figure 4.22 – Definitions used for stress non-uniformity (HIGHT et al., 1983) 118

Figure 4.23 – Elastic stresses across the wall, (a) mean normal stress 300kPa, R=σ_1'/ σ_3'=3, b=0, α=45^o; (b) Mean normal stress 300kPa, R=σ_1'/ σ_3'=3, b=0.5, α=0^o (VAID et al., 1990) 119

Figure 4.24 – Correction of hollow cylinder sample dimension (SAYÃO & VAID, 1991) . 120

Figure 4.25 – Zoom on hollow cylinder wall: membrane penetration induced by internal (P_i) and external (P_o) pressure (MANDOLINI, 2014) 122

Figure 4.26 – Membrane penetration linear relationships: (a) effective lateral stress σ_3 and unit membrane penetration Δv_m; (b) particle size d and slope S of membrane penetration curves (FRYDMAN et al, 1973) 123

Figure 4.27 – HCTA schematic representation (YOON, 2005) 126

Figure 4.28 – Hollow cylinder torsional apparatus of the University of Bristol 127

Figure 4.29 – (a) Manual pressure regulator and (b) air water interface devices 128

Figure 4.30 – (a) Submersible load and torque cell (b) external LVDT and (c) RCDT located on top of the confining cell 129

Figure 4.31 – (a) Electronic pressure transducer and (b) gauges for inner, cell and pore pressures. 129

Figure 4.32 – (a) Sample volume change and (b) inner chamber volume change 130

Figure 4.33 – Schematic representation of the eddy current effect between the sensors and a conductive material (MANDOLINI, 2018) 133

Figure 4.34 – Schematic representation of the strain measurement system mounted around the specimen (MANDOLINI, 2018) 133

Figure 4.35 – Deflections of the central part of the sample, in the circumferential (a and b) , axial (c) and radial directions (d) 135

Figure 4.36 – Transmitter and received signals of S-waves at different frequencies 138

Figure 4.37 – Example of time domain interpretation methods (FERREIRA, 2008) 139

Figure 4.38 – Representation of *xyz* rectangular coordinates 141

Figure 4.39 – (a) 3-D printed scaffolding for inner ring positioned; (b) positioning bottom ring and (c) positioning top ring 144

Figure 4.40 – (a) Measurement of rings distance; (b) measurement of radial distance to target; (c) sample ready for testing 144

Figure 5.1 – Unconfined compressive strength (q_u) with cement content (C) 147

Figure 5.2 – Unconfined compressive strength (q_u) with porosity (η) 148

Figure 5.3 – Variation of unconfined compressive strength (q_u) with porosity/cement index (η/C_{iv}) 149

Figure 5.4 –Split tensile strength (q_t) with cement content (C) 150

Figure 5.5 – Split tensile strength (q_t) with porosity (η) 150

Figure 5.6 – Variation of splitting tensile strength (q_t) with voids/cement ratio (η/C_{iv}) 151

Figure 5.7 – Variation of the initial shear modulus (G_0) with cement content (C) 152

Figure 5.8 – Variation of the initial shear modulus (G_0) with porosity (η) 152

Figure 5.9 – Variation of the initial shear modulus (G_0) with adjusted porosity/cement index 153

Figure 5.10 – Comparison of q_u from results and model 156

Figure 5.11 – Comparison of G_0 from data and model 158

Figure 5.12 – Stiffness evolution over time and comparison *z* and *x* and *y* directions: (a) and (b) *e*=0.90, C=2.3%; (c) and (d) *e*=0.71, C=1.8%;(e) and (f) *e*=0.90, C=6.8% 161

Figure 5.13 – Stiffness evolution over time and comparison *z* and *x* and *y* directions: (g) and (h) *e*=0.74, C=7.0%;(i) and (j) *e*=0.72, C=7.0%;(k) and (l) *e*=0.90, C=10.0%;..... 162

Figure 6.1 – Stress-strain response for the principal directions for the first set of samples (*e* = 0.90 and C = 2.3%): (a) $\theta = 0^o$; (b) $\theta = 30^o$; (c) $\theta = 60^o$; (d) $\theta = 90^o$; (e) $\theta = 120^o$; (f) $\theta = 150^o$; (g) $\theta = 180^o$ 166

Figure 6.2 – Stress-strain response for the principal directions for the second set of samples (*e* = 0.71 and C = 1.8%): (a) $\theta = 0^o$; (b) $\theta = 30^o$; (c) $\theta = 60^o$; (d) $\theta = 90^o$; (e) $\theta = 120^o$; (f) $\theta = 150^o$; (g) $\theta = 180^o$ 168

Figure 6.3 – Distortional stress, *q*, against distortional strain, ε_q, of (a) first set of samples (*e* = 0.90 and C = 2.3%) and (b) second set of samples (*e* = 0.71 and C = 1.8%)..... 169

Figure 6.4 – Volumetric strain, ε_v, against distortional strain, ε_q, of (a) first set of samples (*e* = 0.90 and C = 2.3%) and (b) second set of samples (*e* = 0.71 and C = 1.8%)..... 169

Figure 6.5 – (a) q_z and q_x;(b) *q* versus θ 170

Figure 6.6 – Orthogonal deviatoric stress components: q_x and q_z of (a) first set of samples (*e* = 0.90 and C = 2.3%) and (b) second set of samples (*e* = 0.71 and C = 1.8%)..... 171

Figure 6.7 – Pictures of the reinforced sand after shearing 173

Figure 6.8 – Failure surface from modelling prediction and the experimental results..... 177

Figure 7.1 – Response of cemented sand (C = 2.3%, *e* = 0.90) with $\alpha = 0^o$ under stress and strain controlled test 180

Figure 7.2 – Tests with *e* = 0.90 and C = 2.3%: (a) *q* versus ε_q; (b) *q* versus *p'*; (c) ε_v versus ε_q; (d) τ/p' versus $(\sigma_z - \sigma_\theta)/2p'$; (e) $\tau_{z\theta}$ versus $\gamma_{z\theta}$..... 182

Figure 7.3 – Maximum deviatoric stress with the variation of principal stress direction 183

Figure 7.4 – Initial strains in the tests performed: (a) σ_z versus ε_z; (b) *q* versus ε_q..... 183

Figure 7.5 – Response of cemented sand (C = 1.8%, *e* = 0.71) with $\alpha = 0^o$ under stress and strain controlled test 185

Figure 7.6 –*e* = 0.90 and C = 2.3%: (a) *q* versus ε_q; (b) *q* versus *p'*; (c) ε_v versus ε_q; (d) τ/p' versus $(\sigma_z - \sigma_\theta)/2p'$; (e) $\tau_{z\theta}$ versus $\gamma_{z\theta}$ 187

Figure 7.7 – Maximum deviatoric stress with the variation of principal stress direction 187

Figure 7.8 – Initial strains in the tests performed: (a) σ_z versus ε_z; (b) *q* versus ε_q..... 188

Figure 7.9 – Comparison response of the tests performed with $\alpha = 0^o$ 190

Figure 7.10 – Comparison response of tests with α = 15º and 30º 191

Figure 7.11 – Comparison response of tests with α = 45º and 60º 192

Figure 7.12 – Comparison response of tests with α = 75º and 90º 192

Figure 7.13 – Deviatoric stress with principal stress direction..... 193

Figure 7.14 – Comparison on the rosettes of HC1 (e=0.90, C=2.3%) and HC2 (e=0.71, C=1.8%)..... 194

Figure 7.15 – Comparison on the rosettes normalized of HC1 (e=0.90, C=2.3%) and HC2 (e=0.71, C=1.8%) 194

Figure 7.16 – Pictures of the cemented samples at the end of shearing 195

Figure 7.17 – Comparison of experimental rosette and Drucker-Prager, Lade and Matsuoka-Nakai failure criterion..... 196

Figure 7.18 – Detailing loading stages of testing 200

Figure 7.19 – Cyclic amplitudes imposed at each stage: (a) axial cycles and (b) torque cycles 201

Figure 7.20 – Variation of the amplitude of cycles for (a, b, c) Young's moduli and (d, e, f) shear moduli 202

Figure 7.21 – Equivalent modulus, (a) E_{eq} and with the simple amplitude strain $(\varepsilon_z)_{sa}$ and (b) G_{eq} with $(\gamma_{z\theta})_{sa}$ – HC1 α = 0º 203

Figure 7.22 – Equivalent modulus, (a) E_{eq} and with the simple amplitude strain $(\varepsilon_z)_{sa}$ and (b) G_{eq} with $(\gamma_{z\theta})_{sa}$ – HC1 α = 30º 204

Figure 7.23 – Equivalent modulus, (a) E_{eq} and with the simple amplitude strain $(\varepsilon_z)_{sa}$ and (b) G_{eq} with $(\gamma_{z\theta})_{sa}$ – HC2 α = 0º 205

Figure 7.24 – Equivalent modulus, (a) E_{eq} and with the simple amplitude strain $(\varepsilon_z)_{sa}$ and (b) G_{eq} with $(\gamma_{z\theta})_{sa}$ – HC2 α = 15º 206

Figure 7.25 – Equivalent modulus, (a) E_{eq} and with the simple amplitude strain $(\varepsilon_z)_{sa}$ and (b) G_{eq} with $(\gamma_{z\theta})_{sa}$ – HC2 α = 45º 207

Figure 7.26- Moduli at initial q=0kPa: (a) Young's Moduli for HC1; (b) Young's Moduli for HC2; (c) Shear Moduli for HC1; and (d) Shear Moduli for HC2; 208

Figure 7.27 – Deviatoric stress over deviatoric strain with the points where small cycles were measured..... 209

Figure 7.28 – Deviatoric stress over time with detailed small cycles imposition on the cemented sand..... 209

Figure 7.29 – Procedure to obtain the Young's modulus were small cycles were not performed 210

Figure 7.30 – Typical stress-strain curve in monotonic loading with creep test: HC1 $\alpha=0^o$. 213

Figure 7.31 – Cycles after creep for determination of (a) E_z and (b) $G_{z\theta}$ 214

Figure 7.32 – Stress level dependency of (a) Young's moduli, E_z, and (b) shear moduli, $G_{z\theta}$; (HC2 $\alpha=0^o$) 215

Figure 7.33 – Stress level dependency of (a) and (c) Young's moduli, E_z, and (b) and (d) shear moduli, $G_{z\theta}$; (HC2 $\alpha=15^o$) 216

Figure 7.36 – Stress level dependency of (a) and (c) Young's moduli, E_z, and (b) and (d) shear moduli, $G_{z\theta}$; (HC2 $\alpha=30^o$) 217

Figure 7.35 – Stress level dependency of (a) and (c) Young's moduli, E_z, and (b) and (d) shear moduli, $G_{z\theta}$; (HC2 $\alpha=45^o$) 218

Figure 7.36 – Stress level dependency of (a) and (c) Young's moduli, E_z, and (b) and (d) shear moduli, $G_{z\theta}$; (HC2 $\alpha=60^o$) 219

Figure 7.37 – Stress level dependency of (a) and (c) Young's moduli, E_z, and (b) and (d) shear moduli, $G_{z\theta}$; (HC2 $\alpha=75^o$) 220

Figure 7.38 – Stress level dependency of (a) Young's moduli, E_z, and (b) shear moduli, $G_{z\theta}$; (HC2 $\alpha=90^o$) 221

Figure 7.39 – Stress level dependency of (a) Young's moduli, E_z, and (b) shear moduli, $G_{z\theta}$; (HC1 $\alpha=0^o$) 221

Figure 7.40 – Stress level dependency of (a) and (c) Young's moduli, E_z, and (b) and (d) shear moduli, $G_{z\theta}$; (HC1 $\alpha=15^o$) 222

Figure 7.41 – Stress level dependency of (a) and (c) Young's moduli, E_z, and (b) and (d) shear moduli, $G_{z\theta}$; (HC1 $\alpha=30^o$) 223

Figure 7.42 – Stress level dependency of (a) and (c) Young's moduli, E_z, and (b) and (d) shear moduli, $G_{z\theta}$; (HC1 $\alpha=45^o$) 224

Figure 7.43 – Stress level dependency of (a) and (c) Young's moduli, E_z, and (b) and (d) shear moduli, $G_{z\theta}$; (HC1 $\alpha=75^o$) 225

Figure 7.44 – Stress level dependency of (a) Young's moduli, E_z, and (b) shear moduli, $G_{z\theta}$; (HC1 $\alpha=90^o$) 226

Figure 7.45 – Effect of principal stress on Young's and shear moduli; HC1 (e=0.90, C=2.3%) 227

Figure 7.46 – Effect of principal stress on Young's and shear moduli; HC2 (e=0.71, C=1.8%) 227

Figure 8.1 – Shear orientation on the octahedral plane 229

Figure 8.2 – *b*-values that each constant α-values originates..... 230

Figure 8.3 – Deviatoric stress varying with θ and b on the cubical samples 230

Figure 8.4 – Deviatoric stress varying with α and b o n the hollow cylinder samples 231

Figure 8.5 – Normalized deviatoric stress versus deviatoric strain, $b = 0$..... 232

Figure 8.6 – Normalized deviatoric stress versus deviatoric strain, $b = 0.5$..... 232

Figure 8.7 - Normalized deviatoric stress versus deviatoric strain, $b = 1$ 233

LIST OF TABLES

Table 2.1 Cement content according to soil type for pavement construction (INGLES & METCALF, 1972) 76

Table 2.2 – Equation parameter for the unconfined compression strength prediction to distinguish soil types (after FOPPA, 2016) 78

Table 3.1 – Samples dosages prepared for the unconfined tests 81

Table 3.2 – Samples prepared for cubical bender element testing 82

Table 3.3 – Samples prepared for cubical cell testing 82

Table 3.4 – Specimens specification for the hollow cylinder tests 84

Table 4.1 – Bender element testing: associated electronics equipment 99

Table 4.2 – Equations for stress and strain components of hollow cylinder specimens (HIGHT et al., 1983; VAID et al., 1990) 114

Table 4.3 – True triaxial loading conditions 141

Table 5.1 – Parameters to the theoretical derivation model 156

Table 6.1 – Characteristics of testing conditions for the specimens prepared with 2.3% cement and 0.90 void ratio target 172

Table 6.2 – Characteristics of testing conditions for the specimens prepared with 1.8% cement and 0.71 void ratio target 172

Table 6.3 – Failure stresses under different stress paths for both cement contents and void ratio 174

Table 7.1 – Summary of testing cycles; HC1: C=2.3%; e=0.90 211

Table 7.2 – Summary of testing cycles; HC2: C=1.8%; e=0.71 212

LIST OF SYMBOLS AND ABBREVIATIONS

ASTM – American Society of Testing Materials

b – Relative magnitude of the intermediate principal stress

B – Skempton's pressure coefficient

BE – bender elements

C – cement content (expressed in relation to mass of dry soil)

c – cohesion intercept

CCA – cubical cell apparatus

C_g – gradation coefficient

C_{iv} – volumetric cement content (expressed in relation to the total specimen volume)

C_u – uniformity coefficient

D_{50} – mean effective diameter

D_r – dry density

e – void ratio

E – Young's elastic modulus

e_{max} – maximum void ratio

e_{min} – minimum void ratio

F(e) – void ratio function

G – shear modulus

G_o – initial shear modulus

G_s – specific gravity

G_{sec} – secant shear modulus

HCTA – hollow cylinder torsional apparatus

LVDT – linear variable differential transformer

p' – effective mean stress

p'_0 – initial mean stress

P_i – inner pressure

P_o – outer pressure

q – deviatoric stress

q_t – splitting tensile strength

q_u – unconfined compressive strength

q_x, q_z – x and z strength direction

UCS – unconfined compressive strength

V_s – shear wave velocity

η – porosity

σ_{oct} – octahedral stress

σ_t – tensile stress

α – inclination of the major principal stresses

ε_1, ε_2, ε_3 – major, intermediate and minor principal strains

ε_a – axial strains

ε_q – deviatoric strain component

ε_v – volumetric strain

ε_z, ε_r, ε_θ – axial, radial and circumferential deformations

ϕ' – effective friction angle

γ_d – dry unit weight

γ_{oct} – octahedric shear deformation

$\gamma_{\theta z}$ – shear deformation

η – porosity

η/C_{iv} – vois/cement index

θ – direction of principal stress (cubical cell)

ρ – specific bulk density

σ_1, σ_2, σ_3 – major, intermediate and minor principal stress

σ_x, σ_y, σ_z – x, y and z stress direction

σ_z, σ_r, σ_θ – axial, radial and circumferential stress

$\tau_{z\theta}$ – shear stress

ω – moisture content

SUMMARY

1 INTRODUCTION 29

1.1 SCOPE 31

1.2 OUTLINE OF THE THESIS 32

2 BACKGROUND REVIEW 34

2.1 INTRODUCTION TO SOIL STABILIZATION 34

2.2 CEMENT STABILIZATION 35

2.2.1 Materials 36

2.2.1.1 Cement 36

2.2.1.2 Soil 37

2.2.1.3 Water 37

2.2.2 Chemistry of cementation 37

2.2.2.1 Chemical analysis 37

2.2.2.2 Cementation bonding 38

2.2.3 Parameters controlling the behavior of soil-cement mixtures 41

2.2.3.1 Cement content 41

2.2.3.2 Porosity 43

2.2.3.3 Water content 45

2.2.3.4 Curing time 45

2.2.3.5 Temperature 47

2.3 SOIL-CEMENT BEHAVIOUR 48

2.3.1 Stress-strain response of cemented soils 49

2.3.2 Unconfined compressive and tensile strength 51

2.3.3 Isotropic compression 52

2.3.4 Triaxial Compression 54

2.3.5 Cubical Triaxial 58

2.4 STIFFNESS DEGRADATION OF CEMENTED SOILS 61

2.4.1 Debonding 62
2.4.2 Small strain behavior 65
2.4.3 Large Strain behavior 68
2.5 failure surface 70
2.5.1 Mohr-Coulomb 70
2.5.2 Failure criterion 71
2.5.3 Effect of the intermediate principal stress 73
2.5.4 Theoretical constitutive modelling 74
2.6 LOW CEMENTATION 75
2.7 Dosage of soil-cement 75
2.8 SUMMARY 79
3 RESEARCH PROGRAM 81
3.1 UNCONFINED COMPRESSION AND SPLIT TENSILE TESTS 81
3.2 STIFFNESS MEASUREMENTS WITH BENDER ELEMENTS 81
3.3 CUBICAL CELL TESTING 82
3.4 HOLLOW CYLINDER TESTING 83
3.5 SUMMARY 84
4 EXPERIMENTAL SET UP AND PROCEDURES 86
4.1 INTRODUCTION 86
4.2 MATERIALS 86
4.2.1 Hostun Sand 86
4.2.2 Cement 87
4.2.3 Water 87
4.3 SAMPLE PREPARATION 87
4.3.1 Unconfined compressive and split tensile strength 88
4.3.2 Cubical sample 89
4.3.3 Hollow Cylinder 91

4.4 UNCONFINED COMPRESSION AND SPLIT TENSILE TESTS 93
4.5 BENDER ELEMENT TESTING 94
4.5.1 Principles of Bender Elements 96
4.5.2 Manufacturing bender elements 97
4.5.3 Associated electronics equipment 98
4.5.4 Specific seismic wave measurement software 99
4.5.5 BE: performance and calibration checks 100
4.6 CUBICAL CELL APARATUS 102
4.6.1 Principles of the Cubical Cell 103
4.6.2 The CCA 106
4.6.3 Stress application system 107
4.6.4 Measurement system and software 108
4.6.5 Displacement transducers 110
4.6.6 Cushion effect 111
4.7 HOLLOW CYLINDER TORSIONAL APPARATUS 111
4.7.1 Principles of the Hollow Cylinder Torsional Apparatus 112
4.7.1.1 Stress state in Hollow cylinder sample 112
4.7.1.2 Strain state in a hollow cylinder sample 116
4.7.2 Stress non-uniformities 117
4.7.3 Influence of rubber membrane 121
4.7.3.1 Membrane penetration 121
4.7.3.2 Membrane resistance 124
4.7.4 HCTA facilities 125
4.7.4.1 Confining cell 126
4.7.4.2 Hydraulic dynamic loading system 127
4.7.4.3 Cell and back/pore pressure system 127
4.7.4.4 Measuring instrumentation 128

4.7.4.5 Inner cell and sample volume measurements 130
4.7.4.6 Data acquisition system and control 131
4.7.5 Small strain measurement system 131
4.7.5.1 Non-contact displacement transducers 132
4.7.5.2 Laboratory set-up 133
4.7.5.3 Analysis of the three-dimensional strains 134
4.8 SAMPLE INSTALLATION AND TEST PROCEDURE 136
4.8.1 Bender elements 136
4.8.1.1 Installation 137
4.8.1.2 Signal processing 138
4.8.1.3 Obtaining time of arrival 138
4.8.2 Cubical Cell 140
4.8.3 Hollow Cylinder 142
4.8.3.1 Setting the small-strain measurement system 142
4.8.3.2 Saturation 144
4.8.3.3 Consolidation 145
4.8.3.4 Monotonic loading 145
4.8.3.5 Small loading 145
4.9 SUMMARY 145
5 UNCONFINED TESTS 147
5.1 UNCONFINED COMPRESSION STRENGTH 147
5.2 SPLIT TENSILE STRENGTH 149
5.3 INITIAL SHEAR MODULUS 151
5.4 EFFECT OF POROSITY/CEMENT INDEX 153
5.5 COMPARISON WITH MODELLING PREDICTIONS 154
5.5.1 Comparison with modeling: q_u 154
5.5.2 Comparison with modeling: G_0 156

5.6 FAILURE ENVELOPE THROUGH MODELLING 158
5.7 STIFFNESS EVOLUTION 158
5.8 SUMMARY 162
6 CUBICAL CELL TESTS 164
6.1 STRESS-STRAIN BEHAVIOUR 164
6.2 FAILURE SURFACE 170
6.3 MODELLING PREDICTION 173
6.4 SUMMARY 178
7 HOLLOW CYLINDER TESTS 179
7.1 e=0.90 AND C=2.3% 179
7.2 e=0.71 and C=1.8% 184
7.3 ANALYSIS OF BOTH SAMPLE COMPOSITIONS 189
7.4 FAILURE ENVELOPE 196
7.5 SMALL STRAIN STIFFNESS 197
7.5.1 Compliance matrix 197
7.5.2 Stress paths 199
7.5.3 Effect of the cycle's amplitude 201
7.5.4 Effect of the stress paths 207
7.5.4.1 Initial *E* and *G* analysis 207
7.5.4.2 Typical test result 208
7.5.4.3 Creep characteristics of cemented Hostun sand 212
7.5.4.4 Effect of stress level dependency of small-strain stiffness 214
7.5.4.5 Effect of principal stress direction 226
7.6 SUMMARY 228
8 COMPARISON OF CUBICAL CELL AND HOLLOW CYLINDER TORSIONAL TESTS REGARDING A CEMENTED SAND 229
8.1 STRESS CONDITIONS 229

8.2 COMPARISON 231
8.3 SUMMARY 233
9 CONCLUSIONS 235
9.1 SUMMARY OF MAIN CONCLUSIONS 235
9.2 FURTHER RESEARCH 238
9.3 CLOSURE 239

1 INTRODUCTION

Cemented soil has become a common alternative to stabilise a soil matrix and improve its characteristics. The study of soil stabilization techniques has increased all over the world, with a significant contribution from the Graduation Program in Civil Engineering at the Federal University of Rio Grande do Sul (PPGEC/UFRGS). Vendruscolo (2003), Prietto (2004), Rotta (2005), dos Santos (2008), Cruz (2008), Dalla Rosa (2009), Ruver (2011), Festugato (2011), Floss (2012), Fonini (2012), Faro (2014), Foppa (2016), and Marques (2016) studied the use of cement to reinforce a soil matrix, focusing on the response under laboratory tests, such as triaxial compression, and field tests, with the use of plate load test and pile analysis. The behaviour of cemented soil has also been analysed focusing on bonding creation, stress-strain deformation and peak and post-peak strength behaviour (SAXENA et al, 1988a; CLOUGH et al., 1981; REDDY & SAXENA, 1993; RINALDI & SANTAMARINA, 2008).

Geotechnical engineers often face the situation of dealing with artificially or naturally cemented soils, which have complex and variable behaviours. The inclusion of cement is usually related to brittle behaviour and significant strain-softening (SAXENA & LASTRICO, 1978). The inclusion of cement can be affected by many factors, such as physical-chemical properties of the soil and the amount of cement and moisture of the mixture (e.g. MOORE et al., 1970; CLOUGH et. al., 1981; CONSOLI et al. 2007, FESTUGATO & CORTE, 2018).

Since the cementation changes the soil structure, this solution can be adopted in pavement base layers, channel linings, and slope protection for earth dams, as a base layer to shallow foundations and to prevent sand liquefaction (e.g. PORBAHA et al., 1998; CONSOLI et al., 2009a). Considering that rotation of the principal stress and strain axes invariably occurs in almost all geotechnical field applications, such as vertical shear wave propagation through a soil column, the model of shearing to a pile shaft, under an offshore gravity base platform, and through the failure of a slope, further investigation under generalised multiaxial loading conditions is necessary (RANDOLPH & WROTH, 1981, ANDERSEN et al., 1981, LEROUEIL & HIGHT, 2003). Heavy traffic, detonations and natural seismic activity also impose cyclic loads to the soil (FESTUGATO, 2011).

The cyclic response of soils requires investigation under multiaxial loading conditions. The analysis of cemented sands through the rotation of the principal axes in a cubical cell and the

effect of the intermediate principal stress has been reported to influence the cemented soil behaviour (REDDY & SAXENA, 1993). Authors observed that the failure envelope for cemented sand was similar to the one for uncemented sand in shape on triaxial and octahedral planes. The analysis of different stress paths on cemented sands is still limited using a true triaxial device. To date, no tests on cemented soils have been reported using a hollow cylinder device to investigate the behaviour along the different stress paths that this apparatus can impose.

The dosage for the cemented soils has already been described as depending principally on the cement amount and void ratio of the mixture (CONSOLI et al., 2007). The amount of cement in the mixture determines the behaviour of the newly created material. The content is also directly related to the cost involved in the soil improvement technique. Small amounts of cement generate a lightly cemented soil, which have been reported as economically and less aggressive to the environment and could also be associated with naturally weak cemented materials.

The addition of small amounts of cement to the soil has been related to an increase of the peak strength, a creation of bonding, and an increment of dynamic moduli and damping ratios of sand at low strain amplitudes (SAXENA & LASTRICO, 1978; SAXENA et al., 1988b; CLOUGH et al, 1981; REDDY & SAXENA, 1993; COOP & ATKINSON, 1993; ROTTA, et al, 2003). Reddy (1990), Saxena et al. (1988a, 1988b, 1988c) and Reddy and Saxena (1993) described the use of small amounts of cement (2% cement based on the dry weight of sand):

a) use of more than 2% cement for improving static and dynamic strength of sands was found to be overconservative;

b) use of more than 2% cement for artificial cementation of sands may not be economically viable;

c) less content (less than 2%) was found not to be enough for effective dispersion of cement throughout the sand.

Particle-to-particle contact area determines the behaviour of granular materials at small strains; these contacts are increased with cementation (LEE et al., 2010). Cemented soils may be divided into two regions according to their stiffness responses: the cementation-controlled region and the stress-controlled region. The cementation considerably affects the strength and

stiffness at low stress levels because the cemented soils (or bonded soils) behave similarly to composite materials rather than to particulate materials. With the increase of confining stresses over the bonding forces, a degradation of the cemented mixture is observed. When bond degradation occurs, the behaviour of soils is controlled by the confining stress. The transition stress from the cemented to the stress-controlled region depends on the amount and type of cementation agent. Bond degradation can also be observed when unloading the cemented soil. This occurs when the cement-soil mixture expands due to stress relaxation and the cementation bond is broken at the interparticle contact (ZANG & WONG, 1995; FERNANDEZ & SANTAMARINA, 2001). Although the stiffness and stiffness evolution (over loading) have been reported to be influenced by the confining pressure, strain deformation and amplitude of loading (SAXENA & LASTRICO, 1978; SHARMA & FAHEY, 2003), the Young's and shear moduli under different stress paths have not been reported.

Therefore, this study aims to extend the knowledge of the behaviour of artificially lightly cemented sands under various stress conditions. The thesis presents results from a series of Cubical Cell tests conducted with two cement contents and two sand densities. The same specimen characteristics were tested on a Hollow Cylinder Torsional Apparatus to study the mechanical behaviour of the lightly cemented sand in the generalised multiaxial stress space imposed by this equipment.

1.1 SCOPE

Cemented soils as a stabilization technique are requested to be durable, resistant, stiff, economically feasible and environmental effective. Therefore, a better understanding specially of the effects of the rotation of the principal axes and the intermediate principal stress on cemented sands are necessary.

The main purpose of this thesis is to comprehend the behaviour of a cemented sand under multiaxial loading. The following objectives will help towards this endeavour:

a) to approach the behaviour of a lightly cemented sand under a wide variation of stress path;

b) to verify the influence of the intermediate principal stress on the behaviour of the cemented sand;

c) to evaluate the effect of rotation of the principal axes on the strength and stiffness of the cemented sand;

d) to understand the behaviour of a granular cemented soil under small amplitude multiaxial cyclic loading conditions;

e) to investigate the evolution of the small-strain (quasi elastic) stiffness of a cemented sand during shear;

f) to analyse the effect of progressive cement hydration focusing on the stiffness of cemented sand samples;

g) to compare the experimental results with modelling predictions from the literature.

1.2 OUTLINE OF THE THESIS

This thesis is divided into nine chapters. The current chapter presented the general motivation of this research.

Chapter 2 gives the results of literature review on the general concepts related to cemented soil behaviour under different loading conditions. This same chapter presents the failure mechanisms encountered for cemented materials, guidelines on dosage of the phases and a brief discussion about the light cementation.

Chapter 3 presents the experimental programme developed to reach the objectives presented in Section 1.1. The testing programme and testing strategy adopted is presented.

Chapter 4 is devoted to the description of the materials used, and the procedures for specimen preparation (cylindrical, cubical and hollow cylinder samples), specific testing set up and methodologies. The apparatus and instrumentation used in the research are detailed. The procedures used for the interpretation of the results produces by the bender element data are discussed.

Chapter 5 presents the results obtained for the unconfined compressive and tensile strength. The stiffness evolution of cubic sample over time is presented at the end of the chapter.

The main experimental results of this thesis are presented in Chapter 6 and Chapter 7. The former includes the results obtained in the cubical cell apparatus, while the latter focuses on the tests performed with the hollow cylinder torsional apparatus.

Chapter 8 contains a comparison of the results from the cubical cell and the hollow cylinder sample.

General summary and conclusions of this research including a discussion on limitations and suggestions for future work are finally presented in Chapter 9.

2 BACKGROUND REVIEW

This chapter includes general concepts regarding cemented sand behaviour: previous results and important aspects of cemented materials. Results with low cementation are also shown. A discussion of the main concepts related to the general stress-strain behaviour of cemented materials, failure limits and criteria are considered. Finally, an introduction to small strains concepts is presented.

2.1 INTRODUCTION TO SOIL STABILIZATION

When soil properties are inadequate for the task at hand, stabilization may be considered (INGLES & METCALF, 1972). The technique of stabilization adopted varies according to the soil and the properties required for engineering purposes. The two primary, current practice stabilization methods in geotechnical engineering are mechanical and chemical, and both will be presented in this section.

Compaction of soils is known to be the first technique of soil stabilization ever used. When the densification of soil is imposed, the material is expected to gain in strength. Ingles and Metcalf (1972) described the two features during compaction: the saturation, or zero air voids, and the maximum density, obtained by an optimum moisture content and compaction. The densification of soil can be obtained through various techniques, such as steamrollers, vibration and heavy tamping.

The insertion of inclusions to increase soils properties is classified as a mechanical reinforcement technique. The reinforcement of soils with fibres, geotextiles, and geomembranes have increased significantly over the last decades. Polypropylene fibres incorporated into soils have demonstrated to improve mechanical behaviour (e.g., FESTUGATO et al., 2017; CONSOLI et al., 2009a; 2009b; 2010a; 2012; CHEN et al., 2015; DIAMBRA & IBRAIM, 2015). Mixing glass fibres into soils also have been successfully reported in the literature (e.g., MAHER & GRAY, 1990; CONSOLI et al., 1998, 2012a, 2014; MUJAH et al., 2013). Numerous materials were shown to be successfully incorporated in geotechnical engineering to soil treatment, including geogrids, meshes, rubber filaments, metal fibres, natural fibres and geomembranes, in numerous applications.

Ingles and Metcalf (1972) indicated that when a selected material or combination of materials with adequate mechanical stability cannot be obtained, or where enhanced strength or resistance to water softening is required, it is advisable to chemically stabilize the soil. Techniques adding cement, lime, bituminous material and fly ash have been proven to successfully increase soil properties.

The use of lime has also been proven effective in stabilizing clayey soils, though it is less suitable for granular materials (INGLES & METCALF, 1972). The efficiency of lime into soil matrix have been described by several authors (e.g., HERRIN & MITCHELL, 1961; MITCHELL, 1981; PUPPALA et al., 2005; CONSOLI et al, 2011a; 2011b; 2012a; 2012b).

Experiments regarding the addition of fly ash and lime for soil stabilization have also been successfully performed in recent decades by numerous researchers (e.g., MITCHELL & KATTI, 1981; LITTLE et al., 1986; KAMON & NONTANANANDH, 1991; MAHER et al., 1993; JALALI et al., 1997; CARRARO, 1997; CONSOLI et al., 1997, 2001, 2014, 2015; THOMÉ et al., 1998).

It can be noticed that a wide range of studies have investigated soil improved through chemical stabilization. Nevertheless, the most used material to treat soils in geotechnical engineering is cement. Cement is also the material used in this research. The following section focuses on the cement soil stabilization and the key parameters related to the addition of cement to a soil matrix.

2.2 CEMENT STABILIZATION

Naturally cemented sands are found in many places in the world and one of their distinguishing characteristics is their ability to stand in steep natural slopes. Cementation is generally attributed to precipitation of calcite cement in naturally cemented sands (SAXENA & LASTRICO, 1978). Clough et al. (1981) indicated that cementation in sand is provided by small amounts of agents, creating points of contact between sand particles. The cementation process of artificially cemented sands is detailed in the section 2.2.2.

Ingles and Metcalf (1972) advised that “when a material or combination of materials with adequate mechanical stability cannot be obtained, or where enhanced strength or resistance to water softening is required, then it may be advisable to consider stabilization by the addition of

cement, lime or bituminous material". Among all stabilization agents, cement is by far the most commonly used. Also, the addition of even small quantities of cement, up to 2%, will modify the properties of the soil, whereas large amounts will radically alter the properties; a clean gravel with 5 to 10% cement will behave almost like concrete.

Soils-cement has been used to improve soils in facing road base layers, slope protection for earth dams, base for shallow foundation to prevent liquefaction and, more recently, improving deeper layers, using grouting techniques (CATTON, 1962; INGLES & METCALF, 1972; DUPAS & PECKER, 1979; PORBAHA et al., 1998; THOMÉ et al., 2005; CONSOLI et al., 2003, 2007, 2008, 2009, 2012, 2017).

It should be noted that authors named the addition of cement into soils differently. Commonly used terms include soil stabilization, reinforcement, modification or treatment. In general, the difference between these denominations is the degree of modification of the natural properties of the soil, depending on the amount of cemented added. Ingles and Metcalf (1978) related the effects of two processes – cement "modification" and "stabilization" – differently, principally on degree and will of cementation; therefore, the practices in road construction have trended away from high cement contents, producing concrete-like material, to lower cement contents and materials stabilized only as far as necessary for the desirable level of mechanical stability.

Although the soil reinforcement technique term may vary, the concept of cementation is the same in all techniques, meaning that the addition of cement to soil has a unique goal, the improvement of soil properties such as strength or deformability for engineering purposes. In this literature review, there is no distinction between the terms used.

2.2.1 Materials

Naturally, the analysis of the behaviour of cemented stabilized soils must consider the interaction that results from the addition of cement into the soil. Water, both its quantity and its quality are relevant. This section presents the materials considered in soil-cement mixtures.

2.2.1.1 Cement

Portland cement is the most widely used material for soil-cement mixtures. Ingles and Metcalf (1972) advised that regardless of the cement used, it is important to verify the amount of cement necessary to stabilize the soil and prevent shrinkage and high heat of hydration. Consoli et al. (2013) verified the effect of cement types I, III and IV on a non-plastic uniform sand. The three

cement types have proven to increase strength and stiffness to the soil matrix, type III presented highest gains at the 28 day curing, followed by type I and IV.

2.2.1.2 Soil

According to Ingles and Metcalf (1972), any soil, apart from highly organic materials, may be treated with cement and will exhibit an improvement in properties, including an increase in strength. The authors advise that sandy soils are more efficient for cement treatment once the mixing process is also easier and higher strengths are observed. The chemical and mineralogical composition of the soil can also determine the efficiency of the cement stabilization (CROFT, 1967).

2.2.1.3 Water

Generally, potable water is considerate satisfactory for cement reactions (INGLES & METCALF, 1972), while highly organic water should be avoided. The amount of water required is related to the compaction instead of the cement hydration.

2.2.2 Chemistry of cementation

2.2.2.1 Chemical analysis

Natural cementation in sands is generally attributed to precipitation of carbonates or oxides (SAXENA & LASTRICO, 1978). Cementation can vary from small to large scale, attributed to the unequal precipitation of calcite cement. Soils can also be artificially cemented through the addition of a cementation agent. This thesis will focus on the artificially stabilization of a sand with cement.

Moh (1965) described the reactions on soil-cement mixtures in aqueous extracts: “In a mineral-cement mix, any calcium ions liberated from the cement, or directly from lime, during hydration and hydrolysis react rapidly with silicates and aluminates from the soil mineral to dorm insoluble products. Therefore, the amount of extractable silica (Si) and alumina (Al) will be low throughout the curing period. The extractable calcium (Ca) is the portion of the lime Ca in excess of that reacting with Si and/or Al. Therefore, it is apparent that the amount of extractable Ca at any given time is controlled by the rate of cement hydration and the pH of the system, and the latter depends on the nature of the soil in the system. The Ca concentration in extract, is low at a start, increases to a maximum after a short period of cure, and then decreases to nothing with time”.

The reaction scheme is presented by the following equations:

$$C_3S + H_2O \rightarrow C_3S_2H_x \text{ (hydrated compounds)} + Ca(OH)_2 \quad (2.1)$$

$$Ca(OH)_2 \rightarrow Ca^{++} + 2(OH)^- \quad (2.2)$$

$$Ca^{++} + 2(OH)^- \; SiO_2 \text{ (soil silica)} \rightarrow CSH \quad (2.3)$$

$$Al_2O_3 \text{ (soil alumina)} \rightarrow CAH$$

$$Ca^{++} + NS \text{ (soil silicate)} \rightarrow CSH + Na^+ \quad (2.4)$$

$$NA \text{ (soil aluminate)} \rightarrow CAH + Na^+$$

CSH and CAH are responsible for the strength gain.

2.2.2.2 Cementation bonding

Independently of natural or artificially cementation on soils, the main result of cementation is that a saturated soil can resist tensile and shear stress at zero confinement. Nevertheless, cemented soil is stiffer than non-cemented soil (MITCHELL & SOGA, 2005; BUDHU, 2011; SALGADO, 2013). Portland cement needs a long time (months to years) to achieve complete hydration (ASHBY & JONES, 1980).

Knowing that cementation takes time to occur, Chang and Woods (1992) analysed the evolution of the cementation over time. The authors observed that the cementation level in terms of percent in weight does not provide an adequate indication of how much the interparticle bonding can be developed as cementation is added into the soil deposit. Instead, the authors represented the cementation level in terms of the percent of void filling by cementation material.

Chang and Woods (1992) described the microstructure of a cemented sand with three seperate zones (Figure 2.1). Zone I represent the early stages of cementation (less than 20% - 25%); the cement partially covers the surface of soil particles with some initial bonding. This phase was named Stage I. Stage II occurs when the cementation is significant at the contact points between soil particles, representing 20% - 25% up to 60% - 80% of cementation. This is represented in Zone II in Figure 2.1. Zone III represents Stage III, where cements fills most of the void space between soil particles, development of chemical bonds has been completed, and the additional cement mainly plays the role of a filler. This stage takes place when the degree of cementation is higher than 80%.

Figure 2.2 presents the microstructure of cemented sand studied by examining the photos taken with a scanning electron microscope. The microstructure of soils with low cementation levels (Zone I) is shown is Figure 2.2a. Initial bonding at various contact points between soil particles with the cement partially covering the surface of the soil can be observed. At Zone II (Figure 2.2b), more contact points have developed chemical bonds as manifested by pendular cement rings between soil particles. The authors highlight that these contacts demonstrate that bonding of soil particles is significant as cement is introduced, thus increasing the shear modulus of the soil skeleton. In Figure 2.2c, highly cemented sand is present. At this stage, the cement fills most of the void spaces between soil particles. It is also hard to distinguish the soil particles from the cement.

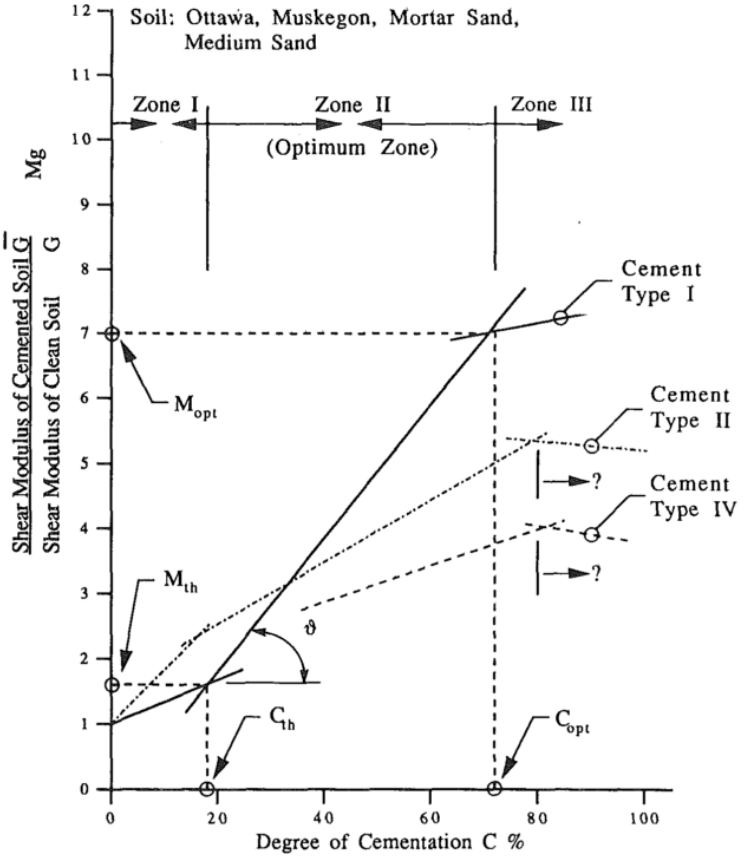


Figure 2.1 – Typical shear modulus versus degree of cementation of cemented sands (CHANG & WOODS, 1992)

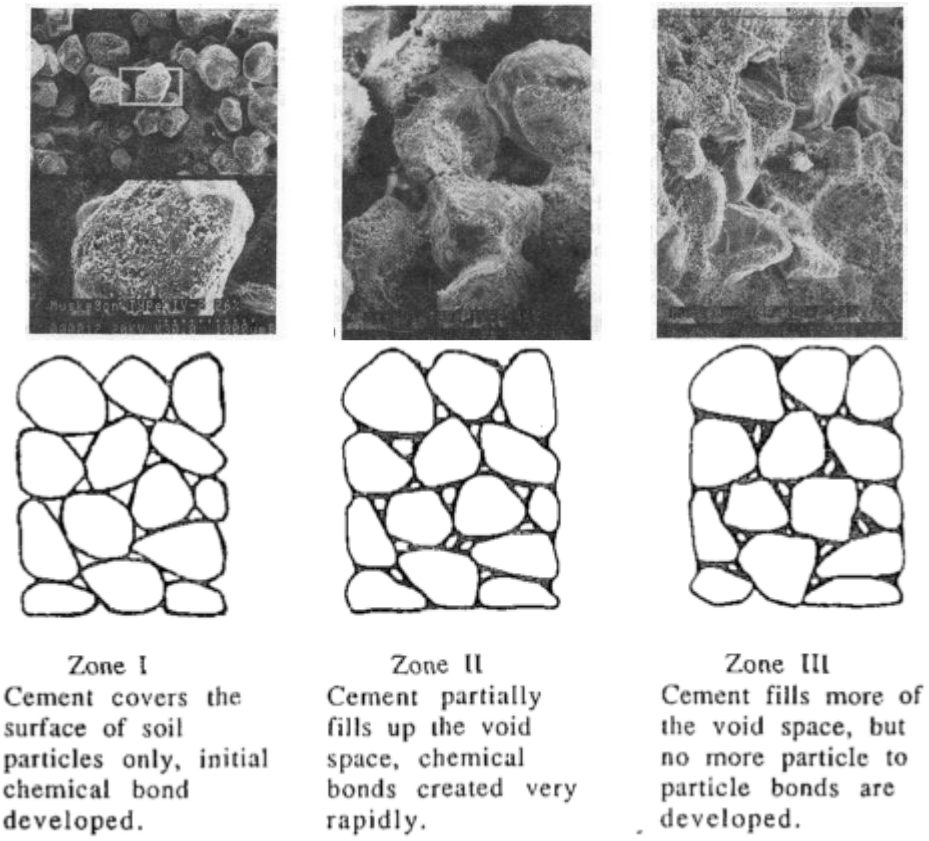


Figure 2.2 – Basic cementing phenomenon of stabilization
(after CHANG &WOODS, 1992)

Ismail et al. (2002) carried out a microscopy investigation on cementation with various agents. Figure 2.3 shows the granular nature of the Portland cement within the soil matrix after curing. The authors indicated that as some cement particles accumulate, the periphery of those grains starts to hydrate first; as they hardened, it forms a partial barrier, delaying hydration of the interior parts.

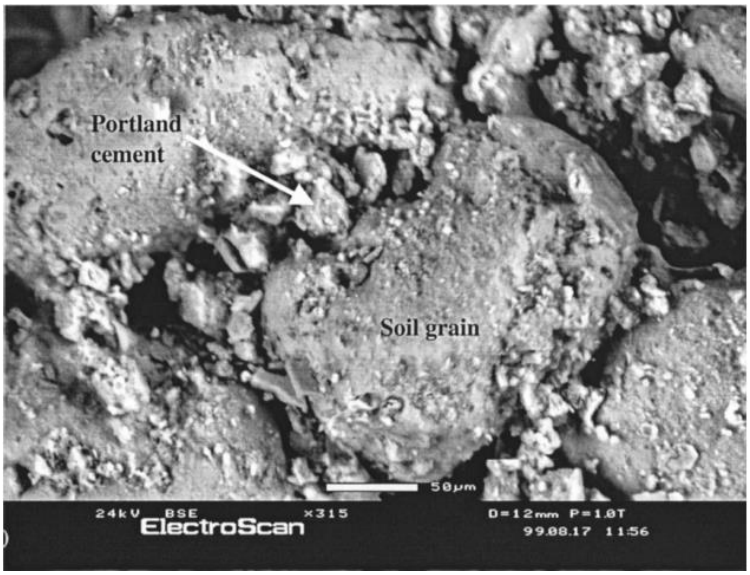


Figure 2.3 – Calcareous sand with 8% Portland cement
(ISMAEL et al., 2002)

2.2.3 Parameters controlling the behavior of soil-cement mixtures

The efficiency of the soil improvement by the addition of cement to a soil matrix is directly related to the amount of cement added to the soil, the degree of compaction, the water content, time of curing and temperature of curing. These factors are dominant "key factors" for the strength of artificially cemented soils (CONSOLI et al., 2007). The most common test of the effectiveness of cementation stabilization is the unconfined compressive strength, and/or CBR, and the resistance to cycles of freezing/thawing or wetting/drying conditions (INGLES & METCALF, 1972). In this section, the key parameters and their variations are detailed, focusing primarily, but not only, on the unconfined compression strength response.

2.2.3.1 Cement content

The properties of cemented soils change with increasing cement content. In general, strength increases linearly with cement content, but this occurs at different rates for different soils, as shown in Figure 2.4 (INGLES & METCALF, 1972)

Catton (1962) demonstrated that when small amounts of cement where added to a mixture, a reduction of water absorption and plasticity index were observed. Also, for the same confinement strength, the increment of cement content resulted in higher peak strength and a lower strain corresponding to this peak strength (CLOUGH et al, 1981).

Concomitantly, the increment in the unconfined compression strength by the increase in the cement content was explored by numerous researchers (e.g. CLOUGH et al, 1981; CONSOLI et al 2013, 2016, 2017; DASS et al., 1994; SILVA et al., 2013). Figure 2.5 shows the effect of the increment of cement to Osorio uniform sand and to Porto Well-graded sand. Each line represents dry unit weights, and the increment of unconfined compressive strength with the variation of cement content is observed. For both soils, the increment of cement effects on the soil strength and these increments are approximately linear.

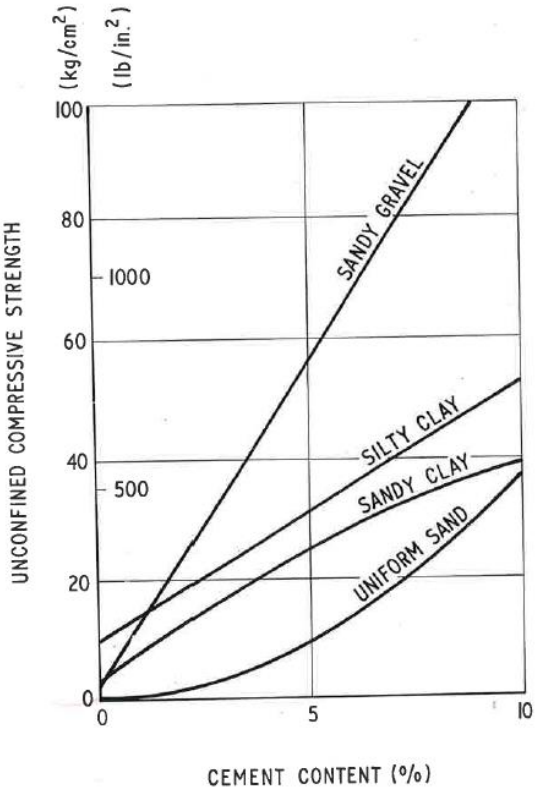


Figure 2.4 – Effect of cement content on strength for various soils stabilized with cement, cured for 7 days
(INGLES & METCALF, 1972)

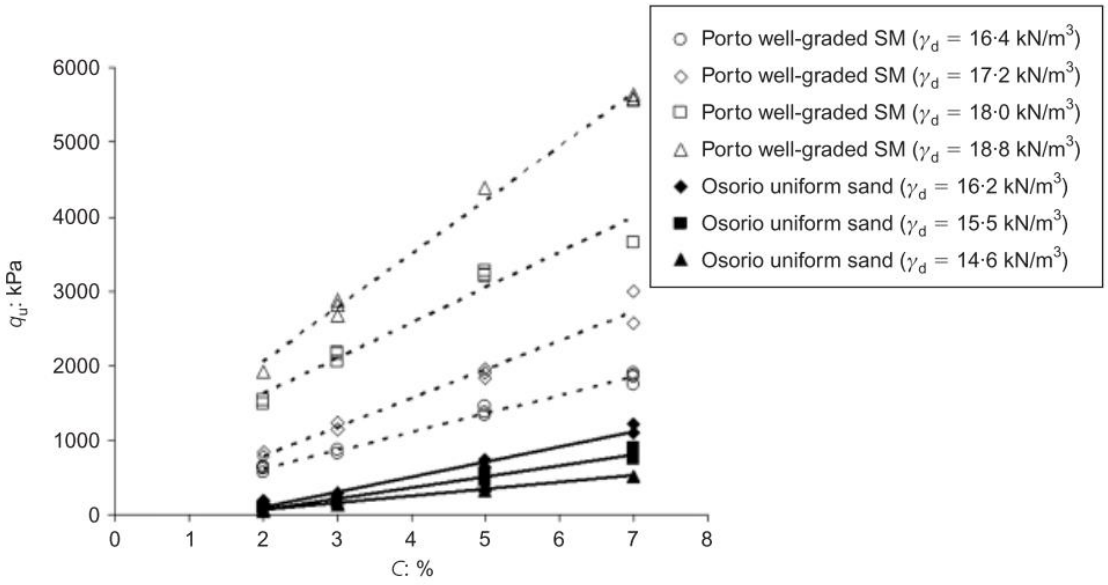


Figure 2.5 – Variation of unconfined compressive strength for two cemented soils with cement content (CONSOLI et al., 2012a)

2.2.3.2 Porosity

Accordant to Ingles and Metcalf (1972), the variation in the degree of comparison of cemented soil samples is almost as important as the cement content. Figure 2.6 shows that a reduction in density from 100 to 80 kg/m^3 may cause a 20% reduction in strength.

Clough at al. (1981) demonstrated that density has a significant effect in the behaviour of a cemented sand. The authors observed an increase of the cohesion intercept and the friction angle when a variation of relative density in the triaxial tests (keeping the cement content constant). This result is presented in Figure 2.7.

Consoli et al (2007) showed that the unconfined compressive strength reduces with the increase of the porosity. In Figure 2.8, the effect of porosity is presented for each cement content. Every cement content presents a reduction in q_u with the porosity. The effect of decreasing porosity in soil-cement mixtures was also observed by Felt (1955), Ismail et al. (2002), and Consoli et al. (2006, 2007, 2012a, 2012b, 2013, 2016, 2017).

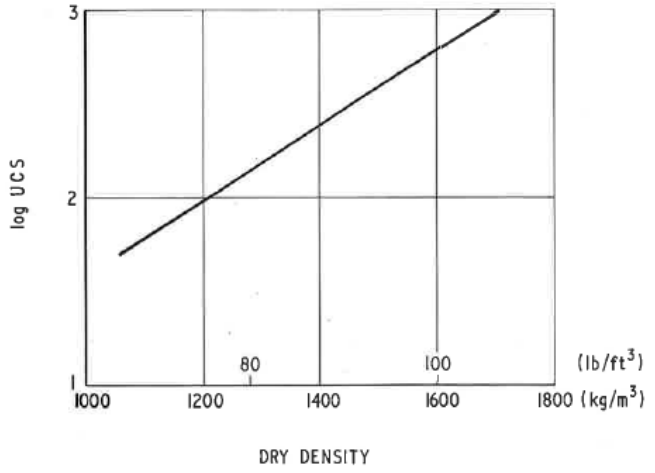


Figure 2.6 – Effect of density on the strength of a clay stabilised with 10% cement (INGLES & METCALF, 1972)

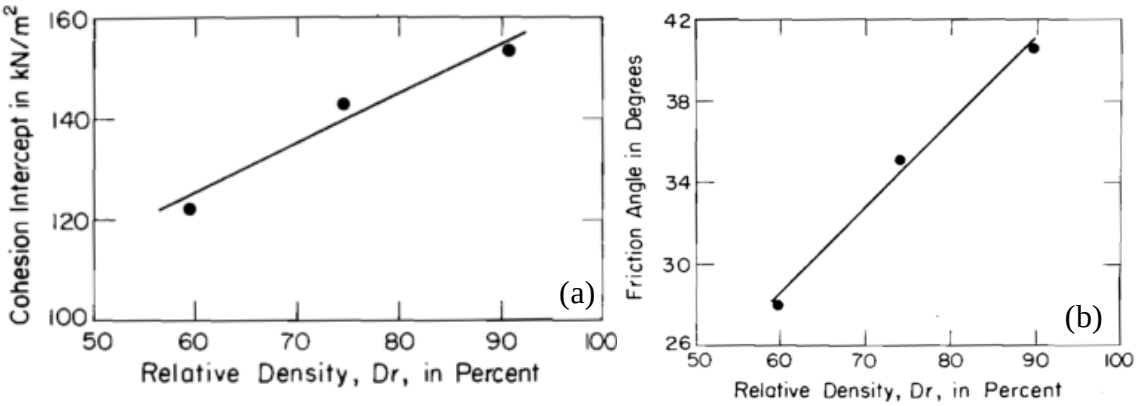


Figure 2.7 – Variation of (a) cohesion intercept with relative density and (b) friction angle with the relative density for samples with 4% cement (CLOUGH et al, 1981)

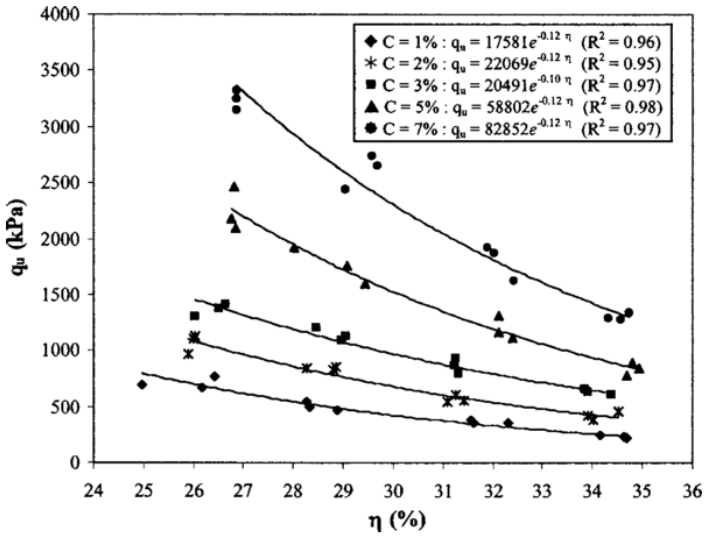


Figure 2.8 – Variation of unconfined compression strength with porosity (CONSOLI et al., 2007)

2.2.3.3 Water content

Stabilized soils are frequently compacted in situ at the optimum moisture content, determined through compaction curves. Felt (1955) verified the effect in the variation of moisture content in the unconfined compression strength and durability for various soil types. Regarding the behaviour of a sandy soil, the author concluded that samples prepared with a slightly lower moisture contents than the optimum one reaches lower mass losses and higher unconfined compression strength.

Consoli et al. (2007) verified the effect of moulding moisture content on unconfined compression strength for a clayey sand stabilized with 2, 9 and 12% cement. Figure 2.9 shows that when 2% cement is added to the soil, the moisture content does not affect the UCS, although when 9 and 12% cement is added to the soil matrix, the effect of the moisture content is observed. The UCS increases with moisture content increments until a maximum value and after that decreases. The maximum strength value is reached at a moisture content of approximately 10% for the soil studied.

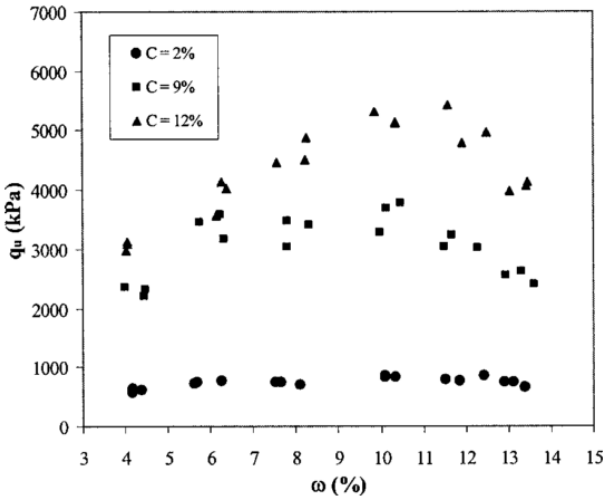


Figure 2.9 – Effect of moulding moisture content on unconfined compression strength (CONSOLI et al., 2007)

2.2.3.4 Curing time

Strength increases gradually with age of curing. Ingles and Metcalf (1972) showed the curing time effect on the unconfined compression strength on soil samples with the addition of 5% cement (Figure 2.10). The results clearly demonstrated a linear variation of the unconfined compressive strength with the age of samples. It can also be noticed that the effect of time is more pronounced on the sandy gravel soil presented.

The influence of the curing time on a uniform sand was evaluated by Consoli et al. (2011c). As expected, the authors showed that the same porosity, an increase in the curing time induces a higher unconfined compressive strength, for 2, 7 and 28 days of curing. In Figure 2.11a, it is evident that the time effect is more pronounced for higher cement contents; similar behaviour was found regardless of the porosity of samples. Figure 2.11b shows that time has an important effect on the unconfined compressive strength of sand with 7% cement.

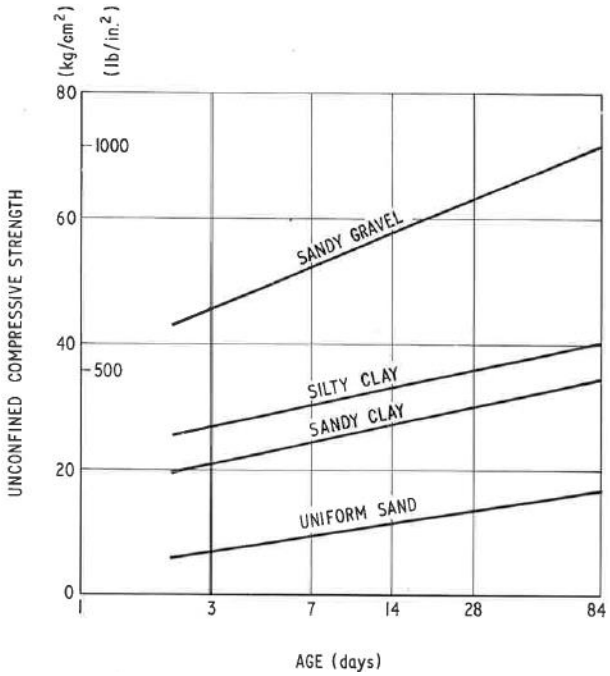


Figure 2.10 – Effect of age on strength of various soils stabilized with 5% cement (INGLES & METCALF, 1972)

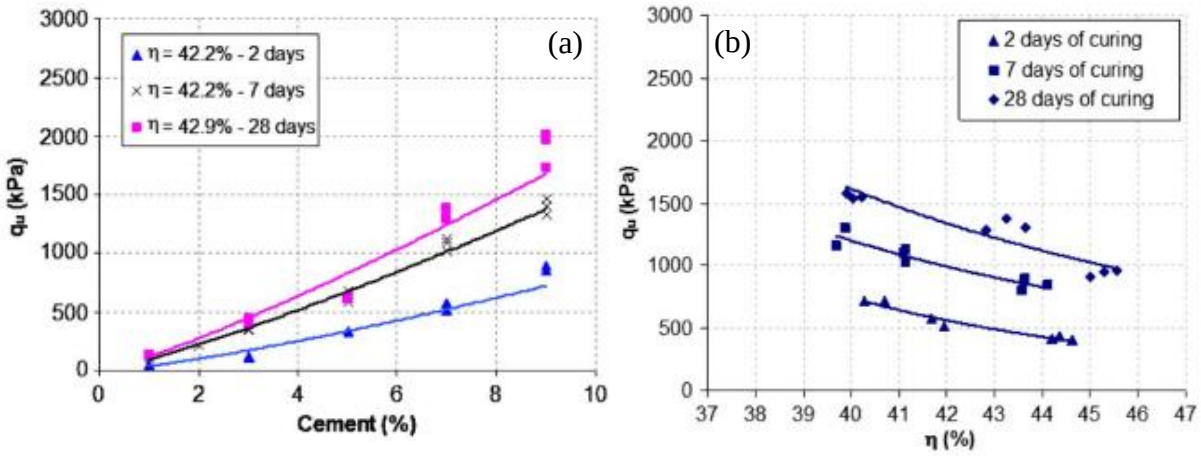


Figure 2.11 – Variation of unconfined compression strength with (a) cement content and (b) porosity for three curing times (after CONSOLI et al., 2011)

2.2.3.5 Temperature

Specimens of five different soils were stabilized with cement and cured for up to three months with temperatures from 0 º to 140º Celsius (CLARE & POLLARD, 1954). The content of 15% cement was added to a clay soil, while gravel, sand, organic sand and a silty clay were treated with 10% cement. Specimens of the five soils stabilized with cement were cured for 7 days at temperatures ranging from 0º C to 90 º C.

Figure 2.12a shows the relationship between the unconfined compressive strength and curing temperature for specimens of three soils stabilized with Portland cement. It can be noticed that for all temperatures presented, the increment of the temperature implies an increase of shear compressive strength at the seventh day of curing.

Ingles and Metcalf (1972) also presented the effect of curing temperature for a cemented organic clay. Results show that for 7 days curing time, the temperature increases linearly from 4º to 43º C. Beyond this temperature, the temperature appears not to be as effective on the unconfined compressive strength, up to 62ºC.

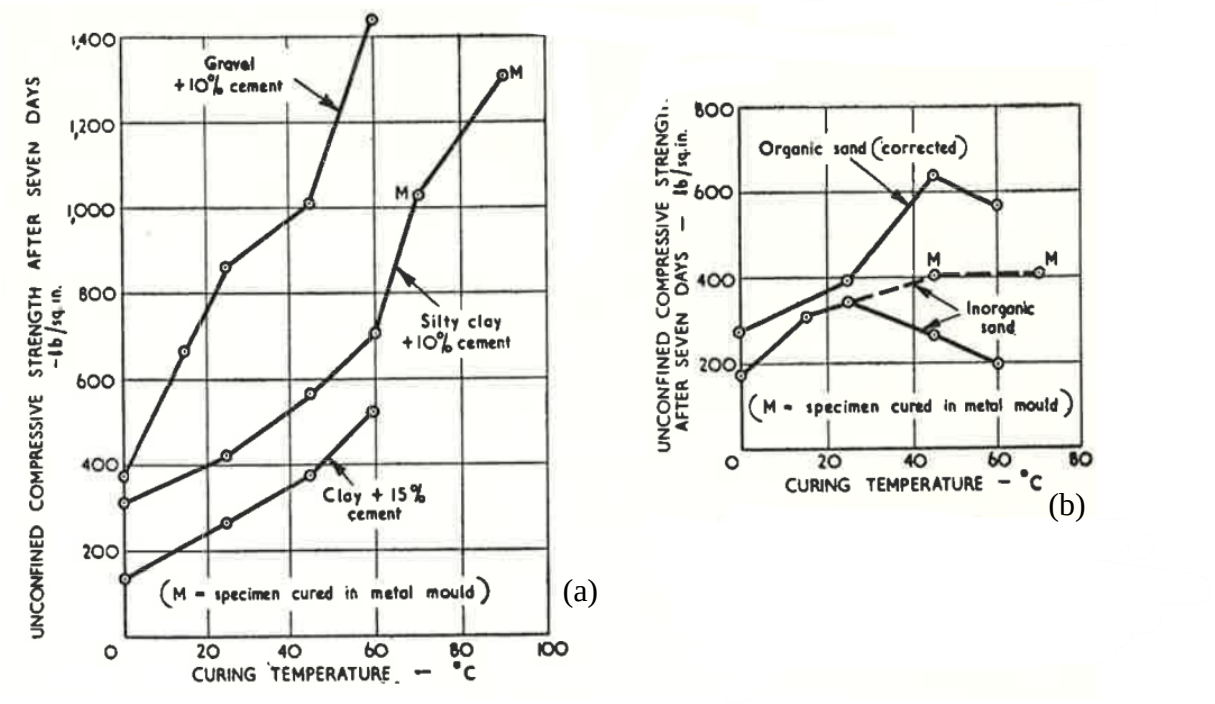


Figure 2.12 – Relationships between unconfined compressive strength and curing temperature (a) inorganic soils and (b) organic soil (note: 100 lb/in2 = 689.5 kPa) (CLARE & POLLARD, 1954)

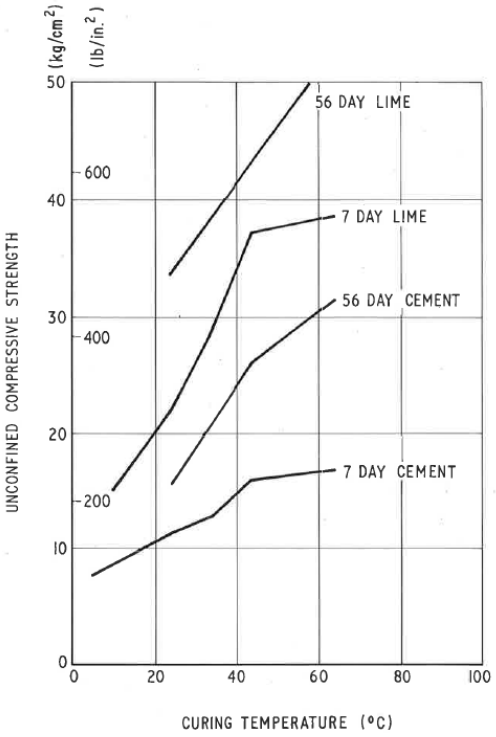


Figure 2.13 – Effect of curing temperature on strength of stabilized clay (INGLES & METCALF, 1972)

2.3 SOIL-CEMENT BEHAVIOUR

When referring to geotechnical engineering, the two main aspects of the analysis of soil behaviour are the strength and stiffness. Cemented soils are not different from that.

Lambe and Whitman (1969) indicated that the deformation of a mass of soil is mainly controlled by the interactions between individual particles, especially by sliding particles. When a cementation is added to the soils, a bond between soil particles is created, as described in 2.2.2.2. For this reason, the break of this bonding points is relevant for the analysis of the behaviour of cemented soils and is addressed in section 2.4.1.

The strength behaviour of a soil can be well understood if the three components of shearing resistance – cohesion, dilatance, and friction – are well known (SAXENA & LASTRICO, 1978). Cohesion includes any natural or artificial cementation or interparticle bonds. For Saxena and Lastrico (1978), the strength behaviour depends on the contribution of the cement bonding between particles and the frictional resistance resulting from sliding between particles. The authors observe that the cohesion contribution to the shearing resistance of a cemented soil is predominant at low strain levels. Beyond certain strain levels, there is a gradual breakdown in cementation, making friction between particles predominant. When a soil sample is subjected

to much higher strains, close to failure, a complete breakdown in the structure of cementation is expected and the shearing resistance is mainly controlled by friction. It is relevant to indicate that a breaking of all cementation bonds is not likely to happen.

In this section, results from the analysis of these parameters for cemented soils, naturally-occurring or not, are presented. Results from low cementation studies, when available, are also presented. Nevertheless, cemented soil behaviour will be presented firstly considering large strains, which is followed by small strain increments.

2.3.1 Stress-strain response of cemented soils

Different materials and degrees of cementation leads to various distinguishable responses when load is applied. Consequently, curves expressing the stress x strain behaviour of soils are expected to differ when variation of compaction, cementation, stress state and drainage are imposed.

Stress-dependant behaviour is observed when analysing granular soils. Lambe and Whitman (1969) emphasized that stiffness is highly dependent on the confinement: higher confinement stresses result in higher stiffness of the granular soil. This behaviour is not observed in cemented soils, as the confinement can break the cementation. Lade and Overton (1989) related to this bond-breaks the change of soil behaviour, from brittle at low confinements to ductile when higher confinements are imposed.

The cemented soil behaviour was intensely studied by Coop and Atkinson (1993) and Cuccovilo and Coop (1999). Both studies identified two distinguishable behaviours, depending on the degree of cementation. The behaviours observed are presented in Figures 2.14 and 2.15.

Figure 2.14 indicates that the behaviour of cemented sands is dependent on its initial state relative to the yield curve of the cement bonds. According to the authors, the behaviour at low confining pressures, relative to strength of the bonds, the soil response was elastic, up to a well-defined yield after that, a strain-softening towards a critical state was observed. By increasing confining pressure to an intermediate level, yield was observed before the critical state; but no pronounced peak of strength was obtained and an essentially friction failure is reached. The authors indicated that the only effect of the bonding at theses intermediate pressures was a stiffness on the initial stress-strain behaviour. A ductile behaviour was observed when high confining pressures were imposed on the cement-soil specimens. The highest confining

pressure leads to bond breaks during compression, causing the behaviour to act like an uncemented soil. The authors also observed that the effect of an increase in the cement content expanded the yield curve of the cement bonds. The schematic diagram presented in Figure 2.14 was obtained, considering only the component of soil structure related to bonding.

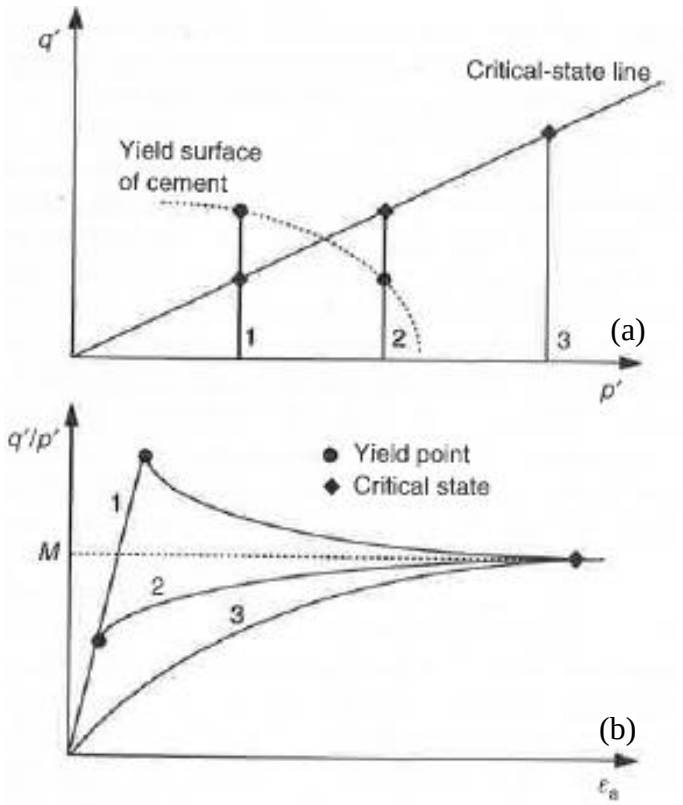


Figure 2.14 – Idealized behaviour of cemented soil during shearing;
(a) deviatoric stress versus mean effective stress and
(b) normalized deviatoric stress versus axial strain
(CUCCOVILO & COOP, 1999 after COOP & ATKINSON, 1993)

Cuccovillo and Coop (1999) presented a model where the behaviour of cemented soils is explained in terms of the stress-volume state of the soil. In this model, dilation is the dominant shear mechanism and is related to peak strength. Figure 2.15 presents the idealized behaviour of cemented soils where the frictional component is predominant. Cuccovillo and Coop (1999) concluded that the stress-strain behaviour would be non-linear for much of the range of confining stresses (case 2b) and, if seen, linearity would be confined to the initial part of shearing (case 2a). Also, only at the very highest confining stresses, compression and particle crushing would be observed (case 3) and peaks would only be seen at the lowest confining stresses (case 1).

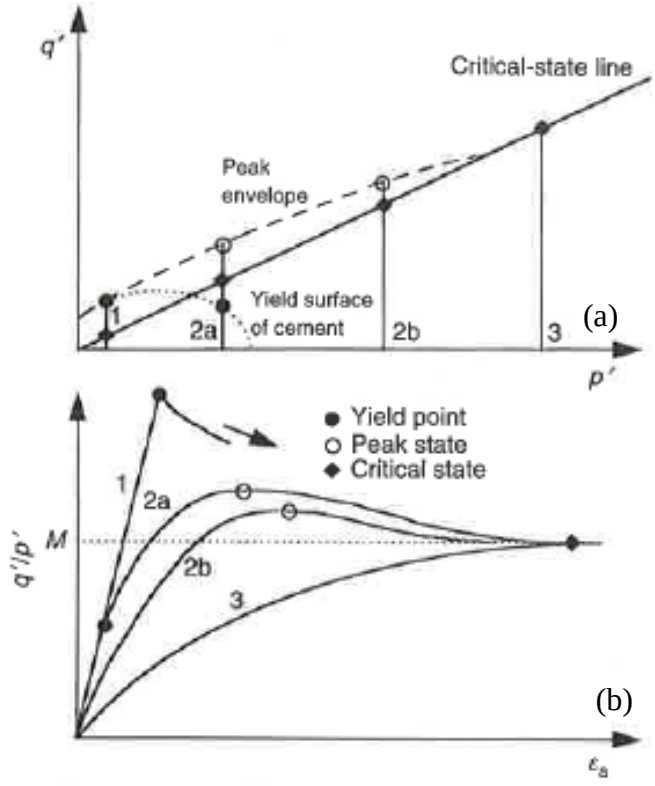


Figure 2.15 – Schematic diagram showing modes of shearing behaviour for the silica sandstone (a) deviatoric stress versus mean effective stress and (b) normalized deviatoric stress versus axial strain (CUCCOVILO & COOP, 1999)

The stress-strain response of cemented sands varies from the amount of cementation, sand density, confining pressure and grain size distribution (CLOUGH et al., 1981). The expected behaviour is also related to the type of loading applied. For this reason, the stress-strain behaviour is presented in different section, according to the type of laboratory test employed.

2.3.2 Unconfined compressive and tensile strength

Unconfined compressive tests are often considered to be the easiest way to verify the efficiency of cementation. A brittle behaviour is expected of cemented material during imposition of unconfined conditions. The strength of the material is controlled primarily by the degree of cementation and the void ratio (e. g. DAS & DASS, 1995; HUANG & AIREY, 1998; CONSOLI et al. 2007, 2010a, 2011, 2012a, 2012b; Lee et al., 2010).

Figure 2.16 presents a conceptual variation of compressive and tensile strength as functions of void ratio and cementation from both studies.

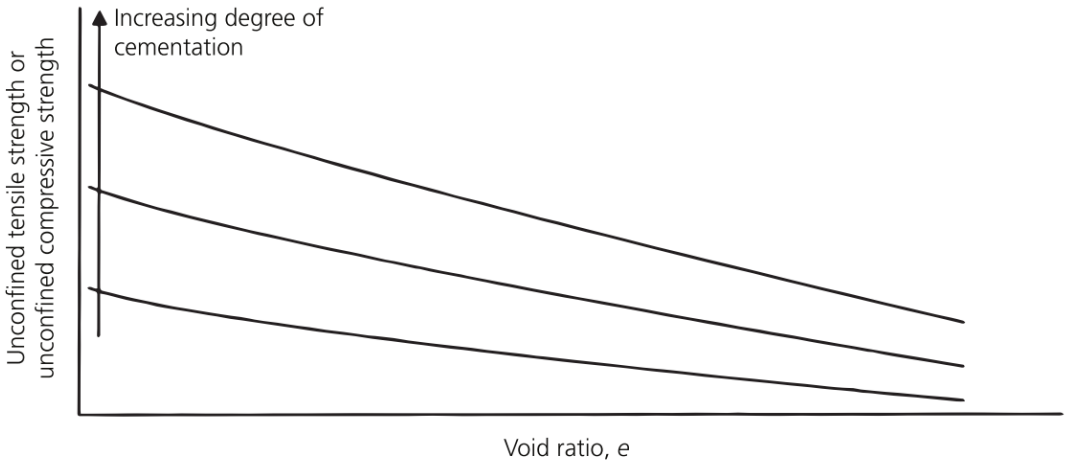


Figure 2.16 -Relationship between unconfined compressive/tensile strength and void ratio with degree of cementation (LADE & TRADS, 2014, after HUANG & AIREY, 1998, and CONSOLI et al., 2007)

In comparison with the compression tests, the Brazilian tests in cemented soils leads to values of the tensile strength of usually 9 – 15% of the unconfined compression test (INGLES & METCALF, 1972, CLOUGH et al., 1981, DASS et al., 1994, CONSOLI et al., 2001, 2007, 2012b).

As detailed in the previous section, the effect of increasing cementation leads to an increase of strength and the opposite behaviour is found when increasing the void ratio. The analysis of unconfined tests indicates a linear behaviour that occurs until plastic yielding initiates at the failure surface when the volumetric dilatation becomes very strong.

2.3.3 Isotropic compression

Behaviour of cemented soils under isotropic compression have been described by Coop and Atkinson (1993), Leroueil and Vaughan (1990), Cuss et al. (2003), Rotta et al. (2003), and Lade and Trads (2014). The cemented soil behaves elastically until yielding and the degree of cementation determines the location of the yield point in comparison with the intrinsic compression line (CUCCOVILO & COOP, 1999). A temporarily unstable behaviour in strain-controlled isotropic compression tests was observed by Lagioia and Nova (1995), corresponding to a reduction in the stress right after yielding. The authors indicated that the behaviour of the uncemented soil is observed after the cementation is broken, which occurs after yielding. Cuss et al. (2003) verified that in some natural soils, the initial behaviour during isotropic compression is softer due to closure of pre-existing cracks and fissures.

Figure 2.17 presents a schematic comparison of the isotropic compression of weakly and strongly cemented carbonate sand. The consequence of cementation is a stiffer and more elastic initial stress-strain behaviour for a looser sand. This behaviour is related to the beginning of particle breakage, and a gradual yield is followed by the breakage itself. The main difference in the behaviour observed in the weakly and strongly cemented materials was the former reached states outside the intrinsic normal consolidation line (NCL) defined by the uncemented soil, while the weakly bonded soil yielded before reaching the NCL.

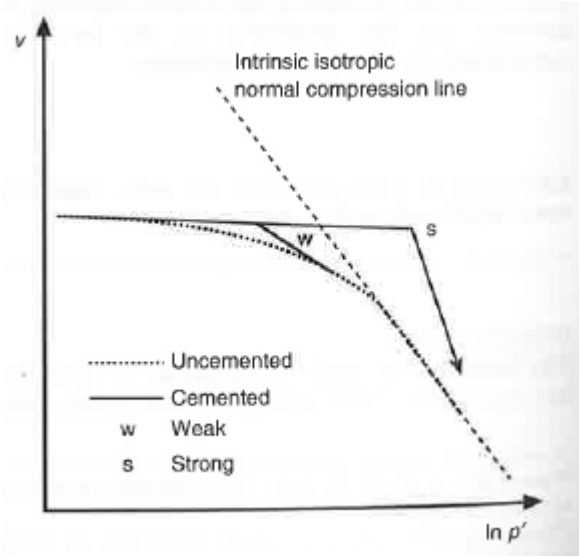


Figure 2.17 – Behaviour of weakly and strongly cemented sand under isotropic compression (CUCCOVILO & COOP, 1999)

Rotta et al. (2003) analysed the response of a soil-cement mixture when isotropic compression was imposed. The study was performed on silty sand stabilized with 0, 1, 2 and 3% cement. Samples were cured under various loads. The results show that the primary yield stress in isotropic compression is a function of the void ratio and cement content. It was also observed that at similar void ratios, the curing confining stress influences the primary yield stress but does not affect the yield stresses.

Figure 2.18a shows that the primary yield stress in isotropic compression increases with higher cement contents for the same void ratio during curing (observed on lines R-S-T). The same figure illustrates that for specimens with the same amount of cement, the primary yield stress increases with the reducing void ratio during curing.

The variation of the primary yield stress with cemented content is presented in Figure 2.18b. It can be observed that where the primary yield stresses increase with curing void ratio for the specimens cured at the same cement content.

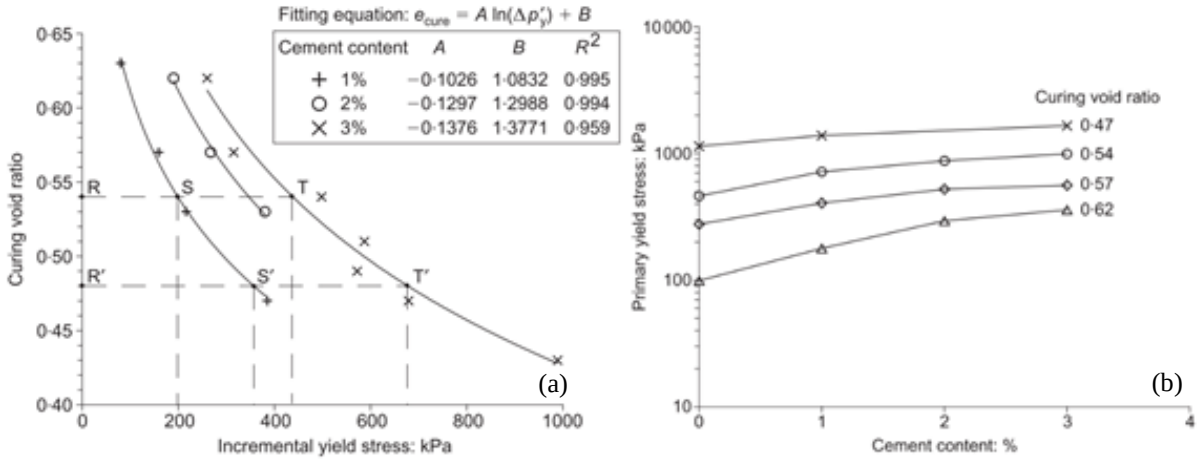


Figure 2.18 – (a) variation of incremental yield stress with curing void ratio; (b) variation of primary yield stress with cement content (ROTTA et al., 2003)

2.3.4 Triaxial Compression

Saxena and Lastrico (1978) studied the behaviour of a lightly cemented sand consolidated isotropically under undrained triaxial tests. It was verified that the cemented soil skeleton initially compresses under a load as would be expected, but with further straining, the cemented soil skeleton tends to dilate (as in dense materials), verified by the pore pressure response and the stress path plots presented (Figure 2.19).

The strength of the cementation agent and sand grains controls the strength of cemented sands. While analysing low strains levels (less than 1%), the cohesion caused by cementation bonding is the major component of strength (SAXENA & LASTRICO, 1978; DASS et al., 1994; DUPAS & PECKER, 1979; ACAR & EL-TAHIR, 1986; SCHNAID et al, 2001). As the strain level increases, cementation bonds are broken, and the frictional strength becomes more predominant. At very high strains (failure conditions), there is a complete breakdown in the cementation and the authors described the shear resistance being entirely frictional (SAXENA et al., 1993; ACAR & EL-TAHIR, 1986; DUPAS & PECKER, 1979). Also, at large strains, the amount of cement added to the soil samples does not significantly change the peak angle of shear strength (SAXENA & LASTRICO, 1978; DASS et al., 1994; DUPAS & PECKER, 1979; REDDY & SAXENA, 1993).

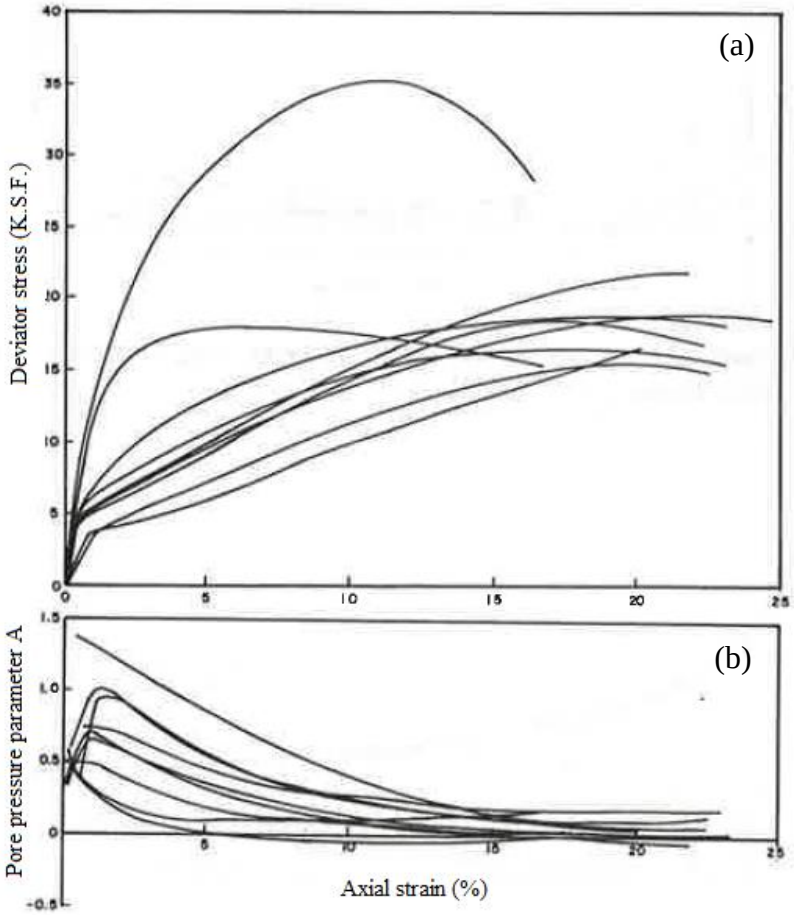


Figure 2.19 – Results from CIU triaxial tests: (a) deviatoris stress and axial strain and (b) porepressure and axial strain (note: 1 ksf = 47.9 kN/m^2) (SAXENA & LASTRICO, 1978)

Saxena and Lastrico (1978) presented the effect of the shear strength of the deposit from a macroscopic view. The undrained strengths were normalized and plotted as a function of the consolidation pressure, as shown in Figure 2.20. It is observed that the consolidation pressure has an immense influence on the undrained shear strength. The increase of consolidation pressure decreases significantly the maximum shear strength of the cemented sand. This behaviour was attributed to bond breakages during consolidation.

It means that the stress-strain behaviour of cemented samples is brittle at low confining pressures and changes to ductile as confinement increases (CLOUGH et al., 1981; AIREY & FAHEY, 1991; LADE & OVERTON, 1989). The post peak behaviour is related to the formation of fractures planes in the cementation (SCHANZ, 1998).

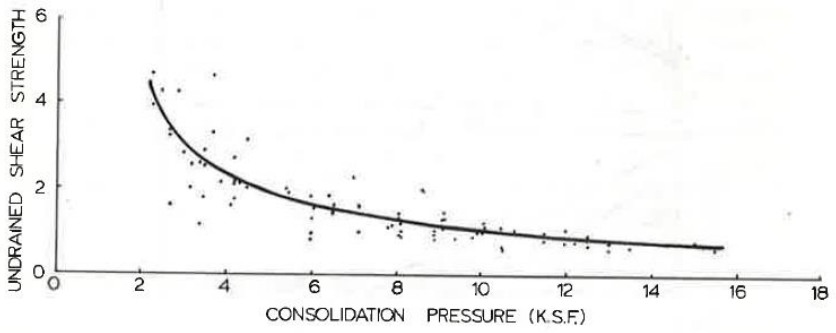


Figure 2.20 – Normalized undrained shear strength versus unconfined pressure (note: 1 ksf = 47.9 kN/m2) (SAXENA & LASTRICO, 1978)

The results observed by Clough et al. (1981) are presented in Figure 2.21. The results are separated by the degree of cementation: Figure 2.21a refers to the strongly cemented sand, Figure 2.21bto the moderately cemented sand and Figure 2.21c to the weakly cemented sand.

The authors verified that stiffness and peak strength increases with the confining pressures for the three cementation degrees. The volume change measurements for moderately and weakly cemented sands shows that strong volumetric expansion is occurring during shear at the lower confinement pressure levels, as the confinement increases, this phenomenon decreases. When a confinement of 414 kN/m^2 is applied, volume change is essentially zero during shearing. Clough et al. (1981) also emphasized that the post-peak behaviour is strongly dependent on the degree of cementation. The strongly cemented soil presents a brittle failure behaviour at all confining pressure levels, while in moderately and weakly cemented soils show a transitional response from brittle to ductile failure as confining pressure increases.

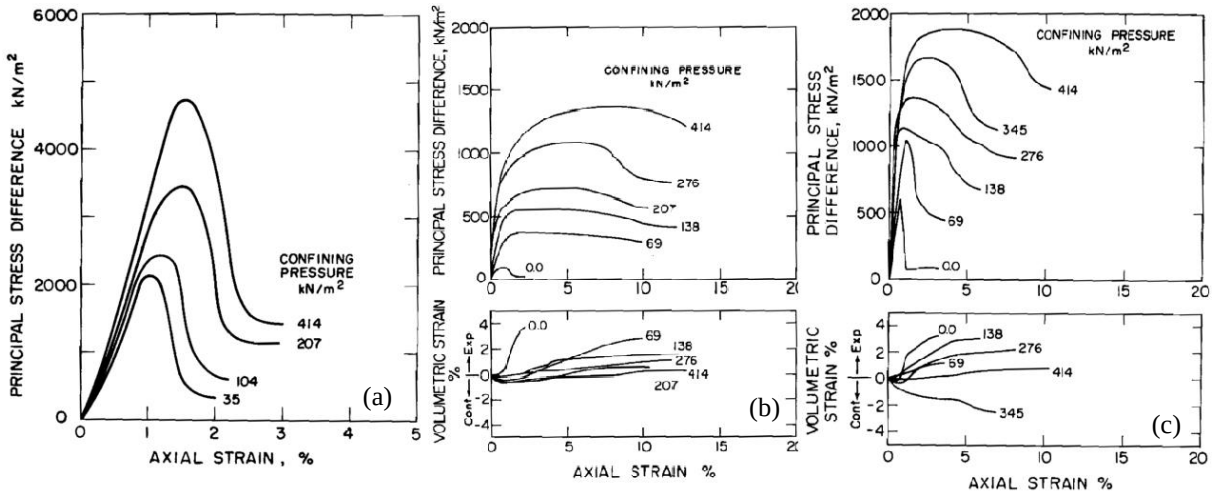


Figure 2.21 – Typical stress-train curves for: (a) strongly cemented; (b) moderately cemented and (c) weakly cemented (after CLOUGH et al., 1981)

Clough et al. (1981) also investigated the response of artificially cemented sand to load. The authors performed triaxial tests with relative density of 74% adding 2 and 4% cement by weight. It is observed that trends for stress-strain and volume change data from the artificially cemented sand are similar to trends for the naturally cemented sand. Figure 2.22 also shows that there is a frictional response in the stiffness and strength increasing with the confining pressure. Further, the transition from brittle to ductile failure with the confining pressure occurs earlier for the less cemented sand.

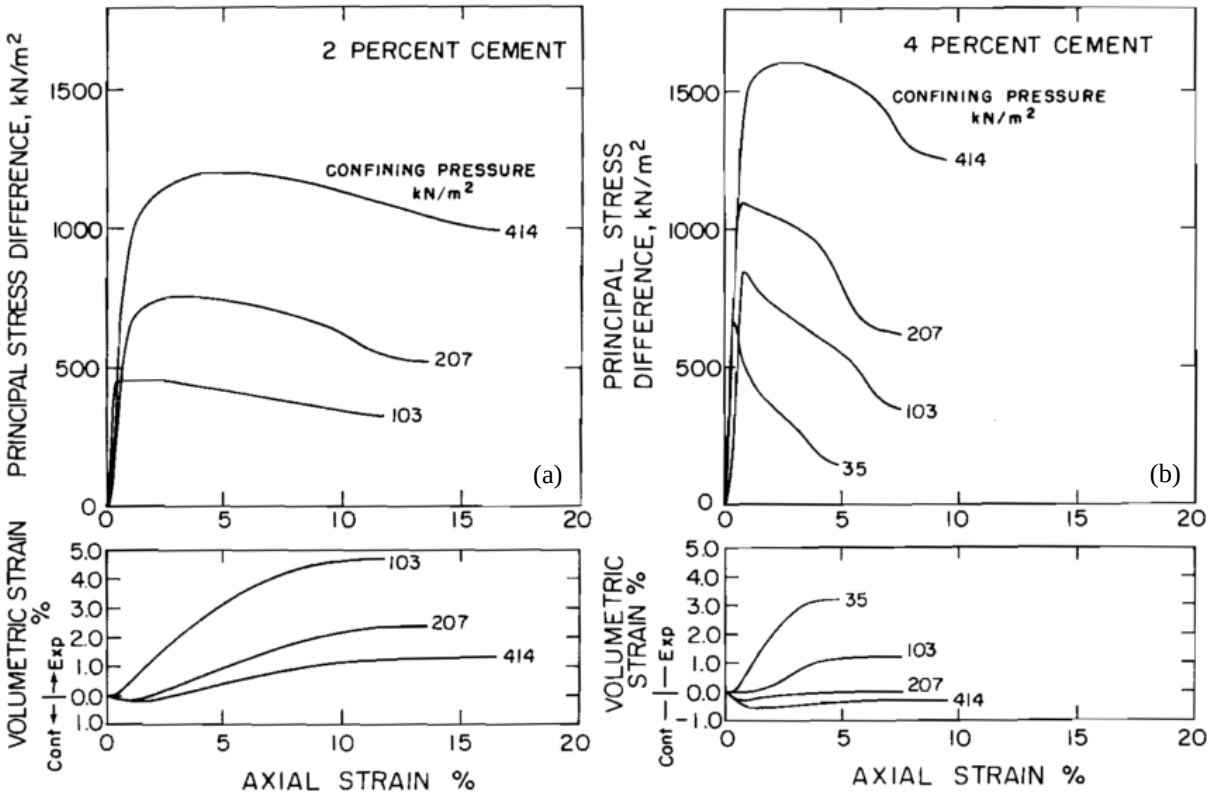


Figure 2.22 – Stress-strain curves for (a) 2% cement and (b) 4% cement (after CLOUGH et al., 1981)

Figure 2.23 illustrates the effect of cement content in the shear response of a cemented soil (SCHNAID et al., 2001). It is observed that the soil behaviour is strongly dependent on the cement content. The stress-strain behaviour of the cemented soil starts linearly and apparently leads up to a well-defined yield point. Beyond this, the soil suffers increasingly plastic deformation until failure. When the cement content increases, both peak strength and initial stiffness increase. A brittle at failure behaviour is observed from the cemented specimens. As for the volumetric response, the cemented specimens show an initial compression followed by strong expansion with the maximum dilation rate just after the peak strength.

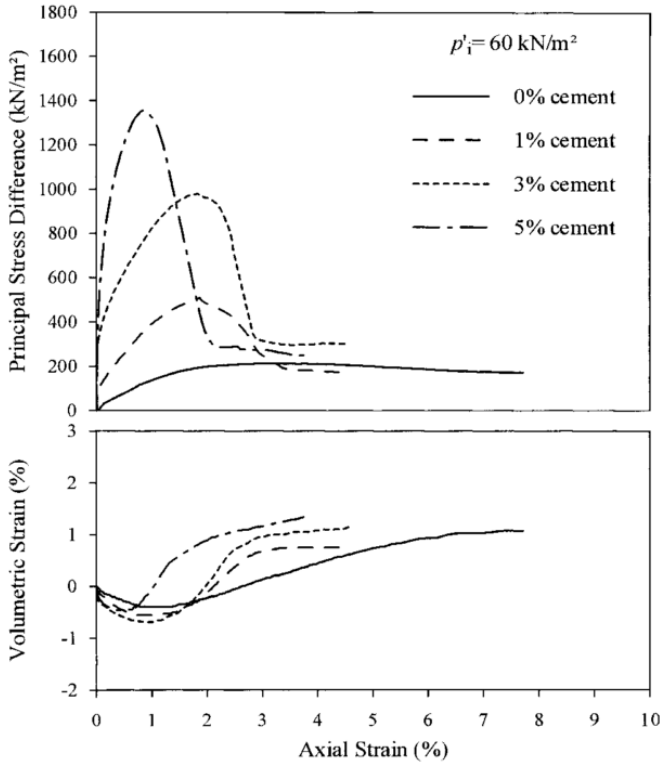


Figure 2.23 – Stress-strain volumetric response for uncemented and cemented sandstone (SCHNAID et al., 2001)

The dilative behaviour observed from cemented specimens is more prone to occur at low confinement because cemented small particles form highly interlocked, large particles (SAXENA et al., 1988; SAXENA & LASTRICO, 1978; LADE & OVENTON, 1989).

Airey and Fahey (1991) described that regions of no breakdown, stable breakdown and rapid breakdown of cementation are formed during loading. These regions correspond to elastic loading without pore-pressure generation, stabilization after pore-pressure generation, stabilization after pore-pressure generation and steady pore-pressure build-up and failure.

Clough et al. (1989) explained that even cemented sand can liquefy: the soil-cement possess high initial resistance to volume change, reducing pore-pressure generation and increasing resistance to liquefaction.

2.3.5 Cubical Triaxial

A series of stress paths including hydrostatic compression, conventional triaxial compression and tests along different octahedral planes were presented by Reddy and Saxena (1993). The uncemented sand and cemented sand (2% cement) tests on the true triaxial were carried by first loading the specimen hydrostatically to the octahedral normal stress pre-defined. The stresses

were then adjusted to stay on the same octahedral plane but following different monotonic shear stress paths. The stress paths are defined by intermediate principal stress parameter *b*-values.

The authors evaluated the effect of these distinguish load conditions upon a sand and a cemented sand mixture. It was observed that the angle of internal friction for the cemented and uncemented sands were very close under all stress paths tested. The increase of *b*-values, up to $b = 0.75$, leads to an increase of internal friction angle, after 0.75, it drops slightly (Figure 2.24). Same behaviour is observed for the cohesion to the cemented sand.

A pronounced effect on the stress-strain and strength behaviour imposed by the intermediate principal stress was observed. Higher *b* values result in higher strains at smaller octahedric stress levels. This behaviour was observed for cemented and uncemented specimens. (Figure 2.25)

The work also observed that dilation at failure did not depend on the *b* values for both cemented and uncemented tests. As for the volumetric strain at failure, it was observed that an increment at *b*-value resulted at an increment of volumetric strain. The dilation for cemented sand was slightly higher than the uncemented sand, as presented in Figure 2.26.

Reddy and Saxena (1993) concluded that though the cemented sand was subject to the same stress state, the behaviour differed depending on the stress path followed to reach the stress state. The same behaviour was observed for uncemented sand.

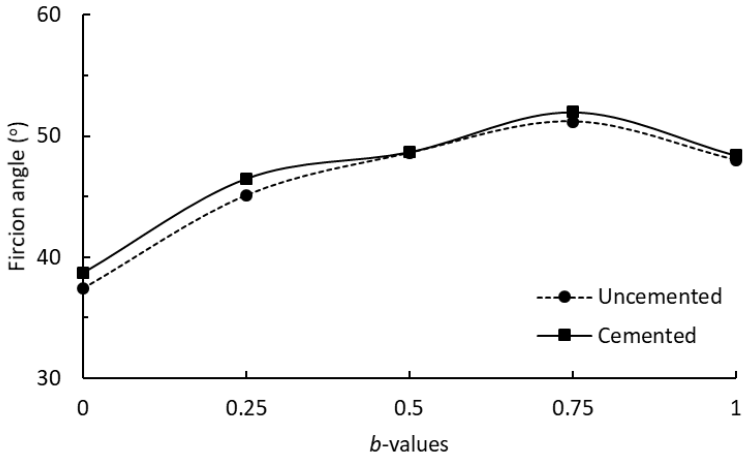


Figure 2.24 – Variation of friction angle with b-value
(after REDDY & SAXENA, 1993)

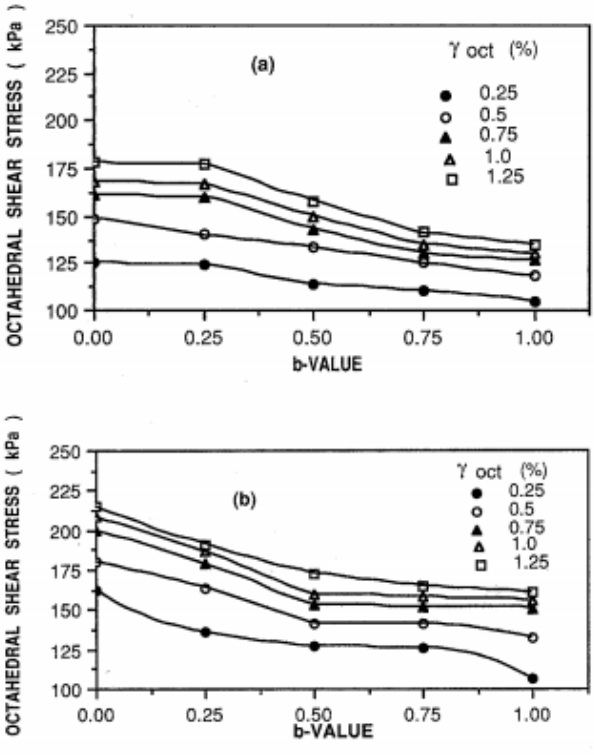


Figure 2.25 – Octahedral stress-strain contours for (a) uncemented and (b) cemented sand (REDDY & SAXENA, 1993)

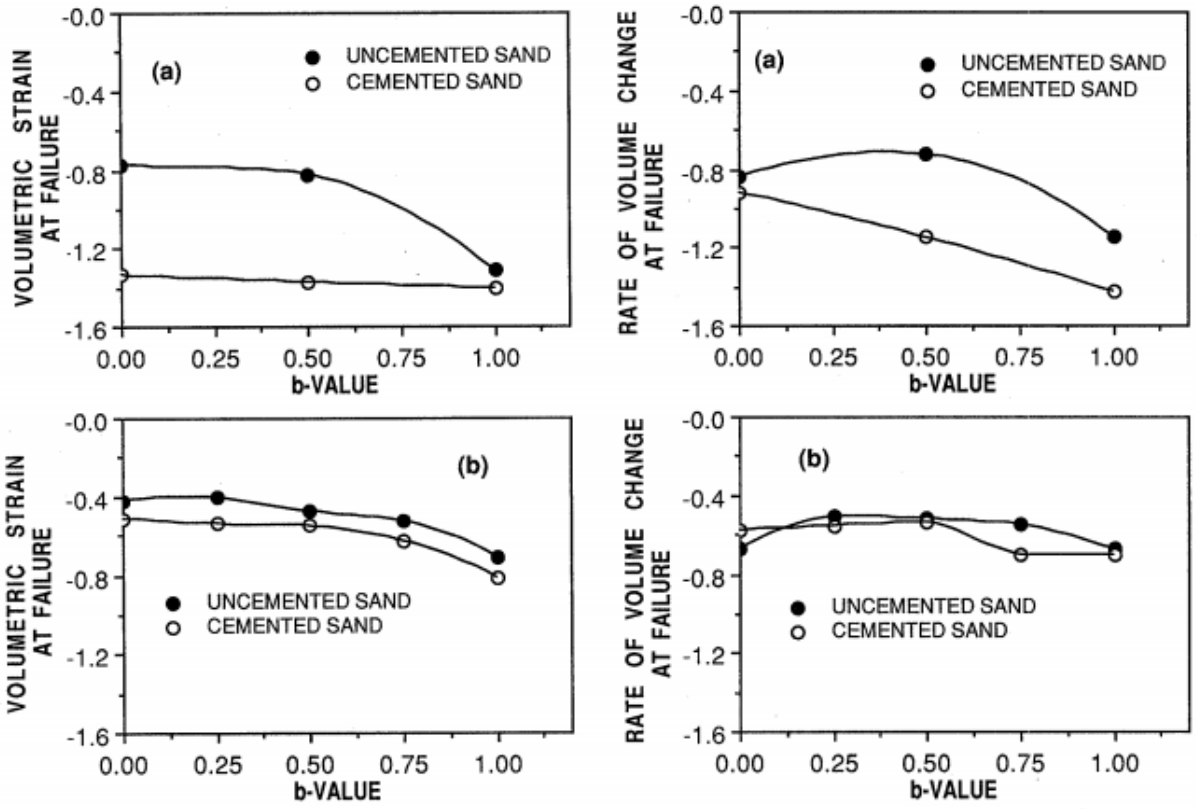


Figure 2.26 – Rate volumetric strain at failure: (a) σ_{oct} = 138 kPa; (b) σ_{oct} = 276 kPa and; rate of volume change at failure under: (a) σ_{oct} = 138 kPa; (b) σ_{oct} = 276 kPa (REDDY & SAXENA, 1993)

2.4 STIFFNESS DEGRADATION OF CEMENTED SOILS

The understanding of soil behaviour relies on the comprehension of the non-linearity of soils. The strain dependent concept of soils is only possible by the concept of non-linearity (ATKINSON, 2000). Also, geotechnical modelling, which is widely applied nowadays, is more precise due to the insertion of non-linear elastic behaviour of soils. For the understanding the non-linear behaviour of soils, it is fundamental to comprehend the stiffness of soils.

Stiffness is the resistance of a body to deformation under applied force; it depends on the shape of the body, boundary conditions, and stiffness properties of the material (CLAYTON, 2011). At *small strain* levels, an isotropic soil can be presumed to behave as a *linear elastic material* and in this case, only two parameters are necessary to characterize deformations: Young's Modulus E and Poisson's Ratio μ, or Shear Modulus G and bulk Modulus K. At *higher strain levels*, nonlinearity of the soils is observed with decay in stiffness. In a shear stress-strain curve, as shown in Figure 2.27a, stiffness at very small strains is represented by a tangent or secant Young's Modulus E_t or E_s, respectively. At peak deviator stress, the soil fails and there is a decrease in stiffness. The non-linear soil behaviour is represented by this change in stiffness.

Picture 2.27b shows the change in stiffness in soils. Three defined regions where the stiffness secant or tangent Young's Modulus changes with the increase of strain: constant stiffness at very small strains, represented by E_0 and limited ε_0, small strain region to a maximum of 0.1% of strain where the stiffness decreases rapidly, and large strain level where stiffness is very low (ATKINSON & SALLFORS, 1991).

Burland (1989) contended that the strain range of stiff soils near structures is generally located in the very small to small strain region and it is represented in Figure 2.28. The small strain stiffness parameters are commonly used as an input value for constitutive models and they are also necessary to characterize the stiffness changes with strain levels. This changes with the level of strain in non-linear soil behaviour (LINGS, 2001).

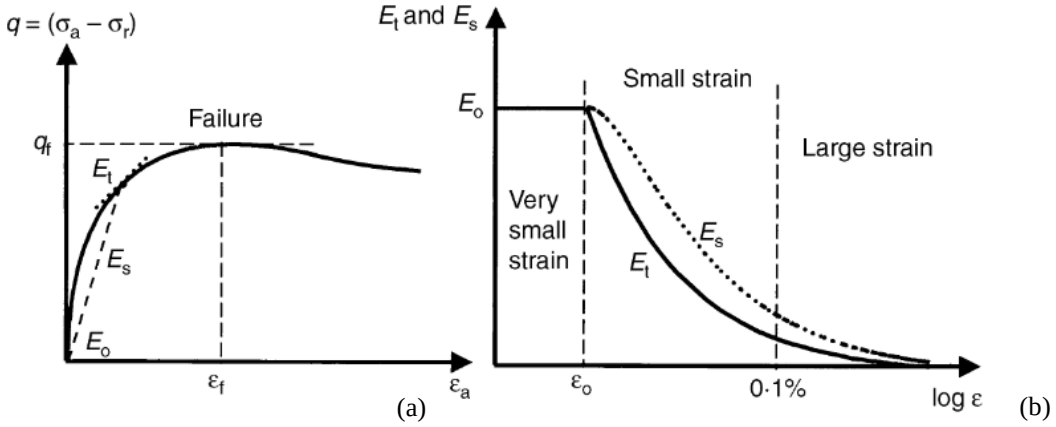


Figure 2.27 – Simple stiffness parameters for non-linear soil (adapted from ATKINSON, 2000)

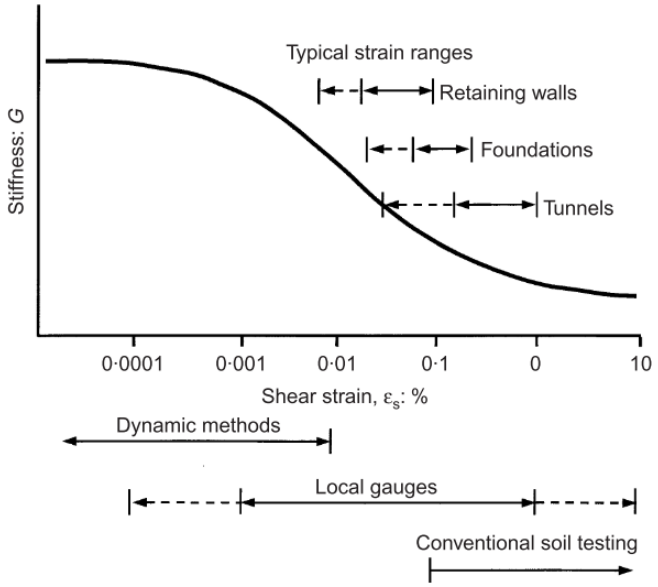


Figure 2.28 – Characteristic stiffness-strain behaviour of soil with typical strain ranges for laboratory tests and structures (ATKINSON, 2000 after ATKINSON & SALLDORS, 1991 and MAIR, 1993)

In order to understand the stiffness and stiffness evolution of cemented soils, it is fundamental to comprehend the mechanisms involved when the load is applied. The next section discusses the debonding of particles and is followed by presentation of small and large strain behaviour.

2.4.1 Debonding

In laboratory artificially cemented soils are prepared by mixing the soil and cementation agent at a pre-determined moisture content and compacting the mixture to the target density within moulds. In most studies, hardening takes place within the mould and then cemented specimens are placed in the testing device so a cementation-before-loading is applied. Sometimes, the

specimen is prepared by placing the fresh soil-cement mixture in the final device (e.g., triaxial cell), and then it is confined and let to cure under constant effective confinement before testing.

Figure 2.29 presents the behaviour of loading before or after cementation takes place. The order of loading before or after cementation has relatively a small effect on the attained stiffness (FERNANDES & SANTAMARINA, 2001; RINALDI & SANTAMARINA, 2008). Still, stiffness seems to be slightly higher in the case of loading-before-cementation. Nevertheless, its impact on the ability of the cementation to survive load removal and sampling is completely different. Figure 2.29a considers the case of cementation-before-loading, where both the cement and the particles mixture develop compressive stress in response to the applied load; when the load is removed, the stresses vanish. In the case of loading-before-cementation (Figure 2.29b), the grain contact is compressed but the cement is not; when the load is removed, the contact stretches and tensions are applied to the cement phase, which may trigger the break of the cemented bridges. Therefore, the case of loading-before- cementation is most sensitive to sampling (FERNANDES & SANTAMARINA, 2001; RINALDI & SANTAMARINA, 2008).

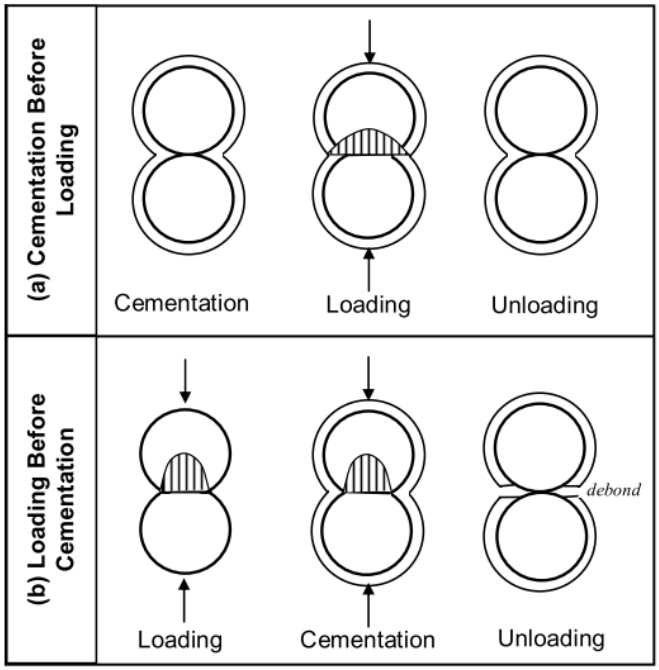


Figure 2.29 – Two different cementation-loading histories: (a) cementation before loading and (b) loading before cementation (RINALDI & SANTAMARINA, 2001 after FERNANDES & SANTAMARINA, 2008).

Debonding or decementation results when the granular skeleton is strained or when the cementing substance is dissolved. Strains may be caused by changes in interparticle forces of

any kind: capillary forces (expansion, saturation collapse, desiccation shrinkage), electrical forces in relation to pore fluid chemistry (both shrinkage and swelling), and interparticle skeletal forces (isotropic loading or unloading including the effects of heating or freezing, deviatoric loading, cyclic loading and fatigue). The dissolution of cementation is primarily associated with changes in moisture content (e.g., dissolution of precipitated salts and dispersion of flocculated clay bridges), changes in pH (e.g., dissolution of carbonates when reservoir water acidifies), and low salt concentration fluid flow (FERNANDES & SANTAMARINA, 2001; LEROUEIL & HIGHT, 2003; RINALDI & SANTAMARINA, 2008).

The bond between soil and cement is gradually destroyed with incremental increase of stresses or strains. The consequence is the contribution to this small cementation degradation to yielding. From the first yielding, bond breakage affects stiffness. The shear modulus starts to degrade, and the behaviour of the cemented soil starts to converge towards the expected behaviour of an uncemented material, a fact observed for both monotonic and cyclic triaxial loading. Equally, yielding can occur even during isotropic compression at high confining stresses. At intermediate stress levels, however, yielding occurs in the initial stages of shearing (AIREY; FAHEY, 1991; COOP; ATKINSON, 1993; CUCCOVILLO; COOP, 1997; SHARMA; FAHEY, 2003, FERNANDES & SANTAMARINA, 2001; LEROUEIL & HIGHT, 2003; RINALDI & SANTAMARINA, 2008).

Fernandes and Santamarina (2001) divided the behaviour of cemented materials in two regions: cement content and uncemented (Figure 2.30). Cemented materials start in the region where cementation prevails. In this region, stiffness is stress independent, as the flat lines indicate, resulting in no change of modulus due to stress increment. Once stress starts to increase, bond breakages occur, and the soil stiffness gradually becomes stress dependent. This behaviour continues until the dividing line is reached, after which the soil presents an uncemented behaviour.

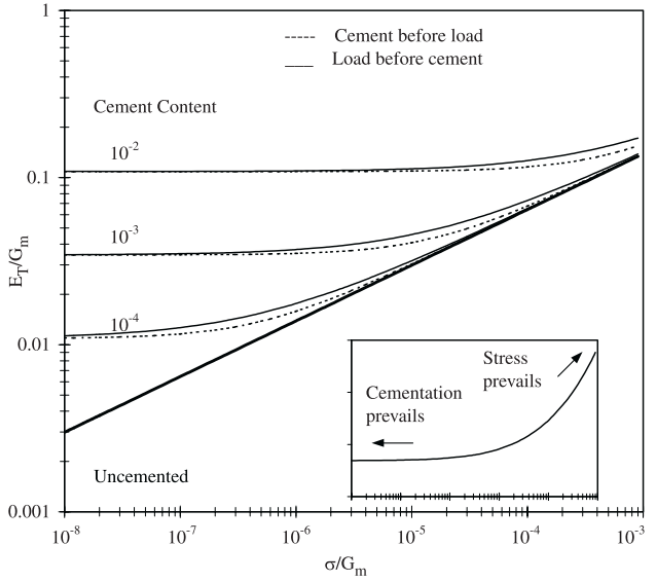


Figure 2.30 – Comparison between the two load-condition histories: micromechanical model (assuming a Poisson's ratio of 0.25) (FERNANDES & SANTAMARINA, 2001)

2.4.2 Small strain behavior

When referring to small strain in this section, the main concept is the elastic behaviour expected inside the cementation yield surface. It is observed that the elastic behaviour inside the cementation surface varies with the degree of cementation (BAIG et al., 1997; CLOUGH et al., 1981; HUANG & AIREY, 1998; SCHNAID et al., 2001; SHARMA & FAHEY, 2003, 2004; FERNANDES & SANTAMARINA, 2001, TRHLÍKOVÁ et al, 2012).

Figure 2.31 schematises the behaviour expected before yield takes place. It is observed that the relation between the elastic modulus and the stress is shown for increasing the degree of cementation. The elastic modulus increases as the stress is increased, increasing the degree of cementation results in higher elastic modulus as well (TRADS & LADE, 2014). Furthermore, the elastic modulus becomes less dependent on the confining pressure with increased cementation.

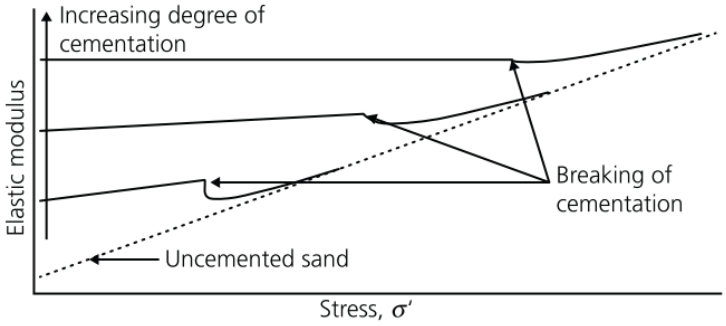


Figure 2.31 – Evolution of elastic modulus with increasing cementation and pressure (TRADS & LADE, 2014)

The elastic modulus becomes less dependent on the confining pressure with increased cementation (SHARMA & FAHEY, 2004). Baig et al. (1997) concluded that the effect of confining pressure was less significant at small strains, rendering the effect of confining pressure negligible for the dynamic properties of cemented soil. Figure 2.32 presents the G_{sec} versus ε_s behaviour of two cemented samples confined at different pressures. The data demonstrates a threshold yield strain $\varepsilon_{s\ yield}$, which separates the plateau of initial constant stiffness from the start of substantial stiffness degradation. Although degradation evolves differently for both tests, $\varepsilon_{s\ yield}$ was about 0.0002 for both. With this result, authors suggested that there was no significant breakage degradation during consolidation.

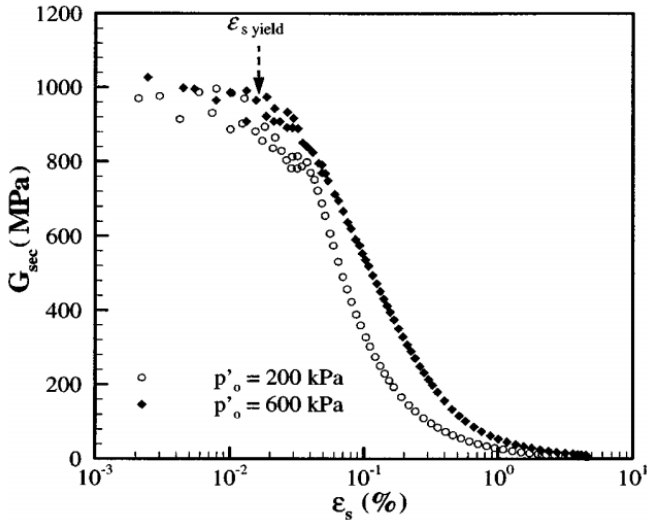


Figure 2.32 – Variation of G_{sec} with deviatoric strain amplitude for cemented samples (SHARMA & FAHEY, 2003)

The elastic behaviour through cementation bond breakage has been studied under different loading conditions: Huang and Airey (1998) determined the static bulk modulus during

isotropic loading, Fernandez and Santamarina (2001) determined the dynamic elastic modulus during isotropic loading, Sharma and Fahey (2003) investigated the degradation of stiffness during triaxial compression, and Yun and Santamarina (2005) examined the dynamic stiffness during K_0 loading. In general, it is observed that as the bonds start breaking, a decrease in elastic modulus is experienced. As the elastic modulus of the cemented soil reaches that of the uncemented soil, the elastic modulus starts increasing, eventually becoming identical to that for the uncemented soil. If the initial degree of cementation is increased, the stress required to break the cementation increases, and the subsequent drop in elastic modulus diminishes. The dynamic elastic modulus has been found to not converge towards the elastic modulus of the uncemented soil as easily as the static elastic modulus.

Elastic modulus has been found to be similar for tension and compression (TALESNICK et al. 2000; LIAO et al., 1997). Liao et al. (1997) found argillite to be stiffer in tension then in compression, attributed to closure of microfissures in compression, indicating that stress history causes different elastic moduli in compression and tension. Figure 2.33 represents the stress-strain relation in compression and tension. In compression, Young's modulus increases as the fissures close and eventually becomes equal to Young's modulus in tension. In tension, the elastic modulus remains constant (LADE & TRADS, 2014).

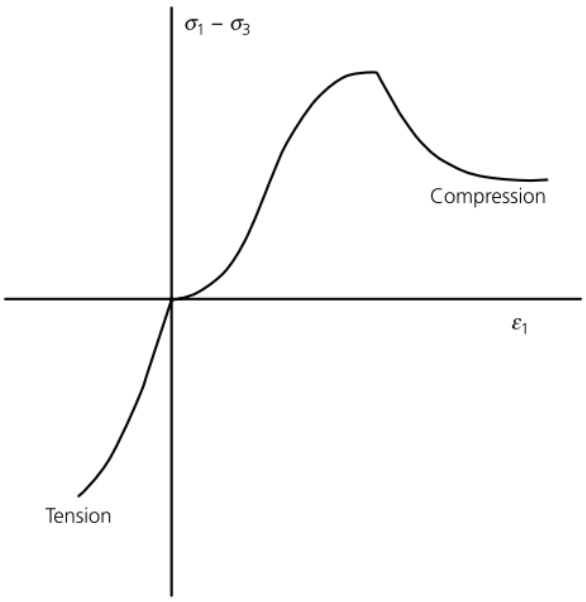


Figure 2.33 – Closure of fissures results in initial lower Young's modulus in compression then in tension
(TRADS & LADE, 2014, after LIAO et al., 1997)

2.4.3 Large Strain behavior

The linear-elastic behaviour is no longer observed after stiffness degradation occurs at certain levels of strain (Figure 2.34). At this point, soils start an elastoplastic path, requiring different analytical approaches. Figure 2.35 illustrates the associated phenomena, soil response, and interpretation method within strain ranges (options for cyclic conditions). At medium and large strains, the soil can be interpreted as a viscoelastic material. The main differences between elasticity and viscoelasticity are related to the fact that viscous elements are both time-dependant and capable of energy dissipation (KARASUDHI, 1991; ISHIHARA, 1996; BARDET, 1997)

As a matter of fact, linear elasticity and viscoelasticity are completely opposite theories, and the majority of materials behave in between these axioms. Elastic materials store energy with no dissipation, whereas viscoelasticity proposes the storage and dissipation of part of the input energy. Therefore, viscoelastic analysis can be simplified to a linear relationship between stress and strain, superimposed by the measurement of its energy dissipation capability. The damping ratio comes to fill in this need to measure the dissipated energy. Moreover, viscoelastic materials are rate dependent, i.e., the soil behaviour is rate dependent (KARASUDHI, 1991; ISHIHARA, 1996; BARDET, 1997).

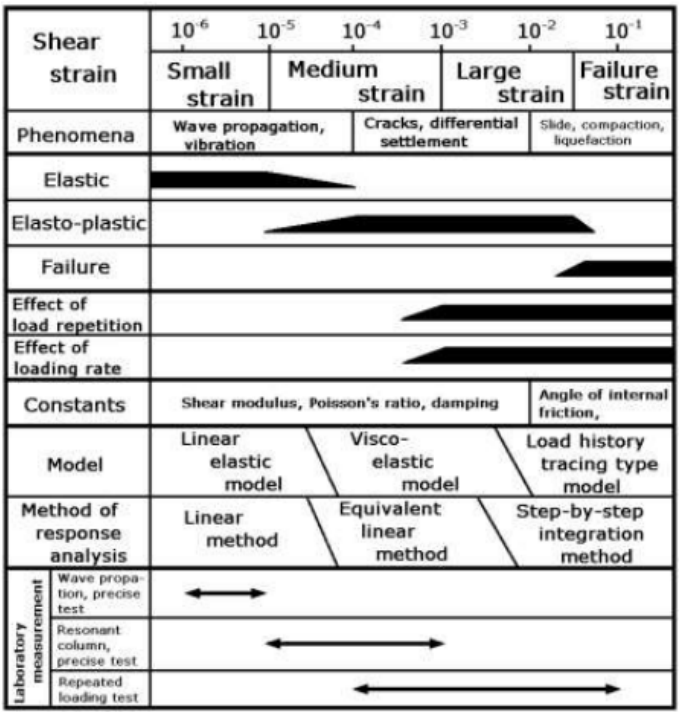


Figure 2.34 – Soil behaviour within the strain-range dependency associated phenomena, theoretical models, and laboratory measurements (BORTOLOTTO, 2017 after ISHIHARA, 1996)

Viscoelasticity is an option to address stiffness degradation (at medium strains) through dynamic methods. However, the energy required to dynamically produce this level of strain is high and is usually associated with instability. On the other hand, repeated loading at low frequency is suitable for these measurements and does not require any theory to interpret system response, as parameters are obtained directly (KARASUDHI, 1991; ISHIHARA, 1996). For instance, Atkinson (2000) generalized his claims for all kinds of soils, while the results obtained by Airey and Fahey (1991) demonstrated the effect-rate independence for calcareous soil. On the other hand, significant outcomes endorsing strain-rate dependence have also been obtained for stiff clays (GASPARRE et al., 2014) and sandy soils (LO PRESTI et al., 1997).

The non-linear stiffness degradation can also be described by the hyperbolic model, presented for the first time in the 19th century. As the name indicates, soil non-linearity is described by a hyperbole on a stress plane versus the corresponding strain (shear stress and strain) (DUNCAN & CHANG, 1970). Santamarina et al. (2001) also present this methodology with a different approach, pointing out the difference between the tangent and secant moduli.

It is widely accepted that the stress–strain curve shows hysteresis and accumulation of irreversible strains with increasing number of cycles if the stress imposed during cyclic loading lies outside the true elastic range (KOKUSHO, 1980; TATSUOKA et al., 1995; LO PRESTI et al., 1997, SHARMA & FAHEY, 2004). The characteristic features of the hysteresis loops are further examined by comparing the degradation of secant stiffness in unloading and reloading loops against deviatoric strain amplitude ε_s, as presented in Figure 2.35. The value of ε_s in unloading is calculated by subtracting the deviatoric strain from the maximum deviatoric strain corresponding to the peak point of the hysteresis loop; the absolute value is shown in the figure. These results clearly show that the values of G_{sec} during unloading and reloading are similar at similar values of ε_s.

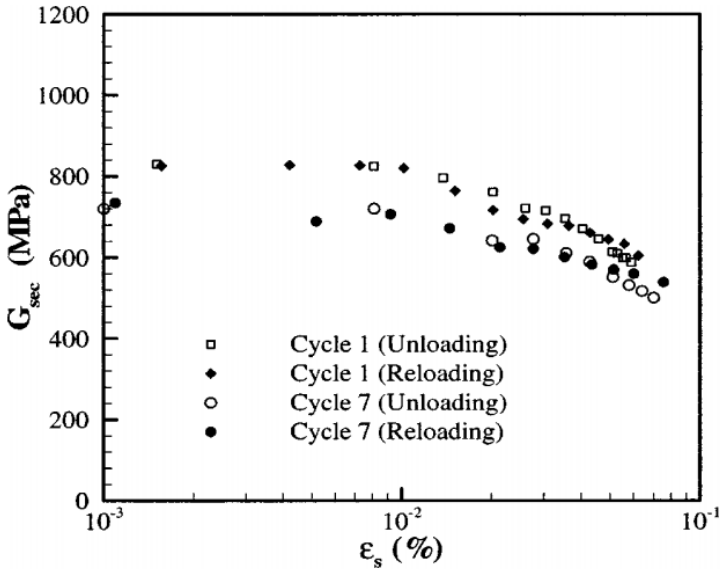


Figure 2.35 – Secant modulus for unload-reload loops against amplitude of deviatoric strain for cemented samples (SHARMA & FAHEY, 2003)

2.5 FAILURE SURFACE

As mentioned previously, the bonds' breakages are the first failure observed when loading cemented soils. After this breakage, the frictional resistance of the soil matrix will control the strength behaviour (COOP & ATKINSON, 1993; RABBI & KUWANO, 2012). When referring to cemented soil resistance, the failure of two phases should be considered: the failure of the cement phase and the failure of the soil phase.

The strength of a material is simply defined as the maximum shear stress that it can sustain. Depending on the material, failure will be sudden and catastrophic, leading to a complete loss of strength or a very large plastic straining. For most soils, failure of slopes and foundations involve a large plastic straining without complete loss of strength and failing soil structures can usually be stabilized by unloading them (ATKINSON, 2001).

2.5.1 Mohr-Coulomb

The strength of soil is usually defined in terms of the stresses developed at the peak of the stress-strain curve. The simpler way to determine this curve is through Mohr circles. First, Mohr circles are drawn to represent the states of stresses at the peak points of the stress-strain curves. Then, a line is drawn tangentially to the Mohr circles (LAMBE & WHITMAN, 1969). This curve is called *Mohr failure envelope* and it is represented in Equation 2.5.

$$\tau = c + \sigma \tan \phi \quad (2.5)$$

where τ is the shear strength, c is the cohesion or cohesion intercept and ϕ is the friction angle or the angle of shearing resistance.

2.5.2 Failure criterion

Figure 2.36 presents the yield and failure surfaces of a cemented soil after Lade and Trads (2014). Due to the tensile strength caused by cementation, the failure surface initiates in the part of the stress space where the stresses are negative, and it opens in the outward direction of the hydrostatic axis. Then, the yield surface bends backwards towards the hydrostatic axis corresponding to lower values of q before it crosses the failure surface. The uniaxial compressive strength corresponds to a point on the yield surface, which is outside or coincides with the failure surface at this point. The stress–strain curve in the uniaxial compression test indicates that yielding and failure coincide, and softening follows immediately after failure.

The tensile strength is helpful in determining the location of the failure surface in the region of low stresses. It is important to model the failure surface correctly in this region because this is where tensile fracture occurs, and the material exhibits very brittle behaviour at low stresses. The locations of the plastic yield point for isotropic and K_0 compression are also indicated in Figure 2.36 (LADE & TRADS, 2014).

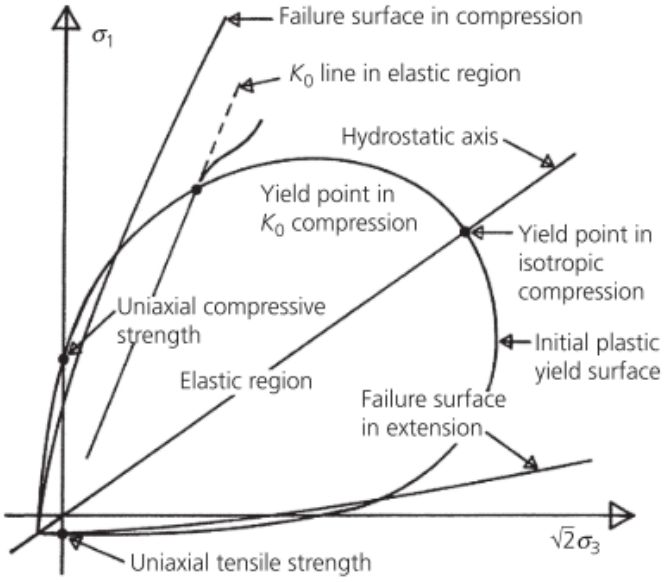


Figure 2.36 – Conceptual model for the tree-dimension conditions shown in triaxial plane (LADE & TRADS, 2014 after LADE & KIM, 1988)

The behaviour is elastic inside the initial plastic yield surface (TRADS & LADE, 2014), as indicated in Figure 2.37. Plastic behaviour is encountered as the stress point moves beyond the yield surface, and softening will occur immediately in the region where the yield surface is outside the failure surface. Thus, in this region, the yield surface is also the failure surface. In fact, in the region where the yield surface becomes the failure surface, the peak failure is caused by and is immediately followed by strain localisation and shear banding. This is in complete agreement with the effects of over-consolidation, as encountered in sands and clays (LADE & PRABUCKI, 1995)

The softening is more pronounced at lower confining pressures, where shear banding follows the peak. This is because the plastic yield surface crosses the failure surface and the yield surface becomes the failure surface at lower confining pressures, as indicated in Figure 2.37a. In the region of larger mean normal stresses, where the yield surface is inside the failure surface, the stress–strain behaviour that exhibits work hardening before failure is encountered at larger strains. In this region, the cementation continuously degrades until it is completely broken at large strains. As the stresses reach further up, smooth peak failure is encountered with smooth transition into softening. The corresponding stress– strain behaviour is shown in Figure 2.37b.

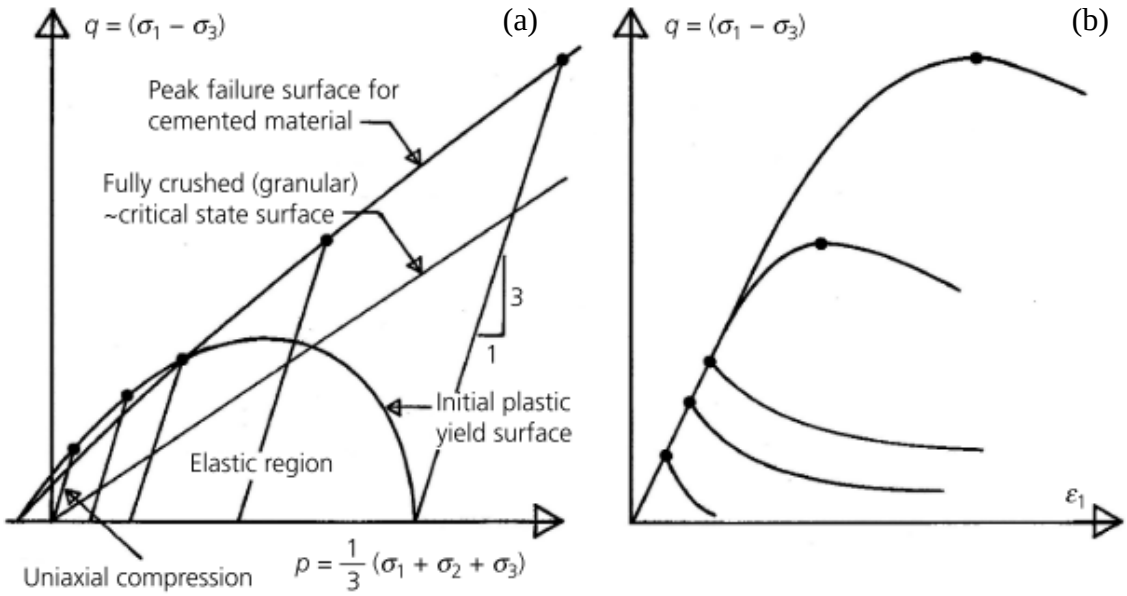


Figure 2.37 – Conceptual model for stress-strain behaviour of cemented material in triaxial tests; (a) q versus p' (b) q versus ε (LADE & TRADS, 2014 after LADE & KIM, 1988)

2.5.3 Effect of the intermediate principal stress

The intermediate principal stress has a pronounced effect on the stress–strain and strength behaviour of all frictional materials. While the Mohr–Coulomb failure criterion is the classic failure criterion for frictional materials, it predicts that the intermediate principal stress has no effect on the strength of frictional materials. The von Mises criterion, on the other hand, predicts a too large and very inaccurate influence of the intermediate principal stress, even when modified as in Drucker and Prager (1952).

Many experiments have been performed on various types of rock as well as on concrete, and they all appear to produce similar and comparable results, as reviewed by Lade (1993). The experimentally observed failure surfaces, indicated in Figure 2.38, are shaped as an asymmetric bullet with the pointed apex located on the negative side of the hydrostatic axis, and with a cross-sectional shape in the octahedral plane that is triangular with smoothly rounded edges. The curved failure surface is concave towards the hydrostatic axis.

Shear banding in the hardening regime of the stress–strain relations for high confining pressures where the cementation has been broken may modify this shape in the midrange of b values, where $b = (\sigma_2 - \sigma_3)/(\sigma_1 - \sigma_3)$.

The effect of the intermediate principal stress on the strength of sandstone and mudstone was also examined by Lee et al. (2010). In both materials, the effect of the intermediate principal stress is like that shown in Figure 2.38. This is also an agreement with tests performed by Reddy and Saxena (1993) on artificially cemented sand. The effect of the intermediate principal stress was also noted by Al-Ajmi and Zimmerman (2005) after compiling triaxial strength data of eight different porous rocks.

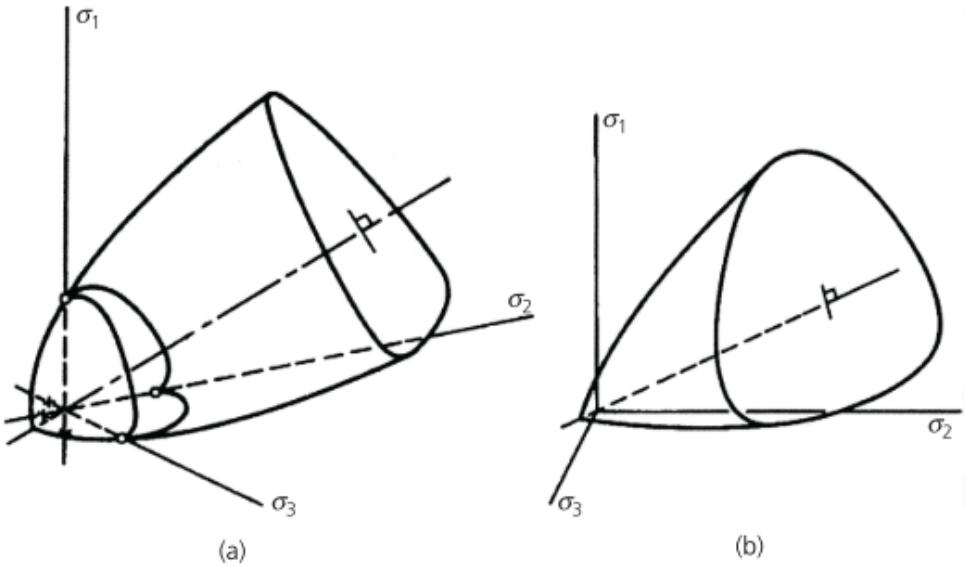


Figure 2.38 – Three-dimensional failure surface produced from experimental evidence and viewed (a) from the side to show curved envelope in triaxial plane and biaxial planes and (b) from the end to show smoothly rounded triangular shape in octahedral plane (TRADS & LADE, 2014 after REDDY & SAXENA, 1988)

2.5.4 Theoretical constitutive modelling

According to Lade and Trads (2014) all aspects of the behaviour of cemented soils may be modelled by elasticity and hardening plasticity theories for which the components of the failure surface, the plastic potential and the yield surface with the associated hardening law are expressed. Thus, the same framework as that used for modelling soils works well for cemented soils. Only a small change in the expression for the normal stresses before substituting into the expression for the failure and yield surfaces is required to account for the cohesion and the tensile strength observed near the stress origin. The parameter values consequently change, but the behaviour is otherwise similar to that of soils.

Several theoretical models have been proposed for predicting the overall constitutive behaviour of cemented soils. They are usually based on modifications of state boundary surfaces and hardening rules adopted for granular soils (e.g., Hirai et al. 1989; Sun and Matsuoka 1999), or they consider the cemented soil as a multiphase material imposing the superposition of the stress contributions of cement bonds and sand grains (e.g., ABDULLA & KIOUSIS 1997; VATSALA et al. 2001).

2.6 LOW CEMENTATION

Rad and Clough (1982) contended that cemented sands are often difficult to describe because there is no formal classification for them. Terms such as weakly cemented, moderately cemented and strongly cemented are used when referring to cemented soils. For this reason, the authors proposed a system to classify the cemented soils. The classification is based on the unconfined compressive strength of undisturbed samples as an index. The classification separates the cemented soils into four different categories:

a) very weakly cemented soils: with UCS < 100 kN/m^2. The cementation is almost unapparent to the touch, and undisturbed sampling is difficult to achieve, if not impossible. However, freezing the soil may be a suitable technique;

b) weakly cemented soils: with 100 < UCS < 300 kN/m^2. The soil breaks under light finger pressure, and a block sampling technique with care can be used to obtain undisturbed samples. This soil can be easily stretched with the fingertip;

c) moderately cemented soils: with 300 < UCS < 1000 kN/m^2. The soil hardly breaks apart under finger pressure, and undisturbed specimens can be easily obtained from a clock sample. The presence of cementation bonds between the particles is readily felt, and the soil can be scratched with the fingernail;

d) strongly cemented soils: with 1000 < UCS < 3000 kN/m^2. A power saw can be used to cut block samples; trimming of specimens with ordinary hand tools is difficult. The soils hardly break under hand pressure and cannot be easily scratched with the fingernail.

Despite this system of classification proposed by Rad and Clough (1982), the terms of poorly cemented, lightly cemented and breaks under finger pressure are still commonly used. For this reason, this chapter will keep the term adopted by the presented author when referring to the cement content.

2.7 DOSAGE OF SOIL-CEMENT

As presented in 2.2.3.1, the amount of cement added to a soil mixture is related to the strength and durability that a certain design requires. The American Society for Testing and Materials

(ASTM, 1944) presented an initial standard of tests to be followed in order to use the soil-cement technique.

Each country has its own criteria for cement content. Ingles and Metcalf (1972) presented a guideline of percentages of cement depending on soil type (Table 2.1).

Table 2.1 Cement content according to soil type for pavement construction (INGLES & METCALF, 1972)

Soil type	Cement requirement (%)
Fine crushed rock	0.5 – 2
Well graded sandy clay gravels	2 – 4
Well graded sand	2 – 4
Poorly graded sand	4 – 6
Sandy clay	4 – 6
Silty clay	6 – 8
Heavy clay	8 – 12
Very heavy clay	12 – 15
Organic soils	10 - 15

Nevertheless, the amount of cement is not the only parameter necessary in order to obtain a rational criterion for the dosage of cemented soils.

Foppa (2005) investigated the key parameters that influence on the shear strength of a cemented soil. The author presented a dosage methodology wherein two parameters control the soil resistance: the porosity (η) and the volumetric amount of cement (C_{iv}). The methodology can be related to the ratio of water and cement content of concrete.

This methodology is express as $\eta/(C_{iv})^k$, where k is an exponent factor for the cement content parcel. The dosage methodology is obtained through a curve void/cement versus the unconfined compression strength. Figure 2.39 expresses the curve presented by Foppa's methodology.

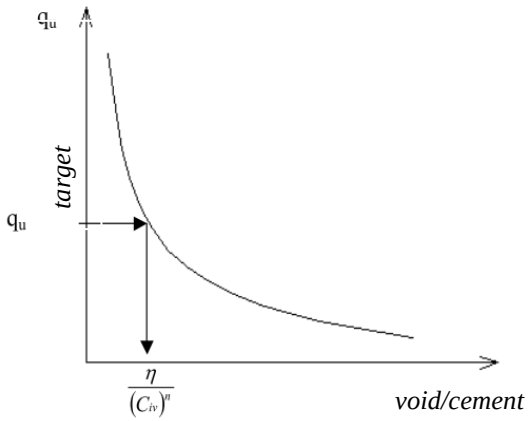


Figure 2.39 – Determination of a void/cement ratio to a q_u target
(after FOPPA, 2005)

Foppa's dosage methodology was then followed by a number of studies aiming to verify the efficiency of the methodology for different soil matrix, cement agents, moisture contents, load conditions, and fibres inclusions (CONSOLI et al. 2012a, 2012b, 2013, 2015, 2018a, 2018b).

Foppa (2016) synthesised some of these results, which is presented in Table 2.2. The results presented include various particle size distribution, from clay to gravels. All tests presented on Table 2.2 were obtained through cylindrical samples with a 5 centimetre diameter and 10 centimetre height. The cement used was the height initial strength and 7 days for curing was adopted.

It is has been verified that all studies present an equation with the following arrangement:

$$q_u = \frac{A}{P^B} \qquad \text{with:} \quad P = \frac{\eta}{(C_{iv})^k} \tag{2.6}$$

Where A, B and *k* are constants adjusted by the strength.

Table 2.2 – Equation parameter for the unconfined compression strength prediction to distinguish soil types (after FOPPA, 2016)

Author	Soil type	Cement content	η (%)	γ_d (kN/m^3)	Equation parameter for the q_u (kPa) prediction		
					A	B	k
FLOSS (2012)	Sandy gravel	1, 2, 3, 5, 7, 9	26.7, 29.1, 32.3	17.1, 17.9, 18.6	1.25E+05	2.10	0.85
FLOSS (2012)	Gravelly sand	2, 3, 5, 7	36.5, 38.3, 40.8, 45.1	14.7, 15.8, 16.5, 17.0	8.78E+04	1.50	0.85
FLOSS (2012)	Fine sand	1, 2, 3, 5, 7, 9	44.7, 48.1, 50.8	13.0, 13.7, 14.6	3.92E+09	4.26	0.23
FLOSS (2012)	Uniform sand	2, 3, 5, 7	57.0, 60.5, 63.2	13.2, 15.3, 17.2	3.09E+16	7.98	0.10
CRUZ (2008)	Fine sand	1, 3, 5, 7, 9, 12	40.5, 41.8, 43.7	16.0, 15.5, 15.0	3.11E+04	1.36	1.00
SEVERO (2008)	Clayey sand	2, 5, 10	32.8, 35.4, 39.0	17.2, 18.0, 18.8	5.95E+05	221	0.55
FOPPA (2005)	Silty sand	1, 2, 3, 5, 7, 9, 12	26.4, 28.8, 31.7, 34.4, 31.7,	17.3, 18.0, 19.0, 19.7	5.03E+07	3.32	0.28
ROSA (2010)	Clayey silt	3, 5, 7, 9	40.4, 44.1, 40.4	14.0, 14.9, 15.9	1.54E+09	3.90	0.35
ROJAS (2012)	Silty-sandy clay	5, 10, 15, 20	55.9, 48.3, 51.9	13.8, 14.8, 15.7	8.16E+07	3.09	0.30
MARQUES (2012)	Silty-sandy clay	3, 5, 7, 9	40.2, 43.3, 47.8	13.8, 15.1, 15.9	6.74E+08	4.16	0.50

The $\eta/(C_{iv})^k$ parameter allows the agreement between the effects of the porosity and the amount of cement within the soil strength. Because of this factor, it is possible to conveniently control the parameters η and C_{iv} in order to keep $+q_u$ constant. Foppa (2016) explained the factor *k* applied to the volumetric content of cement:

a) if k = 1: the increment in any of the parameters (porosity or volumetric cement content) it is enough to change the unconfined compression strength. The porosity and the volumetric cement content are both equivalent, relevant to the soil strength;

b) if k > 1: the cement content is more influent to the soil strength than the porosity of the mixture;

c) if k < 1: the influence of the porosity is bigger than the volumetric cement content. When increasing the porosity, a smaller amount of cement is necessary to keep the same unconfined compression strength.

The use of the ratio porosity/volumetric cement content had been used to successfully correlate other parameters for soil-cement mixtures. Ultimate tensile strength was successfully expressed by the ratio (CONSOLI et al., 2010a, 2010b; 2011; FLOSS, 2012, JOHANN, 2013), the deviator stress in triaxial tests (CONSOLI et al., 2007; CRUZ, 2008), the initial shear modulus (CRUZ, 2008; FLOSS, 2012, JOHANN, 2013), the initial volumetric strain modulus and the plastic strength during isotropic compression (CONSOLI & FOPPA, 2014). Consoli et al. (2012, 2014) showed that the methodology also is applied to estimate the shear envelope in sandy soils and in the evaluation of the relation shear-dilatancy. Recent studies present that the ratio can also be related to stiffness, durability and cyclic response (VENSON, 2015; CONSOLI et al., 2018a; 2018b; CONSOLI & TOMASI, 2018).

2.8 SUMMARY

Artificially cemented soils have been reviewed, focusing on their behaviour through experimental results from literature. A brief discussion on soil improvement was presented. The chemical reactions obtained with the inclusion of cement into soil has been presented, and the influence of the key parameters in the soil-cement mixture was given. The stress-strain behaviour of cemented sands was presented, indicating its elastic behaviour inside the yield surface. The behaviour becomes elastoplastic outside where the cementation begins to break down.

The cementation yield surface crosses the failure surface, and it becomes the failure surface at lower mean normal stresses. The cemented sand continues to break up as the stresses increase beyond the cementation yield surface, and it requires quite high stresses and strains to completely granulate the material. Failure surface, theoretical modelling and dosage methods for the cemented material were also presented.

The knowledge on the cemented soils behaviour is wide, but still do not fill all the gaps. The effect of rotation of principal axes of cemented soils, artificially or not, is not mention on literature. Stiffness through different strength path is also unclear for cemented soils, as well as

the stiffness evolution over time and load. The following chapter presents the research program proposed to fill some of the gaps on the knowledge of cemented sand materials.

3 RESEARCH PROGRAM

This chapter presents the experimental programme developed to investigate the response of the cemented sand in multiaxial loading conditions.

3.1 UNCONFINED COMPRESSION AND SPLIT TENSILE TESTS

The adopted testing strategy to investigate the behaviour of cemented sand under multiple loading conditions started with the determination of the η/C_{iv} index. Distinct cement contents and porosities were adopted to complete a wide range of this curve for unconfined compressive and tensile strength. Table 3.1 presents the set of specimens prepared for this part of the research. For each porosity and cement content, two samples were prepared. In total, 22 samples were performed for the unconfined compression test and 22 for the split tensile test.

Table 3.1 – Samples dosages prepared for the unconfined tests

γ_d (kN/m^3)	Cement Content (%)	Moisture content, ω (%)	Curing time (days)	Number of specimens
0.89	1.7, 3.4, 7	10	7	12
0.816	1.7, 3.4, 7			12
0.742	1.7, 3.4, 7			12
0.90	2.3			4
0.71	1.8			4

3.2 STIFFNESS MEASUREMENTS WITH BENDER ELEMENTS

In previous testing, all samples prepared for the unconfined tests (compression and tensile) had their shear wave velocity measured through bender elements testing. Also, in order to obtain the stiffness evolution with the hydration of the cement, cubical samples were prepared, and three pairs of bender elements were inserted in the six faces of the cube sample. Table 3.2 presents the samples fabricated for this investigation. In the first week of the sample curing, measurements were made every day. As the time of curing passed, the measurements were carried out every two days until no variation of the wave response was detected.

Table 3.2 – Samples prepared for cubical bender element testing

Void ratio, *e*	Cement content (%)	Moisture content ω (%)	Curing time (days)
0.90	2.3	10	21
0.71	1.8		16
0.90	6.8		32
0.74	7		157
0.74	7		89
0.71	10		24

3.3 CUBICAL CELL TESTING

Once the relation of η/C_{iv} and the unconfined compressive strength was obtained, a maximum strength of 200 kPa was adopted for the following tests. An $\eta/C_{iv} = 47.2$ was targeted with two different cement ratio contents: first, through a void ratio of 0.90 and cement content of 2.3% (corresponding to a loose condition, D_r = 27%) and secondly, a 1.8% cement content to the amount of sand and a void ratio of 0.71 (dense condition, D_r = 77%). With these two sample specifications, two sets of cubical cell tests were performed. Table 3.1. presents the samples prepared for the cubical cell tests. Figure 3.3 introduces the stress paths imposed in the cubical cell; θ applied on the octahedral plane were 0º, 30º, 60º, 90º, 120º, 150º and 180º, where θ is known as Lode's angle.

Table 3.3 – Samples prepared for cubical cell testing

Void ratio, *e*	Cement content (%)	Moisture content, ω (%)	Curing time (days)	*p' (kPa)* shearing	θ	Number of specimens
0.90	2.3	10	7	100	0º, 30º, 60º, 90º, 120º, 150º, 180º	7
0.71	1.8				0º, 30º, 60º, 90º, 120º, 150º, 180º	7

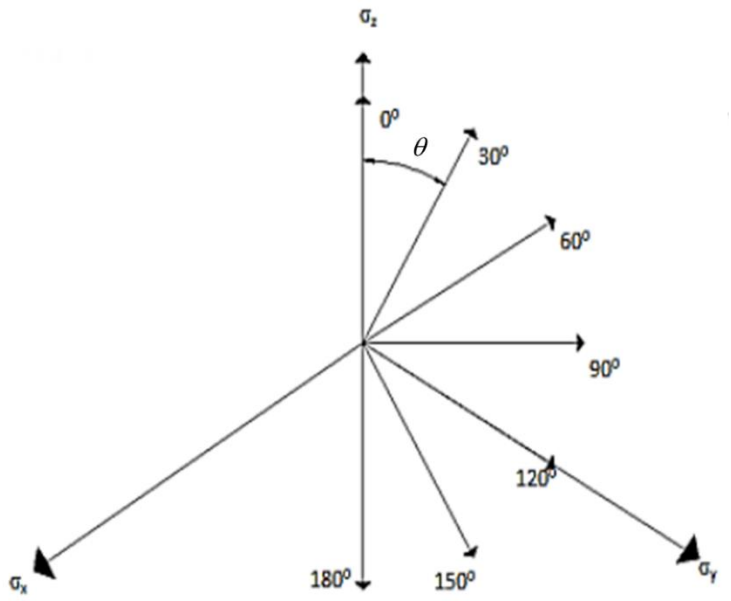


Figure 3.1 – Stress paths imposed in the cubical cell varying the principal stress direction (θ)

3.4 HOLLOW CYLINDER TESTING

As for the hollow cylinder samples, the same criterion adopted to define the dosage of the cubical cell samples were adopted. Samples were also prepared with a compact and a dense sand characteristic and two low cement ratio contents. Same η/C_{iv} = 47.2 was adopted and it was obtained with the same void ratio and cement content (e = 0.90 and C = 2.3%; e = 0.71 and C = 1.8%). Samples characteristics are presented in Table 3.4. The stress paths performed in the hollow cylinder apparatus corresponded to seven combinations of principal stress inclination, α: 0º, 15º, 30º, 45º, 60º, 75º and 90º. The representation of the stress paths followed in the experimental programme is given in Figure 3.2.

On the tests performed on the hollow cylinder, small cycles were applied at different strength levels. The proceedings adopted to the application of the small cycles are presented in Section 7.5.

Table 3.4 – Specimens specification for the hollow cylinder tests

Void ratio, *e*	Cement content (%)	Moisture content, ω (%)	Curing time (days)	p'_o *(kPa)*	α	Number of specimens
0.90	2.3	10	7	100	0º, 15º, 30º, 45º, 60º, 75º, 90º, 0º-45º	9
0.71	1.8				0º, 15º, 30º, 45º, 60º, 75º, 90º	8

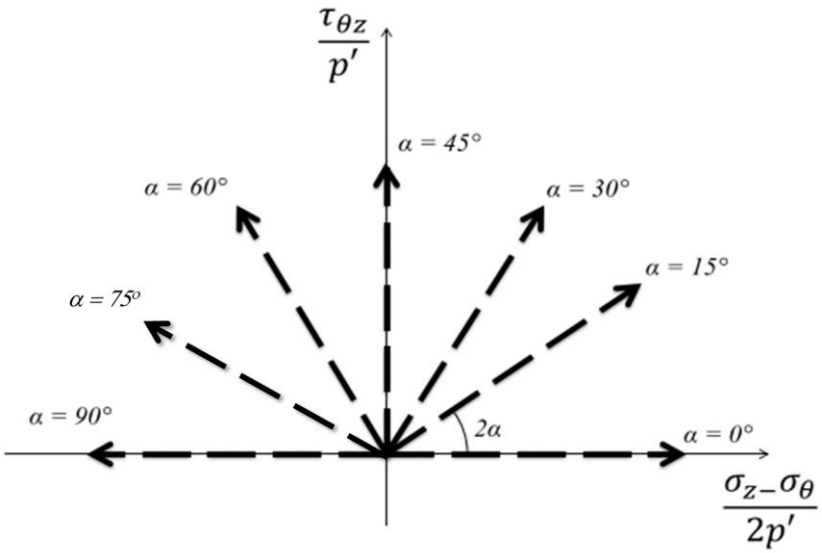


Figure 3.2 – Representation of the imposed stress paths performed in the hollow cylinder

3.5 SUMMARY

This chapter presented the experimental program developed for this research. First, simple compression and tensile tests were proposed, followed by an explanation of the variation of cement content to analyse the stiffness and stiffness evolution on cementation.

The definition of the sample contents for the multiaxial response of the low cemented sand was established through the η/C_{iv} versus unconfined compressive strength curve obtained. With this curve, the cubical and hollow cylinder samples were prepared.

The multiaxial behaviour of the cemented sand was analysed by the variation of the principal stresses. This is achieved in two different apparatus and the tests procedures will be presented in Chapter 4.

4 EXPERIMENTAL SET UP AND PROCEDURES

4.1 INTRODUCTION

This chapter describes the materials, equipment, procedures and sample preparation used in this research. First, the materials are described in Section 4.2.

The sample preparation (item 4.3) is presented considering the type of test that the sample was subjected to and the same is made for the testing procedure.

In this chapter, the equipment used, the control systems, and the special instrumentation for stiffness measurements are described. The true triaxial and the hollow cylinder tests presented in this chapter were developed in the Geomechanics Laboratory of the University of Bristol. The small strain measurements system in the hollow cylinder apparatus is also described in this chapter.

After detailing the apparatus used in this research, the testing procedure is presented.

4.2 MATERIALS

4.2.1 Hostun Sand

The origin of Hostun sand is a place called Hostun, located in the area of Drôme in the southeast of France. It has a colour that ranges between grey-white and rosy-beige, while its chemical components consist of high siliceous amount ($SiO_2 > 98\%$). The grain shape varies from angular to sub-angular. Hostun sand is a commonly used sand in laboratory campaigns and it has been divided in different granular distributions. This research program uses Hostun RF (S28) sand.

The grain size distribution (Figure 4.1) shows an uniform graded sand with: mean grain size, D_{50} = 0.32mm, coefficient of uniformity, $C_u = D_{60}/D_{10}$ = 1.70, coefficient of gradation, $C_g = (D_{30})^2(D_{10}D_{60})$ = 1.1, maximum and minimum void ratio, e_{max} = 1.00, e_{min} = 0.62, and specific gravity G_s = 2.65.

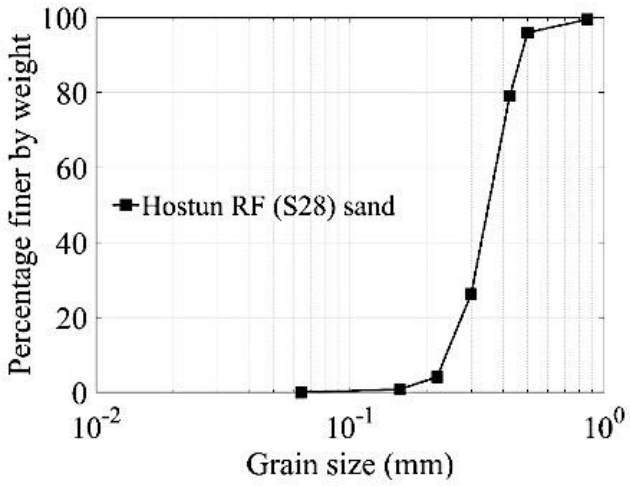


Figure 4.1 – Grain size distribution of Hostun Sand

4.2.2 Cement

The cementation agent used was a Portland cement of high initial strength (Type III, ASTM C 150-09; ASTM, 2009). As the cement has a fast gain of strength (80% at the seventh day), the curing time for the produced specimens was 7 days.

4.2.3 Water

Distilled water was used for sample preparation. De-aired water was adopted when percolation and volume change were measured. Tap water was used to fill the hollow cylinder outer chamber and for immersion of the samples tested on unconfined strength and on the true triaxial.

4.3 SAMPLE PREPARATION

After the soil, cement and water were weighted, the soil and cement were mixed until the mixture acquired a uniform consistency. The water was then added to the soil and cement, and the mixture process continued until a homogeneous material was created. The amount of cement for each mixture was calculated based on the mass of dry soil. The moisture content (10% to all tests) was calculated considering the combination of masses of soil and cement. This process was the same for all specimens prepared in this research.

After the mixture had been prepared, each test had a different shape and procedure of preparation of specimens. For this reason, the sample preparation is presented separately for each test performed.

4.3.1 Unconfined compressive and split tensile strength

For the unconfined compressive and tensile strength tests, cylindrical specimens with 5 cm diameter and 10 cm height were prepared. With the mixture previously described, material was divided into three portions (one for each layer of the specimen). Two small portions of the mixture were taken for moisture content determination.

The specimen was then statically compacted in three layers inside a cylindrical acrylic mould, with a target mark to achieve the target dry density. The top of each layer was scarified to improve bonding between layers. The bottom and the last layer were prepared including the formation of a blank space exactly like the bender element that would be later inserted in the sample for testing (Figure 4.2d).

After compaction, the sample was immediately removed from the mould with an extractor. The sample was then weighted and sealed with plastic film. Samples were cured for six days in the laboratory, where the temperature and humidity were controlled ($22^oC \pm 2^oC$ and 60%). On the sixth day, the sample was measured before immersion in water for 24 hours.

Before testing for compressive or tensile strength, specimens were weighted again, and wave propagation tests were conducted with Bender Elements.

To be considered for testing, the samples had to comply with the following:

a) dry density within ±1% of target value;

b) moisture content within ±0.5% of the target value;

c) diameter within ±0.5 mm;

d) height within ±1 mm.

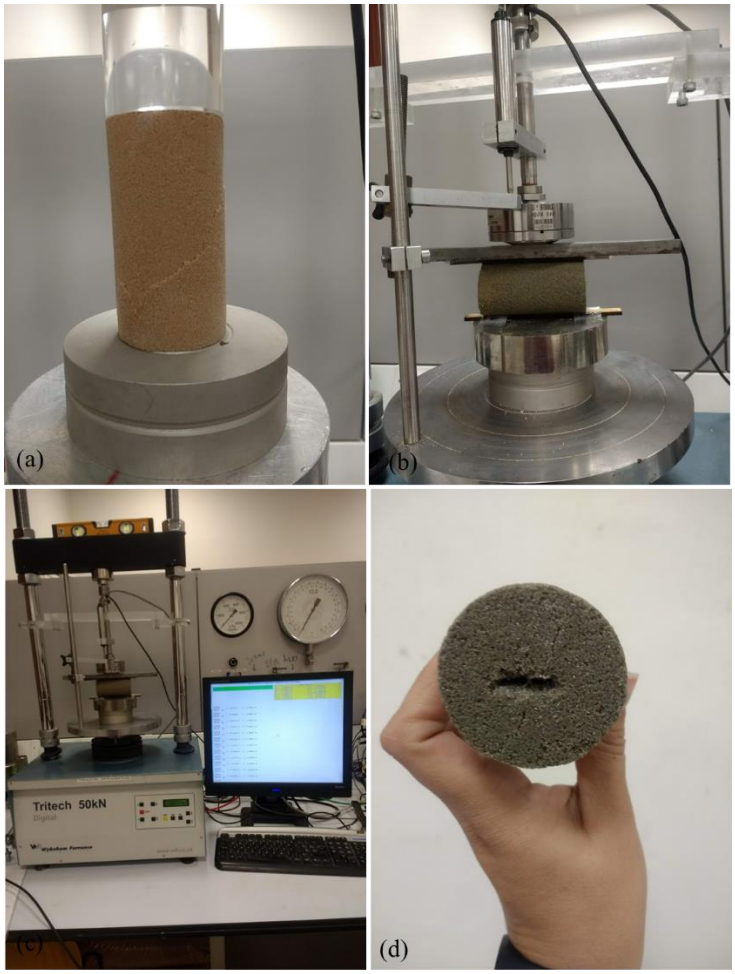


Figure 4.2 – Cylindrical samples: (a) UCS testing; (b) Brazilian test; (c) Triaxial cell used for the unconfined tests; (d) detailed of the space for insertion of the bender elements

4.3.2 Cubical sample

Cubical specimens, 10 cm side, were manufactured to be tested in the cubical cell and with bender elements (bench test). When by visual inspection it was considered that the material appeared satisfactorily homogeneous, the mixture was divided into three portions corresponding of each layer for the fabrication of the samples. Sample layers were then compacted using a square steel tamper, inside of the cubic stainless-steel mould. The upper surface of each layer was scarified in order to meld layers. Two small portions of the mixture were taken for moisture content determination.

After compaction, weight of mould and sample were measured. Specimens tested in the cubical cell were left inside the mould for one day. After this time, sample was removed from the mould (Figure 4.3b), its dimensions were measured, and the specimen was kept in a plastic film for curing for 5 days with environmentally-controlled conditions of 22º C (± 2ºC) and 60%

humidity. On the sixth day, the sample was removed from plastic and immersed in water for 24 hours to minimize suction effects (CONSOLI et al.; 2007; 2010; 2012a; 2012b).

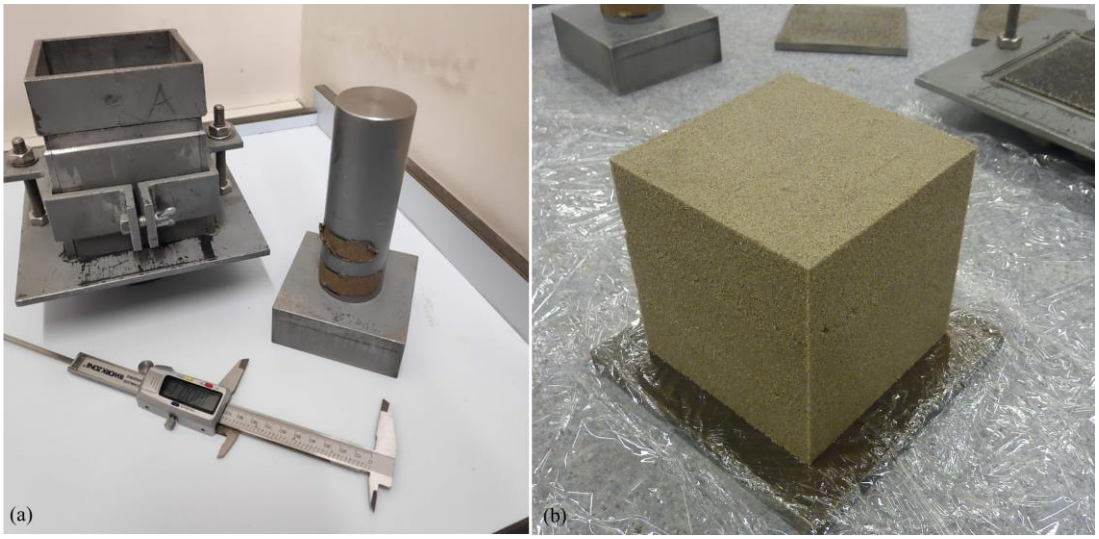


Figure 4.3 – (a) Mould for cubical samples and (b) sample prepared for the cubical cell apparatus

When the sample was moulded to be tested with the bender elements, the specimen was carefully removed from the mould after fabrication. A 3D printed cage for the sample was specially designed to keep the benders in place and the sample was positioned in this cage (Figure 4.4c). Spaces for the insertion of the bender elements were made with a thin needle and the pair of benders was inserted in this space. When the three pairs were positioned in the sample, the first measurements of wave velocity were conducted; thereafter the sample was wrapped in plastic film and the whole cage and benders were positioned inside a plastic sealed bag. Every time readings were made, the plastic bag was opened, but the plastic film around the sample was never removed, keeping sample weight constant during measurements. The bender elements were only removed from the sample when testing was finished, and it was also at this time that sample dimensions were taken.

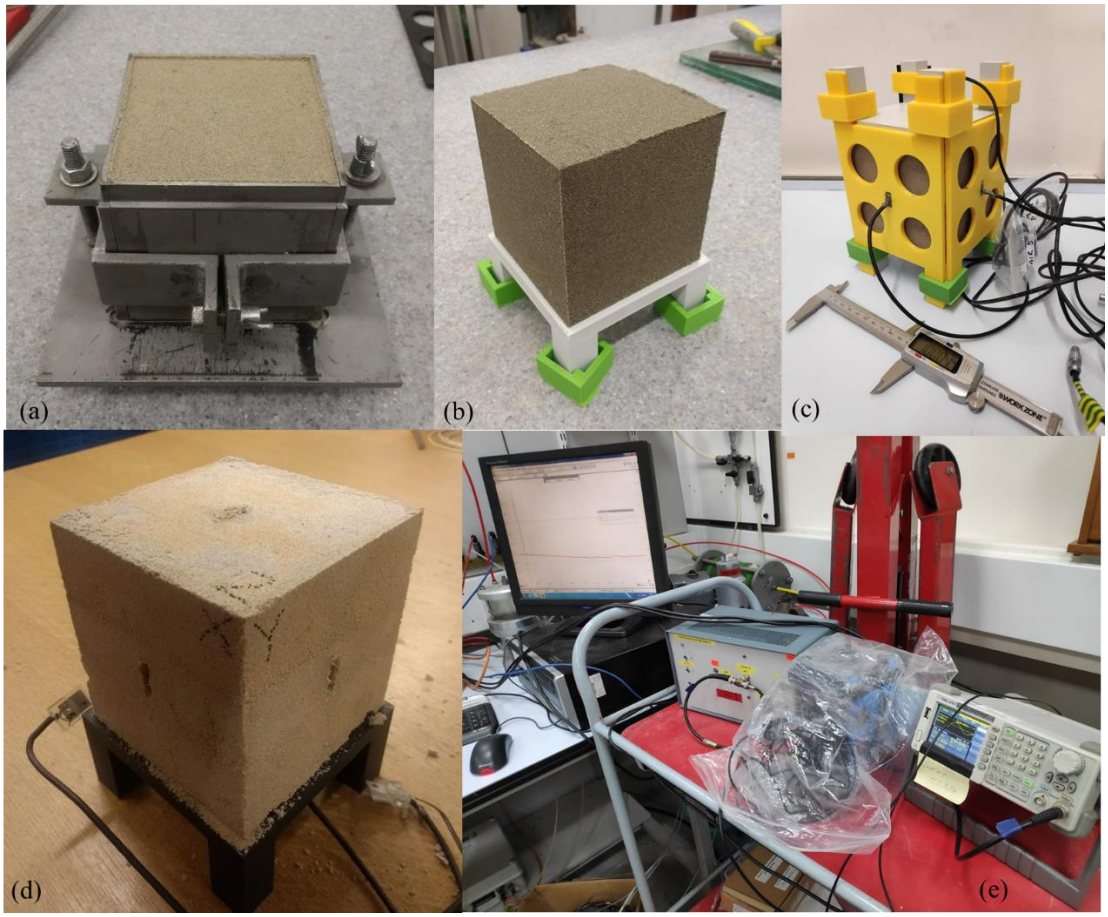


Figure 4.4 – (a) Sample inside the mould; (b) sample positioned in the cage; (c) sample with the bender elements inserted; (d) sample after testing; (e) sample connected to oscilloscope and PicoScope

4.3.3 Hollow Cylinder

The hollow cylinder samples were measured with a 20 cm height, 10 cm outer diameter and 6 cm inner diameter. The 3D printer base and top were specially manufactured to prepare the cemented samples. Both the top and base had the same marks as the top and bottom caps so that the apparatus had to impose torsion in the sample and guarantee the fixation between apparatus and sample.

Once the mixture was ready, it was divided into six portions corresponding to the amount of successive soil layers used for the fabrication of samples. Each layer was statically compacted with a curved steel tamper inside of a curvilinear stainless-steel mould. Between layers, the top surface of the freshly made layer was scarified. When the last layer was compacted, the 3D printed top was positioned in the sample (see Figure 4.5).

After the preparation, the weight of mould and sample were measured, and sample was kept inside the mould for curing, protected with plastic film and in a sealed plastic bag in environmentally controlled conditions of 22ºC temperature and 60% humidity. Two small portions of the mixture were taken for moisture content determination.

After five days of curing, the sample was removed from the mould, its dimensions were measured, and it was gently placed in the hollow cylinder apparatus set up testing.

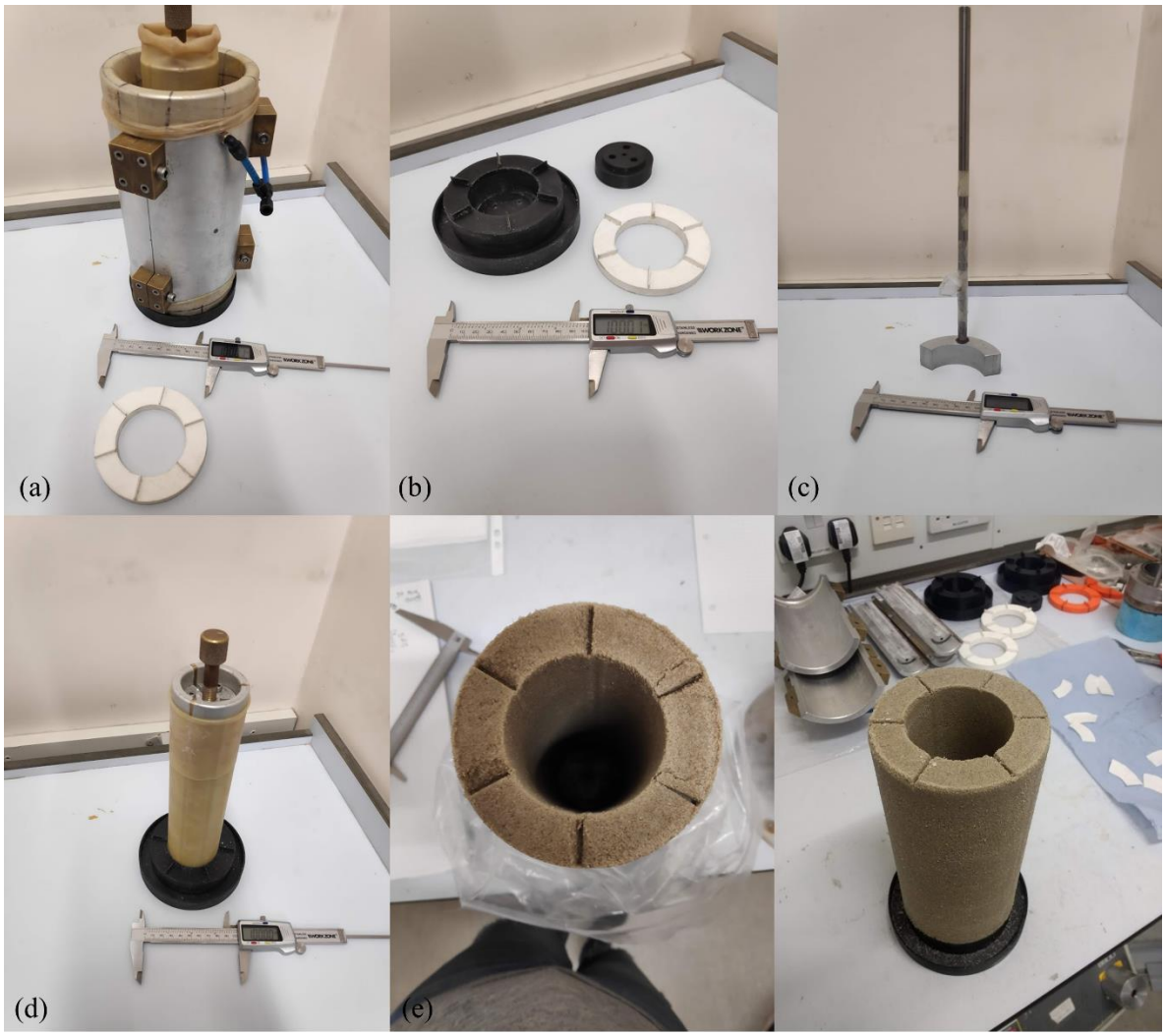


Figure 4.5 – Hollow cylinder samples: (a) prepared mould; (b) base and top cap and inner membrane holder; (c) curvilinear compactor; (d) inner tube prepared; (e) top of specimen detail; (f) specimen ready for testing

4.4 UNCONFINED COMPRESSION AND SPLIT TENSILE TESTS

The use of unconfined compression tests has been reported in the literature as an easy procedure to verify the effectiveness of soil stabilization by reaching the strength of the cemented material. The test is also simple and provides fast results while being reliable and inexpensive (CONSOLI et al., 2007).

The unconfined compression and the split tensile compression tests were performed at the University of Bristol, using a triaxial apparatus without the confinement system. The load cell in the system had a maximum load of 5 kN and the imposed displacement rate was 1.0 millimetre per minute according to the ASTM D 1633.

For the unconfined compression tests, the specimen was positioned vertically (see Figure 4.6a) and a vertical load was applied to the sample and measured through with a load cell. The maximum force imposed to the sample was then used to calculate the maximum unconfined compression strength of the cemented soil specimen.

What distinguishes the unconfined compression test from the Brazilian test is the position of the cemented specimen in the equipment. For the tensile test, the cylindrical sample is positioned horizontally and the load is applied as shown in the Figure 4.6b. Figure 4.7 presents samples tested on the triaxial frame for the unconfined tests.

The maximum load read by the load cell is used to calculate the maximum tensile strength, using Equation 4.1:

$$\sigma_t = \frac{2.P}{\pi\, D\, H} \tag{4.1}$$

Where P is the maximum load measured, D is the diameter and H is the height of the specimen.

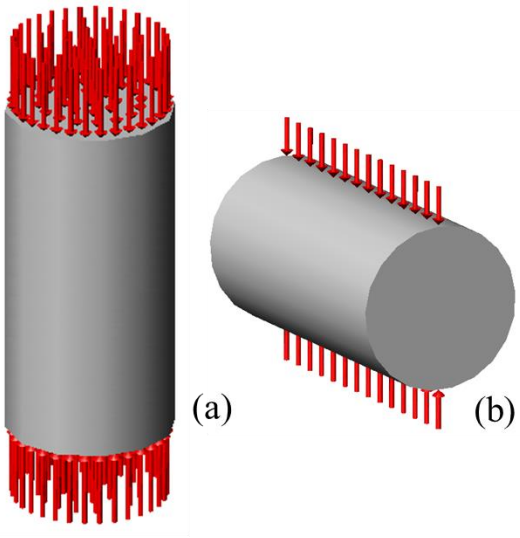


Figure 4.6 – Position of loading in (a) unconfined compression strength and (b) unconfined tensile strength

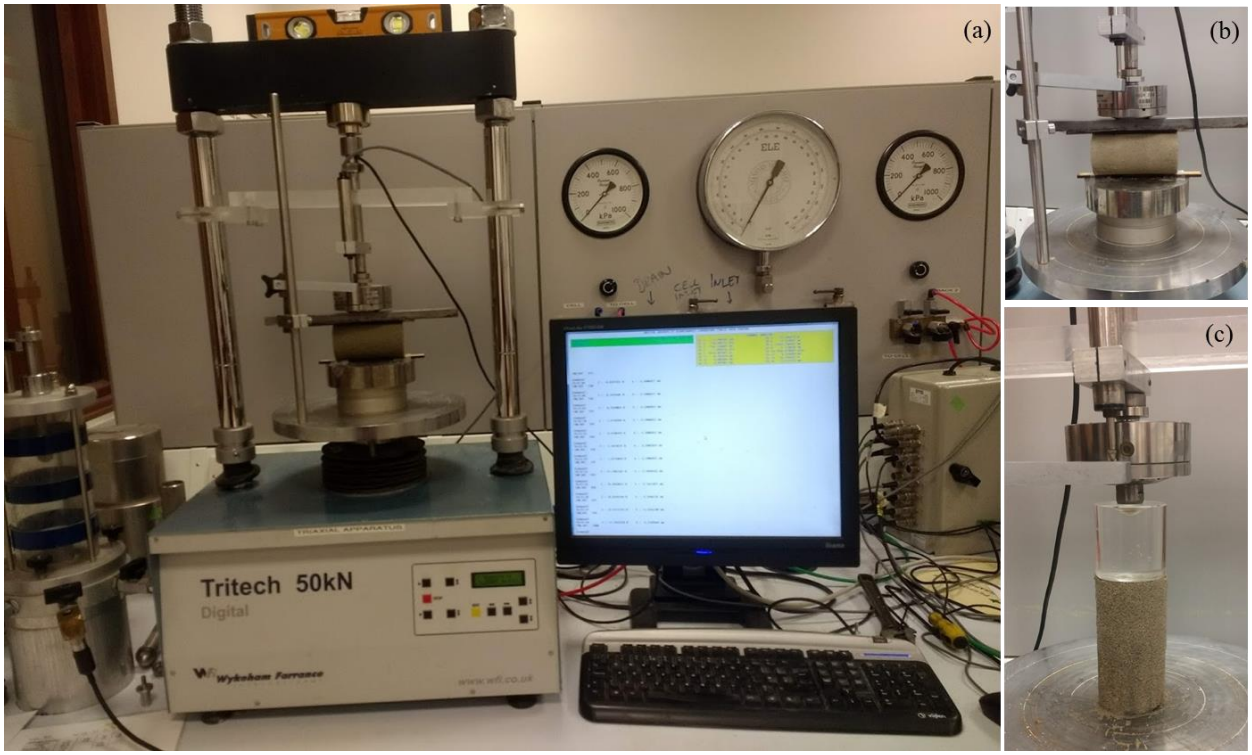


Figure 4.7 – Triaxial frame used for the (a) and (b) split tensile strength; (c) unconfined compression strength

4.5 BENDER ELEMENT TESTING

Elastic shear moduli of soils can be obtained using dynamic laboratory measurements with bender elements. Bender elements were firstly introduced by Shirley and Hampton (1977) and consist of two piezoelectric ceramic materials bonded together in order to work as a bimorph,

allowing one side to contract and the other side to expand producing a bending movement when electrically excited. The bending of the transmitter element produces a shear wave through the soil specimen which is detected by a receiver bender element. The application of a very small shear strain of approximately 10^{-5} % (DYVIK & MADSHUTS, 1985) travels through the sample with a decreasing value due to damping. Numerous authors have successfully performed stiffness measurements in soil materials, reinforced and not reinforced (e.g. VIGGIANI & ATKINSON, 1995; PENNINGTON, 1999; FIAVORANTE, 2000; KUWANO et al.; 2000, BORTOLOTTO, 2017).

The elastic shear modulus is obtained through the values of shear wave velocity. By knowing the tip to tip distance d between the transmitter and receiver bender elements (DYVIC & MADSHUS, 1985) and by obtaining the time t that takes the shear wave to arrive from the transmitted signal to the received signal, the shear wave velocity V_s is calculated (Equation 4.2). The shear modulus will depend on the bulk density of the specimen ρ and it is expressed in Equation 4.3.

$$V_s = \frac{t}{d} \tag{4.2}$$

$$G_0 = \rho {V_s}^2 \tag{4.3}$$

All piezoelectric transducers can be installed in a wide variety of soil testing devices, from conventional to non-conventional and from static to dynamic equipment. The triaxial cell is probably the most common apparatus where these transducers are used, but its use in other devices have also been reported, namely in the oedometer (FAM & SANTAMARINA, 1995; ZENG & GROLEWSKI, 2005) and direct shear apparatus (DYVIK & OLSEN, 1989), the centrifuge (ISMAIL & HOURANI, 2003), in the hollow cylinder apparatus (DI BENEDETTO et al., 1999; GEOFFROY et al., 2003) and in true triaxial and cubical cell apparatuses (ISMAIL et al., 2005; SADEK, 2006). Its installation in the platens of a resonant-column testing apparatus has also been reported (SOUTO et al., 1994; FAM et al., 2002; FERREIRA et al., 2007) and this is particularly interesting as a mean to assess the potentialities of the BE technique, and to compare and calibrate its measurements. In this research, the bender elements were used prior to the unconfined compression and tensile strength tests, and in cubical samples. All the measurements of the wave propagation velocities were performed on bench. G_0 for the cylindrical samples were obtained in one direction (Figure 4.8a) while for the cubical specimen G_0 was obtained in three directions (Figure 4.8b).

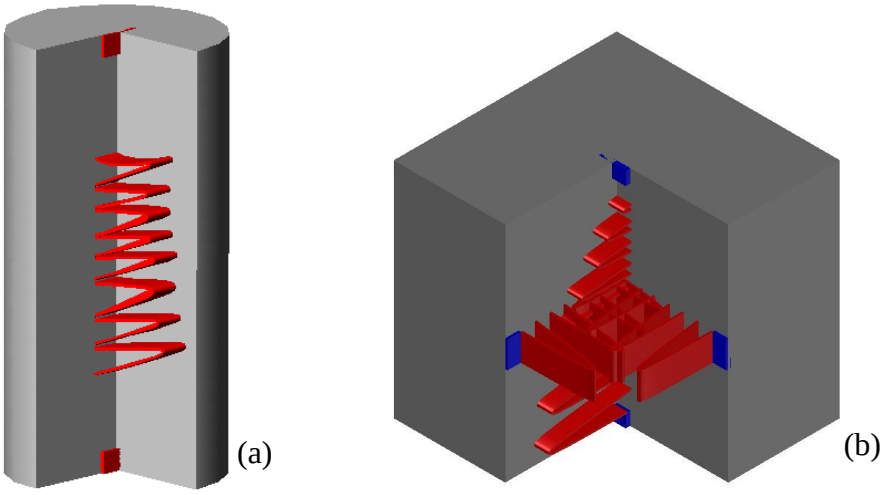


Figure 4.8 – Schematic view of BE in (a) cylindrical sample and (b) cubic sample

4.5.1 Principles of Bender Elements

A bender element [BE] is a double piezoceramic transducer composed of two thin piezoceramic plates, rigidly bonded to a central metallic sheet and to electrodes on its outer surfaces. The metallic sheet acts as reinforcement, since the piezoceramic plates are extremely fragile. This assembly is protected with a rigid epoxy resin coating, in order to electrically isolate and prevent direct contact with the soil and, more importantly, with water. The electrical connection to the plates is made in relation to the polarization directions of the two plates, in order to ensure proper flexural movement: plates polarized in opposite directions are series-connected, while plates polarized in the same direction are parallel-connected. The performance of the transducers is also related to its capability of transmitting or sensing shear waves: a series connection is preferable for the receiver element, as a higher output is obtained for the same movement, with twice the energy of a parallel connection. Conversely, a parallel connection is more suitable for the transmitter element, since the distortional movement of the transducer is greater for a given input, hence achieving double the efficiency of series-connected BE if used as transmitters (DYVIK & MADSHUS, 1985; BRIGNOLI et al., 1996).

The model presented by Dyvik and Madshus (1985), in Figure 4.9, is still the basis of current design, though variations have been made, namely to its size and to arrangements (usually T-shaped) of pairs of transducers in a single probe. These variations are consequences of the need to adjust to new testing challenges: in order to observe vertical and horizontal homogeneity in triaxial specimens, and thus assess anisotropy. The combination of two BE placed orthogonally in a single probe has also resulted from the interest in measuring vertically- and horizontally-

polarized waves. And so, the miniature and/or T-shaped BE have been developed and manufactured with great success, especially when horizontally mounted in a triaxial specimen (PENNINGTON et al., 1997; 2001).

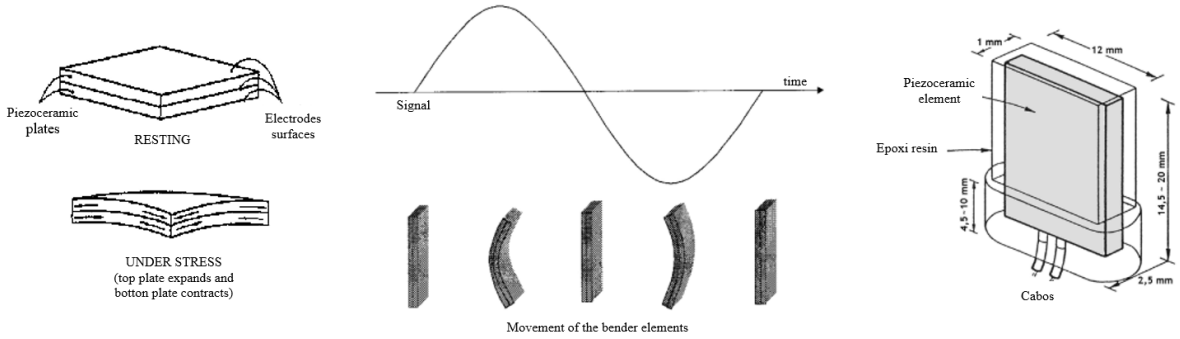


Figure 4.9 – Bender element movement diagram and model

4.5.2 Manufacturing bender elements

As mentioned previously, sevens pairs of benders were manufactured for this research. The first step was to weld in the piezoceramic three cables responsible for carrying the signals through the bender. After welding was finished, the BE was positioned in an acrylic mould. The mould was filled with transparent epoxy resin, previously subjected to vacuum for 30 minutes. The resin was carefully placed with a syringe so that no air bubbles were inside the mould. The pair was then set aside to dry for 24 hours.

When dried, the bender elements were tested and signal delay (zeros) were measured. Figure 4.10 presents an overview of the preparation and fabrication stages of the BE.

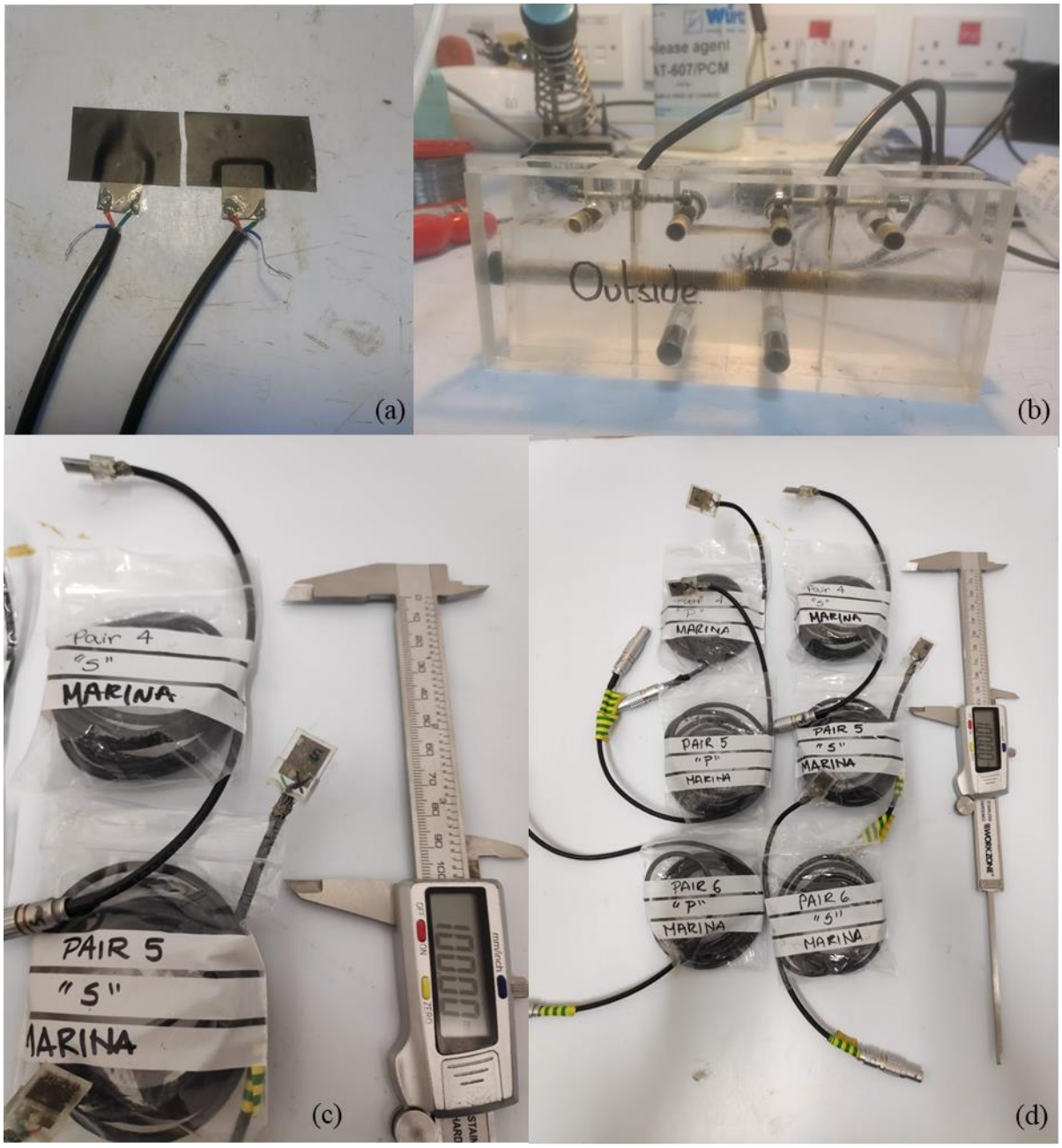
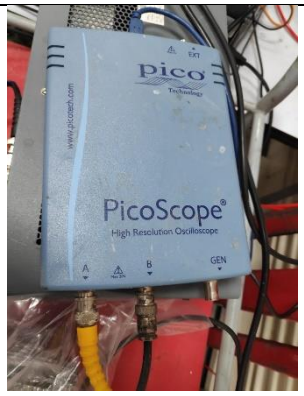


Figure 4.10 – BE manufacture: (a) BE, (b) mould, (c and d) pairs prepared

4.5.3 Associated electronics equipment

For seismic waves measurements, piezoelectric transducers themselves are not enough. An external signal source is necessary, as well as an acquisition device for viewing and recording the wave results. Amplification is often fundamental in order to appropriately visualise and interpret the signals, and it was used in this research. The set of electronics equipment used in this experimental programme is listed and detailed in Table 4.1.

Table 4.1 – Bender element testing: associated electronics equipment

	Function waveform generator (SIGLENT, SDG1010) capable of generating an electrical signal with various configurations (frequencies, amplitudes and offsets)
	2-channel amplifier of both input and output signals, which amplifies the signal by 8x
	PicoScope 4262: dual channel; 16-bit resolution connected to the computer to dig the signals using an analogue-to-digital converter

The signals from the oscilloscopes can be directly transferred and stored in a personal or laptop computer, connected using series and/or parallel ports. The same lab PC was used in this research.

4.5.4 Specific seismic wave measurement software

For seismic wave measurements, the PicoTech oscilloscope with the data acquisition program, PicoScope 6, was used for registering the wave traces in the time domain. The analyses in the time domain are similar, as well as the measurement procedures. Screenshots of the program used are presented in Figure 4.11.

The readings were performed individually and automated with the software PicoScope 6. Every change of frequency was manually made on the function generator. The analysis was also conducted individually, based on best-practice interpretation principles, which is discussed in the following chapter. In summary, an educated eye and experienced judgement are essential requirements towards a reliable interpretation of BE results in the time domain.

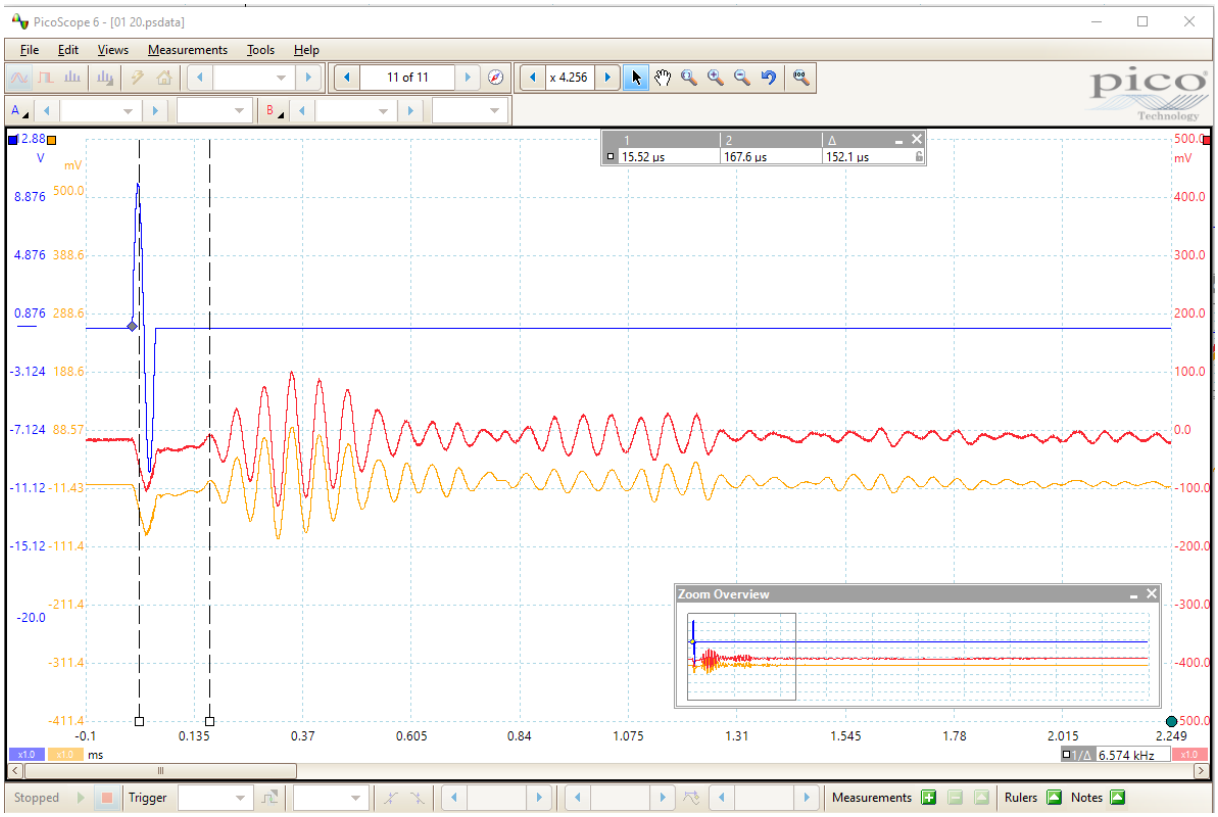


Figure 4.11 – Screenshot of the program used for the seismic data acquisition in the time domain (PicoScope 6)

4.5.5 BE: performance and calibration checks

Prior to cemented-soil testing, the functioning of the BE system was checked. The first test involved checking that each transducer, directly connected to the function generator, "sings" when an audible input signal is generated, usually for continuous sinusoidal signals within the 1-15 kHz frequency range. Despite being more or less efficient in transforming such input signals into movement (that is, whether it is to be used as transmitter or as receiver), each transducer should respond clearly in an audible manner to the excitation signal. If that audible response occurs, then the transducer is operational and can be used as intended, either as a transmitter or a receiver.

The next procedure consists of manually holding both transducers in direct contact. The results derived from this exercise are extremely relevant, providing information on three different aspects:

a) the minimum time delay or calibration time;

b) the polarity of the input-to-output signals;

c) the optimal performance in relation to function.

The minimum time delay between transmitter and receiver BE can be observed when both transducers are placed in direct contact. An input signal is fed to the transmitter and the output signal of the receiver is observed in the oscilloscope. In theory, the time delay should be null, since the tips of the transducers are in contact, that is, at null travel distance. Despite the direct contact of the transducers, the obtained signals are a reflection of the whole BE testing setup, which is in fact a system composed not only by the transducers but also by the electronic devices and cables. All these elements introduce some delay, even if that delay is minimal. Hence, from the instant the signal is generated to the instant it is picked up by the receiver, even when in direct contact with the transmitter, a time lag may be expected. The small distance between the transducers due to the resin involved in the piezoceramic contributes to this delay. This distance was also measured and computed as an initial distance between the bender that should be considered.

Another important conclusion can be drawn from this check, which refers to the polarity of the input-to-output signals. When the transmitter and the receiver BE are in direct contact, the wave traces should be very similar in the oscilloscope, but the polarity may be positive or negative (inverted signal). By rotating one of the transducers by 180 degrees, the polarity should reverse and the positions corresponding to positive polarity can be simply marked on one side of each transducer for identification. This characteristic of reversible polarity is exclusive to shear-wave transducers; hence, it is only applicable to bender elements and shear-plates.

The transducers must be installed taking the polarity into account, defining the direction of the first true arrival of the wave: upwards for positive polarity and downwards for inverse polarity. This information is essential to the correct interpretation of the signals in the time domain. In fact, when propagating a shear wave through a soil specimen, the wave is inevitably altered by a number of factors, such as reflections, distortions and noise.

This check also enables the confirmation of the efficiency of the transducer as transmitter. As mentioned above, the type of polarization and the electrical connection of each transducer influence its performance in relation to the respective function as transmitter or receiver.

4.6 CUBICAL CELL APARATUS

The conventional triaxial apparatus is a widely used laboratory device for exploring deformation characteristics and shearing resistance of soils. The expression *triaxial* is somehow misleading since the intermediate principal stress must be equal to at least one of the other principal stresses in the apparatus; such a testing device has two degrees of freedom and can test soil elements under confined uniaxial or axisymmetric stress states. In practice, soil elements in the ground or around any geotechnical structure are generally subjected to six independent stress variables (Figure 4.12).

The cubical cell provides the possibility of controlling the three principal stresses or strains without allowing for the rotation of the direction of principal axes (observed in the hollow cylinder apparatus) (KO & SCOTT, 1967; STURE & DESAI, 1979; SADEK, 2006).

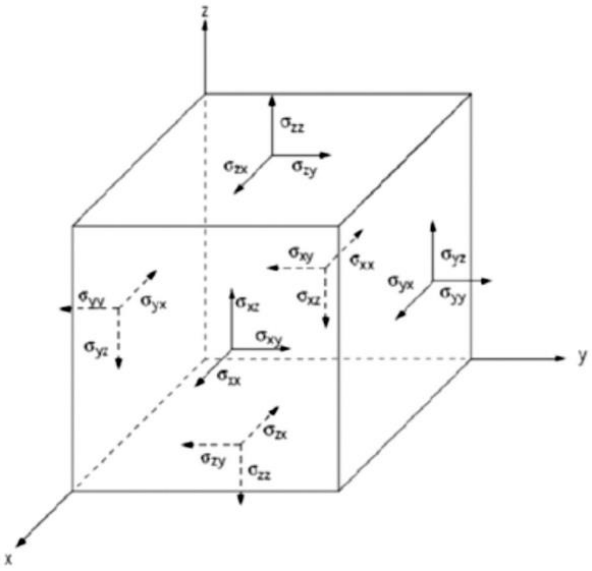


Figure 4.12 – Soil element under general stress state

One of the major advantages of the cubical cell apparatus (CCA) is the capability of applying either uniform deformation or uniform stresses to a cubical sample independently in three orthogonal directions. The strong interaction and cooperative feedback between analytical and experimental work is the basic principle to improve soil modelling philosophy. The results

gained from true triaxial testing have become a cornerstone for judging the competency of constitutive models.

In this research, a flexible CCA with three degrees of freedom with independent control of principal stresses and fixed principal axes was used. The CCA is described in this section.

4.6.1 Principles of the Cubical Cell

A cubical cell consists in a soil sample with cubic shape placed inside a chamber. The apparatus is described in the following section. In this chamber, the three directions of the stresses can differ from each other. The intermediate principal stress parameter *b* introduced by Habib (1953) and later used by Broms and Casbarian (1964) and Bishop (1966) is presented in Equation 4.4.

$$b = \frac{\sigma_2 - \sigma_3}{\sigma_1 - \sigma_3} \tag{4.4}$$

The value of b indicates the relative magnitude of the intermediate principal stress: b is zero for triaxial compression in which $\sigma_2 = \sigma_3$; and it is unity for triaxial extension in which $\sigma_2 = \sigma_1$; for intermediate values of σ_2 the value of b is between zero and unity (LADE & DUNCAN, 1973). When b is 0.5, simple shear conditions are imposed to the soil specimen.

Also, on the cubical cell, no friction on the faces of the specimen is assumed; therefore, the normal stresses (σ_x, σ_y, σ_z) and strains (ε_x, ε_y, ε_z) on the sides of the specimen are principal components of the stress and strain tensors.

In order to observe the stress paths in the deviatoric plane, stress states can be presented in terms of orthogonal deviatoric stress components q_x and q_z (Eq. 4.5 and Eq. 4.6). These components provide a view of π plane down the diagonal space ($\sigma_x = \sigma_y = \sigma_z$), in which the projection of σ_z axis coincides with q_z axis. Usually, the subscripts *x* and *y* refer to the horizontal directions and *z* refers to the vertical direction (Figure 4.13).

$$q_x = \frac{\sigma_y - \sigma_x}{\sqrt{2}} \tag{4.5}$$

$$q_z = \frac{2\sigma_z - \sigma_y - \sigma_x}{\sqrt{6}} \tag{4.6}$$

Determining the deviatoric stress and strain is possible with Equation 4.7 and 4.8:

$$q = \sqrt{\frac{(\sigma'_y - \sigma'_z)^2 + (\sigma'_z - \sigma'_x)^2 + (\sigma'_x - \sigma'_y)^2}{2}} \quad (4.7)$$

$$\varepsilon_q = \frac{1}{3}\sqrt{2\left[(\varepsilon_y - \varepsilon_z)^2 + (\varepsilon_z - \varepsilon_x)^2 + (\varepsilon_x - \varepsilon_y)^2\right]} \quad (4.8)$$

The shear stress changes on the cubical cell is often represented with the octahedral plane. When considering a plane passing through the three apexes of the cubical sample (Figure 4.13), the shear stress induced in this plane can be made to change not only in amplitude but also in direction by applying programmed changes in the three principal stresses. The tangential component, σ_{oct}, and its direction on the *octahedric plane* are given as a function of the three principal stresses σ'_x, σ'_y and σ'_z (Eq. 4.9). Equation 4.10 expresses the octahedric shear stress.The principal stress direction, θ, is expressed in Equation 4.11.

$$\sigma_{oct} = \frac{1}{3}(\sigma'_x - \sigma'_y + \sigma'_z) \quad (4.9)$$

$$\tau_{oct} = \frac{1}{3}\sqrt{(\sigma'_x - \sigma'_y)^2 + (\sigma'_y - \sigma'_z)^2 + (\sigma'_z - \sigma'_x)^2} \quad (4.10)$$

$$\theta = \tan^{-1}\left(\frac{\sqrt{3}(\sigma'_y - \sigma'_x)}{2\sigma'_z - \sigma'_x - \sigma'_y}\right) \quad (4.11)$$

The octahedral shear strain, γ_{oct}, and the angle ω, indicating the direction of the γ_{oct} on the octahedral plane, are given as a function of the three principal strains, ε_x, ε_y and ε_z.

$$\gamma_{oct} = \frac{2}{3}\sqrt{(\varepsilon_x - \varepsilon_y)^2 + (\varepsilon_y - \varepsilon_z)^2 + (\varepsilon_z - \varepsilon_x)^2} \quad (4.12)$$

$$\tan\omega = \frac{\sqrt{3}(\varepsilon_y - \varepsilon_x)}{2\varepsilon_z - \varepsilon_x - \varepsilon_y} \quad (4.13)$$

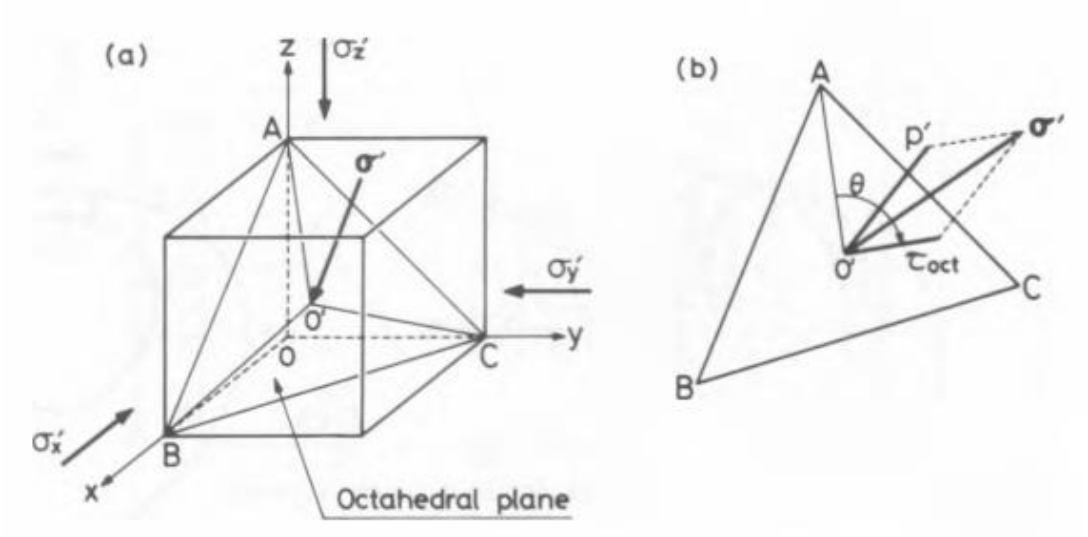


Figure 4.13 – Representation of stress conditions on the octahedral plane (ISHIHARA & YAMADA, 1979)

In order to illustrate this octahedral plane, Figure 4.14 represents the stress path with b = 0, 0.5 and 1 with loads of σ_{oct} = 50, 100 and 200 kPa.

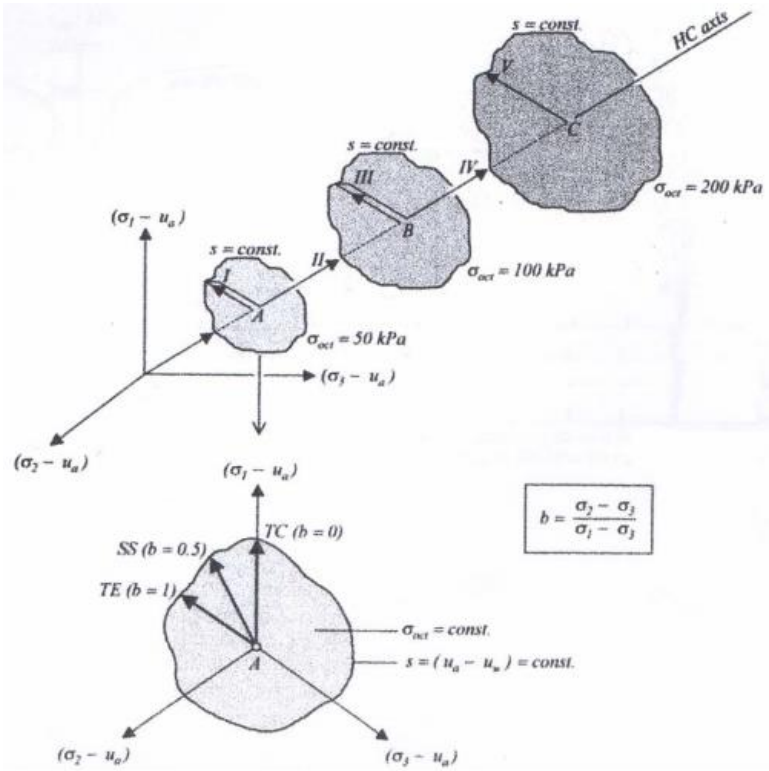


Figure 4.14 – Stress representation on the octahedral plane (REDDY & SAXENA, 1993)

4.6.2 The CCA

The stress controlled CCA enables a thorough investigation of the behaviour of soils along any pre-determined stress path. The design and configuration of the apparatus in the University of Bristol was inspired by the one developed at the University of Colorado at Boulder (DEWOOLKAR et al., 1997). The apparatus consists of a stainless-steel frame, which creates the inner chamber for housing the specimen. Each face of the frame includes a cavity which contains a rubber cushion that is used to transmit uniform controlled normal stresses to the surface of the sample. Two diagonal ports are machined through the rigid frame, providing the potential to connect the specimen to back pressure, drainage or vacuum lines.

The frame is externally closed by six stainless-steel wall assemblies using six connection bolts on each face, from which a perfect seal of the pressurised cushion in the device is guaranteed. Figure 4.15 represents a schematic view of the CCA utilised, including the frame, rubber cushion and wall assemblies. Two inlet connections are located on each wall assembly, one for introducing air pressure to the cushion and hence to the surface of the sample and the other for releasing the pressure after the accomplishment of any test. Three Linear Variable Differential Transformers (LVDTs) are positioned on each face of the apparatus (giving a total of eighteen LVDTs) for measuring sample displacements. The LVDTs lie at the corners of an imaginary equilateral triangle, whose centre coincides with the centre of the wall assembly. The outer stainless-steel tube of the LVDT is fixed to the respective wall assembly and covered with epoxy in order to prevent any leakage from the pressurised air inside the cell, whereas the tip of the inner core is kept permanently in contact with the facing cushion by means of disc magnets that are glued to the latter cushion (SADEK, 2006).

In order to avoid the sample translation inside the cubical cell during the application of the stresses, the tests were performed with three rigid faces while the pressure and displacements are measured in the corresponding opposite flexible faces.

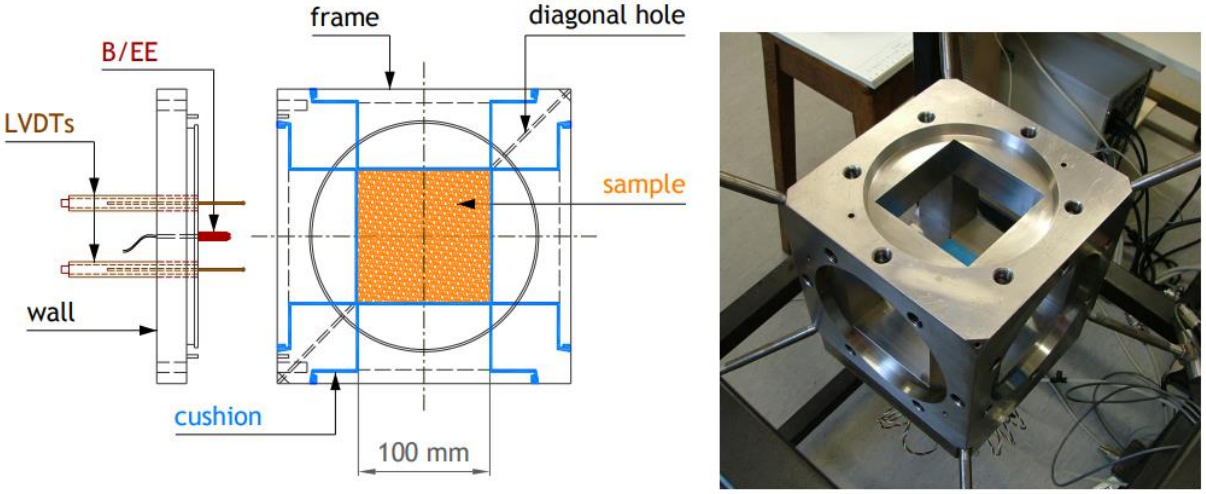


Figure 4.15 – Cubical cell schematic diagram and photograph of the frame (after SADEK, 2006)

4.6.3 Stress application system

A schematic layout of the stress application system, which is organised through the control panel, is presented in Figure 4.16. It consists of an air pressure regulator to adjust the maximum inlet pressure, a filter to prevent any moisture from getting into the electronic regulators, a manual regulator for each axis to control the required pressure independently, a dial gauge to display the current pressure and a number of two-way and three-way valves. The control panel includes also a vacuum control to apply vacuum to the sample when samples required a back-pressure control. During the tests, the three axis pressures were controlled manually. The maximum pressure imposed by the air supply was 800 kPa.

Additional tubing and valves were connected between the *x*, *y* and *z*-axis in order to have the potential to achieve different stress conditions. For example, if testing under isotropic stress conditions is required then the above-mentioned valves are opened, allowing one pressure regulator to control equal stresses on all faces of the sample, whereas the remaining two regulators are inoperable. In the same manner, axi-symmetric conditions (e.g. $\sigma_{xx} = \sigma_{yy}$) could be achieved by opening the *XY* valve and keeping the other valves closed.

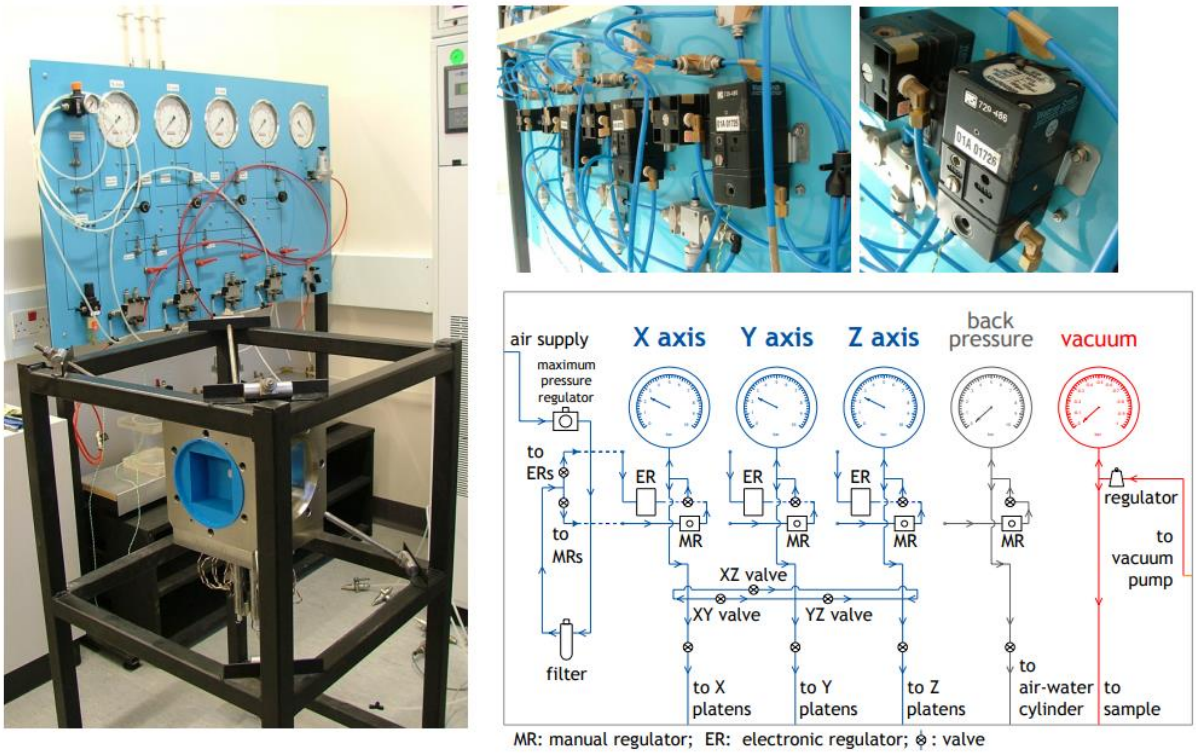


Figure 4.16 – Pressure panel diagram and pictures
(after FERREIRA, 2008)

4.6.4 Measurement system and software

Displacement measurements are performed using Macro Sensors LVDTs of series DC 750 with input power demand of 15V DC at 25mA. The LVDT is a common type of electromechanical transducer that can convert a rectilinear motion of an object to which it is coupled mechanically into a corresponding electrical signal.

Strains on each direction are calculated based on the displacements on each face. The LVDTs have a range of approximately ± 16mm. Each LVDT has been calibrated individually using a micrometre, producing a calibration factor, which is deduced from the statistically best-fit straight line derived by the least squares' method. A Modular 600 Instrumentation Unit is connected to the transducers as a dual channel amplifier.

The inlet pressure to the cushions is measured by means of three pressure transducers, each connected to the pressure lines that are associated with one axis of the apparatus. The pressure transducers were also re-calibrated. The transducer is positioned directly behind the wall assembly in order to assess the exact pressure transmitted to the cushion.

For data acquisition, the NI PCI-6031E analogue input card was used, complemented by a SCB-100 connector box. All eighteen LVDTs and the three pressure transducers are connected in this box. In order to wire all the cables from the instruments correctly, it is necessary to know how the card recognizes each channel, as provided by its quick reference chart (Figure 4.17). After allocating each channel to each transducer, these must be correctly introduced in the software for correct channel configuration, using LabView Measurement and Automation Explorer [MAX].

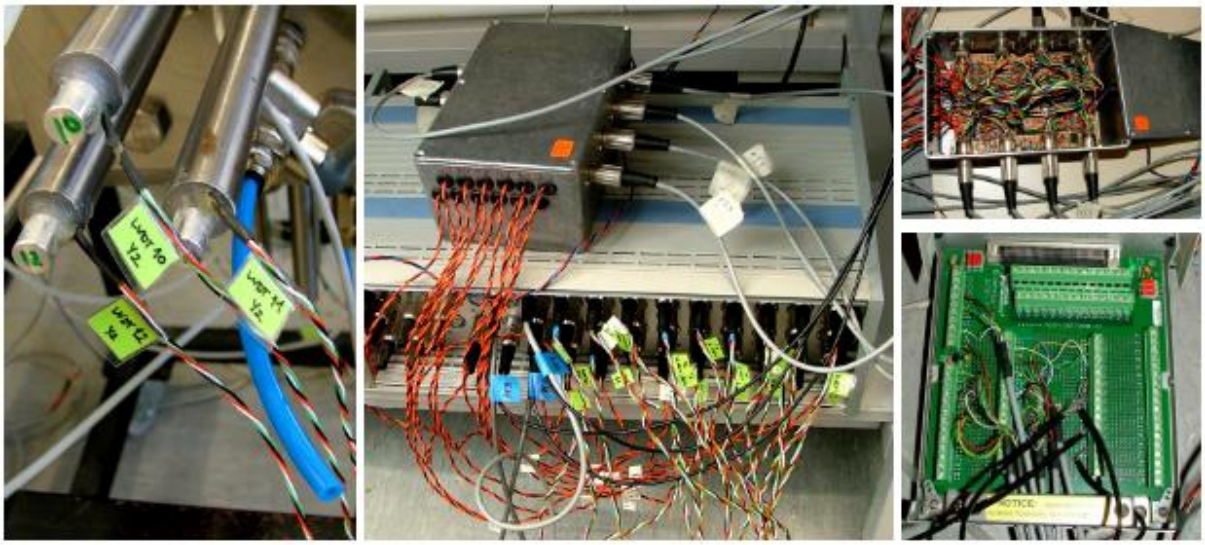


Figure 4.17 – LVDT connections to the reading system

The control system consists of a computer connected to an Analog Input Card NI 6031E connected to a SCB-100 Connector block. LabVIEW software was updated to register the data of the pressure transducers and the LVDTs. The software is not used to control testing, just for reading the sensors. The layout of the cubical cell is presented in Figure 4.18.

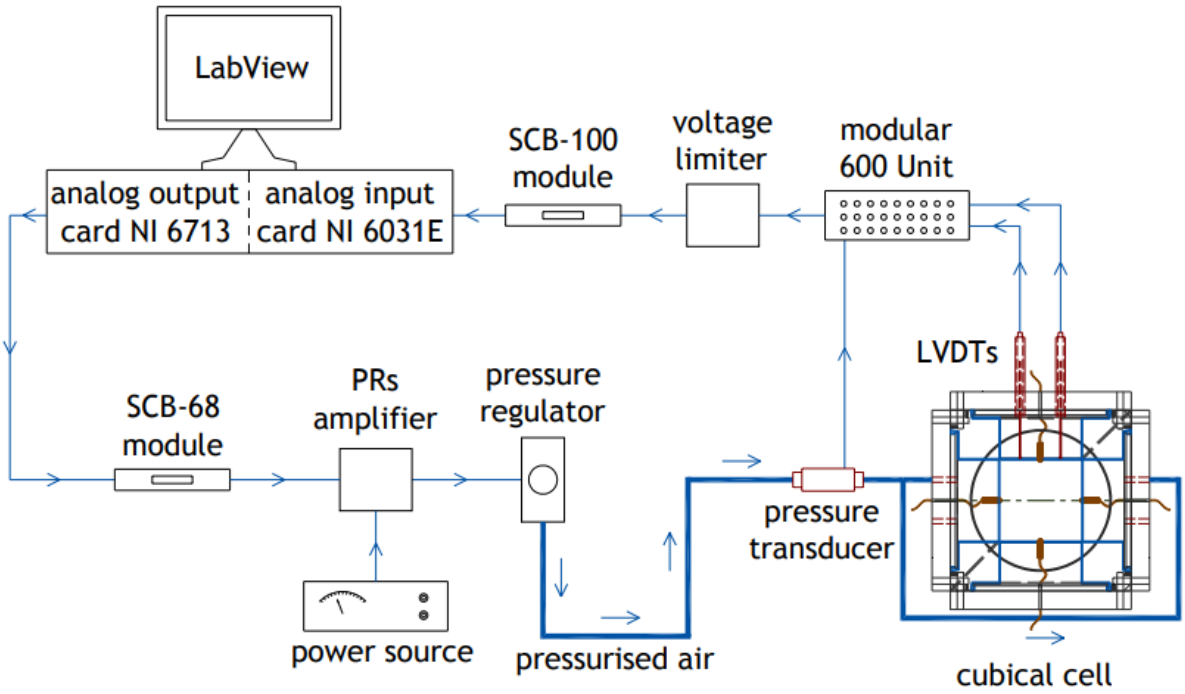


Figure 4.18 – General layout of the instrumentation components of the CCA testing system (after FERREIRA, 2008)

4.6.5 Displacement transducers

As previously mention, the cubical cell contains three LVDTs on each face of the cube, totalling eighteen linear measurements. In each face, the transducers are placed in a triangular arrangement.

Each LVDT is intended (and required) to be in permanent contact with the pressurizing cushion in order to monitor the movements and displacements experienced during testing. For this reason, magnets glued to the cushion are applied and the contact between the LVDTs and the cushion can be guaranteed. Three miniature magnetic discs were required to ensure proper contact: while the first disc magnet has to be glued in the cushion, the others are bonded together by the magnetic force (Figure 4.19). The magnet to cushion bond is an important issue because it is crucial that it has long-term stability, especially under testing pressures.

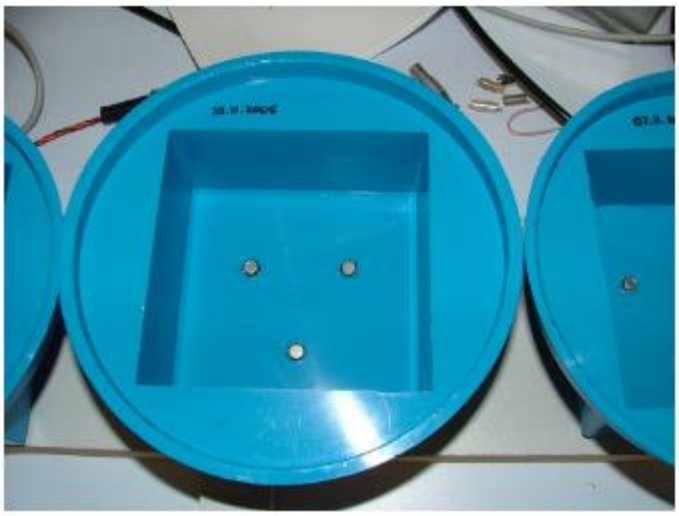


Figure 4.19 – Magnets to assure contact between cushion and LVDT

For the calibration of each LVDT, a micrometre was used, with a range of 25 mm and an accuracy of 1 μm. The calibrator consisted of the micrometre fixed to an aluminium arm, which was attached on the other end to a long-threaded steel rod. Making use of the screw holes in each platen, the calibrator was fastened in place and positioned exactly in line with the LVDT.

The three pressure transducers were also recalibrated for the testing.

4.6.6 Cushion effect

In order to differentiate between the true cemented-soil deformation and cushion, a wide set of calibration has been performed in the CCA using a 100 mm size aluminium cube. The aluminium block was enclosed in a membrane identical to the ones for soil testing (SADEK, 2006). Testing was carried as a soil sample was being tested. Cushion axial deformation was around $5x10^{-3}$ mm at a normal stress of 500kPa, and membrane deformation corrections have been applied to the displacement out for all the tests performed in this research.

4.7 HOLLOW CYLINDER TORSIONAL APPARATUS

This section provides a detailed description of one of the most advanced soil testing devices, namely Hollow Cylinder Torsional Apparatus (HCTA). It presents the unique set of capabilities of the apparatus and includes a discussion of its limitations.

The precision of the instrumentation and a preliminary assessment of the performance of the local measurement system outfitted with the HCTA is presented at the end of the chapter. Three

pairs of non-contact sensors were able to capture the small strain stiffness of the sample. To deal with the limited measuring range offered by the sensors, a complex mounting system was designed to allow the repositioning of each transducer during the test. The calibration of the small strain stiffness is presented together with the verification of previous calibrations performed (MANDOLINI, 2014; 2018) on the ancillary instrumentation of the apparatus.

4.7.1 Principles of the Hollow Cylinder Torsional Apparatus

The HCTA is particularly suited for the investigation of the soil mechanical response under generalized loading conditions. Soil samples tested in the HCTA have a typical hollow cylindrical shape (as shown in Figure 4.20a) and the apparatus has the capability to control axial load (W), torque load (T) and internal and external pressure (P_i, P_o) independently. This allows management of four different stress components: the axial (σ_z), radial (σ_r), circumferential (σ_θ) and shear stress ($\tau_{\theta z}$) which entails respectively axial (ε_z), radial (ε_r), circumferential (ε_θ) and shear ($\gamma_{\theta z}$) strains. The four degrees of freedom are a unique peculiarity of this equipment, making generalised stress path testing in the multiaxial stress space possible.

4.7.1.1 Stress state in Hollow cylinder sample

A typical stress state of a soil element within a hollow cylindrical sample is illustrated in Figure 4.20b, while the resulting stress state in terms of principal stresses is shown in Figure 4.20c.

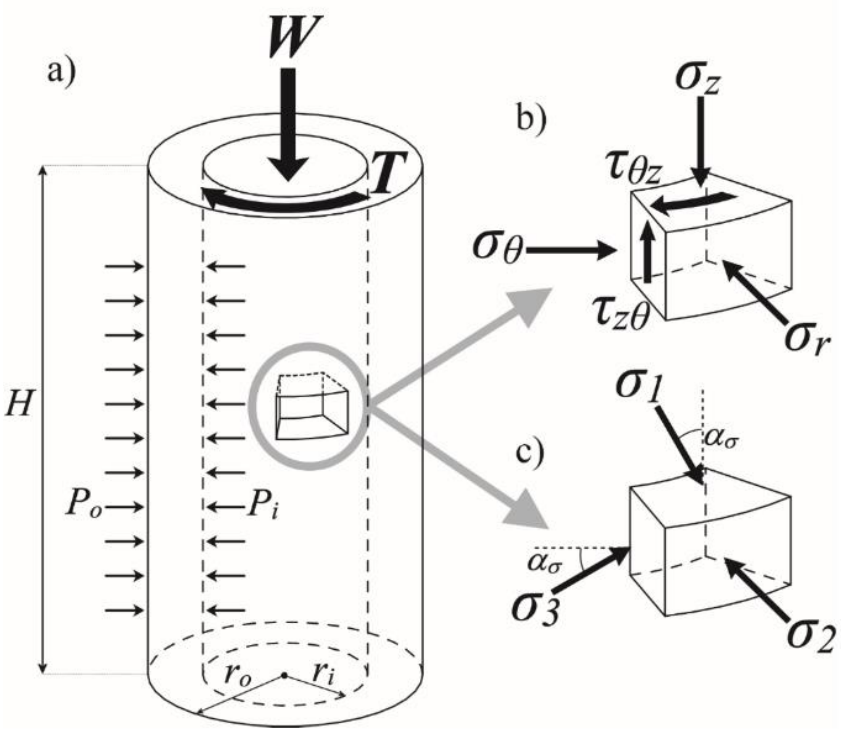


Figure 4.20 – Definition of forces and stresses in hollow cylinder specimen: (a) surface loads, (b) stress components and (c) main principal stresses on a representative element of the specimen's wall (MANDOLINI et al., 2018)

It follows that the stress state σ matrix for a hollow cylinder sample can be defined in Equation 4.13:

$$\sigma = \begin{bmatrix} \sigma_r & 0 & 0 \\ 0 & \sigma_\theta & \tau_{\theta z} \\ 0 & \tau_{z\theta} & \sigma_z \end{bmatrix} \tag{4.14}$$

The four degrees of freedom provide remarkable testing capabilities, but this comes at the expense of unavoidable stress and strain variations within the sample. Thus, any stress/strain is deduced from average quantities. There have been several attempts to propose representative values of average radial and circumferential stresses (σ_r and σ_θ) within the sample (e.g. HIGHT et al., 1983; FRYDMAN et al., 1973). Assuming an isotropic, linear-elastic response of the material and using the Lamé equations for hollow cylinder with thick walls, the relationships in Table 4.2 can be derived. The stresses are integrated over the whole volume of the sample and the curvatures of internal and external lateral walls are accounted for. The expression for the shear stress ($\tau_{z\theta}$) in Table 4.2 can be instead derived assuming a rigid plastic behaviour for the material and a uniform distribution of shear stress within the wall of the specimen. Note that r_o and r_i indicate respectively the outer and inner radii of the hollow cylinder sample, θ_s is the

rotation at its top end and H_s represents its height, while the symbol Δ before the variable indicates its variation.

Table 4.2 – Equations for stress and strain components of hollow cylinder specimens (HIGHT et al., 1983; VAID et al., 1990)

Axis directions	*Stress equations*	*Strain equations*
Axial normal	$\sigma_z = \frac{P_i r_i^2 - P_o r_o^2}{r_o^2 - r_i^2} + \frac{W}{\pi(r_o^2 - r_i^2)}$	$\varepsilon_z = -\frac{\Delta H}{H}$
Radial normal	$\sigma_r = \frac{P_i r_i^2 - P_o r_o^2}{r_o^2 - r_i^2} - \frac{2(Po - Pi) r_o^2 r_i^2 ln\,(r_o/r_i)}{(r_o^2 - r_i^2)^2}$	$\varepsilon_r = -\frac{\Delta r_o - \Delta r_i}{r_o - r_i}$
Circumferential normal	$\sigma_\theta = \frac{P_i r_i^2 - P_o r_o^2}{r_o^2 - r_i^2} + \frac{2(Po - Pi) r_o^2 r_i^2 ln\,(r_o/r_i)}{(r_o^2 - r_i^2)^2}$	$\varepsilon_\theta = -\frac{\Delta r_o + \Delta r_i}{r_o + r_i}$
Circumferential normal	$\tau_{\theta z} = \tau_{z\theta} = \frac{3T}{2\pi(r_o^3 - r_i^3)}$	$\gamma_{\theta z} = \frac{2\Delta\theta\pi(r_o^3 - r_i^3)}{3H(r_o^2 - r_i^2)}$

Using the Mohr's circle described in Figure 4.21 below, it is possible to derive the relationships between the three principal stresses (σ_1, σ_2 and σ_3) and any given stress state of the sample (σ_z, σ_r, σ_θ and $\tau_{z\theta}$):

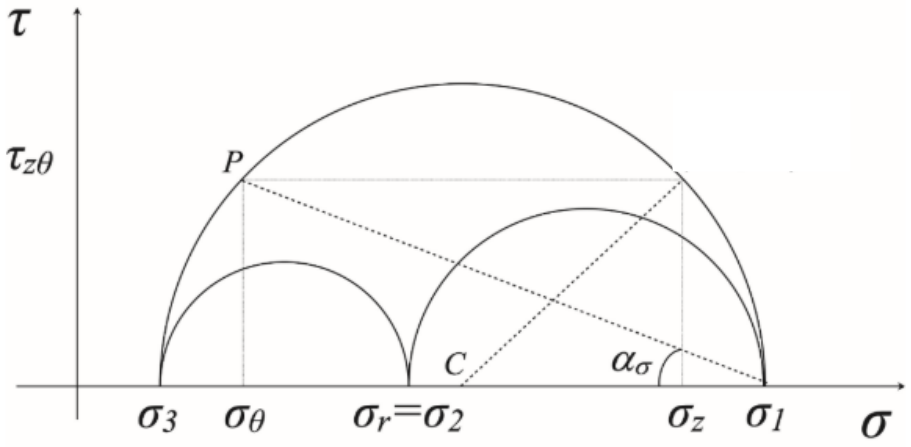


Figure 4.21 – Relationship between applied stresses and principal stresses using the Mohr circle

$$\sigma_1 = \frac{\sigma_z + \sigma_\theta}{2} + \sqrt{\left(\frac{\sigma_z - \sigma_\theta}{2}\right)^2 + \tau^2{}_{\theta z}} \qquad (4.15)$$

$$\sigma_3 = \frac{\sigma_z+\sigma_\theta}{2} - \sqrt{\left(\frac{\sigma_z-\sigma_\theta}{2}\right)^2 + \tau^2{}_{\theta z}} \quad (4.16)$$

$$\sigma_2 = \sigma_r \quad (4.17)$$

From the Mohr's circle, it is also possible to derive an expression for the angle ασ which defines the inclination of the major principal stress (σ_1) to the vertical axes as illustrated previously in Figure 4.20c:

$$\alpha_\sigma = \frac{1}{2}\tan^{-1}\left(\frac{2\tau_{\theta z}}{\sigma_\theta-\sigma_z}\right) \quad (4.18)$$

The inclination of the major principal axis (α_σ) can describe the direction of loading in the generalised multiaxial space, which has a fundamental influence on the mechanical response of anisotropic soils. Its value can vary within the range 0° to 90°. Comparing various laboratories' testing apparatus, α_σ is the parameter which thoroughly interprets the stress path applied to the sample. There is a second stress variable *b* which is necessary to describe the applied state of stress and defines the relative magnitude of the intermediate principal stress:

$$b = \frac{\sigma_2-\sigma_3}{\sigma_1-\sigma_3} \quad (4.19)$$

The variable *b* can vary between 0 and 1 when the intermediate principal stress is equal to the minor ($\sigma_2 = \sigma_3$) or to the major one ($\sigma_2 = \sigma_1$), respectively.

For this particular investigation and for most of the published works on the HCTA, an equal internal and external pressure, $P_i=P_o=P$ has been used, hence σ_r and σ_θ become both equal to applied pressure *P*. From Eq. (4.20) σ_2 must be equal to *P* as well. Therefore, for this case, changes in α_σ angle are accompanied by changes in the magnitude of *b* (HIGHT et al., 1983):

$$b = \sin^2 \alpha_\sigma \quad (4.20)$$

When working in multiaxial stress conditions, it is also useful to define the stress state using the isotropic and deviatoric components which can be derived from the invariants of the stress tensor in Equation 4.21. The isotropic component *p* is defined as one third of the trace of the stress tensor and thus it is the average of the normal stresses on the sample:

$$p = \frac{\sigma_z+\sigma_\theta+\sigma_r}{3} = \frac{\sigma_1+\sigma_2+\sigma_3}{3} \quad (4.21)$$

For the stress state matrix described in Equation 4.22, the deviatoric component of the stress can be expressed in the following way:

$$q = \sqrt{\frac{(\sigma_z-\sigma_r)^2+(\sigma_r-\sigma_\theta)^2+(\sigma_\theta-\sigma_z)^2}{2} + 3{\tau_{\theta z}}^2} \quad (4.22)$$

which turns into the following if expressed with respect to principal stresses:

$$q = \sqrt{(\sigma_1-\sigma_3)^2 + (\sigma_1-\sigma_2)^2 + (\sigma_2-\sigma_3)^2} \quad (4.23)$$

In the case of pure axi-symmetric (i.e. conventional triaxial) compression (α_σ = 0°) and extension tests (α_σ = 90°), the value of q is governed by the difference between the axial stress σ_z and the other two perpendicular stresses (σ_r and σ_θ). For pure torsional tests instead (α_σ = 45°), the value of q is totally governed by the value of the shear stress $\tau_{\theta z}$, being the axial, radial and circumferential stresses equal among them ($\sigma_z = \sigma_\theta = \sigma_r$). For any other test, the value of the deviatoric stress q is the result of a combined contribution of $\tau_{\theta z}$ and the differences among the three normal stress components.

4.7.1.2 Strain state in a hollow cylinder sample

The strain state of the sample can be expressed by the matrix in Equation 4.23

$$\varepsilon = \begin{bmatrix} \varepsilon_r & 0 & 0 \\ 0 & \varepsilon_\theta & \varepsilon_{\theta z} \\ 0 & \varepsilon_{z\theta} & \varepsilon_z \end{bmatrix} \quad (4.24)$$

where ε_r, ε_θ and ε_z are respectively the radial, circumferential and axial strains and $\gamma_{\theta z}$ is the shear strain. The strains are also averaged within the sample. The various average strain components are calculated using the equations proposed by Hight et al. (1983) and Vaid et al. (1990) and the expressions are summarised in Table 4.2, in which H_s is the sample height, ΔH_s represents the axial displacement, Δr_o and Δr_i are respectively the change in the outer and inner radii and θ_s denotes the angle of torque relative to the top of the specimen.

Note that average values of strains are derived using a procedure which is based on strain compatibility only and, different from the resulting expressions for the stresses, are thus independent of the constitutive law assumed for soil behaviour.

Using a Mohr's circle for strain similar to the one proposed for stresses in Figure 4.21, it is now possible to derive the following relationships between principal and actual strains:

$$\varepsilon_1 = \frac{\varepsilon_z+\varepsilon_\theta}{2} + \sqrt{\left(\frac{\varepsilon_z-\varepsilon_\theta}{2}\right)^2 + \gamma^2{}_{\theta z}} \quad (4.25)$$

$$\varepsilon_3 = \frac{\varepsilon_z+\varepsilon_\theta}{2} - \sqrt{\left(\frac{\varepsilon_z-\varepsilon_\theta}{2}\right)^2 + \gamma^2{}_{\theta z}} \quad (4.26)$$

$$\varepsilon_2 = \varepsilon_r \quad (4.27)$$

It is now convenient to introduce also the isotropic (or volumetric) and deviatoric components of the strains which are derived from invariants of the stain tensor. The volumetric strain ε_v component is defined as:

$$\varepsilon_V = \varepsilon_z + \varepsilon_r + \varepsilon_\theta \quad (4.28)$$

While the deviatoric strain component ε_q is:

$$\varepsilon_q = \sqrt{\frac{2(\varepsilon_z-\varepsilon_r)^2+2(\varepsilon_r-\varepsilon_\theta)^2+2(\varepsilon_\theta-\varepsilon_z)^2+3\gamma_{\theta r}{}^2}{3}} \quad (4.29)$$

4.7.2 Stress non-uniformities

As previously mentioned, the advantage of having four degrees of freedom comes at the expense of dealing with a soil system rather than a uniform soil element. Generally, stresses (therefore strains) will not be uniform within the sample and this may produce inaccurate predictions of the calculated average stresses necessary to consider the sample as a hollow cylindrical element.

Non-uniform distribution of stresses across the specimen wall arises because of the sample's curvature and restraint ends effect. The end restraints may develop a radial shear stress due to the friction of the sample ends with the top and bottom platens. However, the extent of the disturbed area depends on the sample geometry.

For cylindrical solid samples, such as those used in conventional triaxial tests, enlarged lubricated ends may be used to minimise end restraints effects. Unfortunately, these lubricated ends cannot be applied to the HCTA samples tested in this research.

Some theoretical attempts proposed in literature have endeavoured to estimate the magnitude of stress non-uniformities. Hight et al. (1983), aware of the difficulties in evaluating either the stresses or the strains across the wall of the hollow cylinder sample, investigated the theoretical

differences between the calculated σ (using the relationship in Table 4.2) and real averages determined using a finite element method where a Cam-Clay constitutive model for soil was adopted. A coefficient β_1 which measures the difference between calculated and real average but normalised by a stress level factor (σ_L) was proposed:

$$\beta_1 = \frac{|\overline{\sigma^*} + \bar{\sigma}|}{\sigma_L} \tag{4.30}$$

where σ_L represents an average value of the stress component expressed by:

$$\sigma_L = \frac{|\bar{\sigma}_\theta + \bar{\sigma}_r|}{2} \tag{4.31}$$

An additional coefficient (β_3) was also introduced to quantify the level of non-uniformity of stresses:

$$\beta_3 = \frac{\int_{r_i}^{r_o} |\sigma(r) - \bar{\sigma}^*| dr}{(r_o + r_i)\sigma_L} \tag{4.32}$$

where $\sigma(r)$ is the distribution of the particular stress component (σ_z, σ_θ or $\tau_{\theta z}$) under consideration across the hollow cylinder specimen (Figure 4.22). Hight et al. (1983) suggested keeping the value of $\beta_3 < 0.11$ and $0.9 < P_o/P_i < 1.2$ in order to achieve an acceptable degree of non-uniformity.

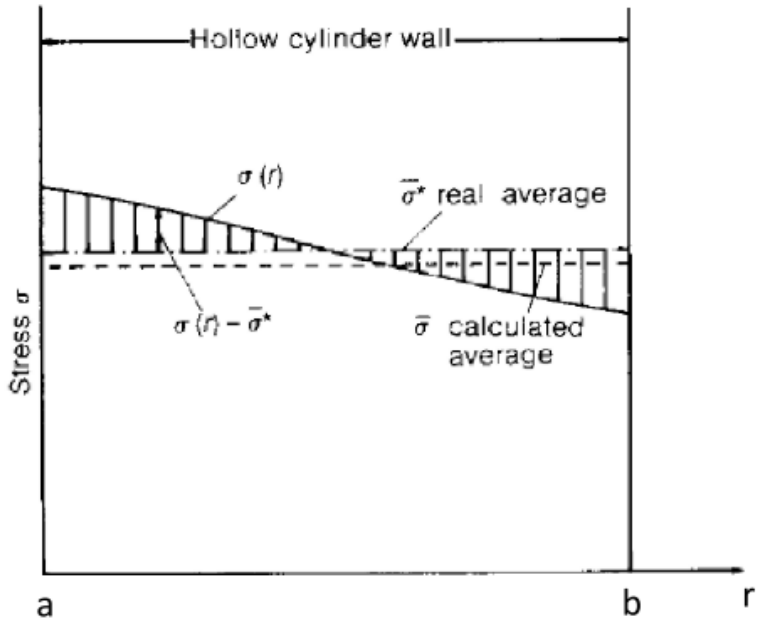


Figure 4.22 – Definitions used for stress non-uniformity
(HIGHT et al., 1983)

A few years later, Vaid et al. (1990) demonstrated that the coefficient β_3 proposed by Hight et al. (1983) may underestimate non-uniformities of stresses for particular stress paths.

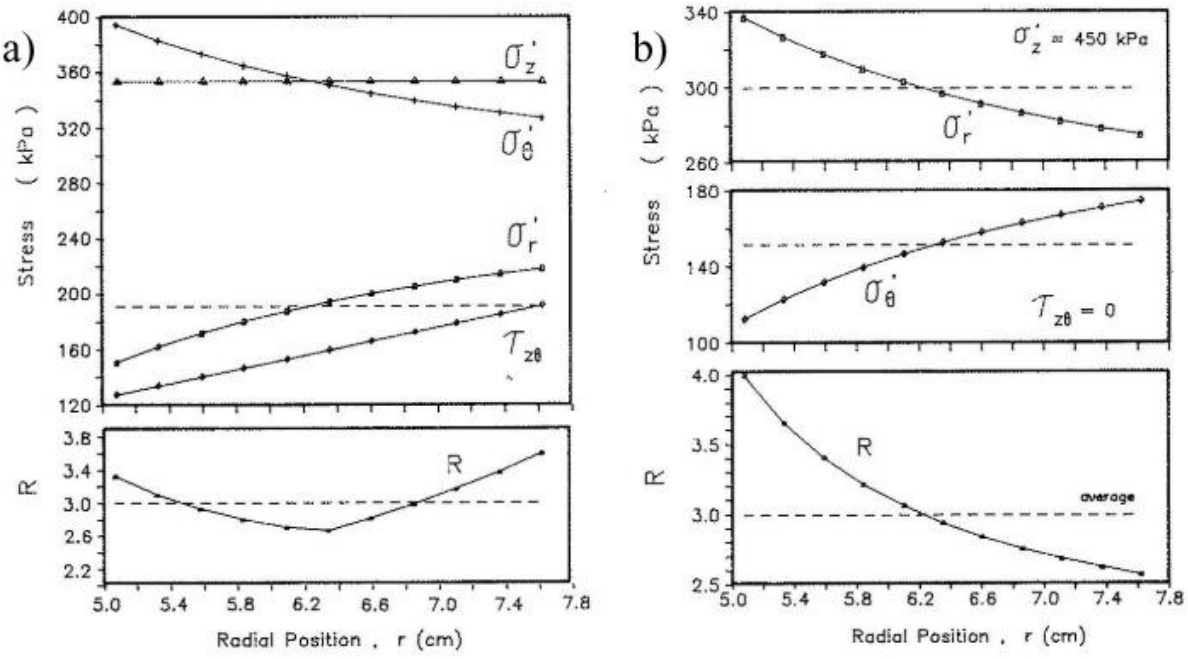


Figure 4.23 – Elastic stresses across the wall, (a) mean normal stress 300kPa, R=σ_1'/ σ_3'=3, b=0, α=45°; (b) Mean normal stress 300kPa, R=σ_1'/ σ_3'=3, b=0.5, α=0° (VAID et al., 1990)

Figure 4.23 presents the stress trends across the wall of the specimen for two different tests at α_σ=45° (Figure 4.23a) and α_σ=0° (Figure 4.23b) along with the ratio between the minimum and maximum principal effective stress ratio (R=σ_1'/σ_3'). β_3 values (HIGHT et al, 1983) indicated an acceptable degree of non-uniformity for both tests, but R trend in Figure 4.23b clearly shows an intolerable non-uniformity across the wall. Thus, a new index β_r was introduced by Vaid et al. (1990) to assess the degree of non-uniformity in terms of the ratio between the minimum and maximum principal effective stress

$$\beta_r = \frac{(R_{max}+R_{min})}{R_{av}} \tag{4.33}$$

where R_{max}, R_{min} and R_{av} are respectively the maximum, minimum and average value of stress ratios. Vaid et al. (1990) suggested that stress non-uniformity could be considered acceptable if the maximum difference between R_{max} and R_{av} was kept below 10%, which basically means $\beta_r \leq 0.2$.

The size of the specimen can significantly affect the development of stress non-uniformities during the tests. Non-uniformity of stress distribution across the wall of the hollow cylindrical specimen can be minimized by selecting suitable specimen dimensions and by using the same internal and external pressure, as recommended by Saada et al. (1983). When the wall thickness is reduced or the inner radius is increased, the stress distribution becomes more uniform (SAYÃO & VAID, 1991). Analysing a wide survey of hollow cylinder shear devices used by various researchers in the past, Sayão and Vaid, (1991) proposed the following Figure 4.24 where the sample geometries are plotted on the axes ($R_e - R_i$, R_i/R_e, $H/2R_e$) and the points within the boxes represent those tests for which non-uniformities were within an acceptable range. R_e and R_i represent respectively the outer and inner radii which before were indicated as r_o and r_i. The authors finally recommended this range of dimensions referring to the outer radius of the sample:

a) wall thickness: $R_o - R_i = 20 \div 26$mm;

b) inner radius: $0.65 < R_i/R_o < 0.82$;

c) height: $1.8 < H/2R_o < 2.2$.

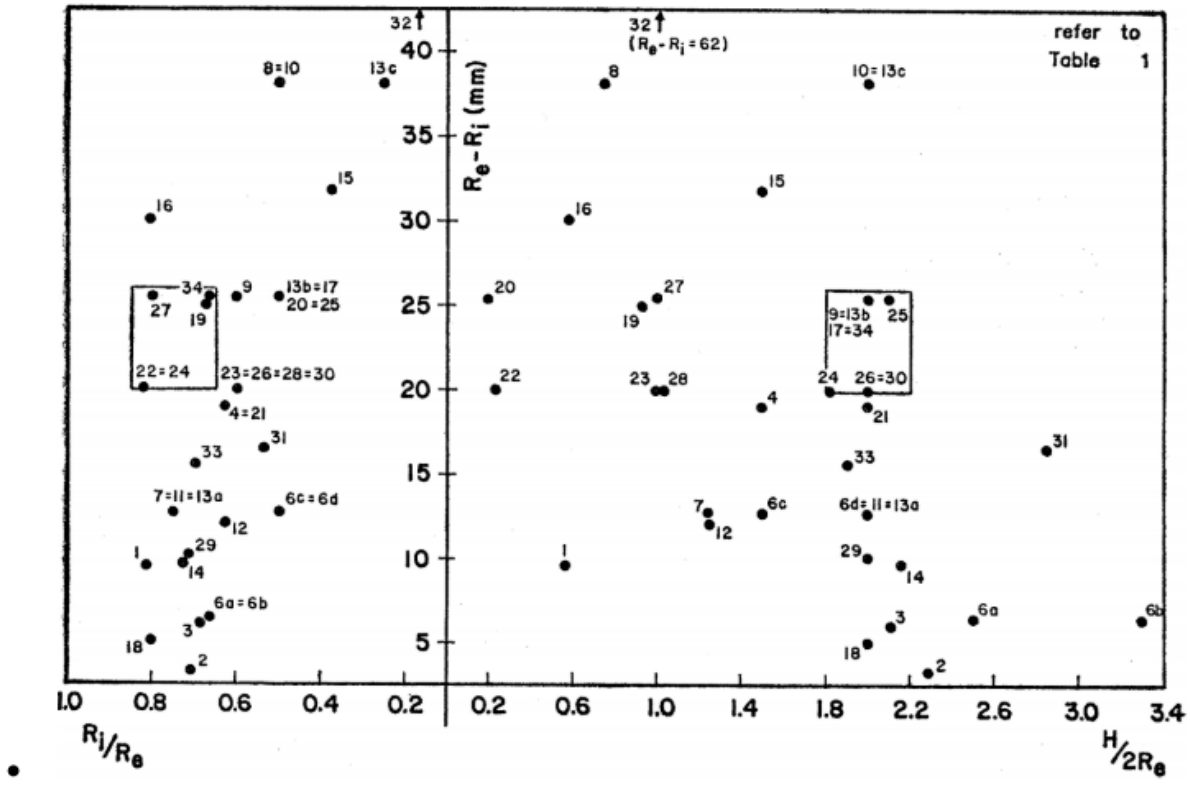


Figure 4.24 – Correction of hollow cylinder sample dimension
(SAYÃO & VAID, 1991)

4.7.3 Influence of rubber membrane

Two membranes, made from rubber latex material but with different diameters, are used to isolate the sample within the triaxial cell in the HCTA tests. Both membranes influence the boundary conditions of the sample: they both provide a restraining effect, but they can be pressed and penetrate into peripheral voids affecting volumetric measurement of the tested sample. These two effects are discussed in the following analysis.

4.7.3.1 Membrane penetration

When the investigation implies a confining pressure applied to granular soil samples enclosed by two thin membranes, membrane penetration is a concern. Within a sand matrix, there are relatively large spaces between granular particles which are filled up with air or water. In the lateral boundaries of the sample, where the latex membrane separates the sand from pressurised water in the cell, the membrane tightly covers the outline of the specimen, following all the irregularity between grains. This effect is called the membrane penetration. Under changes of cell and inner sample pressures, the amount of membrane penetration varies, and it may influence the volume change measurements of the sample, as illustrated in Figure 4.25. In the case of undrained tests, variation of membrane penetration may affect the volume constant conditions and largely influence the development of pore water pressure within the sample.

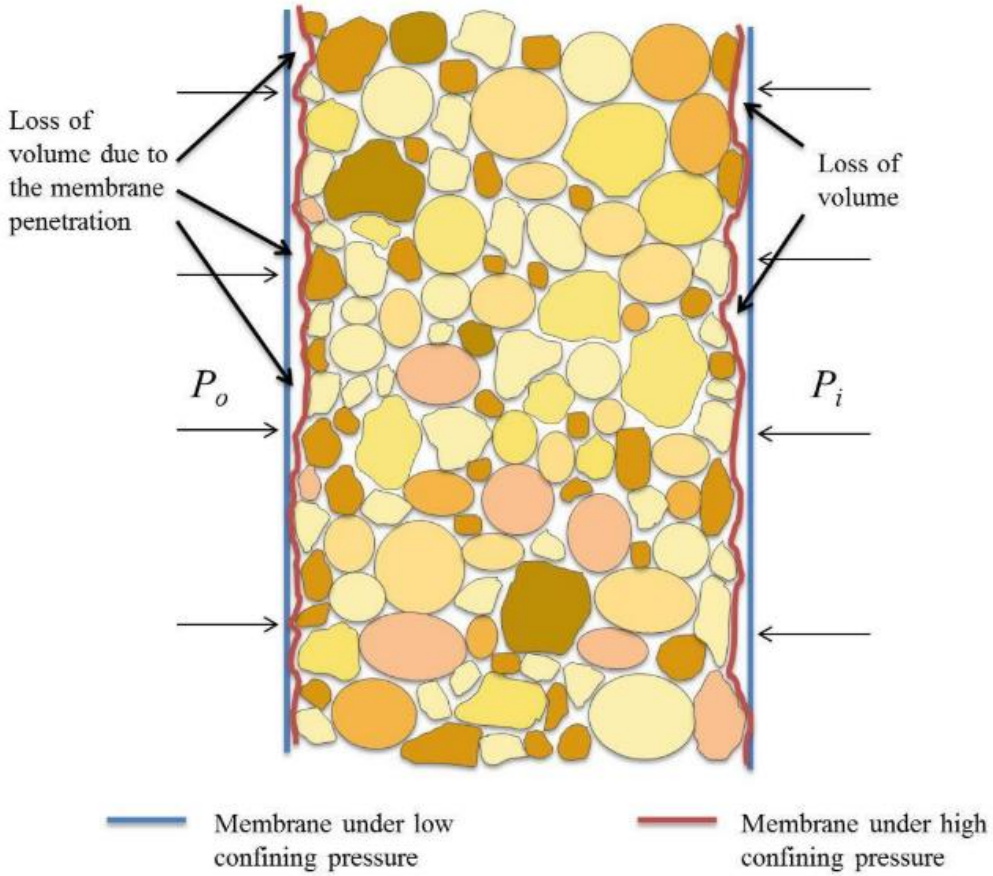


Figure 4.25 – Zoom on hollow cylinder wall: membrane penetration induced by internal (P_i) and external (P_o) pressure (MANDOLINI, 2014)

One of the first attempts to evaluate the membrane penetration was made by Newland and Allely (1957) in drained triaxial samples. They proposed a correction considering material isotropy under hydrostatic load increments ($\varepsilon_z = \varepsilon_\theta = \varepsilon_r$). The volumetric change due to the membrane penetration was computed as the difference between the total volumetric strain (ε_v) and three times the observed axial strain (ε_z). However, granular soils behave as anisotropic material, which makes this method not completely accurate. Later, the research of an accurate method to evaluate the magnitude of membrane penetration was directed toward the investigation on both the membrane surface area and the volume of the sample. Frydman et al. (1973), for example, investigated membrane penetration in both conventional triaxial and HCTA samples using different volumes and changing, particularly for the hollow cylinder samples, the internal diameter while the external was kept constant. The authors found a linear increment of the membrane penetration effect with the logarithm of cell pressure and they also proposed a relationship between the mean particle size D_{50} and the slope of the penetration curves (Figure 4.26).

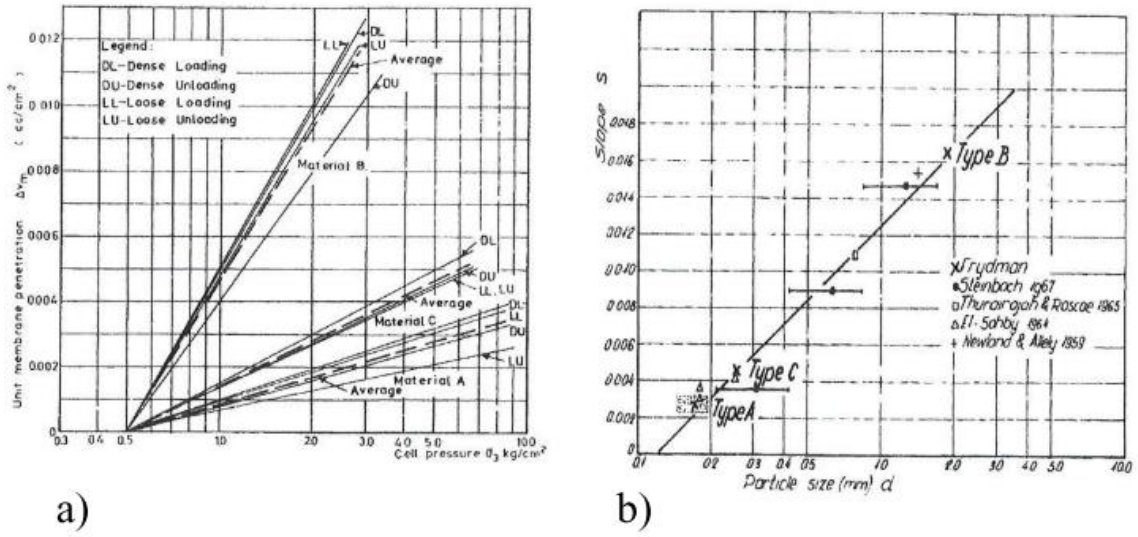


Figure 4.26 – Membrane penetration linear relationships: (a) effective lateral stress σ_3 and unit membrane penetration Δv_m; (b) particle size d and slope S of membrane penetration curves (FRYDMAN et al, 1973)

For medium sand sample with a mean particle size of $D_{50} \geq 0.1$mm the membrane penetration becomes a relevant issue and a correction should be applied, whereas it may be negligible for fine-grained soils (MOLENKAMP & LUGER, 1981).

Sivathayalan and Vaid (1998) suggested an alternative method for correction of the membrane penetration effects. They studied the difference between volumetric strain measurement directly on the specimen and those from the inner chamber of a single hollow cylindrical specimen hydrostatically loaded. The membrane penetration expression was proposed as:

$$\varepsilon_m = \frac{\Delta V_s - \Delta V_i(\chi^2 - 1)}{\chi(A_{mi} + A_{me})} \qquad (4.34)$$

in which ε_m is the unit membrane penetration (mm^3/mm^2), ΔV_i and ΔV_s are the measured volume changes of the inner chamber and sample, χ is the ratio between the outer and inner sample radii and A_{mi} and A_{me} are respectively the internal and external surface areas of the sample covered by the membranes.

Baldi and Nova (1984) formulated two methods to correct the measured values for undrained and drained tests considering all the main factors which influence the membrane penetration effect. Factors which can influence this effect (such as grain size, confining pressure, rigidity and thickness of the membrane and volume of the sample) are all considered in the following relationship for estimating the membrane penetration V_m (mm^3):

$$V_m = \frac{D_{50}V_o}{2D}\left[\frac{D_{50}}{E_m t_m}\right]^{1/3}\left[(\sigma'_3)^{1/3} - (\sigma'_{30})^{1/3}\right] \quad (4.35)$$

where D is the diameter of the specimen, V_0 is the volume of the specimen, E_m and t_m are respectively the Young's modulus and the thickness of the membrane, D_{50} is the mean grain size of the soil, σ'_{30} and σ'_3 are respectively the initial and final effective confining pressures applied.

Mandolini (2014) estimated the membrane penetration volume (V_m) for the outer and inner membranes accounting for the penetration effect on both the surfaces. The mean grain size (D_{50}) used was 0.32mm, membrane elastic modulus (E_m) of 2MPa, and thickness of the outer membrane ($t_{m,o}$) 0.5mm, while for the inner a thickness ($t_{m,i}$) of 0.3mm was considered. Calculations have been performed for the sample tested under the initial confining pressure (σ'_3) of 30kPa and final confining pressure (σ'_{30}) of 200kPa. The variation of volume due to both the inner and outer membrane penetration is finally 823.3 mm^3 which represents 0.08% of the initial volume. Therefore, volume variations because of the membrane penetration have been found negligible for the purpose of this research.

4.7.3.2 Membrane resistance

In order to obtain accurate results of computed stresses, Tatsuoka et al. (1986) suggested several equations which consider the adding strength provided by the inner and outer rubber membranes during the torsional shear. These stress corrections for the membrane forces are obtained using the theory of elasticity and considering the Poisson ratio of 0.5 for the rubber membranes.

$$\Delta\sigma_z = -\frac{4}{3}\frac{E_m t_m}{{r_o}^2 - {r_i}^2}\left\{r_o\left[2\left(\varepsilon_{z_m}\right)_0 + \left(\varepsilon_{\theta_m}\right)_0\right] + r_i\left[2\left(\varepsilon_{z_m}\right)_i + \left(\varepsilon_{\theta_m}\right)_i\right]\right\} \quad (4.36)$$

$$\Delta\sigma_\theta = -\frac{2}{3}\frac{E_m t_m}{r_o - r_i}\left\{\left[\left(\varepsilon_{z_m}\right)_0 + 2\left(\varepsilon_{\theta_m}\right)_0\right] + \left[\left(\varepsilon_{z_m}\right)_i + 2\left(\varepsilon_{\theta_m}\right)_i\right]\right\} \quad (4.37)$$

$$\Delta\sigma_r = -\frac{2}{3}\frac{E_m t_m}{r_o + r_i}\left\{\left[\left(\varepsilon_{z_m}\right)_0 + 2\left(\varepsilon_{\theta_m}\right)_0\right] - \left[\left(\varepsilon_{z_m}\right)_i + 2\left(\varepsilon_{\theta_m}\right)_i\right]\right\} \quad (4.38)$$

$$\Delta\tau_{\theta z} = -2E_m t_m \frac{{r_o}^3 + {r_i}^3}{({r_o}^3 + {r_i}^3)r_o - r_i}\gamma_{\theta z} \quad (4.39)$$

in which $(\varepsilon_{zm})_o$ and $(\varepsilon_{zm})_i$ are the average circumferential strains in the outer and inner membrane; $(\varepsilon_{\theta m})_o$ and $(\varepsilon_{\theta m})_i$ are the average circumferential strains in the outer and inner membrane; in particular these strains were calculated as:

$$\varepsilon_{z_m} = \varepsilon^*_{z_m} + \varepsilon_{z_k} + \varepsilon_z \tag{4.40}$$

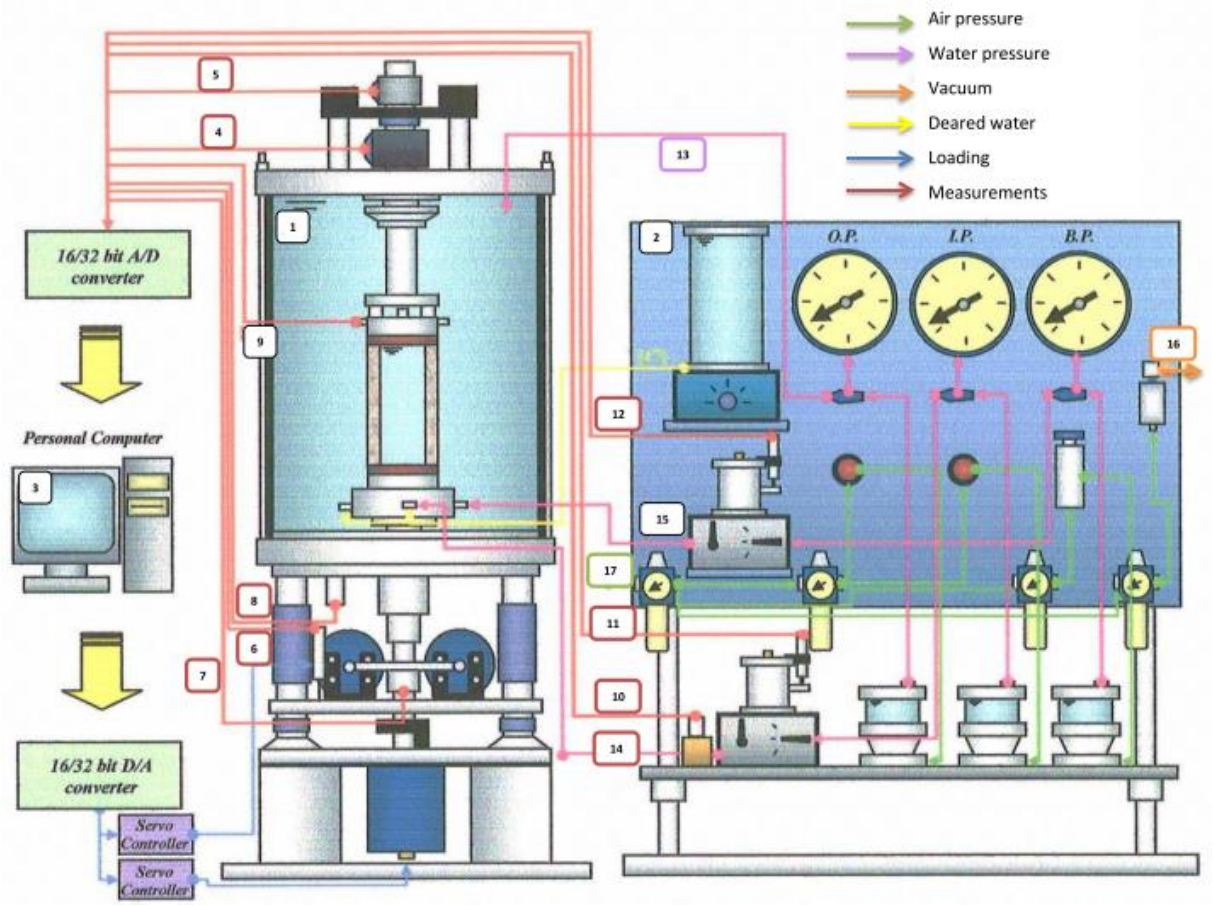
$$\varepsilon_{\theta_m} = \varepsilon^*_{\theta_m} + \varepsilon_{r_k} + \varepsilon_\theta \tag{4.41}$$

Where ε^*_{zm} and $\varepsilon^*_{\theta m}$ are the initial membrane strains at the setting of membranes, ε_{zk} and ε_{rk} are the strains along the radial and axial directions during compression and $\varepsilon_{z\ and}\ \varepsilon_\theta$ are the average axial and circumferential normal strains of the sample during torsional shear.

As for Mandolini (2014, 2018), in this study, in order to measure the membrane resistance, it was assumed that all strains were equal for both inner and outer membranes and the initial strains in the axial direction (ε^*_{zm}) were considered null while the initial strain along the circumference (ε^*_{zm}) was for both membranes in the order of -0.02, according to Tatsuoka et al. (1986).

4.7.4 HCTA facilities

The HCTA is a relatively recent apparatus developed at the University of Bristol and its description is provided by Yoon (2005) (i.e. first commissioning of the apparatus) and more recently by Mandolini (2014; 2018). The HCTA allows exploring advanced features of the soil behaviour in the multiaxial stress space, including cyclic variation of the principal stress direction. A schematic representation of the experimental arrangement is described in Figure 4.27 which includes a synthetic view of the confining cell, volume change measurement setup, data acquisition and control system, manual pressure control scheme and the hydraulic loading apparatus. Recently, the apparatus has been upgraded and the servo controller motor is no longer is use for the application of torque and load; instead, a hydraulic system is attached to the top of the apparatus (close to 5 in Figure 4.27) and the loads are applied through the top of the soil sample. A detailed description of the HCTA constituents is given in the following sections.



1	Confining cell	7	Torsional displacement measurement	13	Applied outer cell pressure
2	Manual Controlling System	8	Outer cell pressure measurement	14	Applied inner cell pressure
3	Data acquisition	9	Back/Pore pressure measurement	15	Applied back pressure
4	Axial load measurement	10	Inner cell pressure measurement	16	Vacuum
5	Torsional load measurement	11	Inner volume change measurement	17	Air pressure
6	Axial displacement measurement	12	Sample volume change measurement		

Figure 4.27 – HCTA schematic representation (YOON, 2005)

4.7.4.1 Confining cell

The confining cell (Figure 4.28) is made of thick transparent Perspex and is designed to sustain internal water pressure up to 1 MPa. Twelve stainless steel bars are placed around the cell to connect the bottom and top corrosion resistant stainless-steel rings and plates. With a dimension of 960mm in overall height, 597mm in external diameter and 521mm in internal diameter, the confining cell offers a spacious working plane around the specimens during both installation and testing. A capacity of almost 200 litres allows a wide variety of measuring instrumentation.

The top and the base surfaces of the cell are composed of corrosion-resistant stainless steel with high stiffness and include the air bleed valve or outlet valve for draining water filled in the cell.

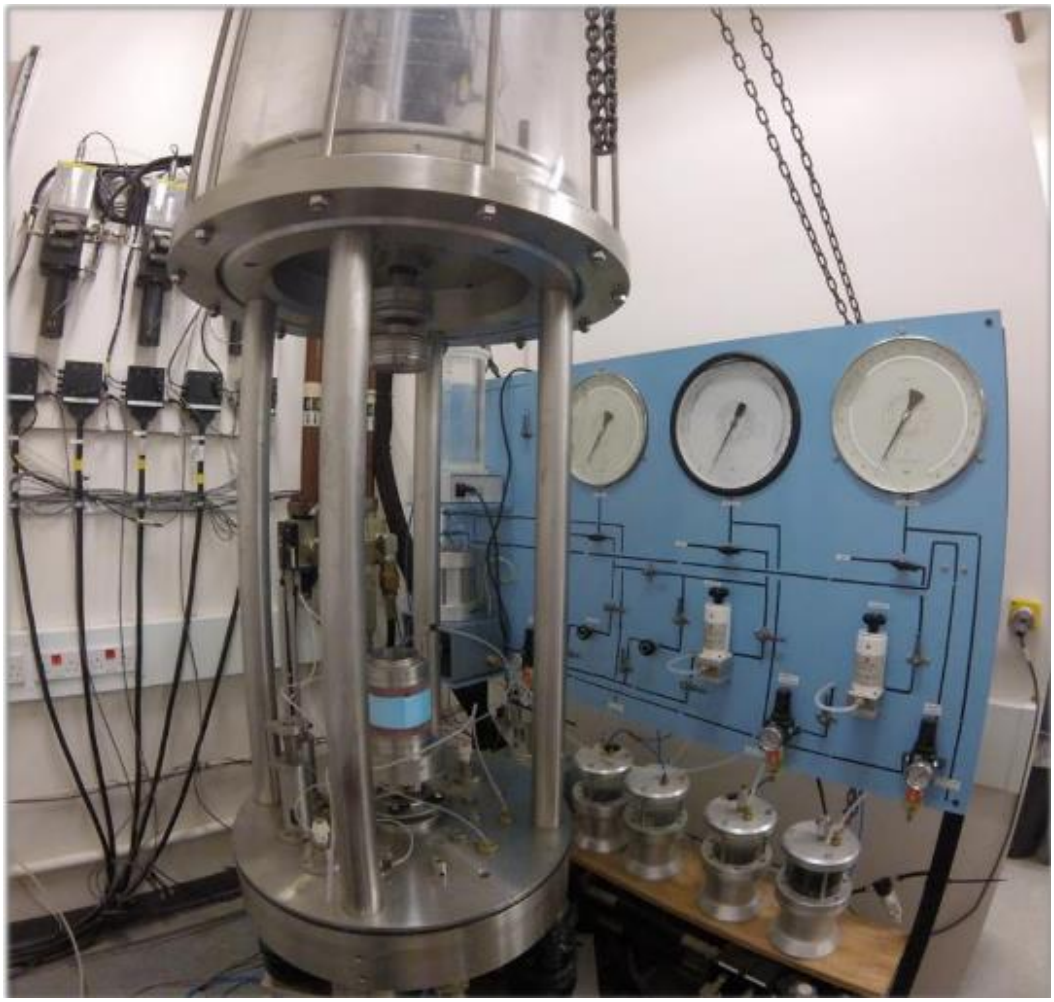


Figure 4.28 – Hollow cylinder torsional apparatus of the University of Bristol

4.7.4.2 Hydraulic dynamic loading system

The hydraulics system allows loading of the specimen and could supply the axial force, torque, external and internal pressure. The HCTA can be operated under two regimes of loading modes: hydraulic and pneumatic loading systems but in this investigation, only the hydraulic has been used. Two servo hydraulic actuators located on the top of the triaxial cell apply the axial force and torque independently to the sample thanks to the hydraulic flow system. The hydraulic power comes from another laboratory with a flow of 200 l/s in the form of incompressible oil.

4.7.4.3 Cell and back/pore pressure system

A central air compressor provides compressed air which can be manually regulated with manometers from the main panel (Figure 4.29a). Air under high pressure is split into 3 different air/water interfaces or “bladders” (Figure 4.29b) which can turn the incoming air pressure to water pressure. These units basically consist of sealed chambers with two compartments

separated by an elastomeric diaphragm or membrane. The air pressure is applied to the bottom chamber while the top chamber is filled with water. Air water interface devices provide pressure for the triaxial cell, for the sample and for the inner chamber; these will be denoted respectively as cell pressure (*CP*) back pressure (*BP*) and inner pressure (*IP*).

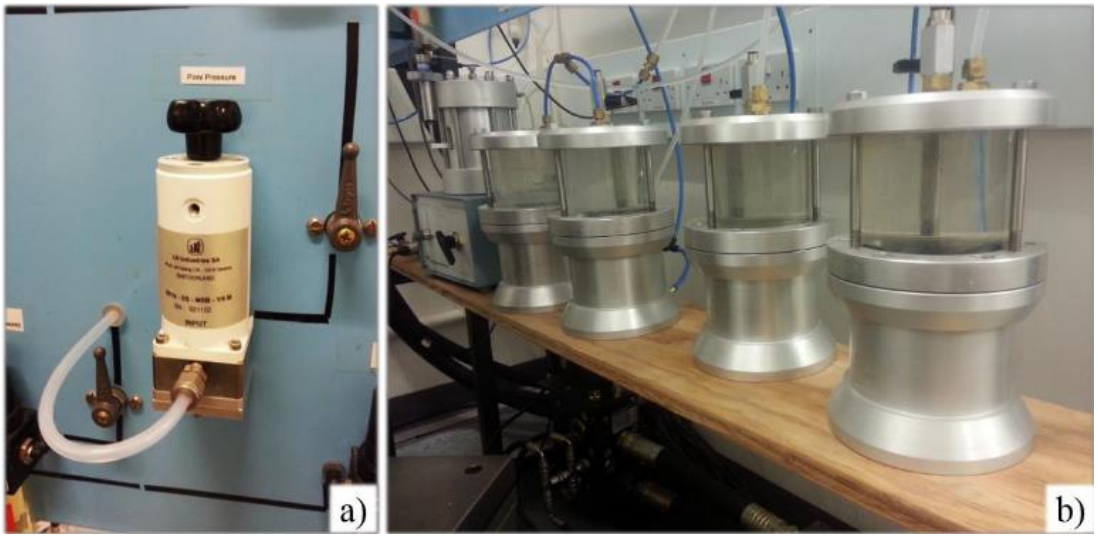


Figure 4.29 – (a) Manual pressure regulator and
(b) air water interface devices

4.7.4.4 Measuring instrumentation

In this investigation, the measuring instrumentation system had been found to be already recently calibrated. Also, all the devices involved (such as: load cell, sample and inner cell volume change, cell, pore and inner pressure transducers) had been recently checked in order to confirm the accuracy of the measurements.

Force and torque imposed on the hollow cylindrical sample are measured by a submersible internal combined load cell (Figure 4.30a). It is situated inside the triaxial cell on its top surface, along the central loading ram for the hydraulic loading system. The outstanding advantage of the submersible load cell is the elimination of the effects of piston friction from the load measurement. The load comes with its own factory calibration parameter (checked at regular intervals) and it can valuate a maximum axial load up to 8000 N and maximum torque to 400 Nm. During the loading, a linear variable displacement transducer (Model: ATC1000) and a rotary capacitive displacement transducer (Model: RCDT 300) were used for measuring respectively axial displacement and angular rotational displacement (Figure 4.30b and c).

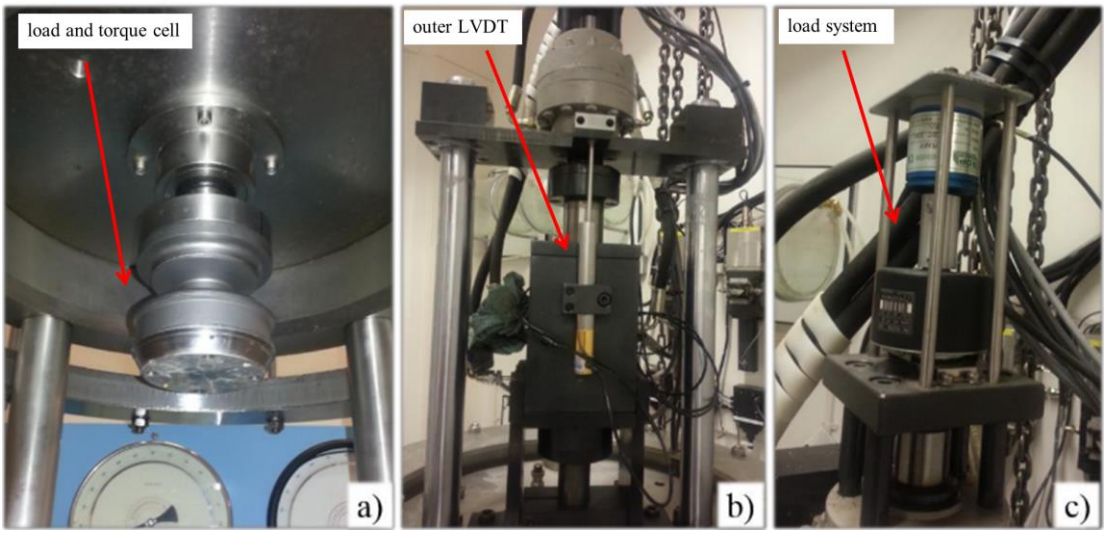


Figure 4.30 – (a) Submersible load and torque cell (b) external LVDT and (c) RCDT located on top of the confining cell

All the main pressures were measured by using electronic pressure transducers (Model PDCR 4010) which link pressure transducer blocks to the acquisition data system (Figure 4.31a). These can cover a wide range of pressures from 0 to 700 kPa.

As shown diagrammatically in Figure 4.27, the outer pressure transducer was placed at the bottom of the cell base and sealed with a thread sealant. The inner pressure transducer was installed on a mounting brass block between volume change and the sample inner chamber while the pore pressure transducer was positioned along the sample saturation line exit and connected to the upper drainage connections of the top cap.

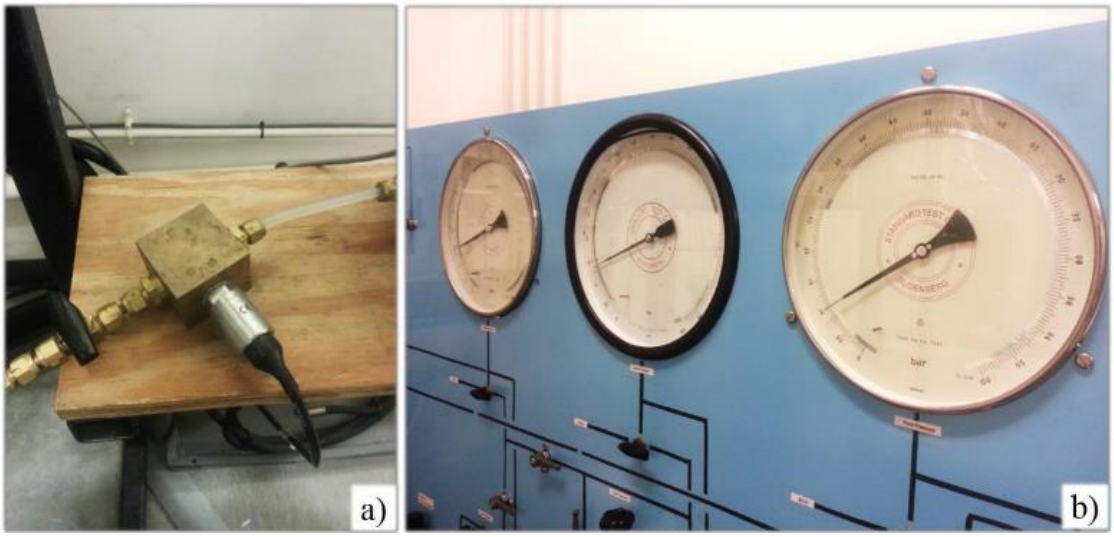


Figure 4.31 – (a) Electronic pressure transducer and (b) gauges for inner, cell and pore pressures.

Analogue pressure gauges for inner/outer and pore pressures were set after all the air/water interfaces to confirm the pressure levels coming from the electro transducers (Figure 4.31b). The operating pressure range of the transducers used in this investigation cover a range of pressures from 0 to 1000 kPa with an accuracy of 2.5 kPa (according to the manufacturer's specifications).

4.7.4.5 Inner cell and sample volume measurements

Thanks to the double chamber units connected to the linear displacement transducer in Figure 4.32, volume change measurements were taken from both the sample and from the inner cell chamber. The volume change gauge is basically a hollow thick-walled cylinder which contains a precision-machined calibration chamber filled with 100ml de-aired water with a floating piston sealed against it. The piston is also externally connected with an LVDT so each volume variation is proportional to a piston linear movement with accuracy of at least ±0.05ml.

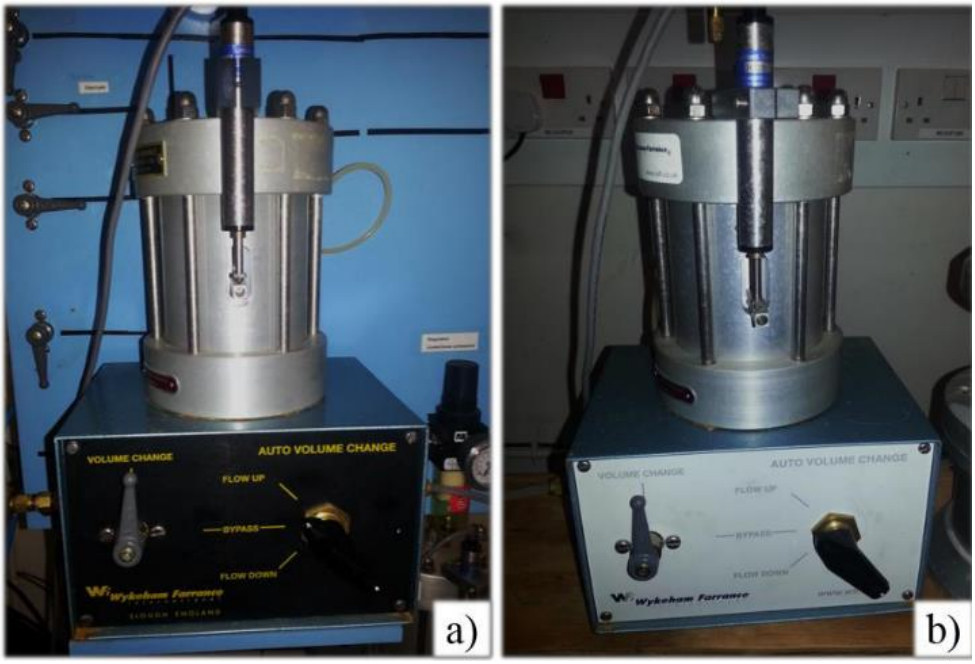


Figure 4.32 – (a) Sample volume change and (b) inner chamber volume change

Inner cell and sample volume measurements are needed to determine the sample deformations during the test for this investigation in which the cylindrical sample is assumed to deform uniformly. For instance, in order to obtain the variation of the internal and external radii (Δr_i and Δr_o) during the tests and thus the thickness of the sample:

$$\Delta r_i = \sqrt{\frac{\mathrm{Hr}_i{}^2}{H-\Delta H} - \frac{\Delta V_i}{\pi(H-\Delta H)}} - r_i \quad (4.42)$$

$$\Delta r_o = \sqrt{\frac{\mathrm{Hr}_o{}^2}{H-\Delta H} + \frac{\Delta V_i+\Delta V_s}{\pi(H-\Delta H)}} - r_o \quad (4.43)$$

where the ΔV_i indicates changes in the inner chamber volume while ΔV_s are the sample volume variations.

4.7.4.6 Data acquisition system and control

The data acquisition module used for collecting all the incoming signals from the electronic measuring system was the Instron multi-axis FastTrack 8800 Controller, which provides up to six axes of control. These signals come from HCTA transducers (e.g. load cell, pressure transducer LVTDs and non-contact sensors); they are converted into digital signals by Instron through a data scan conditioning unit with 16 channels, each having 19-bit resolution, and are sent to a host computer. The data acquisition and display programme are based on a graphical programming language called LabVIEW^{TM}, which allows access to most of the features of Instron controllers from a computer. The software collects measurements by transducers and controllers connected to the data acquisition system and calculates the relative force, pressures, stresses, displacements and strains. These values can be either displayed on the screen or saved in a raw data file. LabVIEW^{TM} embodies a front panel and a block diagram. The front panel is the interface, completely customizable from the operator, which also allows the monitoring and the control of test condition during the loading. Parallel to LabVIEW^{TM}, Instron MAX was employed as data acquisition back- up system. Instron MAX was also used to capture the signal when a faster or more detailed recording was required (e.g. investigation points, higher cyclic loading frequencies) as the software allowed a recording time up to 10 Hz.

4.7.5 Small strain measurement system

The determination of small strain provided by external measurement systems contains errors and should be avoided. For small-strain stiffness evaluation, the accuracy required is at least 10^{-3}% and can only be achieved by measuring strains locally, remotely from the end platen and typically within the central part of the sample (SCHOLEY et al., 1995). The errors are not only due the limit on the resolution of conventional instrumentation, but they are also due to tilting of the sample, bedding at the end platens and the effects of compliance in the apparatus (VIGGIANI & ATKINSON, 1995; JARDINE et al., 1984; HOQUE & TATSUOKA, 2004;

SCHOLEY et al., 1995). Internal strain transducer in axial, radial and circumferential direction help to minimise these errors in order to get more realistic soil strains.

Local transducers are a direct point-wise measurement of small strain and stress amplitudes. The system of different transducer can single out the central portion of the cylinder sample, avoiding issues such as compliance of the loading system and bedding/seating errors (IBRAIM et al., 2011). Local small strain stiffness can reach resolution of a lew 10^{-6}-10^{-4} m/m; on the downside, the measurement range is usually limited. Therefore in case of an analysis on soil stiffness with evolution of the stress level, re-positioning of the transducer is necessary.

4.7.5.1 Non-contact displacement transducers

Within the local transducers, non-contact sensors have excellent technical qualities and they can offer very high-performances in terms of resolution of the measurements, linearity, long-term stability particularly when submerged (IBRAIM et al., 2011). The measuring system operates without contact but using the eddy current effect built from the interaction with a conductive material.

The eddy currents operate with magnetic fields: the sensor generates an alternate current (Figure 4.33) which induces small currents (eddy) in the target material. The interaction of the magnetic fields is dependent on the distance between the probe (sensor tip) and the target; therefore, as the distance changes, the electronics sense the change and send an output voltage to the data acquisition system.

In the study of the small strain stiffness at different stress levels using non-contact transducers, the technical challenge is represented by the limited measurement range of these instruments. However, the setting developed at the University of Bristol was designed to allow the independent reposition of the transducers from outside the HCTA cell. The strain measurement system was accommodated around the sample using a structure of coupled sensors to determine the three-dimensional displacement.

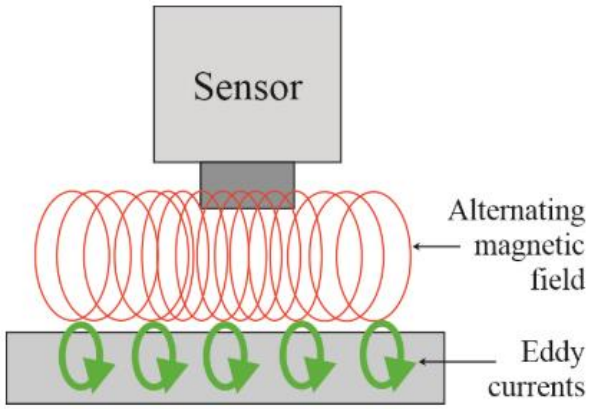


Figure 4.33 – Schematic representation of the eddy current effect between the sensors and a conductive material (MANDOLINI, 2018)

4.7.5.2 Laboratory set-up

The HCTA is equipped with a complex system of six non-contact transducer with the aim to provide access to the soil stiffness including its evolution with the general strain and stress levels. Although all six sensors were designed to move independently in order to allow small adjustments of their position during the test, the targets, towards which the sensors were aiming, were instead fixed with the sample (Figure 4.34).

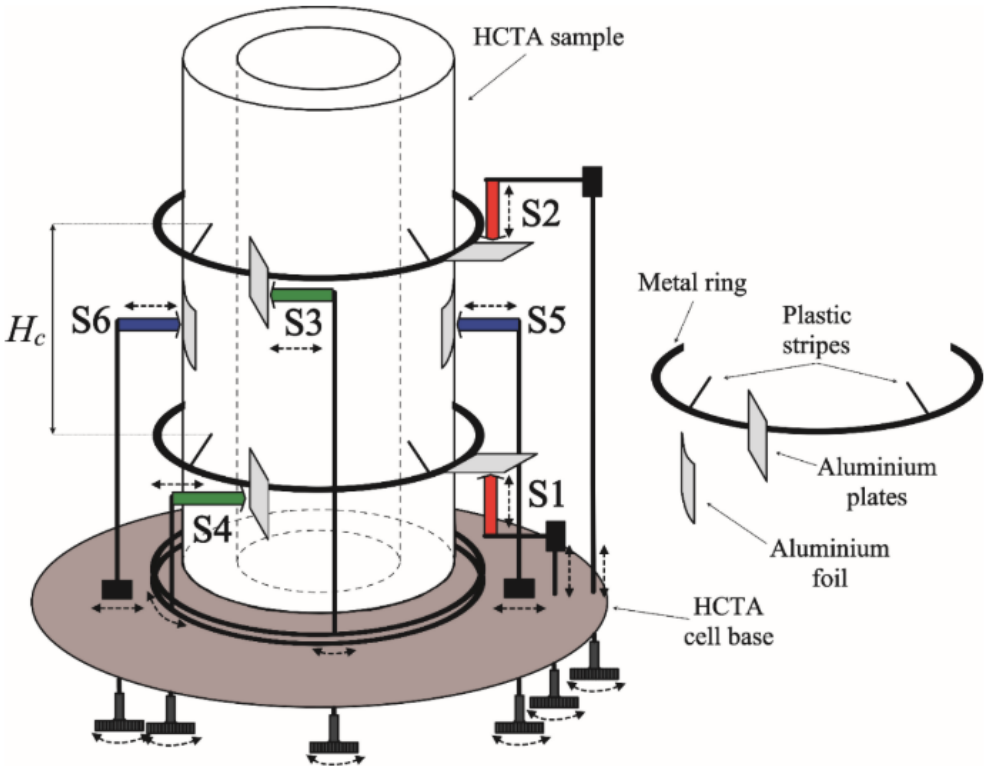


Figure 4.34 – Schematic representation of the strain measurement system mounted around the specimen (MANDOLINI, 2018)

The measuring system required a target made of electrically conductive non-ferromagnetic material (e.g. aluminium) with a dimension larger than 1.5 times the probe diameter. Sensors S1, S2, S3 and S4 (Figure 4.34) aimed towards thin aluminium plates screwed into two metal rings with diameter about 20% larger than the sample diameter. Each of the rings was fixed to the sample using three 3D printed thin stripes glued to the outer membrane. The synthetic thermoplastic polymer stripes (20 mm in length), despite being very light in weight, had high tensile yield resistance with good bending properties. This provided flexibility during the installation and ensured horizontality of the rings during shearing. Outer radius sensors, S5 and S6 in Figure 4.34, aimed towards square-shaped aluminium foils placed, prior the dry sand deposition, on the internal side of the outer membrane. Both non-contact transducers were mounted on two stainless steel bars alongside the specimen (Figure 4.34). Details of the mounting procedure will be provided in the next sections.

4.7.5.3 Analysis of the three-dimensional strains

The small strain measurement system evaluated the deformations of the central part of the hollow cylinder specimen volume. This smaller volume of height *Hc* (see Figure 4.34) could deform in the axial *z*, radial *r* and circumferential θ direction, as shown in Figure 4.35. The components of the central hollow cylinder strain matrix ($\varepsilon_{z,c}$, $\varepsilon_{r,c}$, $\varepsilon_{\theta,c}$ and $\gamma_{\theta z,c}$) were evaluated by the data collected by the sensors and defined as:

$$\varepsilon_{z,c} = -d_z/H_c \tag{4.44}$$

$$\varepsilon_{r,c} = -(\Delta_{ro,c} - \Delta_{ri,c})/(r_o - r_i) \tag{4.45}$$

$$\varepsilon_{\theta,c} = -(\Delta_{ro,c} + \Delta_{ri,c})/(r_o + r_i) \tag{4.46}$$

$$\gamma_{\theta z,c} = \theta_{,c} r_{ave,c}/H_c \tag{4.47}$$

The axial deformations ($\varepsilon_{z,c}$) depend on the axial displacement measured by the distance between the S2 and S1 sensors (d_{S2} and d_{S1}) with their relative targets.

$$d_z = d_{S2} - d_{S1} \tag{4.48}$$

The sign was decided in agreement with the external strain measurement convention. Accounting for (*i*) $|d_{S2}|>|d_{S1}|$ as the forces were applied at the top of the specimen hence the *S2*

transducer measure a larger displacement than *S1* and (*ii*) the direction of the sensors as *S2* and *S1* were installed facing each other (Figure 4.35c).

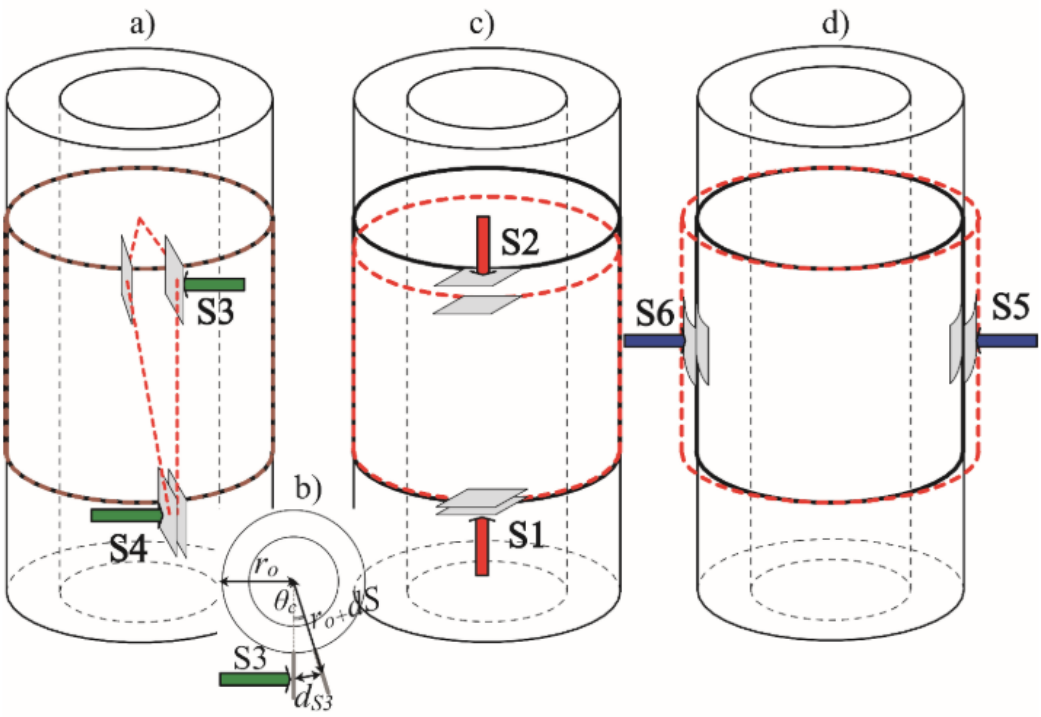


Figure 4.35 – Deflections of the central part of the sample, in the circumferential (a and b) , axial (c) and radial directions (d)

In the radial and circumferential directions, $\Delta r_{o,c}$ and $\Delta r_{i,c}$ (Eq. 4.42 and 4.43) represented the variations of outer and inner radius of the central volume of the sample. Inner radius variations were assumed uniform along the height of the sample (i.e. $\Delta r_{i,c} = \Delta r_i$) and so were evaluated from the volume change of the inner chamber combined with the vertical sample displacement (Eq. 4.49). The outer radial sample displacements ($\Delta r_{o,c}$) were instead measured directly by the sensors S5 and S6 (Figure 4.35d) and deducted from the average radial displacements (d_{S5} and d_{S6}):

$$\Delta r_{o,c} = (d_{S5} + d_{S6})/2 \tag{4.49}$$

The shear strains of the central part of the sample (Eq. 4.50) were calculated as function of the angle of twist θ_c, the average between $r_{o,c}$ and $r_{i,c}$ and the height H_c. In particular, the twist was measured as the difference between displacements of the circumferential non-contact transducer (S3 and S4 in Figure 4.35a) divided by r_o+dS (Figure 4.35b):

$$\theta_o = (d_{S3} - d_{S4})/(r_o + dS) \tag{4.50}$$

Note that the factor (r_o+dS) represents the distance from the centre of the sample to point where the sensor meets the target. The distance H_c and dS were measured with a calibre at the beginning of the test and assumed constant throughout the shearing.

4.8 SAMPLE INSTALLATION AND TEST PROCEDURE

After detailing the apparatus, this section describes the procedures adopted for testing. The sample preparation is presented considering the type of test that the sample is subjected to and the same is made for the testing procedure.

As demonstrated in the previous section, the sample installation is also divided according to the test performed. The description of the unconfined tests has already been presented; therefore, it will not be discussed again.

4.8.1 Bender elements

Bender elements, as well as other piezoceramic transducers, have opened a new window in laboratory testing by enabling the performance of standard mechanical, static or cyclic tests simultaneously with seismic wave dynamic tests.

The attraction of the BE technique is its apparent simplicity: one of the transducers is excited at one end of a specimen using a single pulse excitation, and the time required for this to be registered by the receiving bender element at the other end of the specimen can be simply read off an oscilloscope to obtain the travel time, and hence the shear wave velocity. The installation of these transducers is relatively straightforward and quick.

However, there has been much discussion on the details of the test procedure and the most appropriate method of interpreting the results to obtain the shear wave velocity. The potential and benefit of bender element testing is clear; the interpretation of its results, unfortunately, is not so, as demonstrated by many authors (VIGGIANI & ATKINSON, 1995; BRIGNOLI et al., 1996; JOVICIC et al., 1996; ARULNATHAN et al., 1998; GREENING et al., 2003; GREENING & NASH, 2004; LEONG et al., 2005; VIANA DA FONSECA et al., 2009). In effect, despite the various advantages of the bender element technique, namely its simplicity and ease of use and application, there is not yet a standard procedure and interpretation framework developed for this technique. The interpretation of the results remains subjective, requiring some degree of judgement.

For this reason, in this section, the method of interpretation and installation of bender elements adopted is presented.

4.8.1.1 Installation

There are several difficulties associated with bender element installations, which result in potential factors of error involved in BE testing. Some of these errors derive from the properties and quality of the transducers, the details of the insulation, electrical crosstalk due to electromagnetic coupling through the soil, mixed radiation of both P- and S-waves, and near field effects, all leading towards uncertainty in the detection of first arrivals.

With regard to the BEs themselves, most issues have already been addressed in the previous chapter. In practical terms, a few technical requirements and boundary conditions should be applied, as recommended by Jovicic (2004) and Lee and Santamarina (2005).

As for the insertion of the BE into the soil, since the transducers are rather fragile in comparison with the surrounding soil, it is important to occasionally assess wear-and-tear degradation. The insulating epoxy coating and the cable shielding are particularly susceptible to this type of deterioration, leading to short-circuiting. Santamarina and Fam (1997) presented examples of typical responses for a BE with deteriorated insulation in a saturated silty soil, evidencing early energy arrival often confused with near field effects. The authors provided solutions for minimising this problem using more durable coating materials and presented suggestions for mitigating its effects if the short-circuit condition develops during testing.

For the tests performed, the two procedures were specifically observed during measurements. Firstly, the alignment of the BE pair had to be guaranteed. For good alignments, the cylindrical samples were manufactured with a spare space made with a nonfunction BE during compaction. The preparation of the spaces for the cubical sample were made with a needle; this step was followed by insertion of the BE. The BE were kept inside the sample for as long as the sample was tested.

The remainder of the BE in the cubical sample guaranteed the second procedure on the installation of the bender elements to provide good contact between the BE and the soil. As the sample received the BE previously cementation, within the following curing days cementation hydrates and the specimen was kept without any movement. To guarantee the contact of the cylindrical samples, BE pair was manually held during the measurements.

4.8.1.2 Signal processing

For this experimental program, the signal processing was prepared considering the wave form and the frequency.

It is generally considered that a sine wave pulse gives the clearest data for evaluating the arrival time (VIGGIANI & ATKINSON, 1995; JOVICIC, 1997, SUKOLRAT, 2007). Viggiani and Atkinson (1995) concluded that a sine wave rather than a square wave presented less error when determining the arrival time by visual identification. Zenghita et at. (2009) reported that 15 of 18 laboratories used a sinusoidal wave as the input signal. Sine wave was adopted in this research.

The effect of changing input wave frequency on transmitted and received shear waves can be observed in Figure 4.36. Yamashita et al. (2009) concluded that the frequency has a very low influence in the final value of G_0. For this experimental program four frequencies were adopted; 15, 20, 25 and 30 kHz and the interval between each wave was 500 ms. Each frequency provides 32 wave forms and an average of all.

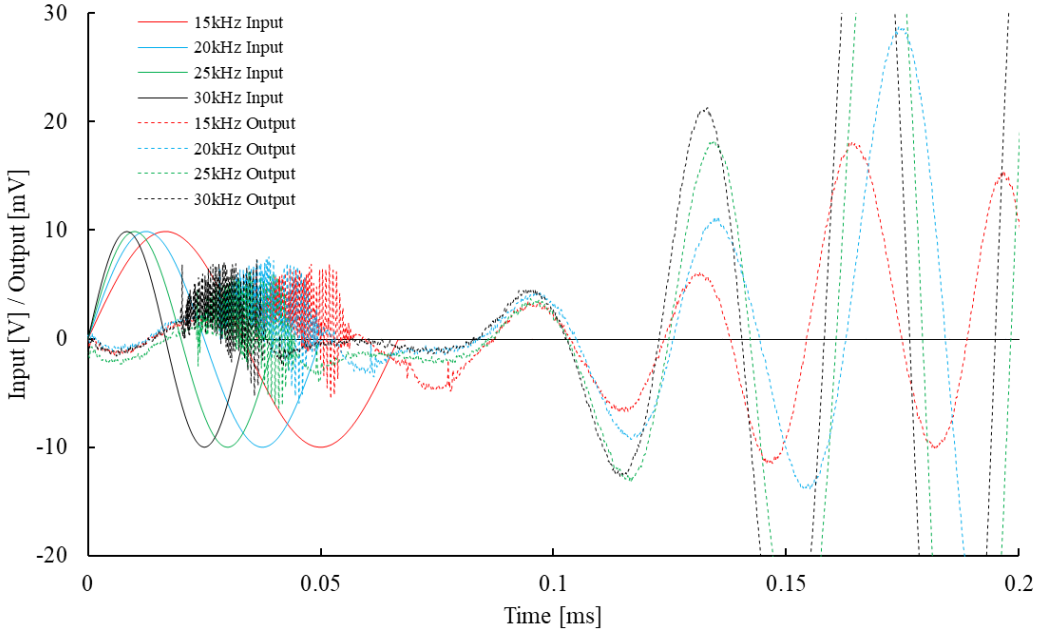


Figure 4.36 – Transmitter and received signals of S-waves at different frequencies

4.8.1.3 Obtaining time of arrival

The arrival time is a difficult parameter to obtain when using bender elements data. The direct measurement of the time interval between the input and output waves is the most immediate

and intuitive interpretation technique, similar to the method used in field geophysical testing (ABBISS, 1981; DYVIK & MADSHUS, 1985; JAMIOLKOWSKI et al., 1995; JOVICIC et al., 1996; PENNINGTON, 1999). This method of interpretation assumes plane wave-fronts and the absence of any reflected or refracted waves (ARULNATHAN et al., 1998). Figure 4.37 shows an example of a typical sine-wave input pulse (OABC) and the resulting output signal. The identification of the instant of first inflection of the output wave is simple but subjective: that is, different users may select different arrival points, as indicated by the multiple 'arrow' indicators in the upper signal in Figure 4.37 (FERREIRA, 2008).

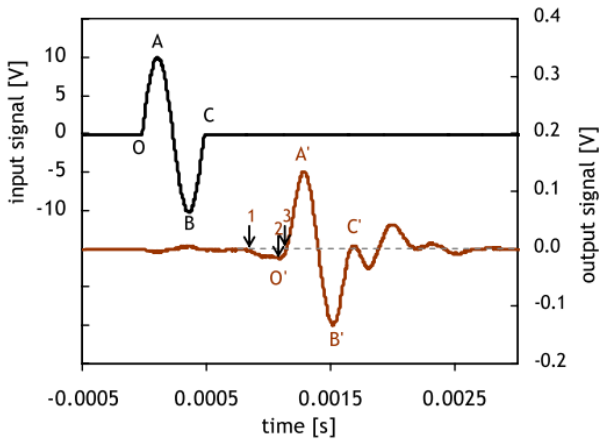


Figure 4.37 – Example of time domain interpretation methods (FERREIRA, 2008)

The most common method of a visual identification of the shear wave arrival is in the time domain (Figure 4.37). Characteristic points of the input and output waves, such as peaks, troughs and zero intercepts, are easy to identify, and the intervals between corresponding points (AA' and BB' in Figure 4.37) can be considered as representing the travel time of the shear wave, again under the assumption of plane wave propagation and absence of reflections or refractions (VIGGIANI & ATKINSON, 1995; ARULNATHAN et al., 1998). These methods assume a plane front to the shear waves and neglects reflected and refracted waves from the boundaries (ARULNATHAN et al., 1998). It is usually considered that the first deflection point (B=B' in Figure 4.37) is masked by near field effects and because it has an inverse polarity compared with transmitted wave it is not considered to be the best first arrival (FERREIRA, 2008). In this research, the peak-to-peak method was adopted (A-A').

4.8.2 Cubical Cell

On the seventh day of curing, after specimens were immersed, the cubical samples were ready to be tested on the cubical cell.

The setup of the sample prior to the testing consisted of placing the sample against the three rigid walls, followed by installation of flexible cushions on the opposite sides and rigid platens including the LVDTs for sample displacement measurements.

Next, the wall assembly was mounted on the apparatus, followed by a check of the screws, nuts and bolts on the apparatus for safety reasons. The three pressure transducers were then placed, and the connections with the air compressed system established for all three loading directions, *x*, *y* and *z*. When two faces received the same pressure (e.g. $\theta = 0^o$ and 180^o), the faces with same pressure received one pressure transducer and a connector, inducing the exact sample pressure to the cushions.

Once connected, pressure valves of each face were opened, and the *zeros* of pressure were measured.

As samples were in a near to saturated state, the test started with the consolidation procedure. Increments of 10 kPa were applied isotopically on the three faces of the cube every 10 minutes, which is approximately the time required for samples to consolidate. The consolidation pressure for all the tests was 100 kPa.

Once consolidation was completed, the sample was sheared. Seven different stress paths were applied, $\theta = 0^o$, 30^o, 60^o, 90^o, 120^o, 150^o and 180^o in the octahedral plane, which represent a full rosette of tests. The b parameters for the tests were 0, 0.5, 1, 0.5, 0, 0.5, and 1, respectively.

In the *xyz* rectangular coordinate system (Figure 4.38), *z* represents the vertical direction while *x* and *y* are the horizontal directions. For all tests, the mean effective pressure, *p'* was kept constant at 100 kPa during shearing.

The stress paths were generated under stress controlled conditions with stages of 10 kPa stress increase on one direction and 5 kPa stress decrease on the other directions (for the $\theta = 0^o$ and 120^o paths), of 10 kPa stress increase on one direction, 10 kPa stress decrease on another direction and the stress on third direction kept constant (for the $\theta = 30^o$, 90° and 150^o paths),

and of 10 kPa stress decrease on one direction and 5 kPa stress increase on the other directions (for the $\theta = 60^o$ and 180^o paths) (see Table 4.3).

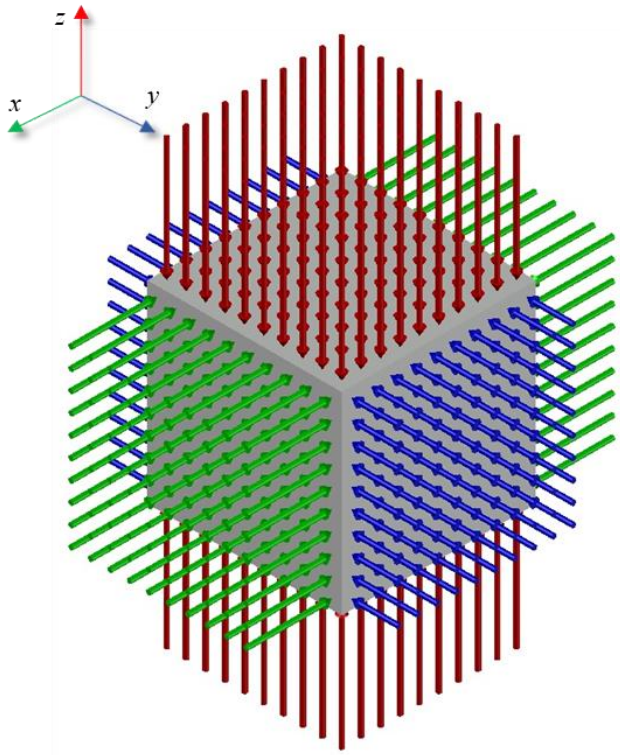


Figure 4.38 – Representation of *xyz* rectangular coordinates

Table 4.3 – True triaxial loading conditions

θ	Maximum principal stress	Intermediate principal stress	Minimum principal stress	b	Loading increment (kPa)		
					$\Delta\sigma_z$	$\Delta\sigma_y$	$\Delta\sigma_x$
0^o	σ_z	-	σ_y and σ_x	0	+10	-5	-5
30^o	σ_z	σ_y	σ_x	0.5	+10	0	-10
60^o	σ_z and σ_y	-	σ_x	1	+5	+5	-10
90^o	σ_y	σ_z	σ_x	0.5	0	+10	-10
120^o	σ_y	-	σ_z and σ_x	0	-5	+10	-5
150^o	σ_y	σ_x	σ_z	0.5	-10	+10	0
180^o	σ_y and σ_x	-	σ_z	1	-10	+5	+5

4.8.3 Hollow Cylinder

Once the specimen reached the fifth day curing, the sample was removed from the mould and installed in the hollow cylinder apparatus. The inner membrane was positioned in the bottom cap, fixed with a metal membrane holder. A paper filter was then positioned on the top of the porous stone and the sample was positioned in the bottom cap.

The next step was positioning aluminium foil where the radial internal measurements would target the sample. Then outer membrane was positioned around the sample. The top cap with a paper filter was placed on the top of the sample. Two O-rings were used to fix the latex membrane on the top and on the bottom caps.

The inner membrane was then fixed on the top cap with two O-rings. The target rings for the contactless sensors were positioned on the top of the sample and the specimen was transfer to the hollow cylinder apparatus.

At this time, the pipes were connected on the top and bottom of the sample and a vacuum pressure of 30 kPa was applied. If the sample was not able to keep this pressure, the sealing would be reviewed. Liquid latex was used for this sealing and, when necessary, new membranes were used.

When the sealing was confirmed, the top cover was positioned on the top cap correctly and progressively tightened using clamping screws. Four small hexagons on the top cover were filled up with a strong resin called Araldite 2014-1. Araldite 2014-1 is a two-component resin (resin and hardener) which cures at room temperature and is used for bonding metals. Four bolts placed in the bottom of the loading ram were screwed into the Araldite while it was still soft and malleable. The resin had to cure for at least 4 hours to achieve the maximum strength, the small strain measurement rig was installed in the meantime.

4.8.3.1 Setting the small-strain measurement system

With the sample firmly fixed with the load cell ram and the bottom tightened with the triaxial cell base, it was possible to install the small-strain measurement system, which has been already described. The procedure consisted of fixing the remaining targets to the sample and positioning the six non-contact sensors on stainless steel support which can be moved independently from outside the cell.

Two metal rings carried the targets of the vertical and circumferential sensors (*S1-S2* and *S3-S4*). Each ring had to be attached to the outer membrane at three points using flexible suspended connections as proposed by Ibraim et al. (2011) and Di Benedetto et al. (2001). The 3-D printed scaffolding in Figure 4.39a was used to ensure the horizontal level and to keep a consistent distance of about 100mm between the rings. The bottom scaffolding was first laid on the base pedestal in order to position correctly the bottom metal ring (Figure 4.39b), then super glue was applied between the three plastic stripes (20mm long) to the sample wall. Once the glue cured, the top scaffolding was rested on top of the first ring while the other ring was glued into position (Figure 4.39c). A few small pins on the top surface of the first scaffolding were inserted into the bottom surface of the top scaffolding to help achieve a stable balance during this delicate operation (MANDOLINI, 2018).

Once the targets were in position, the scaffolding was removed, and all six sensors were installed (Figure 4.39c). Radial sensor *S5-S6* were attached to vertical beams which were screwed on the base of the triaxial cell (Figure 4.39c). The remaining non-contact sensors were mounted on four thin stainless-steel bars alongside the specimen (Figure 4.39c). Eventually, all six sensors could be moved separately, approaching or distancing the targets, by twisting cogwheels located underneath the cell. Before moving to the next and last step of sample preparation, all the non-contact sensors were positioned towards their relative targets, leaving an offset distance of 1mm between them. The distance (*Hc*) between the top and bottom flexible suspended connections were glued to the membrane (Figure 4.40a) and the distance between the sample walls and the centre of the target were measured with a precision calibre and recorded (Figure 4.40b).

After installing the inner sensors, the inner cell was full of de-aired water and the camber was filled with tap water. The next stages would commence in the next day.

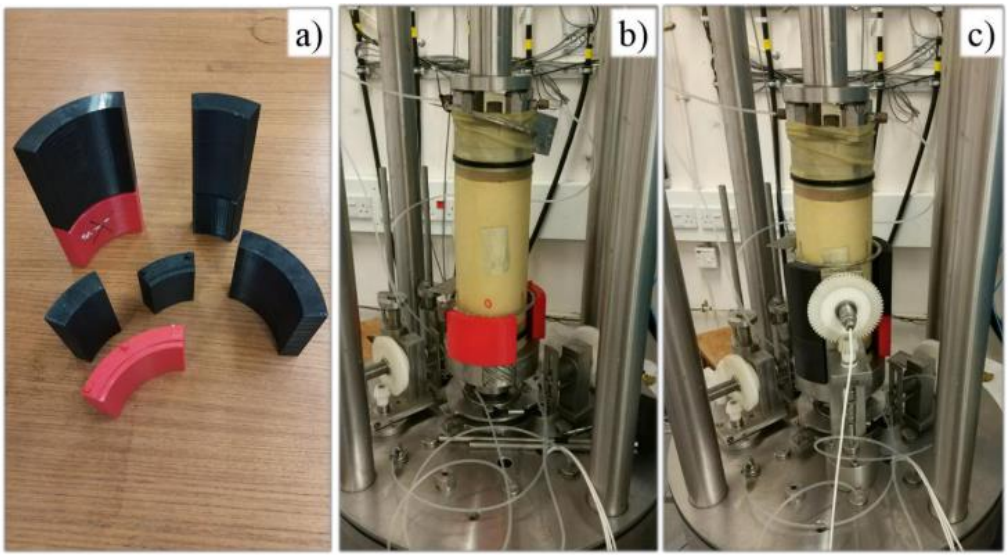


Figure 4.39 – (a) 3-D printed scaffolding for inner ring positioned; (b) positioning bottom ring and (c) positioning top ring

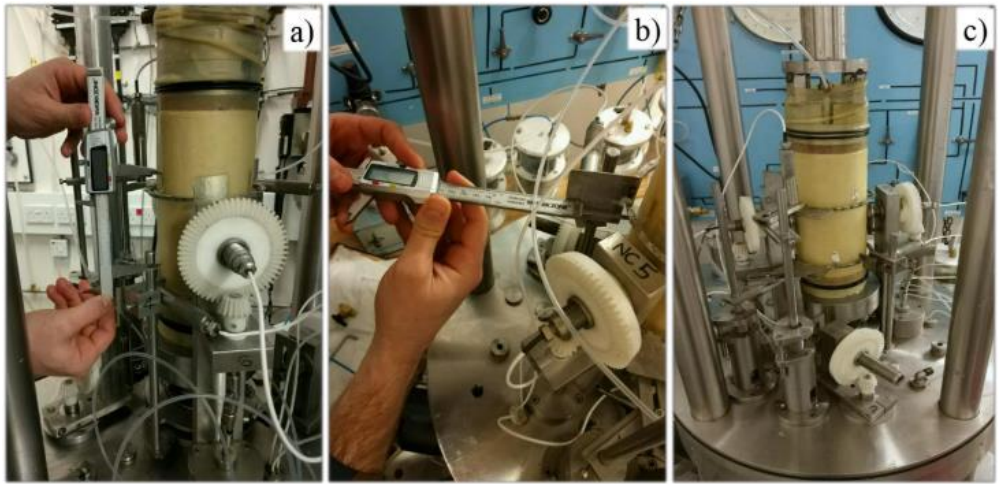


Figure 4.40 – (a) Measurement of rings distance; (b) measurement of radial distance to target; (c) sample ready for testing

4.8.3.2 Saturation

Tests performed in drained conditions required the evaluation of the sample volume and its changes throughout the test. Fully saturated conditions were therefore necessary to accurately measure the volume of water travelling away from/towards the samples. The method used to obtain saturated HCTA specimens and to verify the degree of saturation is presented herein.

Saturation consists, practically, of filling all the voids up with water; this condition is hard to achieve as it is impossible to displace all the air from the voids in the sample. Carbon dioxide (CO_2), as more soluble than air in water, was flushed prior to water saturation with the intent of replacing all the air within voids inside the sample. CO_2 was flushed from the bottom to the

top of the specimen for at least one hour under a small gradient of pressure. Afterwards, de-aired water was flushed through the specimen under a very low gradient of pressure to fill the voids in the specimen and replace the CO_2. Saturation with water lasted for a couple of hours until a quantity of water equal to two times the void volume of the specimen was transited. After the saturation stage, the cell pressure (CP) and the back pressure (BP) were increased in stages until the respective values of 420 and 400kPa. The use of back pressure facilitates the dissolution of CO_2 inside the sample.

The minimum *B* value (SKEMPTON, 1954) measured was 0.94.

4.8.3.3 Consolidation

The isotropic consolidation stage of the specimen was then performed by manually increasing the cell and inner pressure. During this phase, to ensure the isotropic conditions, the hydraulic system of the HCTA had an axial force and imposed torque of *zero*. The procedure lasted until the next day, when no volumetric strains were detected. For all tests, the isotropic consolidation was 100 kPa. In the end of consolidation, sample was ready for shearing.

4.8.3.4 Monotonic loading

On the seventh day, the sample was ready for shearing with an isotropic consolidation of 100 kPa. The samples were sheared in stages of load increment and in each of these stages, the specimen was let under load, so creep was reached. At this stage, small cycles were also applied.

Loading was performed under stress-controlled conditions for $\alpha = 0^o$, 15^o, 30^o, 45^o, 60^o, 75^o, 90^o. Strain controlled was performed on another two $\alpha = 0^o$ tests.

4.8.3.5 Small loading

At the stages mentioned above, after creep, ten cycles of small axial and torque loading were imposed to the cemented specimen. The amplitudes of 5 KPa, 10 kPa and 20 kPa axial and torsional loading were applied at a frequency of 0.1 Hz.

4.9 SUMMARY

This chapter introduced the equipment used in the performance of the unconfined tests, cubical cell, hollow cylinder and bender elements. The instrumentation was also described, and corrections of the testing were presented. A description of the bender element instrumentation

was giving, and the data interpretation technique was explained. Non-contact local transduces used on the hollow cylinder were also presented.

Materials used in this research and sample preparation technique were introduced. Sample fabrication based on damping the soil and cement mixture was used to achieve the desired compaction level.

The multiaxial behaviour of the cemented sand was analysed by the variation of the principal stress, using the b parameter. This was achieved with two different apparatus and the test procedures were presented in this chapter.

One of the main targets in the experimental programme was to determine the stiffness and stiffness evolution of the cemented materials. The procedure to obtain it was presented in this chapter.

5 UNCONFINED TESTS

This chapter presents the results obtained on the unconfined compression and split tensile tests and small strain stiffness measured though bender elements prior testing the specimens. These results helped to make decisions on the specimens later manufactured for the hollow cylinder tests, true triaxial and long-term bender elements on cubical samples.

5.1 UNCONFINED COMPRESSION STRENGTH

The unconfined compression tests were performed in order to obtain η/C_{iv} correlation for artificially cemented Hostun sand. Also, the influence of the porosity and the amount of cement was verified.

Figure 5.1 presents the influence of adding cement into the soil. For the amounts studied in this research, the greater the addition of cement, the higher the unconfined compression strength of the specimens. A tendency of increase is also observed. The scatter results with 7% cement show that this was not a great way to represent the unconfined compressive strength gain with inclusion of cement.

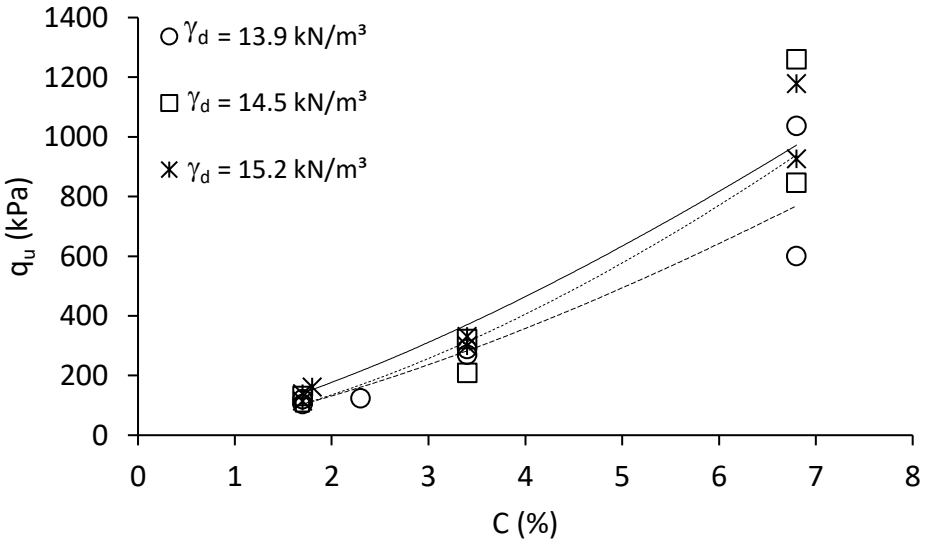


Figure 5.1 – Unconfined compressive strength (q_u) with cement content (C)

Figure 5.2 elucidates the influence of the porosity on the unconfined compression strength of the samples. The amount of 6.8% cement presents an increase of the maximum stress when the

specimen is more compact. For the other cement contents, the effect of the porosity is not so pronounced.

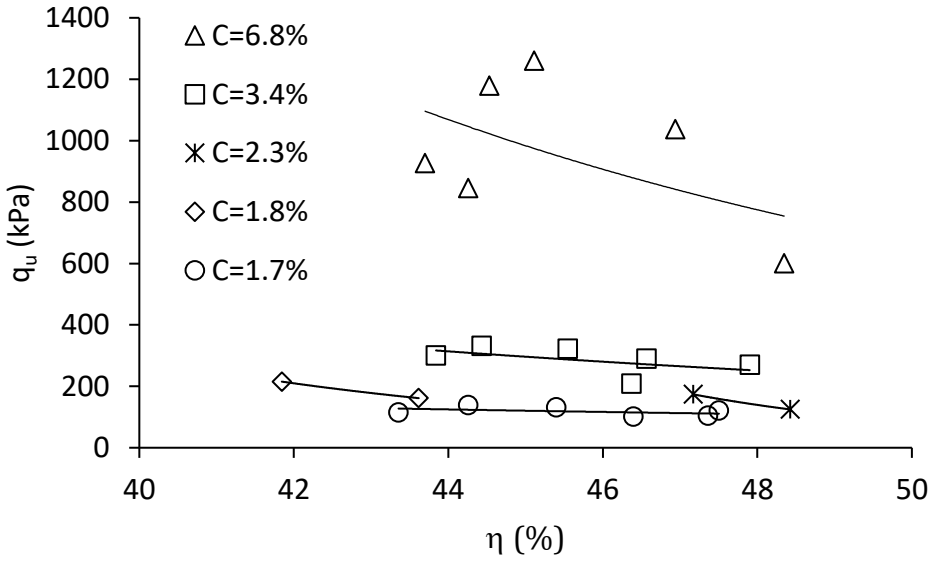


Figure 5.2 – Unconfined compressive strength (q_u) with porosity (η)

To achieve a unique relationship of the stress of samples and their dosage, the $q_u - \eta/C_{iv}$ curve is presented in Figure 5.3. The result is a unique relationship that "englobes" all samples tests in a unique behaviour trend. The results show that increasing the η/C_{iv} exponentially reduces the maximum unconfined compressive strength of the specimens. A correlation coefficient of 0.95 was obtained.

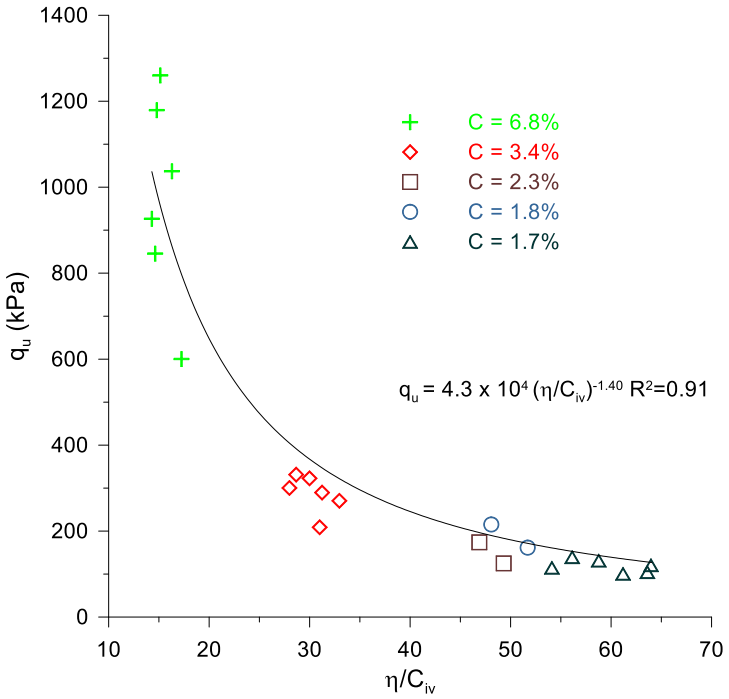


Figure 5.3 – Variation of unconfined compressive strength (q_u) with porosity/cement index (η/C_{iv})

5.2 SPLIT TENSILE STRENGTH

Splitting tensile tests, similar to the unconfined compression tests, were conceived of in such a way to evaluate separately the influence of the cement content and porosity on the mechanical strength of the artificially cemented soil.

Similarly, the results presented in Section 5.1, Figures 5.4, 5.5 and 5.6 indicate the results obtained for the splitting tensile tests. Figure 5.4 demonstrates that the inclusion of cement leads to a linear increase of the split tensile strength of the specimens for all cement contents analysed. The influence of the porosity of specimens does not seem to significantly change the behaviour of the specimens in comparison with the cement content (Figure 5.5). A smooth trend of lower resistance is noticed when the porosity is increased.

The variation of splitting tensile strength (q_t) with the porosity/cement index is presented in Figure 5.6. The observation of Figure 5.6 suggests that the porosity/cement index well describes the tensile strengths of the samples. A correlation coefficient (R^2) equal to 0.87 is observed.

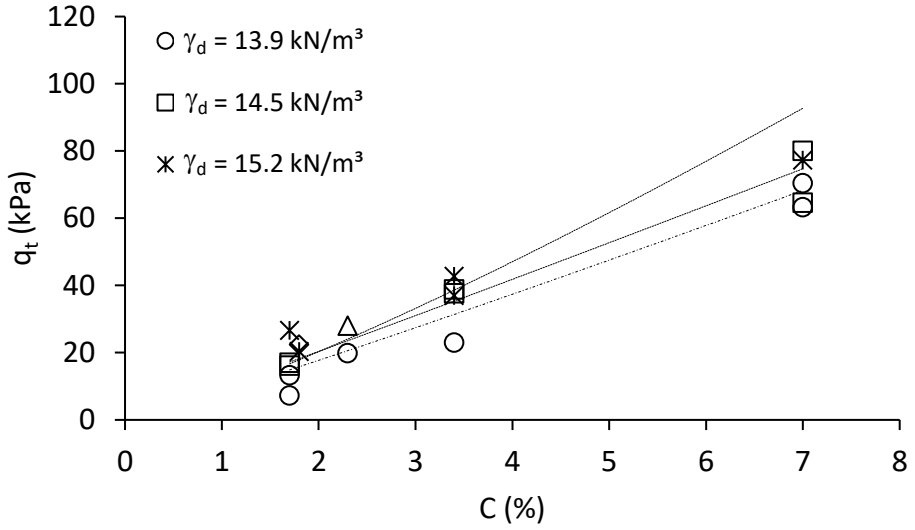


Figure 5.4 –Split tensile strength (q_t) with cement content (C)

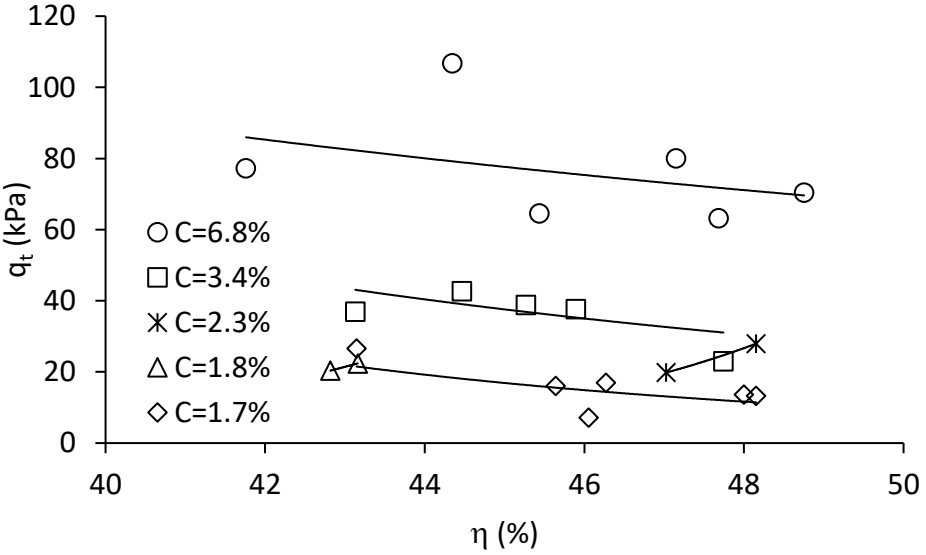


Figure 5.5 – Split tensile strength (q_t) with porosity (η)

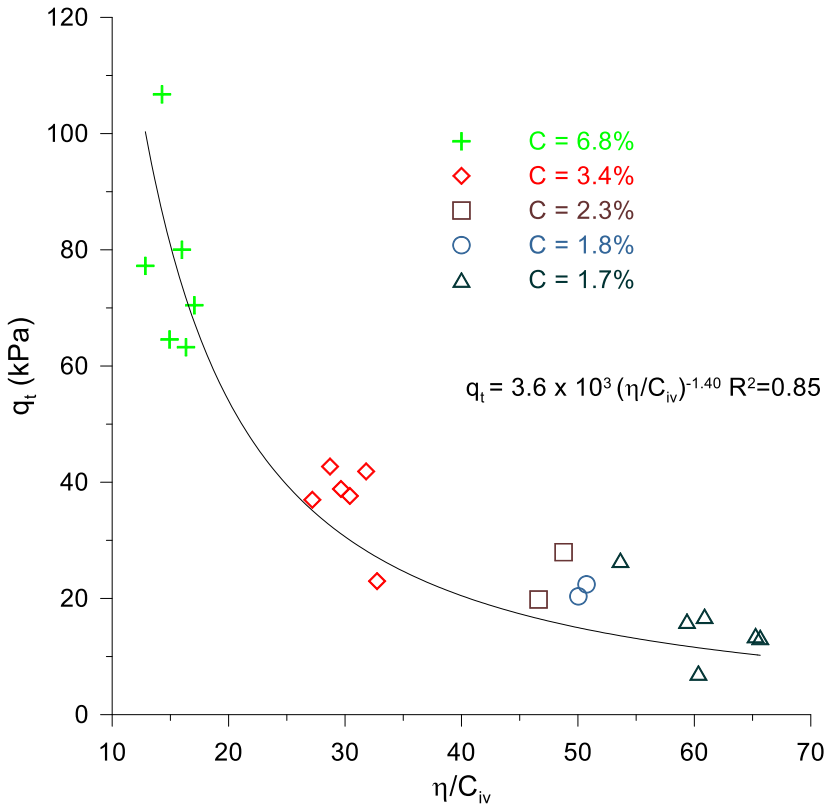


Figure 5.6 – Variation of splitting tensile strength (q_t) with voids/cement ratio (η/C_{iv})

5.3 INITIAL SHEAR MODULUS

Figure 5.7 shows the relationship between the initial shear modulus (G_0) and the cement content (C) for the cemented Hostun sand, considering each dry unit weight used. Similarly, q_u and q_t, G_o increases approximately linearly with the increase in cement content. The effect of the porosity on the initial shear modulus is illustrated in Figure 5.8. For the exception of the porosity effect on samples with 6.8% cement, the variation of the initial shear modulus does not seem to be affected by the porosity of specimens. Again, the results presented are scatter, specially at the higher amounts of cement.

Figure 5.9 presents the variation of the initial shear modulus (G_0) with porosity/cement index for Hostun cemented sand. As seen in previous results for compressive and tensile strengths, a high-quality correlation (coefficient of determination $R^2 = 0.93$) is obtained for the initial shear modulus versus the porosity/cement index.

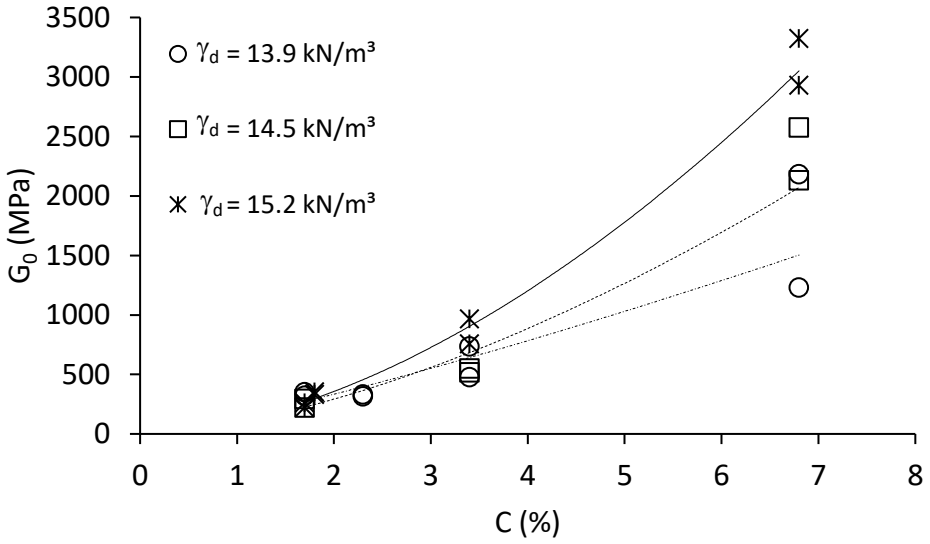


Figure 5.7 – Variation of the initial shear modulus (G_0) with cement content (C)

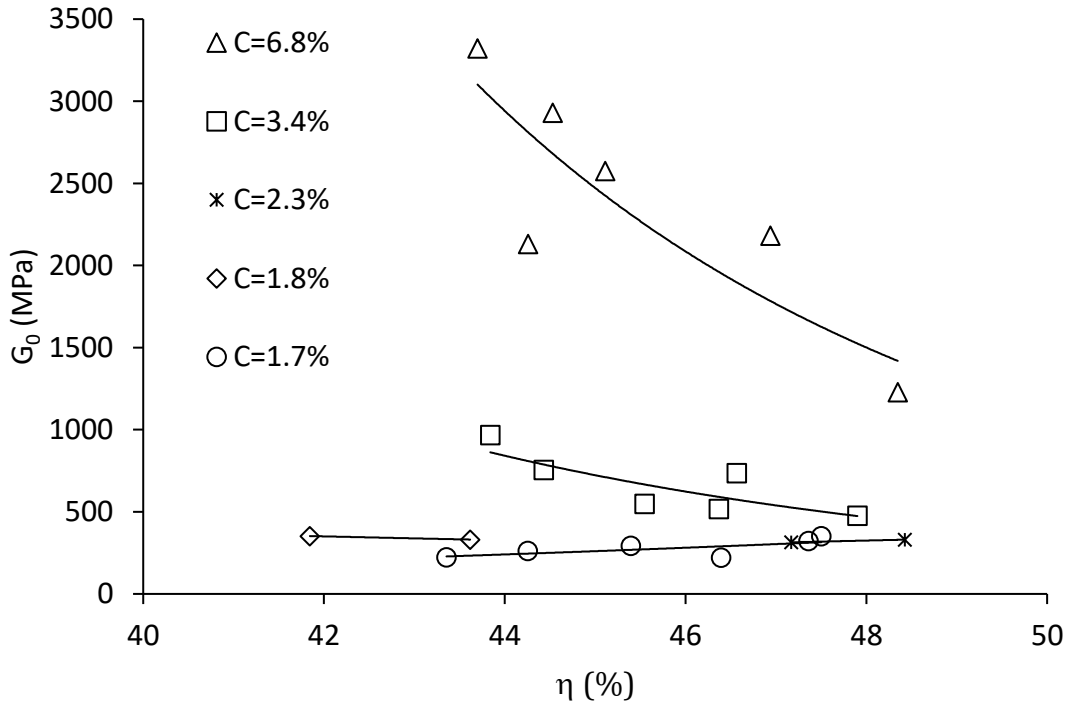


Figure 5.8 – Variation of the initial shear modulus (G_0) with porosity (η)

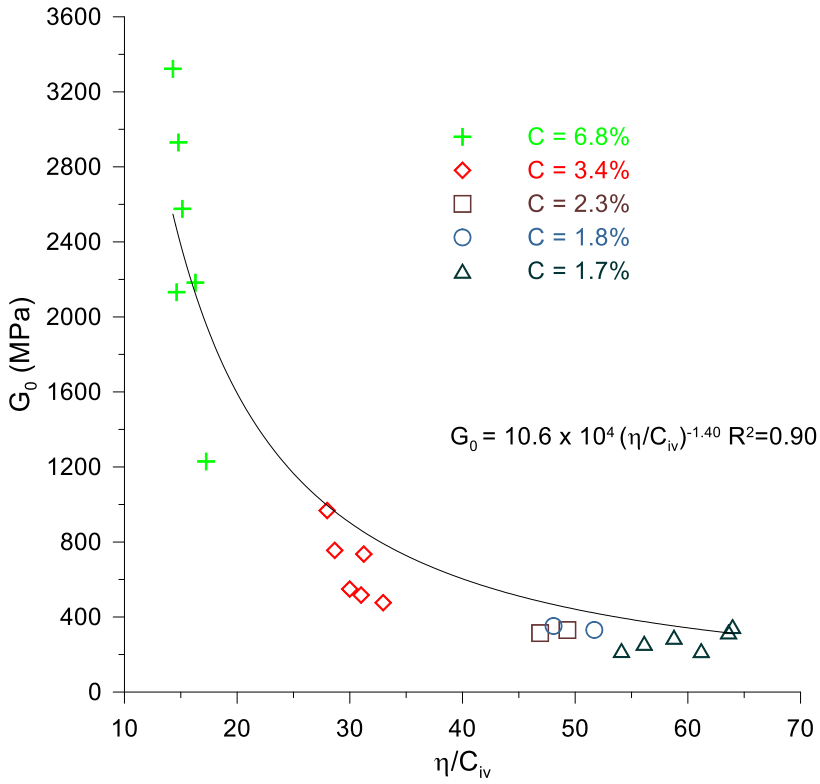


Figure 5.9 – Variation of the initial shear modulus (G_0) with adjusted porosity/cement index

5.4 EFFECT OF POROSITY/CEMENT INDEX

Figure 5.10 presents the relationship between η/C_{iv} and the unconfined compressive strength (q_u) of the cemented Hostun sand with a good correlation ($R^2 = 0.90$). A simple observation of Figure 5.3 suggests that the void ratio is useful in normalizing results. Equation 5.1 presents the correlation obtained:

$$q_u(kPa) = 4.3x10^4 \left(\frac{\eta}{C_{iv}}\right)^{-1.40} \quad (5.1)$$

As for the results obtained for the tensile strength (Figure 5.6), a correlation of $R^2 = 0.85$ was obtained and the equation from the adjustment is presented in Equation 5.2:

$$q_t(kPa) = 3.6x10^3 \left(\frac{\eta}{C_{iv}}\right)^{-1.40} \quad (5.2)$$

It is observed that Figures 5.3 and 5.6 present similar trends. In order to check the relationship between q_t/q_u Equation 5.2 is divided for Equation 5.1 and presented in Equation 5.3:

$$\frac{q_t}{q_u} = \frac{3.6x10^3\left(\frac{\eta}{C_{iv}}\right)^{-1.40}}{4.3x10^4\left(\frac{\eta}{C_{iv}}\right)^{-1.40}} = 0.08 \quad (5.3)$$

It can be seen in Equation 5.3 that q_t/q_u is a scalar for the sand-cement blend, being independent of porosity, cement content, or porosity/cement index. There is a straight proportionality between tensile and compressive strengths, which is valid for the whole range of voids ratio and cement content studied in the present research program.

Therefore, it is possible to conclude that any rational dosage methodology considering the effect of different variables can be centred on tensile or compression tests, once they are intimately related through a scalar (0.08) for the sand-cement studied in the research.

The initial stiffness for the artificially cemented Hostun sand analysed by the porosity/cement index was presented in Figure 5.9. The correlation obtained was R^2 = 0.90 and the equation is presented in Equation 5.4.

$$G_0(MPa) = 10.6x10^4\left(\frac{\eta}{C_{iv}}\right)^{-1.40} \quad (5.4)$$

It is observed that the adjusted porosity/cement index on the unconfined compressive strength on (q_u) and on the initial shear modulus (G_0) of the artificially cemented sand is quite similar, presenting comparable shapes of curves. As previous presented by Consoli et al. (2012), the relation of the G_0/q_u is presented in Equation 5.5. Variation of G_0/q_u is expressed by a constant, 2465.

$$\frac{G_0}{q_u} \cong 2465 \quad (5.5)$$

5.5 COMPARISON WITH MODELLING PREDICTIONS

In this section the results obtained on the unconfined compressive strength and initial shear modulus are compared with theoretical derivations from literature.

5.5.1 Comparison with modeling: q_u

Based on the concept of superposition of failure strength contributions of the soil and cement phases, Diambra et al. (2017) provided a theoretical derivation for the unconfined compression strength of artificially cemented granular soils. The material granular matrix follows concepts

of the critical state soil mechanics, and the strength of the cemented phase is described by the Drucker-Prager failure criterion. Through a volumetric averaging approach (DIAMBRA et al., 2011, 2013; DIAMBRA & IBRAIM, 2015), the stress state of the cemented composite is derived from the stresses of its constituents at failure. To account for the soil matrix strength, the model requires the calibration of the parameter *a*, among others, which can be estimated through triaxial tests results. The parameter *a* links the peak strength of the soil matrix (represented using the density-dependent deviatoric stress and mean stress ratio q_m/p_m) to a state parameter [defined as the ratio between the porosity at the critical state (η_{cs}) and the current porosity (η)], as shown in Equation 5.6, where *M* represents the critical state strength.

$$\frac{q_m}{p_m} = M\left(\frac{\eta_{cs}}{\eta}\right)^a \tag{5.6}$$

The model developments yield in Equation 5.7 to describe unconfined compressive strength of cemented granular soils.

$$q_u = K\left[\frac{\eta}{(B_{iv})^{1/a}}\right]^{-a} \tag{5.7}$$

Diambra et al. (2017) also pointed out the similarity between Equations 5.6 and 5.7 and suggested that the exponents *D* and *E* in Equation 5.6 are dependent on the soil matrix related parameter *a*, $D=1/a$ and $E=-a$. The multiplying parameter *a* in Equation 5.6 is suggested to be the result of combined properties of the sand matrix and cement phase. According to the authors, the key governing parameters seem to be the frictional strength of the matrix and the strength of the cemented phase. The factor *a* is also affected by the exponent *a*, which is controlled by the soil matrix properties. The model used the critical state parameters for the soil matrix, these parameters were obtained from the data of Escribano (2014). The final model prediction of the authors is expressed in Equation 5.8.

$$q_u = \frac{6\mu_c{\sigma_c}^c}{k_c(1-\beta)+3(\beta+1)}\left[\frac{k_c - M\left(\frac{\eta_{cs}}{n}\right)^a}{3 - M\left(\frac{\eta_{cs}}{n}\right)^a}\right] \tag{5.8}$$

Table 5.1 presents the parameters used for the model. For the studied cemented soil matrixes, the observed value of *a* is 1.40, leading to $1/a$ of 0.71, ~1.0, used in the experimental results.

Table 5.1 – Parameters to the theoretical derivation model

Symbol	Variable	Value
M	Critical state soil strength ratio	1.33 (ϕ'=33º)
η_{cs}	Critical; state soil porosity	0.48
A	Parameter governing dependence of soil	1.55
σ^c_c	Cement phase compressive strength	50 MPa
β	Uniaxial and extension cement strength ratio	-6
K_c	Cement stress ratio	4

Using the parameters presented in Table 5.1 and the Equation 5.8, the prediction parameter results in Equation 5.9. Figure 5.10 presents the comparison of the experimental data and the modelling results, showing that modelling and data results in same order of magnitude and trend.

$$q_u = \frac{6\,{}^{C_{iv}}/_{100}\,50000}{4(1-(-6))+3((-6)+1)}\left[\frac{4-1.33\left(\frac{0.48}{{}^{n}/_{100}}\right)^{1.55}}{3-1.33\left(\frac{0.48}{{}^{n}/_{100}}\right)^{1.55}}\right] \tag{5.9}$$

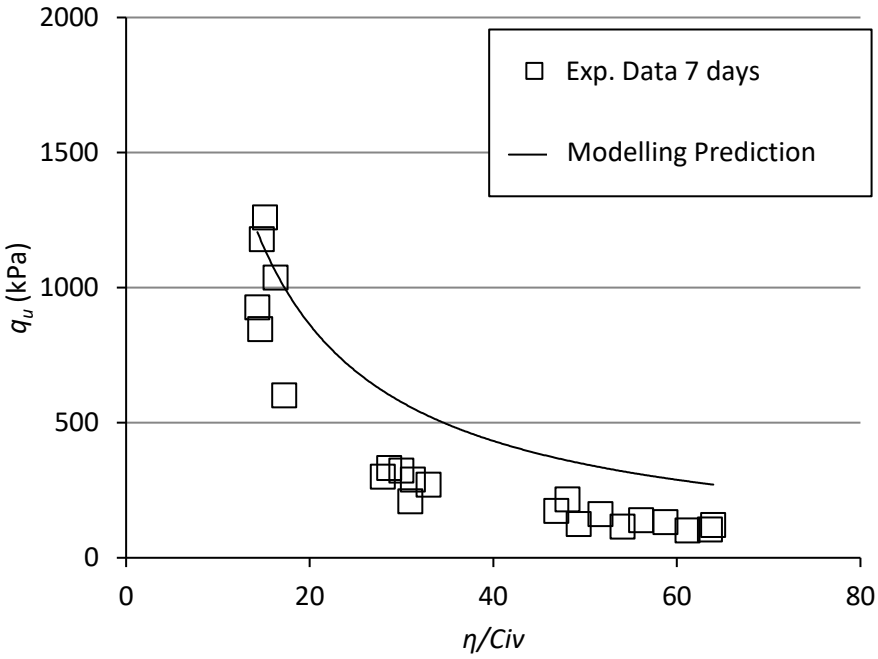


Figure 5.10 – Comparison of q_u from results and model

5.5.2 Comparison with modeling: G_0

Diambra et al. (2020) provided a theoretical justification for the existence of empirical power relationships governed by a porosity over cement content ratio for the evaluation of small strain

stiffness. According to the authors, such a power relationship is a simplification of the well-established Hardin's type relationship for the initial small strain shear stiffness of cemented soils under unconfined loading conditions. Hardin's type relationships usually present materials stiffness as a function of void ratio (or porosity), structure related characteristic and mean effective stress. The power of the porosity η term in the empirical relationship accounts for the shape of the normal compression line (NCL) of the uncemented soil in the η-p' plane, while the cement content C_{iv} term accounts for the shift of the NCL of the cemented soil with respect to its uncemented NCL state. Diambra et al. (2020) showed the exponential term depending on the η may be seen as an approximation of the current Horslev pressure for uncemented soil and it is a term which accounts for the overconsolidation state or *f(e)* function of the material. The exponential term linked to the C_{iv} may represent the shift of the NCL for cemented soil and is a measure of the current state of cementation.

The theoretical model cited assumes that the composite cemented material is isotropic; the behaviour of the cemented soil at the failure is determined by superposing the strength contributions of the two phases: failure of the composite cemented soil occurs as a result of a simultaneous failure of both the cemented and soil matrix phases, and strain compatibility between the composite and its two phases applies.

The theoretical model requires the knowledge of the normal compression line for uncemented and cemented states. The NCL was obtained from previous studies in Hostun sand (Diambra, not published). Hostun sand and Osorio sand presented similar behaviour when NCL line were compared. For this reason and in order to use the theoretical proposition on the paper, it was assumed that the behaviour of 1.4% C_{iv} cemented Hostun sand was similar to 1.4% C_{iv} cemented Osorio sand obtained in the literature. For other cement contents the parameters were interpolated.

The model presents the following correlation expressed in Equation 5.8:

$$\frac{G_0}{p_r} = AD^m L^q \left(\frac{\eta}{C_{iv}{}^{q/(fm)}}\right)^{-fm} \tag{5.10}$$

From the analysis of the modelling prediction, the following values were obtained: AD^mL^q = 5xE^8, fm = 3.744, and q/fm = 0.5. The curve obtained from the model and the experimental results are combined in Figure 5.11.

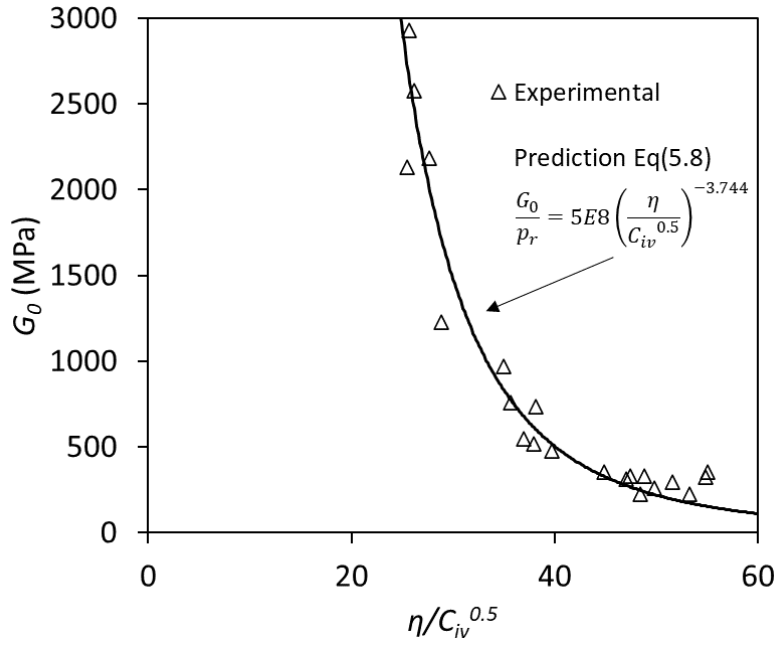


Figure 5.11 – Comparison of G_0 from data and model

5.6 FAILURE ENVELOPE THROUGH MODELLING

Consoli (2014) proposed a method to determine the effective cohesion intercept (*c'*) and the effective angle of shearing resistance (ϕ') for cemented sands. The model is based on the Mohr-Coulomb envelope based on Mohr circles from splitting tensile and unconfined compression tests. The parameters can be obtained from the following equations:

$$\phi' = arcsin\left(\frac{\sigma_c - 4\sigma_t}{\sigma_c - 2\sigma_t}\right) \tag{5.11}$$

$$c' = \frac{\sigma_c\left[1-\left(\frac{\sigma_c-4\sigma_t}{\sigma_c-2\sigma_t}\right)\right]}{2\cos\left[arcsin\left(\frac{\sigma_c-4\sigma_t}{\sigma_c-2\sigma_t}\right)\right]} \tag{5.12}$$

The parameters obtained using equations 5.11 and 5.12 were ϕ' = 39.3º and *c*' = 40 kPa, using the values of compression and tensile strength representing the η/C_{iv} of 47.2. The values obtained in this method will be used for the modelling prediction in Chapters 6 and 7.

5.7 STIFFNESS EVOLUTION

The cubical samples were prepared in order to analyse the evolution of the cemented specimen stiffness with the cement hydration. The specimens prepared for this purpose were left with the

bender elements inserted in the specimen in order to avoid any kind of breakage during testing and moving the specimen. The samples were also placed in a tray with wheels to move the specimen and the reading system if needed. The measurements were made until no variation of the time of arrival of the wave was noticed.

Six samples are presented in this section. *z* direction corresponds to the vertical direction of the specimen (direction of specimen compaction) while *x* and *y* are the horizontal directions of the specimens. In some specimens, due to installation problems of the benders, one of the horizontal measurements was not able to be used. Only shear waves were recorded during the measurements. In the horizontal directions, represented in the research as *x* and *y*, the shear wave propagation was horizontally with horizontal propagation. This means that if an observer looks to the specimen; both faces the bender elements are vertical. As for the vertical direction, the representation is in *z* direction.

Figure 5.12 shows the stiffness evolution of two specimens prepared with the same η/C_{iv} (47.2) with two different proportions of the phases. In the specimen with 2.3% cement content (a), the evolution of stiffness continues until day 16, at which point it remains constant. In the specimen with 1.8% cement (c), this evolution of the stiffness reaches a constant value at day 3. When comparing the ratio between the stiffness of *x* and *z* directions, it is observed that both reach a similar value within less than 3 days. From Figure 5.12b and 5.12d, it is observed that the ratio between the stiffness the horizontal and vertical direction is close to unit (1) at the early days of measurements. When compared to the results presented in Figure 5.12e and 5.12f, the specimen with 6.8% cement takes almost 30 days for the stiffness in both directions to be similar. This is a clear indication of the effect of cementation on reduction of stiffness anisotropy caused by the compaction process.

The anisotropy imposed by preparing the specimens by the method of undercompaction have been described by Ladd (1978). The vertical direction represents the direction of the tamping during sample preparation. This anisotropy induced on the specimens means that the change of the stress state leads to the change of the mechanical properties and parameters of the cemented sand when a complex load is applied in different directions (ARTHUR et al., 1977).

Figure 5.12e and 5.12f present the evolution of stiffness for a specimen prepared with 6.8% cement: this cement content was already used in the unconfined compression strength. It was

observed that a constant value in G_0 is reached after only 27 days, the same time when the vertical and horizontal directions of the specimen reached similar stiffness values.

Figure 5.13 presents the stiffness evolution of specimens prepared with higher cement content. The insertion of the bender elements without disrupting the sample was not easy, and these specimens had to be remoulded several times. This disruption of the specimen is believed to be the reason why Figure 5.13g and 5.13h presents a higher stiffness in *x* and *y* directions. A similar specimen was then remoulded and presented in Figure 5.13e and 5.13f. In this second specimen, it is observed that the stiffness evolves until day 24 and then remains constant. In comparison of *z* with *x* and *y* directions, a constant value is reached also within 24 days.

A specimen with 10% cement was also prepared. Content was used in order to verify the influence of adding a higher amount of cement into the stiffness evolution. Figures 5.13k and 5.13l show that the stiffness reached in the *z* direction is never reached by the *x* and *y* directions, although the difference observed in the stiffness decreases with the cement hydration over time.

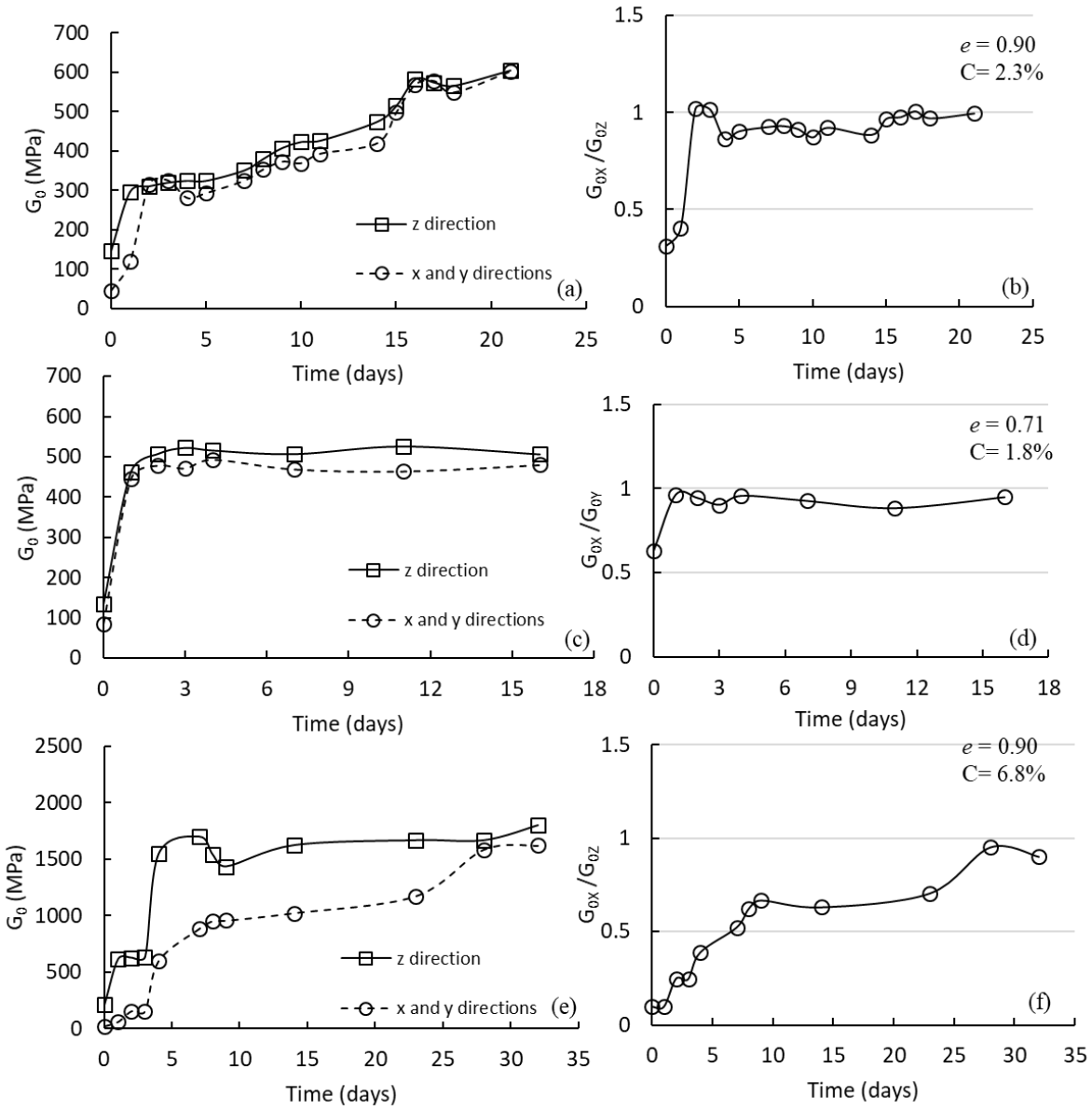


Figure 5.12 – Stiffness evolution over time and comparison *z* and *x* and *y* directions: (a) and (b) *e*=0.90, C=2.3%; (c) and (d) *e*=0.71, C=1.8%;(e) and (f) *e*=0.90, C=6.8%

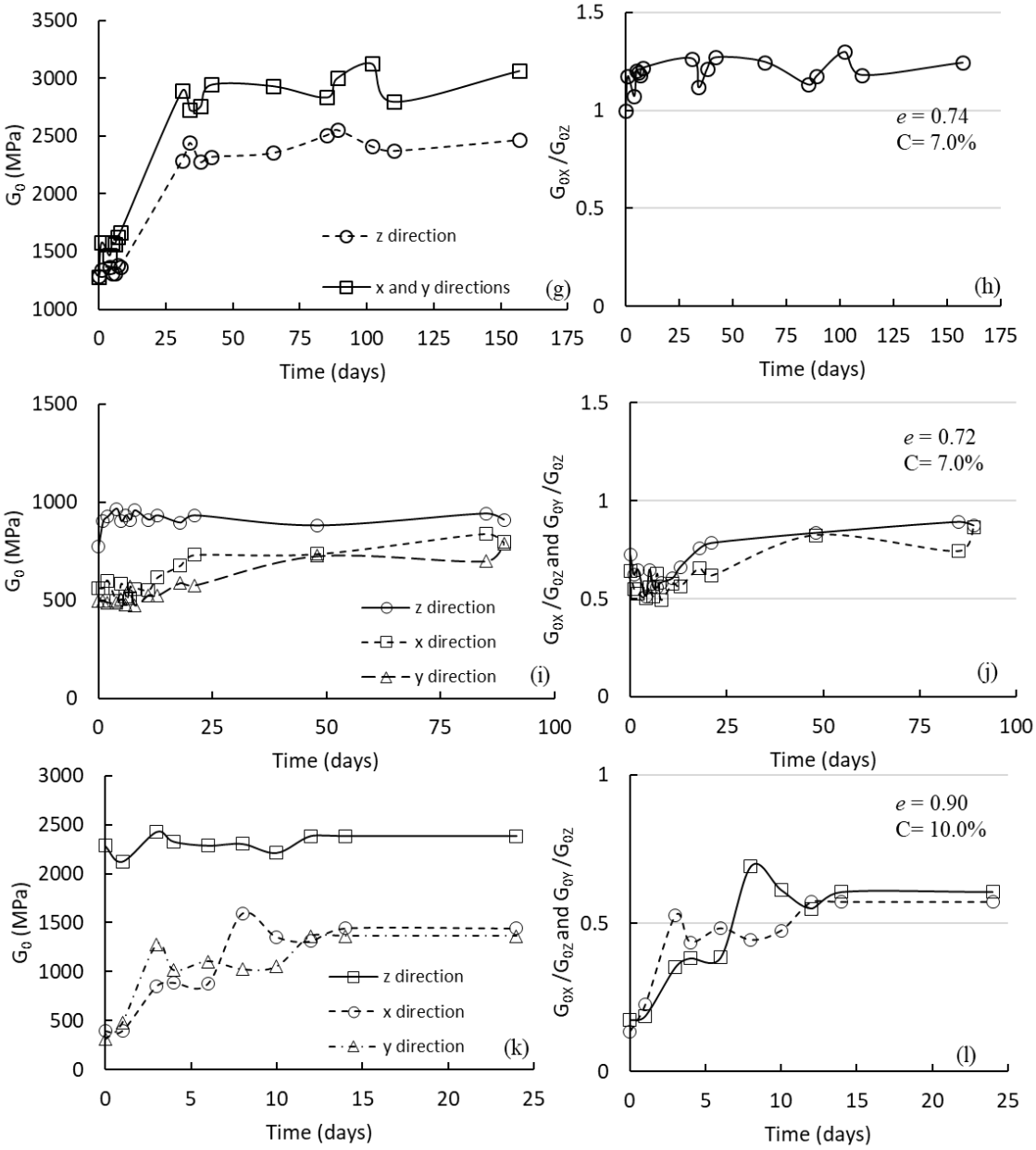


Figure 5.13 – Stiffness evolution over time and comparison *z* and *x* and *y* directions: (g) and (h) *e*=0.74, C=7.0%;(i) and (j) *e*=0.72, C=7.0%;(k) and (l) *e*=0.90, C=10.0%;

5.8 SUMMARY

It was observed that the porosity/cement index curve provided a unique relationship with the unconfined compressive strength, tensile strength and initial stiffness of the artificially cemented Hostun sand. It was also observed that the three relationships had the same adjusted power on the η/C_{iv} (1.40).

The prediction models used on the analysis presented compatible results when comparing to the experimental data.

From Figure 5.3, a η/C_{iv} relationship of 47.2 was adopted, suggesting a maximum unconfined compressive strength of 200 kPa. As mentioned in the testing program, this porosity/cement index was target with two conditions: e = 0.90 and C = 2.3% and e = 0.71 and C = 1.8%. These specimen characteristics were adopted for the tests presented in Chapters 6 and 7.

The strength parameters were obtained using Consoli (2014) were ϕ' = 39.3º and c' = 40 kPa.

As for the evolution of the stiffness on the cemented samples, it was noticed that with the development of the cement hydration, the difference in the stiffness caused by the compaction of the specimens reduced over time.

6 CUBICAL CELL TESTS

In this chapter, the results obtained from the artificially cemented Hostun sand sheared on the cubical cell apparatus are presented. The tests are firstly divided according to the specimen specification; later, the results are presented together. Preliminary conclusions are also presented at the end of this chapter.

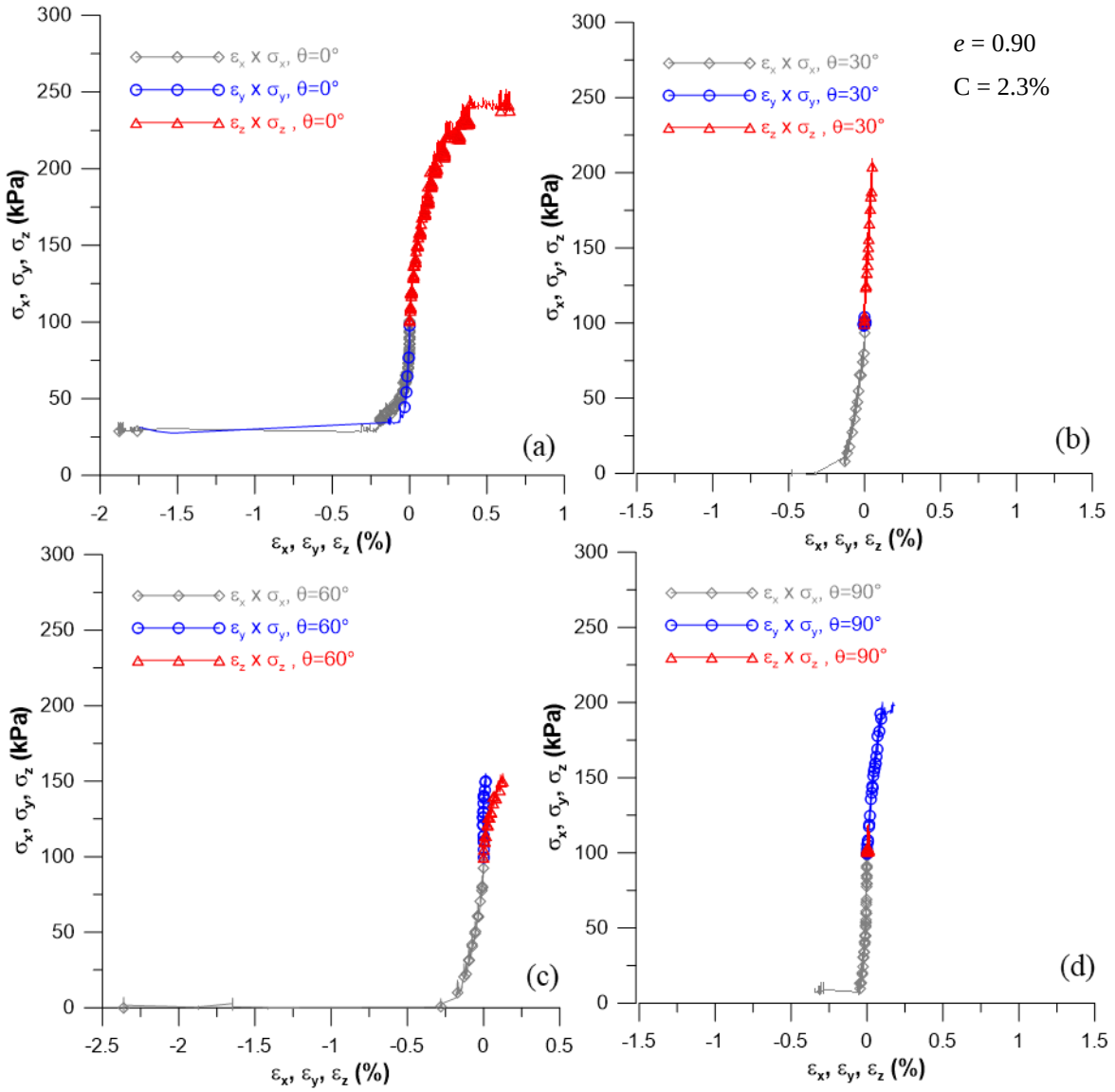
6.1 STRESS-STRAIN BEHAVIOUR

Figure 6.1 shows the stress-strain responses for the principal directions (ε_x, ε_y, and ε_z) for the first set of specimens (e = 0.90 and C = 2.3%). Figure 6.2 presents the stress-strain curves for the principal directions of the second set of specimens (e = 0.71 and C = 1.8%).

The $\theta = 0^o$ and 120^o stress paths has same b value of zero (0). Considering both cemented and void ratio mixtures, under $\theta = 0^o$ stress path, the cemented material exhibited compressive strain in the z direction and extension strains in x and y directions (Figures 6.1a and 6.2a). For the $\theta = 120^o$ stress path, the specimen is compressed in the y direction and extension is taking place in x and z directions (Figures 6.1e and 6.2e). Higher strain limits are observed for the test at $\theta = 120^o$ compared with the test at $\theta = 0^o$. As the tests are controlled in stress, once the failure occurs, the deformations increase steadily at a relatively high rate. The material behaviour is brittle, and the failure points are marked by the arrows in Figures 6.1 and 6.2. However, a relatively similar stress-strain response is observed for the directions where the stress is reduced for both paths and blends.

When the b value assumed the intermediate value of 0.5, for the $\theta = 30^o$, 90° and 150^o stress paths, specimens presented near zero strains in y, z and x directions, respectively. Under $\theta = 30^o$ stress path, the material showed compressive strain in the z direction and extension strain in the x direction (Figures 6.1b and 6.2b). For the $\theta = 90^o$ stress path, compressive strains took place in the y direction and extension strains in x direction were observed (Figures 6.1d and 6.2d). Analogously, compression was observed in the y direction and extension in z direction under $\theta = 150^o$ stress path (Figures 6.1f and 6.2f). For both cemented blends, the observed values of maximum stress were higher for $\theta = 30^o$ stress path, followed by $\theta = 90^o$, and $\theta = 150^o$ paths.

Lower levels of stresses were displayed for the $\theta = 60^o$ and 180^o stress paths, which have the limit b value of 1. Under $\theta = 60^o$ stress path, the cemented material exhibited compressive strain in the z and y directions and extension strains in x direction (Figures 6.1c and 6.2c). For the $\theta = 180^o$ stress path, the sample is compressed in the y and z direction and extension took place in the x direction (Figures 6.1g and 6.2g).



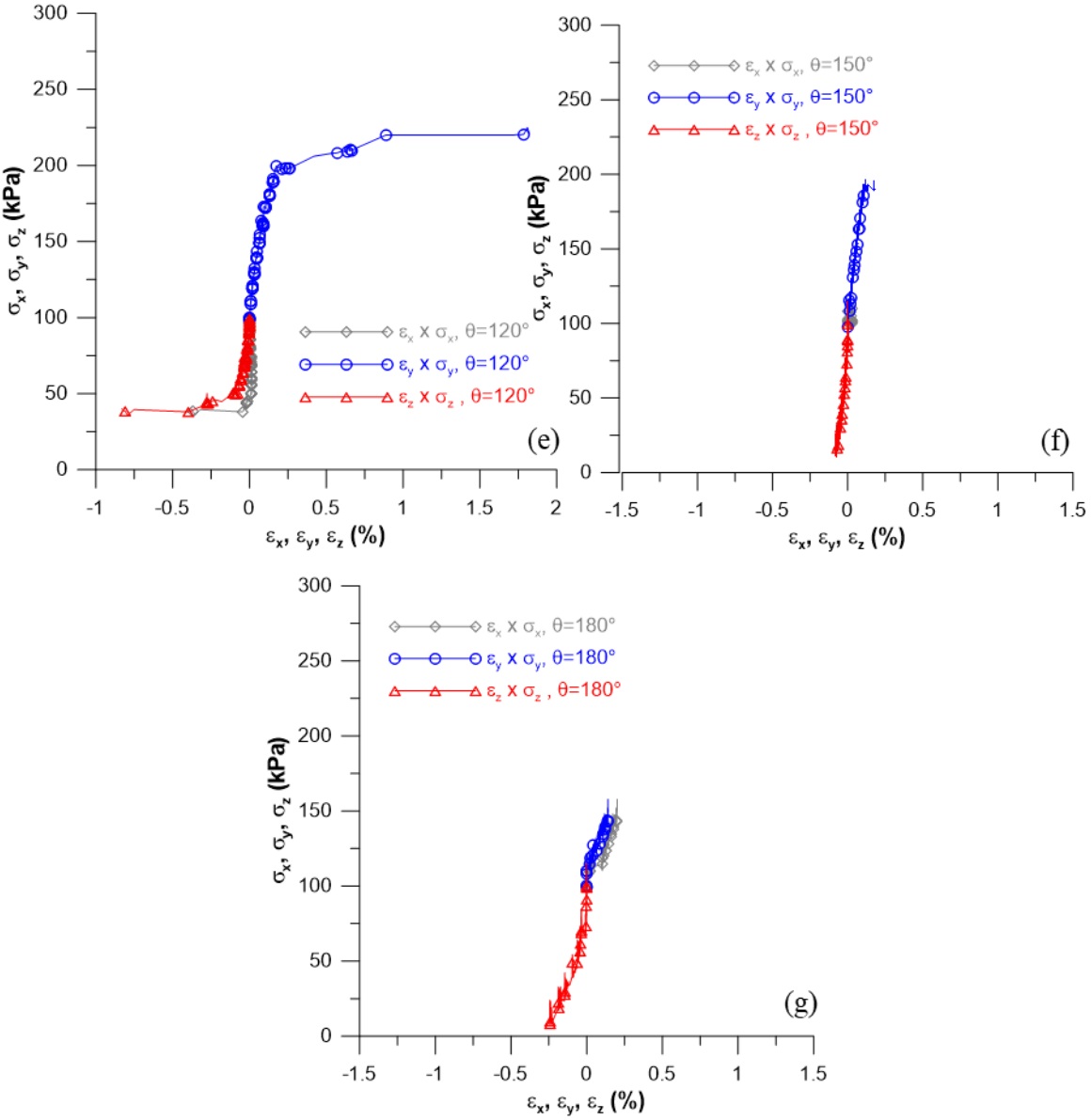
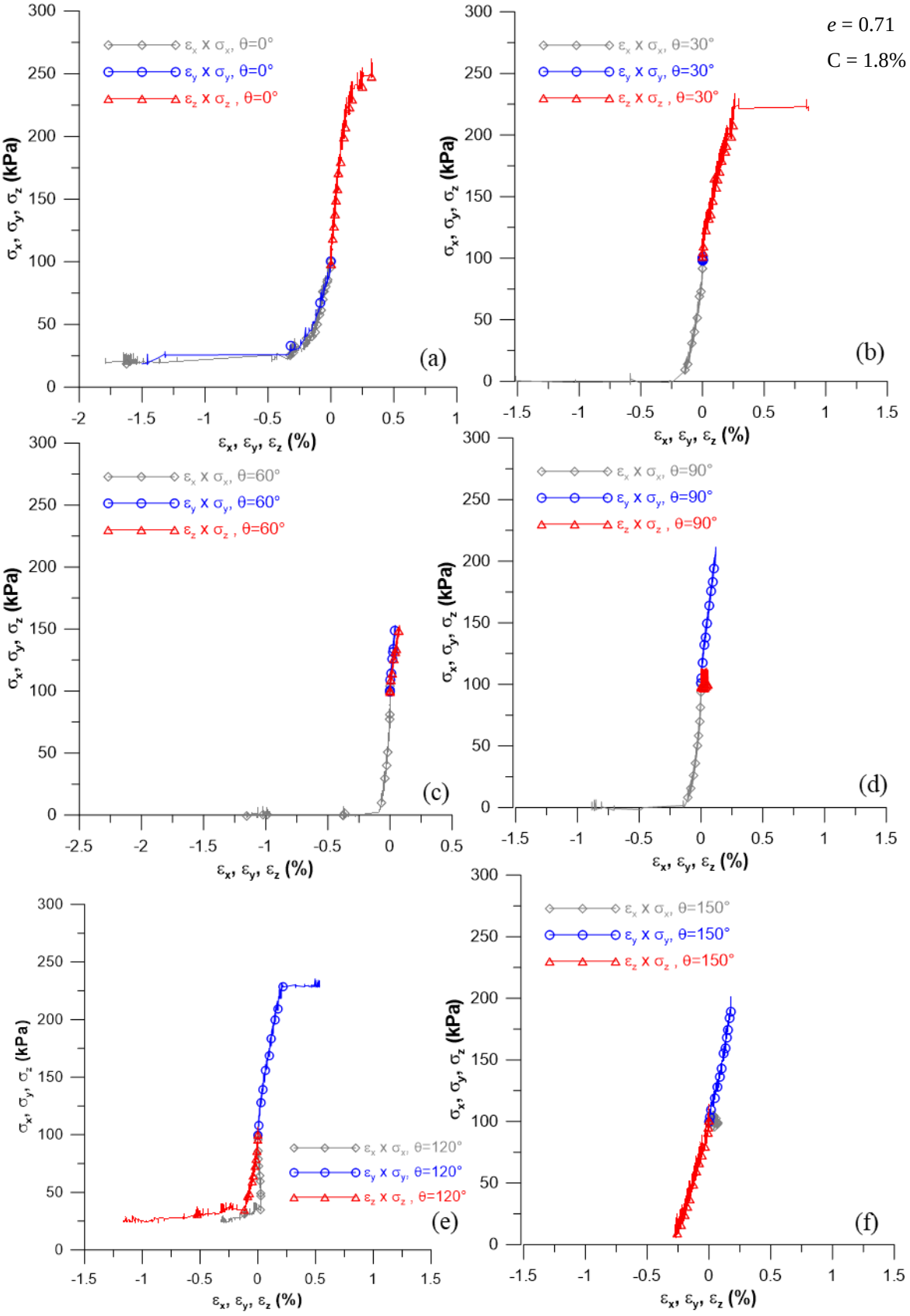


Figure 6.1 – Stress-strain response for the principal directions for the first set of samples (e = 0.90 and C = 2.3%): (a) θ = 0º; (b) θ = 30º; (c) θ = 60º; (d) θ = 90º; (e) θ = 120º; (f) θ = 150º; (g) θ = 180º


e = 0.71
C = 1.8%
εx x σx, θ=0°
εy x σy, θ=0°
εz x σz , θ=0°
(a)
εx x σx, θ=30°
εy x σy, θ=30°
εz x σz , θ=30°
(b)
εx x σx, θ=60°
εy x σy, θ=60°
εz x σz , θ=60°
(c)
εx x σx, θ=90°
εy x σy, θ=90°
εz x σz , θ=90°
(d)
εx x σx, θ=120°
εy x σy, θ=120°
εz x σz , θ=120°
(e)
εx x σx, θ=150°
εy x σy, θ=150°
εz x σz , θ=150°
(f)
σx, σy, σz (kPa)
εx, εy, εz (%)

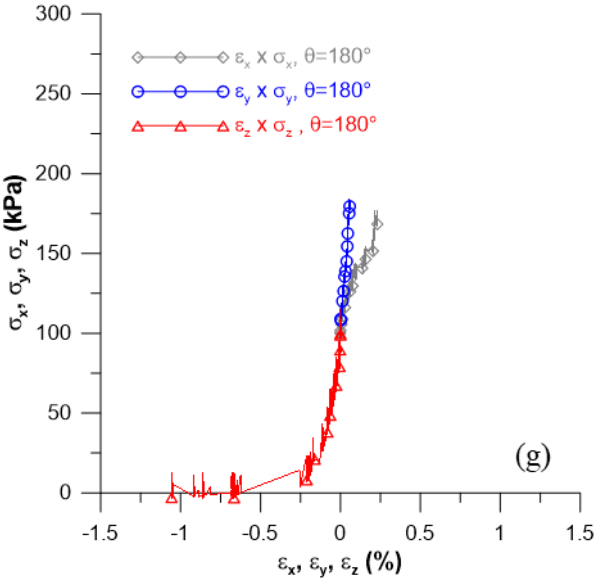


Figure 6.2 – Stress-strain response for the principal directions for the second set of samples (e = 0.71 and C = 1.8%): (a) θ = 0º; (b) θ = 30º; (c) θ = 60º; (d) θ = 90º; (e) θ = 120º; (f) θ = 150º; (g) θ = 180º

A direct comparison of the effect of different stress paths on the stress strain response of the studied mixtures can be observed in Figure 6.3a for the first set of samples (e = 0.90 and C = 2.3%), and Figure 6.3b for the second set of samples (e = 0.71 and C = 1.8%), where the distortional stress, q, is presented with the distortional strain, ε_q. The effect of stress paths on the volumetric response is presented in Figure 6.4a for the first set of samples (e = 0.90 and C = 2.3%), and Figure 6.4b for the second set of samples (e = 0.71 and C = 1.8%), where the volumetric strain, ε_v, against distortional strain, ε_q.

In analysing Figure 6.3a and b, it can be noted that for both mixtures, the highest q is obtained when θ = 0º, followed by 120º, 30º, 90º, 150º, 60º and 180º. Figure 6.4a and b shows that by changing the principal stress angle (θ), the cemented material responds with distinguishable volume strains. When the specimen sheared in 120º, an expansion is observed; specimens performed with 0º, 30º and 90 º responded with a reduction in volume. The cemented sand did not present a clear volume variation when θ = 150º and 180º was imposed.

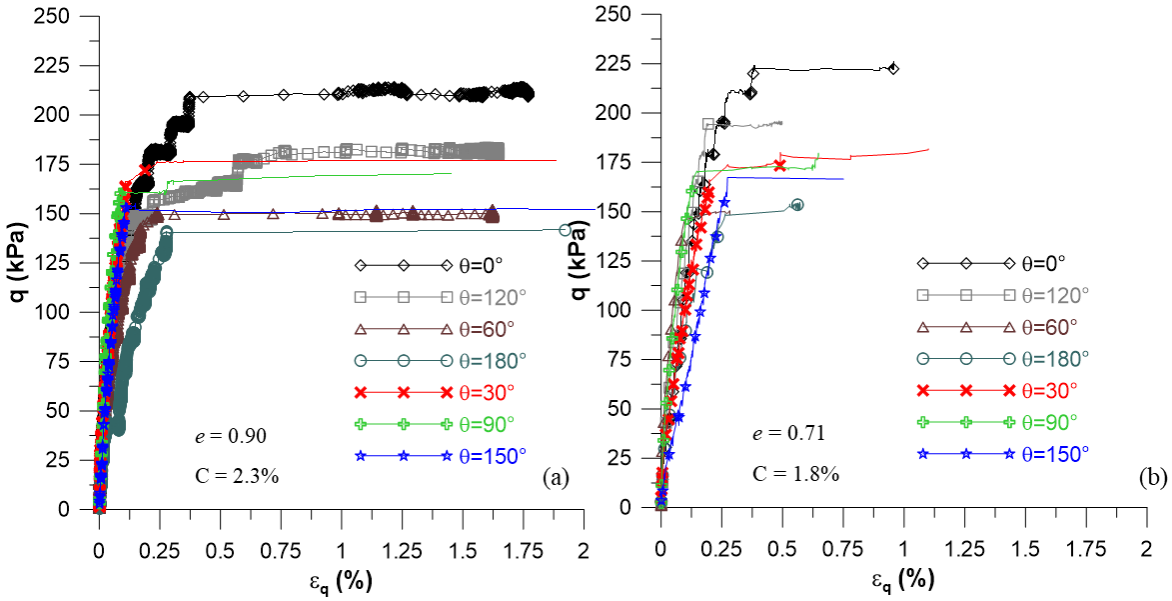


Figure 6.3 – Distortional stress, q, against distortional strain, ε_q, of (a) first set of samples (e = 0.90 and C = 2.3%) and (b) second set of samples (e = 0.71 and C = 1.8%)

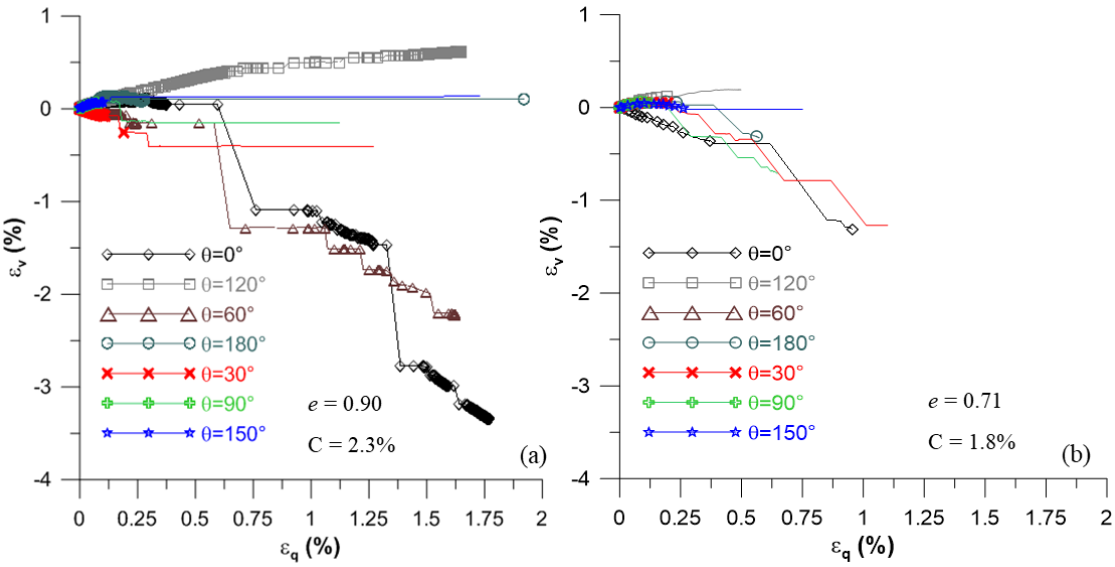


Figure 6.4 – Volumetric strain, ε_v, against distortional strain, ε_q, of (a) first set of samples (e = 0.90 and C = 2.3%) and (b) second set of samples (e = 0.71 and C = 1.8%)

For b value of 0, under $\theta = 0^o$ stress path conditions, the cemented sand strength appears to be higher than the strength recorded under $\theta = 120^o$ stress path case. The higher strength is associated with lower volumetric contraction as shown in Figure 6.4. While one expects an isotropic response induced by a more uniform cementation process, it is possible that the low level of cementitious material would not provide enough particle bonding to overcome the

anisotropy induced by the fabrication process. That was observed for both studied cemented blends. Compaction during fabrication takes place over the vertical, *z*, direction, and this seems to control the material response in multiaxial loading conditions. For *b* value of 0.5, under θ = 30º stress path conditions, the strength observed was higher than under the θ = 90º stress path, followed by the θ = 150º stress path. Lower levels of strength were observed for the θ = 90º and 180º stress paths, which have the *b* value of 1.

6.2 FAILURE SURFACE

The maximum values of strength were presented as a function of θ in Figure 6.5. The image clearly depicts the effect of θ on strength. Also, the observed values of strength for the distinct blends are very similar.

In order to observe the stress paths in the deviatoric plane, stress states were plotted in terms of orthogonal deviatoric stress components q_x and q_z (Figure 6.6a, for the first set of samples, and Figure 6.6b, for the second set of samples). These components provide a view of π plane down the diagonal space ($\sigma_x = \sigma_y = \sigma_z$), in which the projection of σ_z axis coincides with q_z axis.

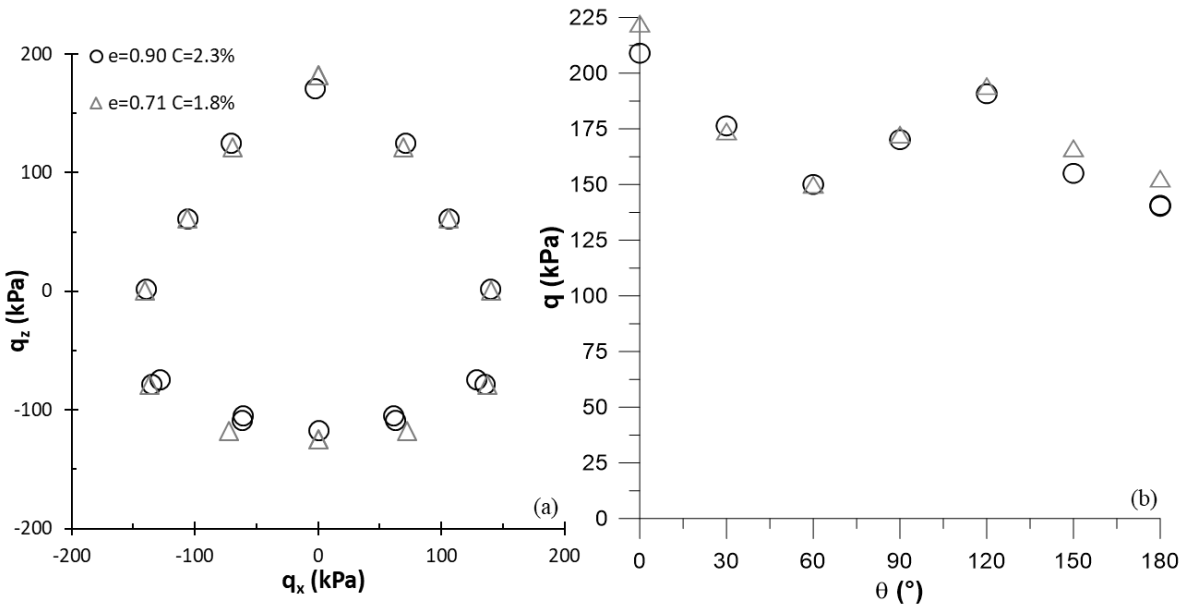


Figure 6.5 – (a) q_z and q_x;(b) q versus θ

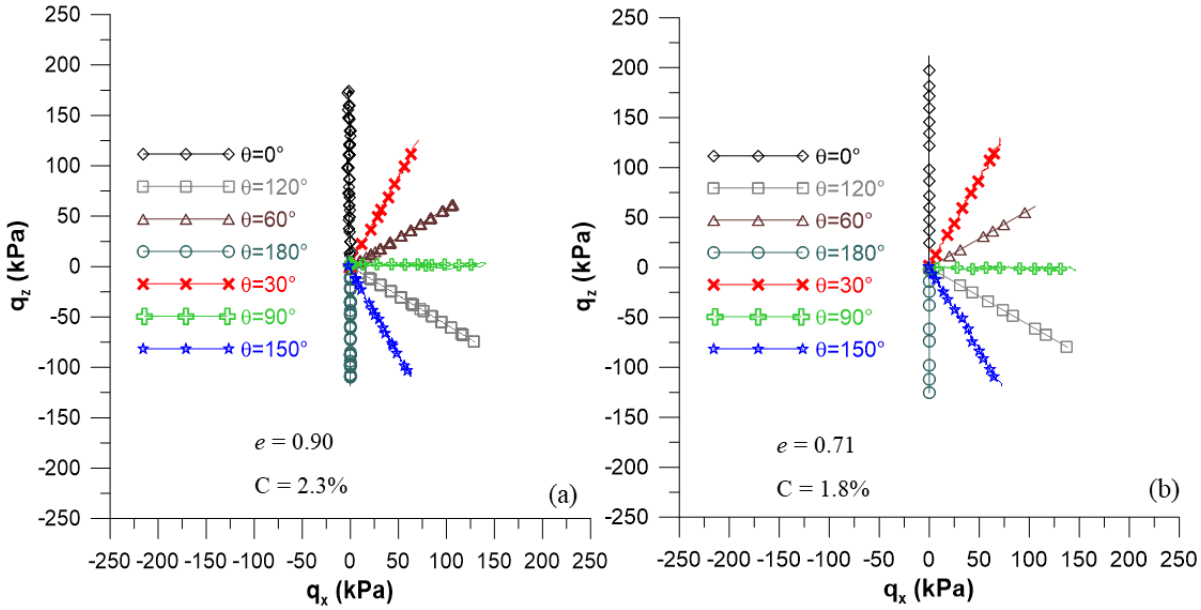


Figure 6.6 – Orthogonal deviatoric stress components: q_x and q_z of
(a) first set of samples (e = 0.90 and C = 2.3%) and
(b) second set of samples (e = 0.71 and C = 1.8%)

Tables 6.1 and 6.2 combines the testing conditions and maximum deviator stress observed in each test. On both tables it is noticed that the η/C_{iv} for all specimens is very similar. Also, the maximum deviator stress for each sample composition is similar.

Figure 6.7 presents a picture of each test sheared in this part of the research program. The observation of the specimens after shearing shows that the deformation recorded is in accordance with specimen shape. The rigid wall face influenced on the format of the specimens and each load condition resulted in a distinct specimen shape after loading.

Table 6.1 – Characteristics of testing conditions for the specimens prepared with 2.3% cement and 0.90 void ratio target

θ^o	*Maximum principal stress*	*b*	*C (%)*	e_{cons}	η/C_{iv}	q_{max} *(kPa)*
0	σ_z	0	2.3	0.90	48.6	209
30	σ_z	0.5	2.3	0.92	48.9	176
60	σ_z and σ_y	1	2.3	0.91	49.0	150
90	σ_y	0.5	2.3	0.92	49.1	170
120	σ_y	0	2.3	0.93	50.1	191
120	σ_y	0	2.3	0.92	49.5	181
150	σ_y	0.5	2.3	0.90	48.5	155
180	σ_y and σ_x	1	2.3	0.90	48.3	140

Table 6.2 – Characteristics of testing conditions for the specimens prepared with 1.8% cement and 0.71 void ratio target

θ^o	*Maximum principal stress*	*b*	*C (%)*	e_{cons}	η/C_{iv}	q_{max} *(kPa)*
0	σ_z	0	1.8	0.71	48.9	241
0	σ_z	0	1.8	0.72	50.1	222
30	σ_z	0.5	1.8	0.72	49.3	174
60	σ_z and σ_y	1	1.8	0.72	49.6	150
90	σ_y	0.5	1.8	0.73	49.9	172
120	σ_y	0	1.8	0.72	49.9	194
150	σ_y	0.5	1.8	0.73	50.1	167
180	σ_y and σ_x	1	1.8	0.71	49.9	153

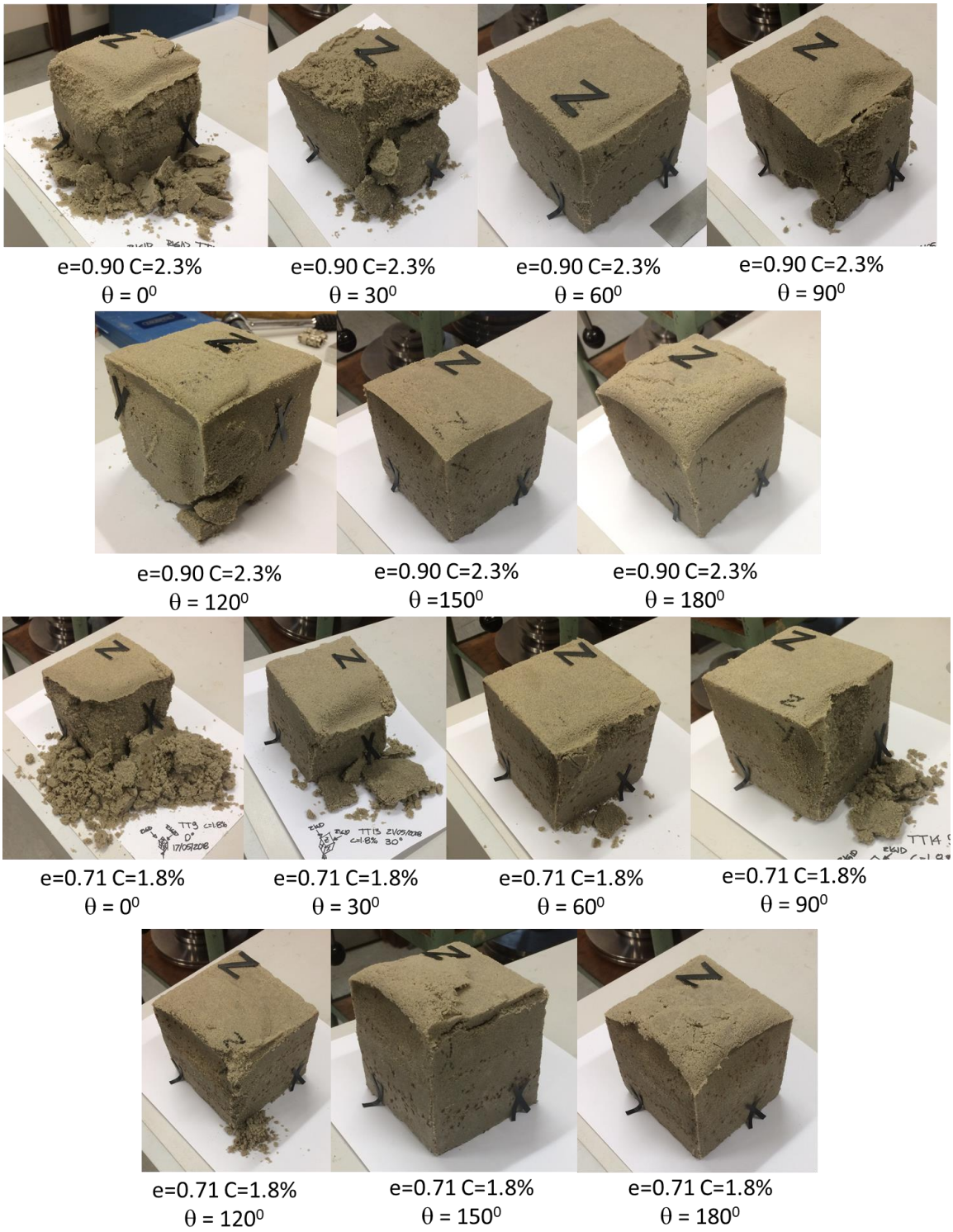


Figure 6.7 – Pictures of the reinforced sand after shearing

6.3 MODELLING PREDICTION

Table 6.3 presents the failure stresses observed in the true triaxial tests presented in Figures 6.1–6.6. With these summarised results, the following step was to analyse the failure surface using different methods. This analysis is presented in this section.

Table 6.3 – Failure stresses under different stress paths for both cement contents and void ratio

θ º	Octahedral Normal Stress (kPa)	C = 2.3% *e* = 0.90			C = 1.8% *e* = 0.71		
		σ_x kPa	σ_y kPa	σ_z kPa	σ_x kPa	σ_y kPa	σ_z kPa
0	100	36.15	31.54	240.97	20.73	20.73	262.09
30		-1.83	100.13	204.33	0.60	98.98	200.43
60		-0.24	149.74	149.74	0.02	150.93	150.93
90		-0.98	200.12	102.20	-1.41	198.11	97.53
120		38.79	220.07	38.79	36.55	227.95	36.55
150		99.68	183.007	17.11	97.05	201.94	8.11
180		148.72	148.72	17.11	151.59	151.59	-0.32

The failure path in the octahedral plane was presented in Figures 6.6a and b. The obtained surface was then analysed with models proposed in the literature and is presented in this section.

The parameter used on the following models came from Section 5.6: the strength parameters were obtained using Consoli (2014). The friction angle, ϕ' = 39.3º was used with the effective cohesion intercept, c' = 40kPa.

Mohr-Coulomb was the first criterion applied in this section. It is a linear criterion, based on the strength parameters ϕ' and c'; the model does not consider the intermediate strength. The shear strength is determined as proposed in Equation 6.1, presented by Coulomb (1773).

$$\tau = c + \sigma \tan \phi' \tag{6.1}$$

The *Drucker–Prager* failure criterion was established as a generalization of the Mohr–Coulomb criterion for soils (Drucker and Prager, 1952). It can be expressed as presented in Equation (6.2).

$$\sqrt{J_2} = A + BI'_1 \tag{6.2}$$

where A and B are material constants, J_2 is the second invariant of the stress deviator tensor and I'_1 is the first invariant of the stress tensor. The criterion, when expressed in terms of octahedral shear stress, τ_{oct}, and octahedral normal stress, σ'_{oct}, takes the form presented in Equation (6.3):

$$\tau_{oct} = \sqrt{\frac{2}{3}}(3A\sigma'_{oct} + B) \tag{6.3}$$

where $\sigma'_{oct} = 1/3\ I_1$' and $\tau_{oct} = \sqrt{\frac{2}{3}J_2}$.

The parameters *A* and *B* can be obtained from standard compression triaxial tests and can be expressed in terms of internal friction angle and cohesion intercept, as presented in Equations (6.4) and (6.5).

$$A = \frac{6c' \cos\phi}{\sqrt{3}(3+\sin\phi)} \tag{6.4}$$

$$B = \frac{2\sin\phi}{\sqrt{3}(3+\sin\phi)} \tag{6.5}$$

where c and ϕ are the cohesion intercept and internal friction angle, respectively.

Willam and Warnke (1975) put forward a yield criterion with three parameters. The yield curve on the deviator plane is close to a triangle, and that on the meridional plane is a straight line. Shortly afterward a criterion of five parameters was put forward, making the yield curve on the meridian plane a curve, in order to match with experimental data better.

The failure curve on the deviator plane is similar to an equilateral triangle. In order to get a smooth curve without sharp corners, due to triple symmetry, Willam and Warnke used part of the ellipse to fit within a scope of $0 \leq \theta \leq 60^o$. This ellipse is orthogonal with two meridian planes $\theta = 0^o$ and $\theta = 60^o$, according to these two conditions, finally the ellipse expressed in polar coordinate is as follows in Equation (6.6):

$$r(\theta) = \frac{2r_c(r_c^2 - r_t^2)\cos\theta + r_c(2r_t - r_c)[4(r_c^2 - r_t^2)\cos^2\theta + 5r_t^2 + 4r_t r_c]^{1/2}}{4(r_c^2 - r_t^2)\cos^2\theta + (r_c - 2r_t)^2} \tag{6.6}$$

where r_t and r_c are the values of r on the tensile meridian plane and compressive meridian plane, respectively.

Using the calculated r_θ the model with three parameters is presented in Equation (6.7):

$$F(\sigma_m, \tau_m, \theta) = \frac{1}{\rho}\frac{\sigma_m}{R_c} + \frac{1}{r(\theta)}\frac{\tau_m}{R_c} - 1 = 0 \tag{6.7}$$

where:

$$\sigma_m = {I_1}/{3} = {\xi}/{\sqrt{3}} \quad and \quad \tau_m = \sqrt{2J_2/5} = r/\sqrt{5} \tag{6.8}$$

The Equation (6.6) can be rewritten as follows:

$$\frac{\tau_m}{R_c} = r(\theta)\left(1 - \frac{1}{\rho}\frac{\sigma_m}{R_c}\right) \tag{6.9}$$

r_θ contains two parameters, r_c, r_t and adding parameter ρ, there ae a total of three parameters. From Equation (6.9), θ is a constant, the relationship between τ_m and σ_m is linear, so on the meridional plane of stress space, the yield line is a straight line; if $r_t = r_c$, it degrades to Drucker-Prager yield criterion, and if $\rho \rightarrow \infty$, it degrades to Mises yield criterion.

Three parameters, r_c, r_t, ρ, are determined by test data. ρ = Compression/Extension ratio, while the compression and extension parameters are obtained from: $M_c = \frac{6\sin\phi'}{3-\sin\phi'}$ and $M_e = \frac{6\sin\phi'}{3+\sin\phi'}$.

The last model used to predict the true triaxial results was proposed by *Kim and Lade* (1988) and Lade and Kim (1988a, 1988b). the constitutive model has been developed based on thorough review and evaluation of data from experiments on frictional materials such as sand, clay, concrete and rock. The model employs a single, isotropic yield surface that expresses a contour of constant plastic work as measured from the origin of stress. It is expressed in terms of stress invariants and is shaped as an asymmetric teardrop with the pointed apex at the origin of the principal stress space. The yield surface, expressed in terms of stress invariants, describes the locus at which the total plastic work is constant. The total plastic work (due to shear strains as well as volumetric strains) serves as the hardening parameter and is used to define the location and shape of the yield surface. The use of contours of constant plastic work as yield surfaces results in mathematical consistency in the model because the measure of yielding and the measure of hardening are uniquely related through one monotonic function. In addition, application of a single yield surface produces computational efficiency when used in large computer programs.

The criterion for soils is expressed in terms of the first and the third stress invariants of the tensor, as presented in Equation (6.10)

$$\left(\frac{{I_1}^3}{I_3} - 27\right)\left(\frac{I_1}{p_a}\right)^m = \eta_1 \tag{6.10}$$

where:

$$I_1 = \sigma_1 + \sigma_2 + \sigma_3 = \sigma_x + \sigma_y + \sigma_z \quad (6.11)$$

$$I_3 = \sigma_1.\sigma_2.\sigma_3 = \sigma_x.\sigma_y.\sigma_z + \tau_{xy}.\tau_{yz}.\tau_{zx} + \tau_{yx}.\tau_{zy}.\tau_{xz} - \left(\sigma_x.\tau_{yz}.\tau_{zy} + \sigma_y.\tau_{zx}.\tau_{xz} + \sigma_z.\tau_{xy}.\tau_{yx}\right) \quad (6.12)$$

and p_a is atmospheric pressure expressed in the same units as the stresses. The value of ${I_1}^3/I_3$ is 27 at the hydrostatic axis where $\sigma_1 = \sigma_2 = \sigma_3$. The parameters used in the method were m = 21189 and η_1 = 6280.

All models are presented in Figure 6.8 along with the experimental data. Its observed that the theoretical models closest to the experimental data are the Willan-Warnke and Kim and Lade propositions. Willan and Warnke proposed the model for concrete while Kim and Lade's was developed for friction materials. Both predictions overestimated the value obtained for $\theta = 0^o$ and overestimated the value found in $\theta = 120^o$. Mohr-Coulomb and Drucker-Prager did not represent the experimental data well.

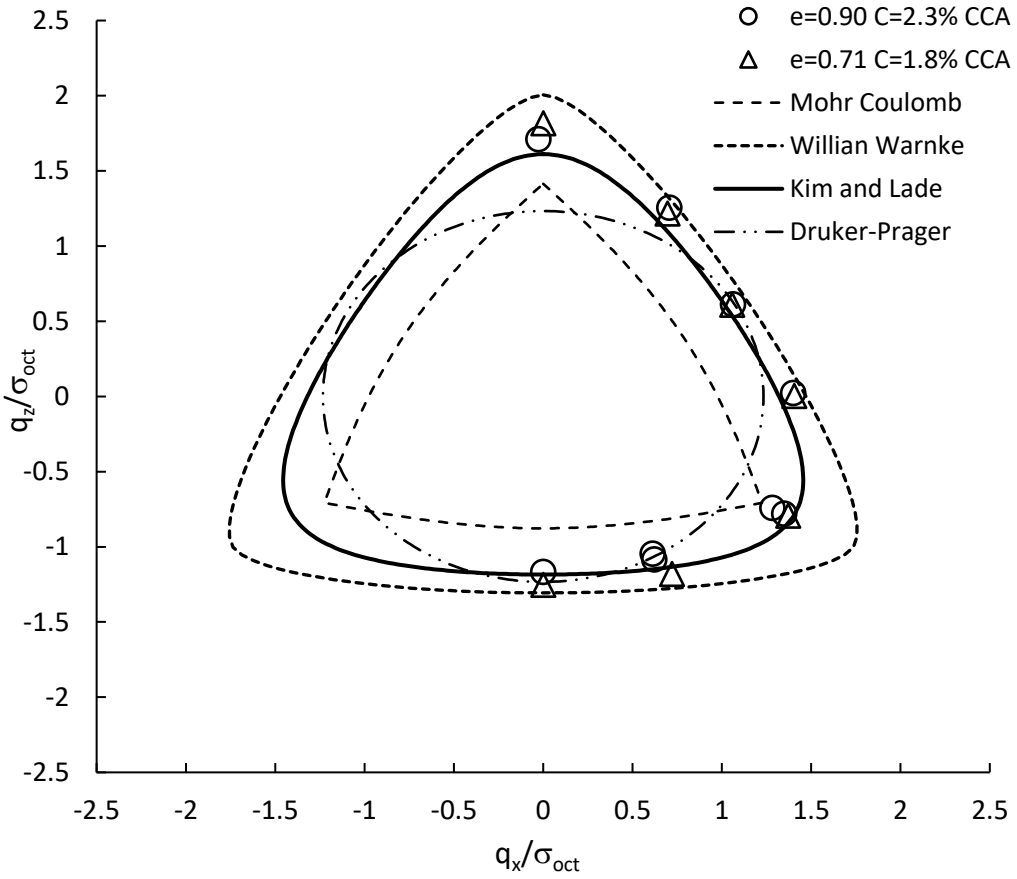


Figure 6.8 – Failure surface from modelling prediction and the experimental results

6.4 SUMMARY

In this chapter, the results from the two sets of true triaxial tests were presented. It is observed that changing θ results in the variation of the maximum deviatoric stress on the cubical samples. This variation confirms that the cemented samples are not isotropic. The anisotropic effect is related to the compaction process by vertically damping the sample.

The effect of the compaction process is also verified when the *b* parameter is observed. When comparing the specimens with *b*=0, there is a gap between the maximum deviatoric stress of θ = 0^o and 120^o; 0^o presents a higher value and it express the direction *z*, which is the direction where the specimen was compacted by damping. When comparing *b*=0.5, the difference in the results is smaller, although where the *z* component of strength is more important, the values are still higher. Finally, *b*=1 values are very close, with an undistinguished difference between θ = 60^o and 180^o.

When both samples compositions are compared, a similar behaviour is observed, leading to an agreement with the results obtained in the unconfined tests, presented in Chapter 5. The η/C_{iv} is proven to control the specimens prepared.

When analysing the prediction models, Willam and Warnke (1975) and Kim and Lade (1988) presented better representation of the experimental results.

7 HOLLOW CYLINDER TESTS

This chapter presents the results and discussion obtained from the hollow cylinder torsional tests performed on the studied cemented sand mixtures. As discussed previously, two distinct sets of specimens were prepared in order to achieve the same η/C_{iv} = 47.2. The two combinations of samples and distinct stress orientation are presented in this Chapter. In Section 7.1, the results from the specimens with 2.3% cement and e = 0.90 (loose specimen) are shown. 7.2 section presents the experimental results following a second stress path rosette, where the amount of cement was 1.8% and the targeting void ratio was 0.71 (dense specimen). The comparison of both dosages is presented in 7.3. Section 7.4 contains the modelling prediction of the results. The small strains analysis is shown in the final 7.5 Section.

7.1 e=0.90 AND C=2.3%

The first series of hollow cylinder tests performed had the η/C_{iv} target of 47.2 obtained through a cement content of 2.3% in weight and a void ratio of 0.90. Eight tests were carried out on specimens with these characteristics. The difference between the tests was the direction of the principal stress, α, during loading conditions, while for one test, α, was controlled and maintained constant throughout the whole test. The angles α, during of the principal stress with the vertical direction were 0^o, 15^o, 30^o, 45^o, 60^o, 75^o and 90^o. The last test performed on this dosage was carried initially at an $\alpha = 0^o$ until q = 150kPa and then an $\alpha = 45^o$ was applied to the specimen. These eight different α were imposed in order to characterise the loading direction dependency of the artificially cemented material. Two triaxial compression tests ($\alpha = 0^o$) were performed, one under stress controlled conditions and other under strain controlled conditions for assessing the effects of the control type and also to have some indication about the post peak material response which cannot be accessible for a stress control mode. These two tests also allowed to explore the repeatability of testing and as shown in in Figure 7.1, a very good repeatability of the results was obtained.

It is observed that the stress-strain behaviour (Figure 7.1b) has great reproduction and the peak is the same, as shown in Figure 7.1a. An excellent repeatability of the volumetric response is also achieved (Figure 7.1c). The post peak behaviour is observed on the test conducted under

strain controlled. After reaching the peak of stress a reduction of this value is observed when loading continued.

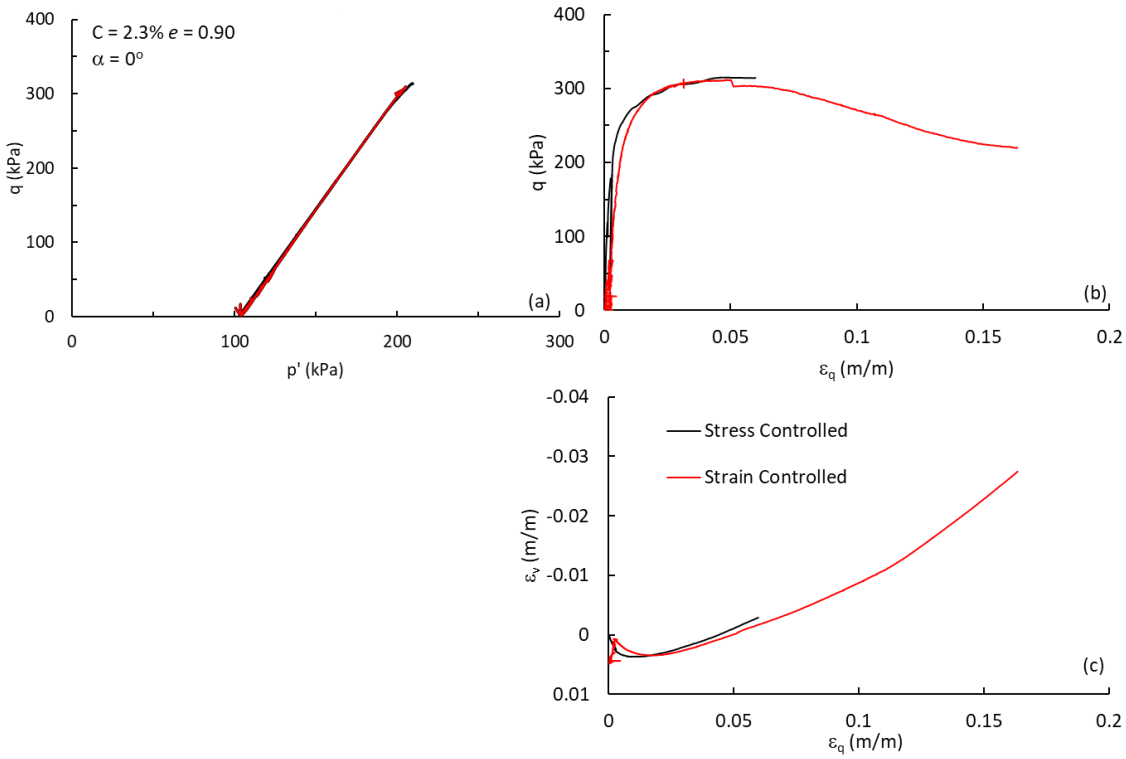


Figure 7.1 – Response of cemented sand (C = 2.3%, *e* = 0.90) with α = 0º under stress and strain controlled test

Seven tests with different α values were imposed on the specimens, and the whole combination of these tests is characterised as a "rosette". The results presented in Figure 7.2 refer to the samples prepared with *e* = 0.90 and 2.3% cement.

The variation of direction of the principal stress on the deviatoric stress is presented in Figure 7.2a. As α increases, there is a clear the effect of reduction the deviatoric stress response of the cemented material. It is also observed that when the specimens were exposed to extension and extension and torque (tests with α = 60º, 75º and 90º), shearing occurred with a smaller deviatoric strain in comparison with the tests where compression and torque were imposed.

Figure 7.2a presents the deviatoric stress versus deviatoric strain for all the tests performed. As tests were conducted on stress controlled, it is not possible to analyse the post peak behaviour of the samples.

Figure 7.2c presents the volumetric strain and deviatoric strain of samples. It is apparent that the initial volume response is progressively more compressive with the increase of α = 15º, 30º

and 0^o, respectively. After the initial compressive behaviour, a small dilatation is developing, and dilatation increases for $\alpha = 15^o$, 30^o and then decreases.

In order to evaluate the stress path in the conventional *q-p'* stress plane, Figure 7.2b is presented. All tests were isotopically consolidated under a pressure of 100 kPa. The trend clearly shows that the lower the α, the greater the shear stress resistance.

The test with an imposed $\alpha = 0^o$ and $\alpha = 15^o$ have similar behaviour. As expected, $\alpha = 0^o/45^o$ has similar initial behaviour in comparison to the test conducted with 0^o during loading on the compression triaxial. The tests performed 30^o, 45^o, 60^o, 75^o and 90^o present a reduction on the maximum load while α is increased. The curves of $\alpha = 90^o$ (triaxial extension) and 75^o shows similar behaviour in Figure 7.2b.

The effect of the rotation of the principal axes is the focus of Figure 7.2d. The imposed stress path is presented in the normalized shear stress-deviators stress plane. As expected, it is observed that the effect of extension on specimens ($\alpha = 60^o$, 75^o and 90^o) effect the maximum load resistance. This effect can be clearly observed in Figure 7.3, where increasing the alpha clearly reduces the deviator stress on the specimens tested.

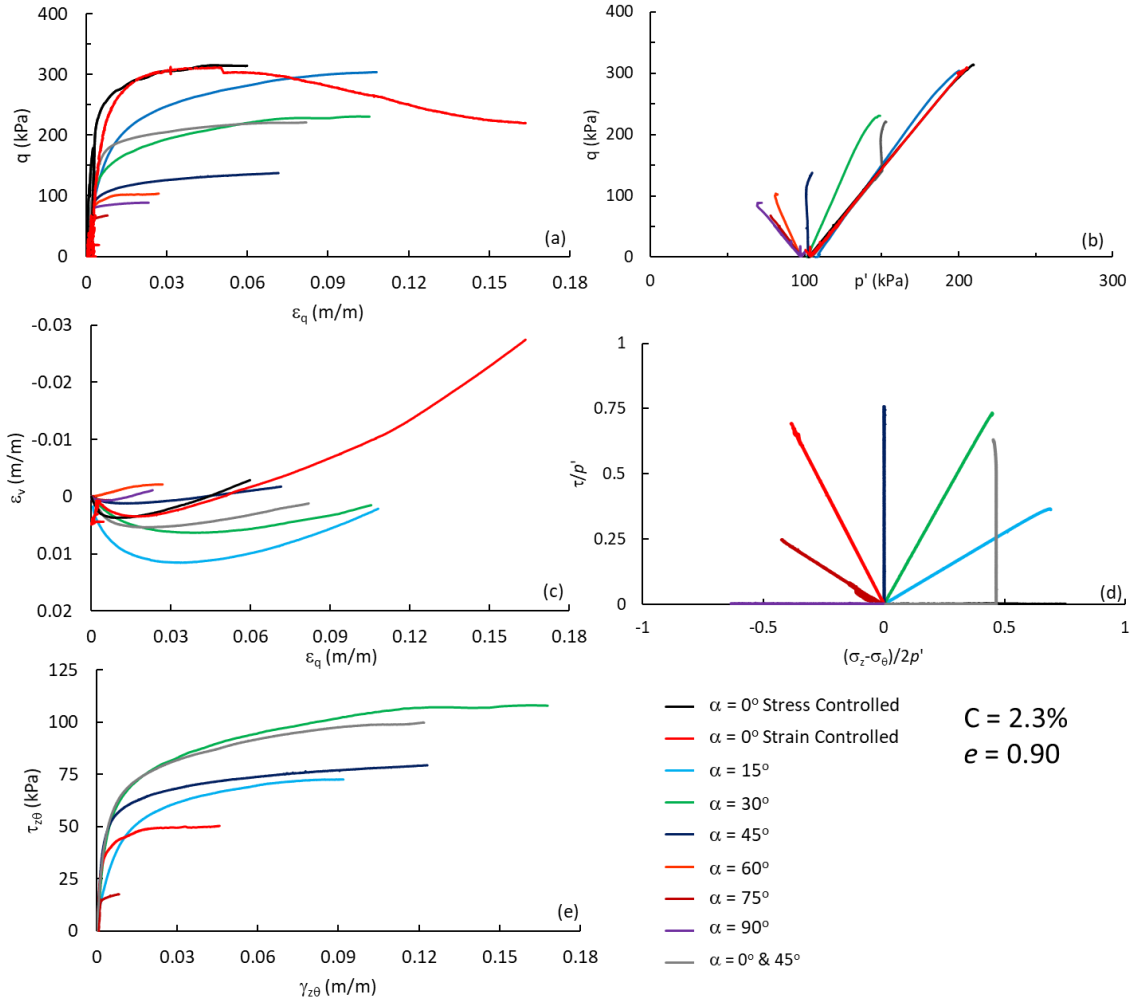


Figure 7.2 – Tests with e = 0.90 and C = 2.3%: (a) q versus ε_q; (b) q versus p'; (c) ε_v versus ε_q; (d) τ/p' versus $(\sigma_z - \sigma_\theta)/2p'$; (e) $\tau_{z\theta}$ versus $\gamma_{z\theta}$

The initial deviatoric strains, measured with the local non-contact measurement system, along with the initial deviatoric stress are presented in Figure 7.4. Figure 7.4a and b shows that the influence of axial stress and torque affect differently the vertical strain and the shear strain. The analysis of the small strains will be readdressed in Section 7.3.

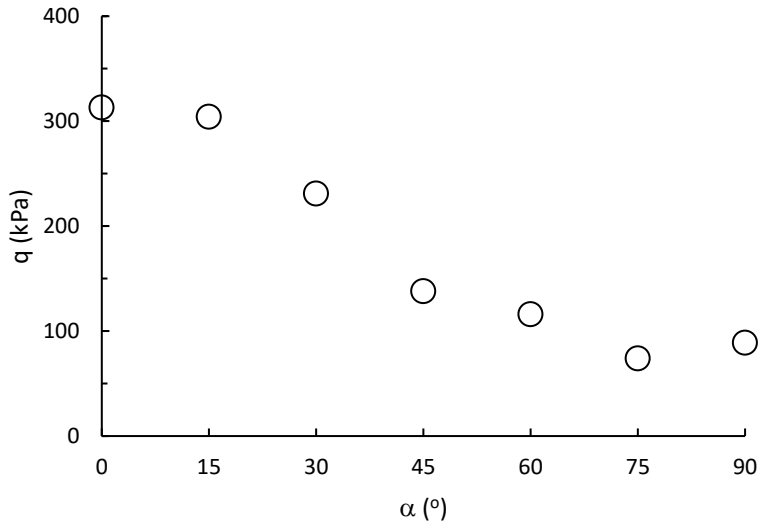


Figure 7.3 – Maximum deviatoric stress with the variation of principal stress direction

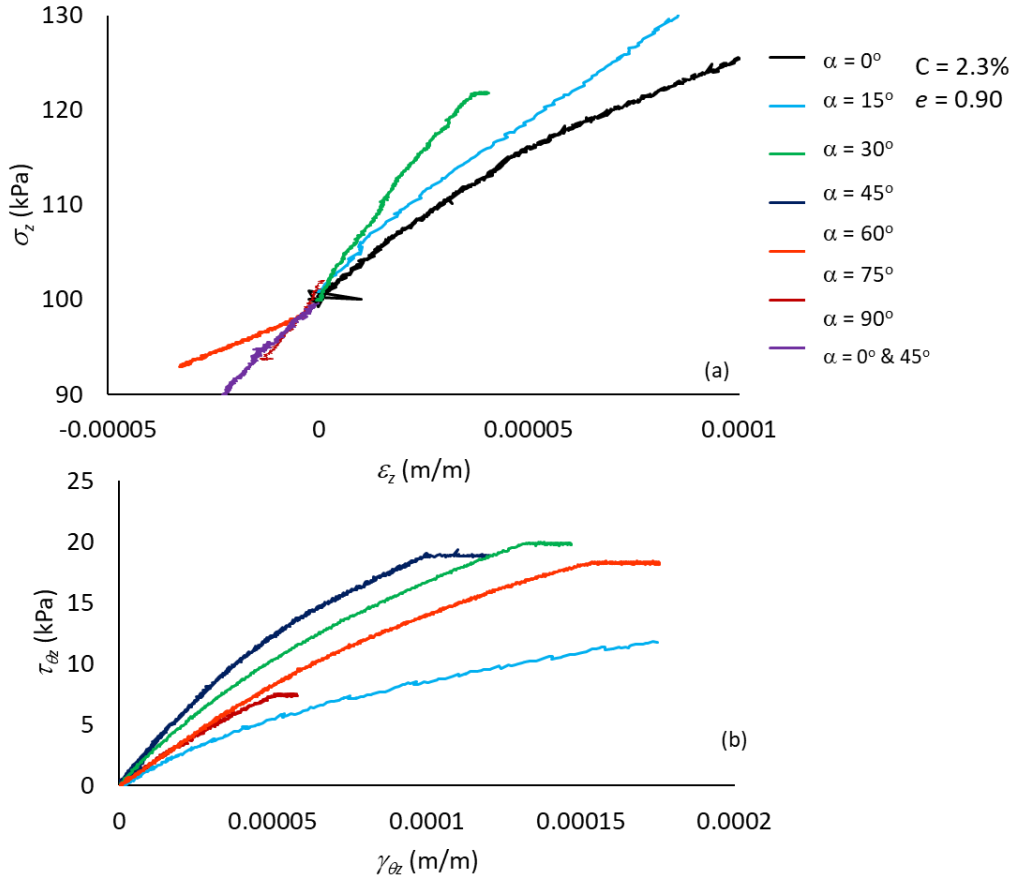


Figure 7.4 – Initial strains in the tests performed:
(a) σ_z versus ε_z; (b) q versus ε_q

Table 7.1 summarises the conditions of loading applied to each test, the direction of the principal stress, the void ratio obtained after a consolidation of 100kPa, the η/C_{iv} and the maximum deviator stress obtained on the test.

Table 7.1 – Specimens characteristics and loading conditions for the rosette HC1

α^o	*Loading type*	*b*	*C (%)*	e_{cons}	η/C_{iv}	σ'_c *(kPa)*	q_{max} *(kPa)*
0	Compression	0	2.3	0.87	48.3	103.3	313
0	Compression Strain Controlled	0	2.3	0.88	47.7	103.5	310
15	Compression + Torque	0.07	2.3	0.88	47.6	103.5	304
30	Compression + Torque	0.25	2.3	0.88	46.5	101.6	231
45	Torque	0.5	2.3	0.89	47.4	100.8	138
60	Extension + Torque	0.75	2.3	0.85	49.4	97.6	116
75	Extension + Torque	0.93	2.3	0.90	48.5	97.8	74
90	Extension	1	2.3	0.92	49.8	96.7	89
0 and 45	Compression Torque	0 / 0.5	2.3	0.89	48.1	105.4	214

7.2 e=0.71 AND C=1.8%

Similar to Section 7.1, this section will present the rosette of tests performed on the second dosage, again, targeting an η/C_{iv} of 47.2. The samples were prepared with a dry amount of cement at 1.8% in comparison of the total weight of sand. The void ratio for the samples was 0.71. Seven tests were performed on the Hollow Cylinder Apparatus with the angles of the principal stress of $\alpha = 0^o$, 15^o, 30^o, 45^o, 60^o, 75^o and 90^o.

In other to represent the repeatability of the results, the test with $\alpha = 0^o$ was performed twice, once with stress controlled and another with strain controlled, as presented in Figure 7.5. Figure 7.5a shows the *p'*x *q* behaviour of both tests performed. It is noticed that the initial mean stress was slightly higher for the stress-controlled test (106 kPa compared with 100 kPa), but the

behaviour observed is similar. No volume variation difference between both tests can be noticed in Figure 7.5c. The same statement is not valid when comparing the deviatoric strain and stress. Figure 7.5b shows that the test performed as strain controlled presented a slightly higher peak and modulus before the peak is reached. Nevertheless, both tests present very similar responses and a great repeatability on testing can be assured.

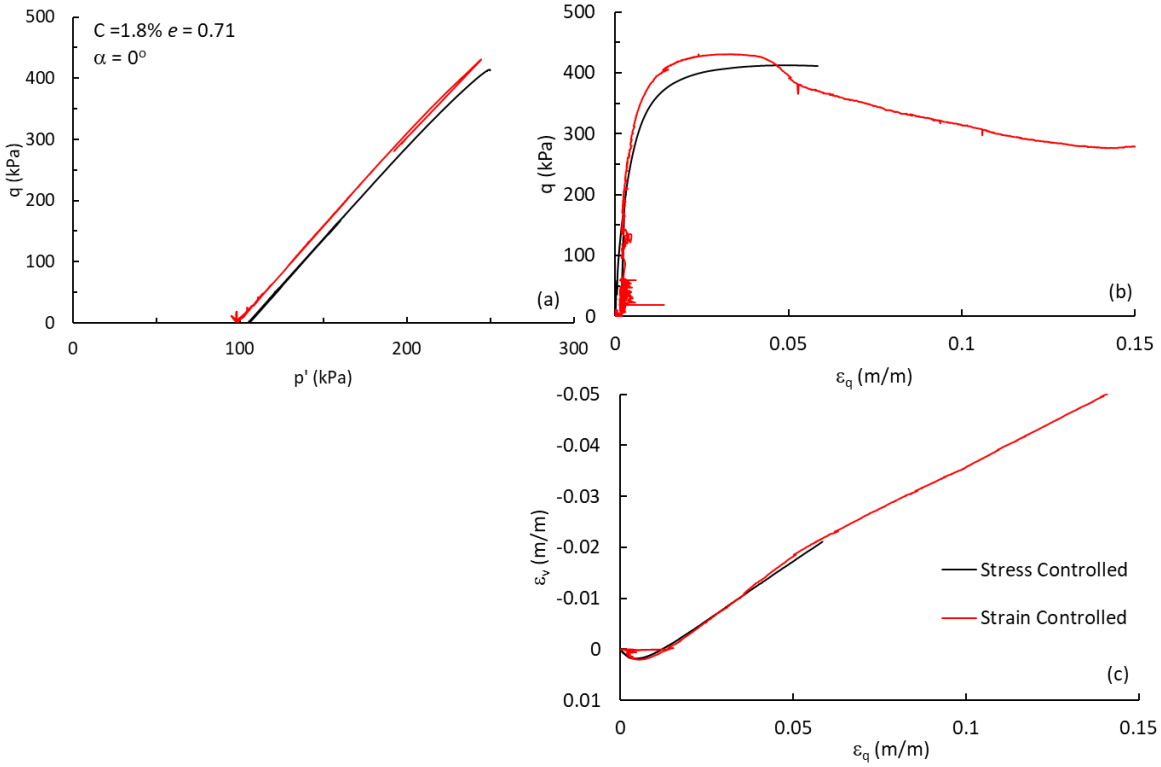


Figure 7.5 – Response of cemented sand (C = 1.8%, *e* = 0.71) with $\alpha = 0^o$ under stress and strain controlled test

Figure 7.6 expresses the influence of the rotation of the principal stress on the deviator stress-strain response. Again, for this rosette, the tests were carried as stress controlled, so it is not possible to see the post peak behaviour, except $\alpha = 0^o$. In Figure 7.6a, a similar initial stiffness can be observed from the tests, followed by the effect of the orientation of the principal stress on the maximum deviatoric stress supported by the samples.

The stress-strain behaviour for $\alpha = 0^o$ and 15^o is very similar and the maximum stress is also very close (Figure 7.6 a and b). The tests with $\alpha = 60^o$ and 75^o also present similar behaviour as these figures, but the rotation of 75^o of the principal stress results in a lower deviatoric stress.

When analysing the volumetric and deviatoric strain behaviour (Figure 7.6c), it is observed that samples $\alpha = 0^o$, 15^o and 30^o have similar behaviour. An initial compression is observed until

0.01 m/m and after that, a dilatancy is the result of the increment of strain. Figure 7.6c also shows that the tests present a trend of reduction of the volume, followed by expansion.

The conventional *q-p'* stress plane is presented in Figure 7.6b. As with the previous rosette, these tests were also consolidated at a pressure of 100kPa. The behaviour observed is similar to that which was obtained for C = 2.3%; by increasing the α, a tendency of reduction on the deviatoric stress is observed.

The rotation of the principal axes of cemented sample is the focus of Figure 7.6d. The imposed stress path is presented in the normalized shear stress-deviators stress plane. Again, it is observed that the effect of extension compression on samples ($\alpha = 60^o$, 75^o and 90^o) affect the maximum load resistance. This effect can be clearly observed in Figure 7.7, where increasing the α clearly reduces the deviator stress on the samples.

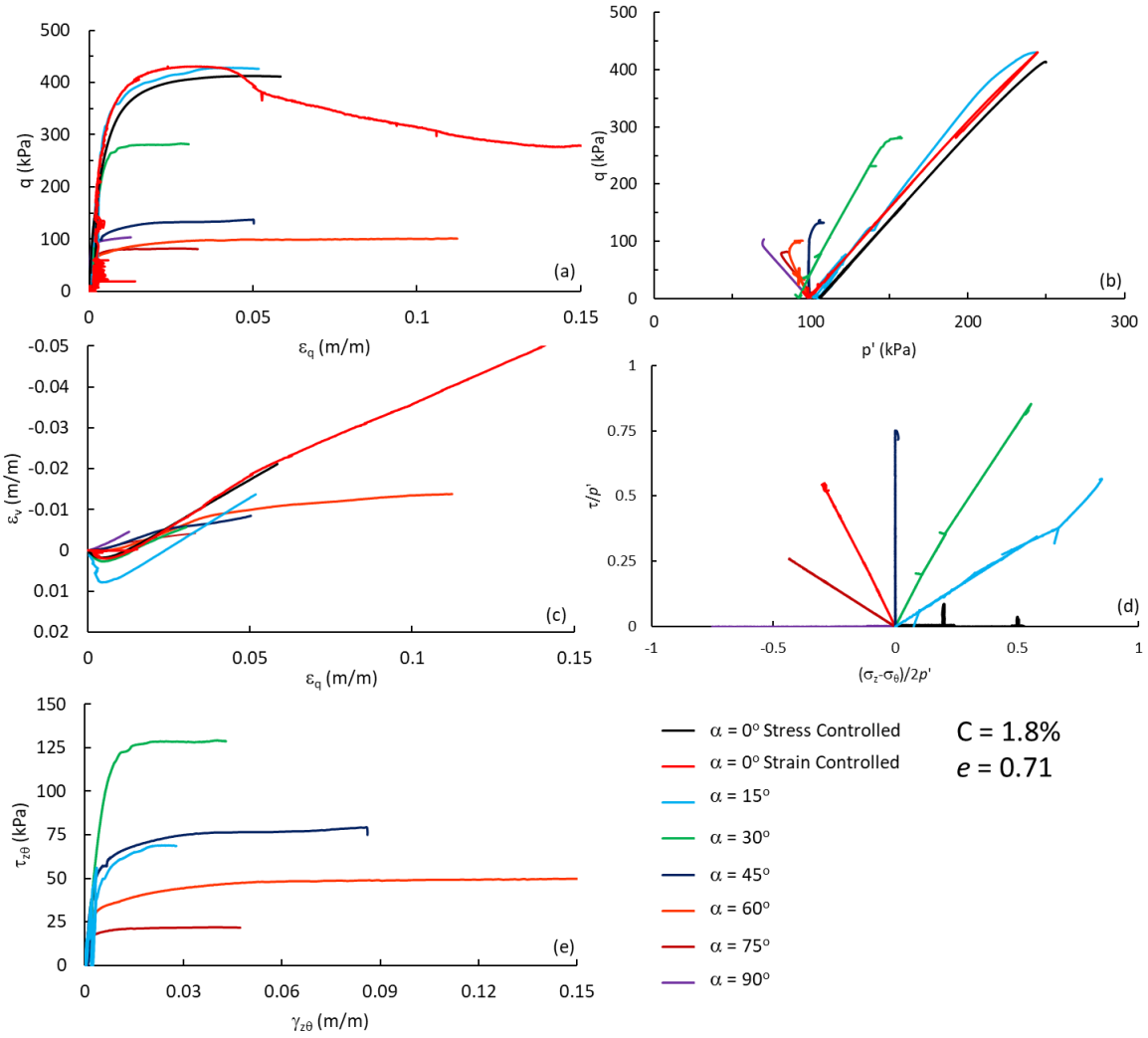


Figure 7.6 –e = 0.90 and C = 2.3%: (a) q versus ε_q; (b) q versus p'; (c) ε_v versus ε_q; (d) τ/p' versus $(\sigma_z - \sigma_\theta)/2p'$; (e) $\tau_{z\theta}$ versus $\gamma_{z\theta}$

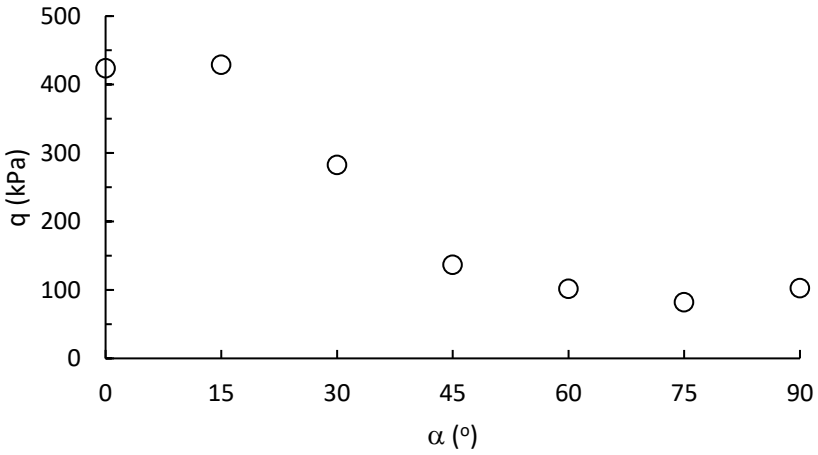


Figure 7.7 – Maximum deviatoric stress with the variation of principal stress direction

The initial deviatoric strains, measures with the inner contactless sensors, and the initial deviatoric stress are presented in Figure 7.8. Figure 7.8a and 7.8b shows that the influence of axial stress and torque differently affect the vertical strain and the shear strain.

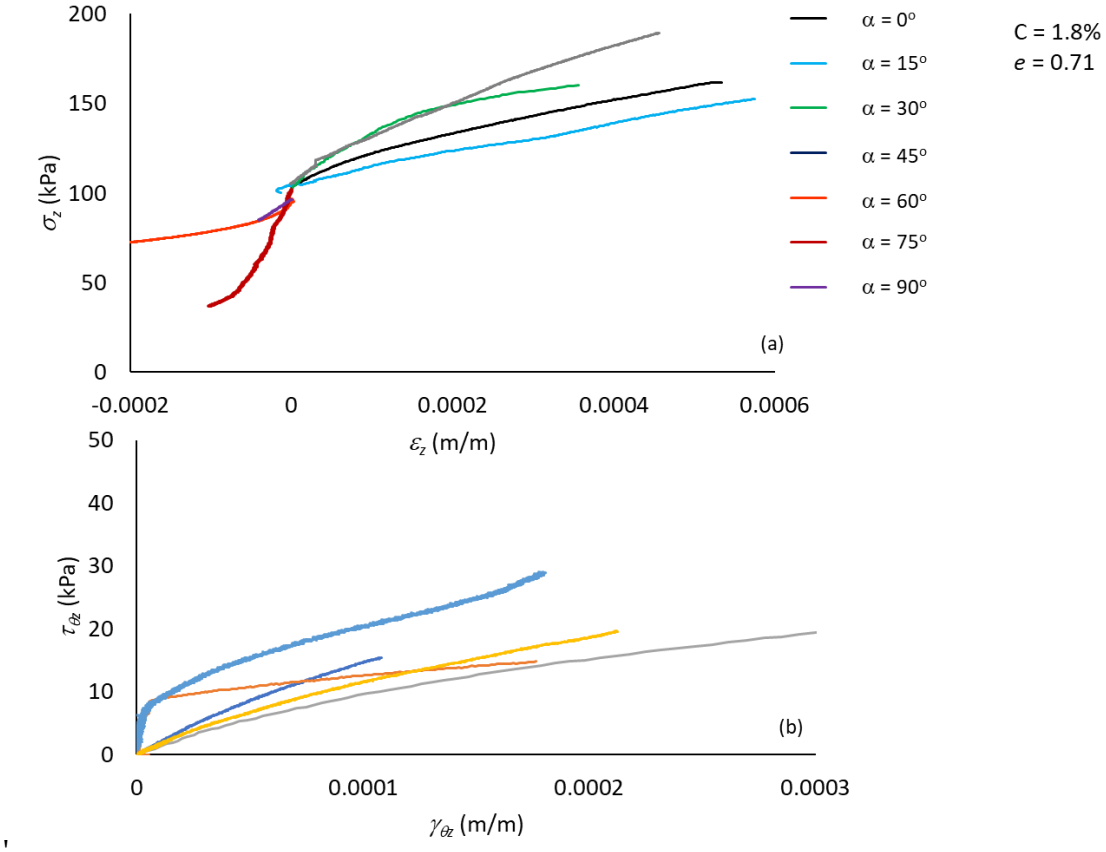


Figure 7.8 – Initial strains in the tests performed:
(a) σ_z versus ε_z; (b) q versus ε_q

Table 7.2 summarises the conditions of loading applied to each test, the direction of the principal stress, the void ratio obtained after a consolidation of 100kPa, the η/C_{iv} and the maximum deviator stress obtained from the test.

Table 7.2 – Samples characterises and loading conditions for the rosette HC2

α (^{o})	*Loading type*	*b*	*C* (%)	e_{cons}	η/C_{iv}	σ'_c (kPa)	q_{max} (kPa)
0	Compression	0	1.8	0.70	48.5	106.0	424
0	Compression Strain Controlled	0	1.8	0.71	48.2	100.0	431
15	Compression + Torque	0.07	1.8	0.71	52.0	100.0	429
30	Compression + Torque	0.25	1.8	0.70	50.0	92.0	283
45	Torque	0.5	1.8	0.71	50.6	98.7	137
60	Extension + Torque	0.75	1.8	0.71	49.3	98.8	102
75	Extension + Torque	0.93	1.8	0.70	48.8	102.5	82
90	Extension	1	1.8	0.71	50.8	99.3	103

7.3 ANALYSIS OF BOTH SAMPLE COMPOSITIONS

This section aims to compare the behaviour observed between the two specimens' characteristics. *HC1* had 2.3% cement content and a void ratio of 0.90 and *HC2* had 1.8% cement and a void ratio of 0.71.

Figures 7.9 to 7.12 present the deviatoric stress-strain behaviour of both specimens for each stress direction analysed. Up to α angles lower than 60^o, HC2 samples with lower amount of cement but denser show systematically higher deviator stresses compared with HC1 samples with higher cement content but lower density of the sand matrix. However, this trend reduces with the increase of α and similar maximum deviator stresses are recorded for both sample conditions for α angles higher than 60^o. This behaviour can be summarised by the results in Figure 7.13.

Figure 7.9 presents the results comparing the tests performed with $\alpha = 0^o$. Figures 7.2a and 7.2b refer to the stress-controlled tests, while 7.2c and 7.2d show the results of the tests conducted under strain-controlled tests. The rates of deviatoric stress observed in the tests are different, but it can be noticed that the peak is reach in the same deviatoric strain for each pair of tests.

The volumetric behaviour is also different between the tests, but the peak of compression behaviour is also observed in the same deviatoric strain.

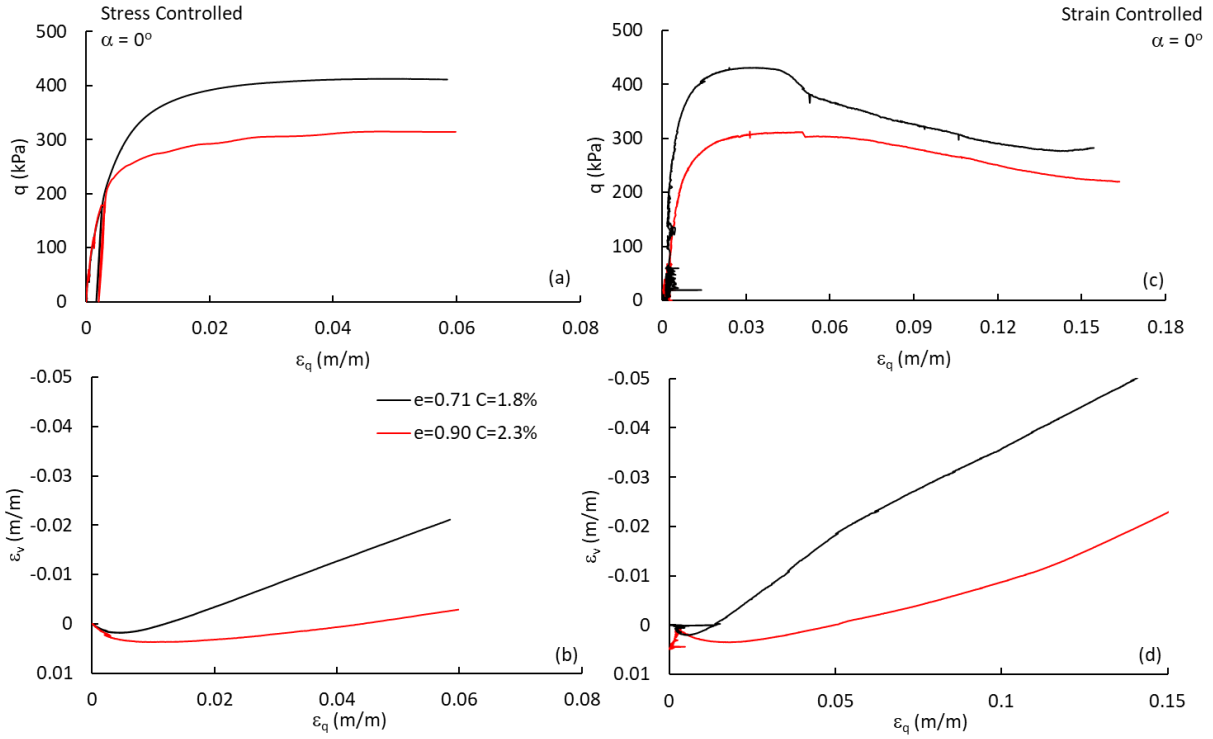


Figure 7.9 – Comparison response of the tests performed with $\alpha = 0^o$

When comparing the tests performed with $\alpha = 15^o$, it is observed that the maximum deviatoric strain in the HC2 is significantly higher than the test HC1. The volumetric behaviour of these tests is also very distinguishable, as showed in Figure 7.10b. HC1 did not present clear expansion, while HC2 starts dilating at a deviator strain of 0.005 m/m.

The difference in the deviatoric stress is not evident when analysing the tests performed with $\alpha = 30^o$. The peaks of these two tests are close (Figure 7.10c) while the volumetric strain in Figure 7.10d follows the same behaviour as presented in Figure 7.10b.

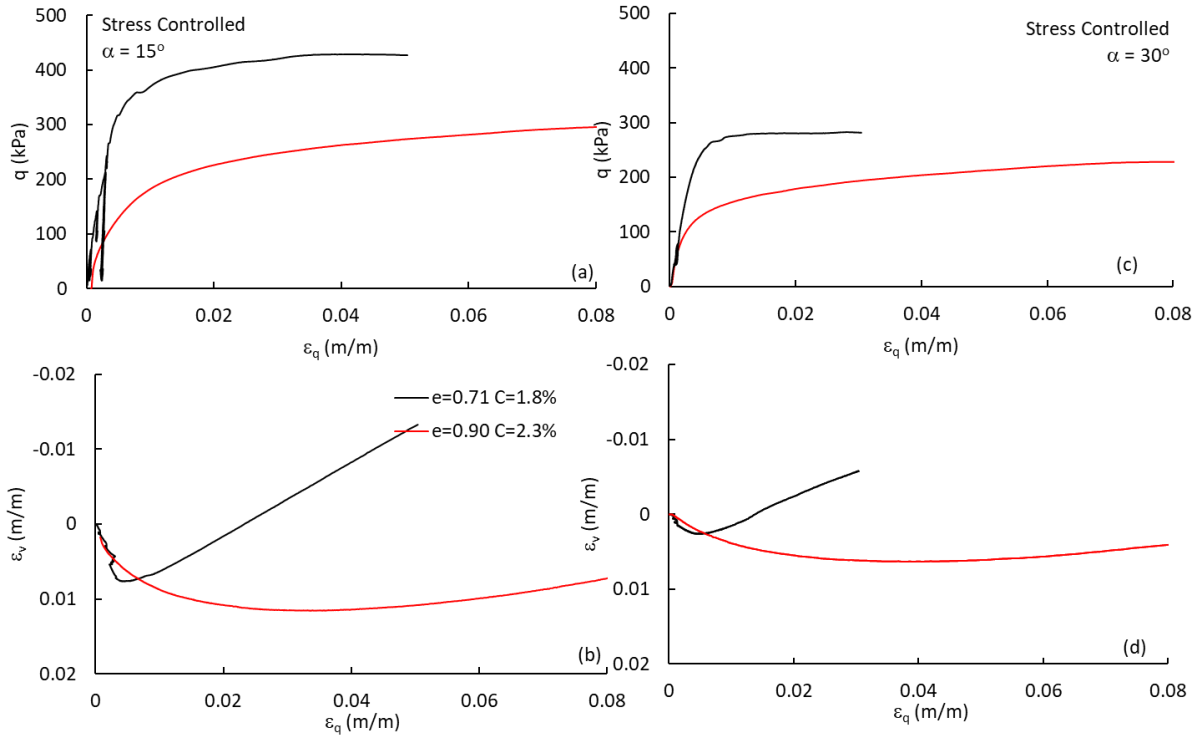


Figure 7.10 – Comparison response of tests with α = 15° and 30°

The pure torque test, α = 45°, presented in Figure 7.11 a and b, shows that the deviatoric strain in HC1 and HC2 are very similar. The deviatoric strain behaviour with the evolution of the deviatoric stress is also similar. However, the differences in the behaviour can be noticed when the volumetric strain responses of both tests are compared. Figure 7.11b shows that volumetric strain response is not significant for the loose sample (HC1), while dilation is observed in the dense sample (HC2).

When stress path with α = 60° and 75° are imposed to the cemented samples, both torque and extension are induced in the soil and the deviatoric stress appears to be very similar in both sample compositions. Figures 7.11c and 7.12a shows the deviatoric stress versus deviatoric strain responses. The analysis of the volumetric strain shows that HC1 did not present change in volume (Figure 7.11d) while HC2 shows a dilative response. In Figure 7.12b, a small dilation is observed in both sample compositions.

Figure 7.12c and 7.12d presents the results performed with α = 90°. These extension tests present a higher peak response showed by HC2. The same behaviour is expressed when the volume change is evaluated.

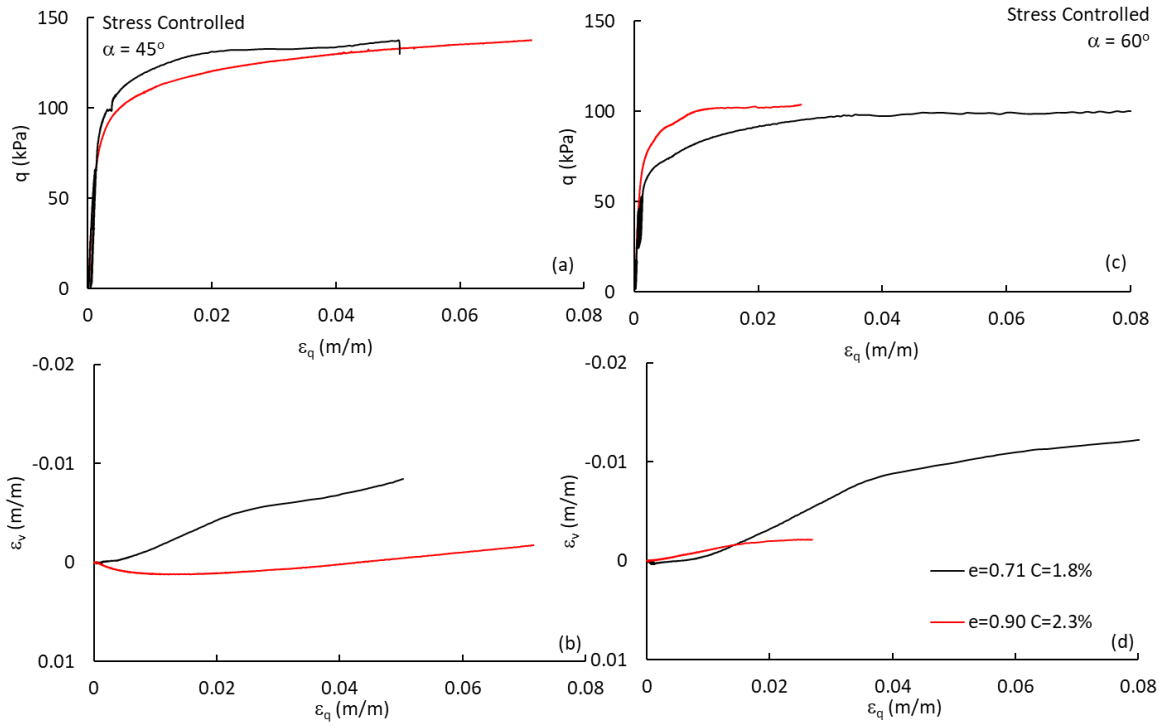


Figure 7.11 – Comparison response of tests with α = 45° and 60°

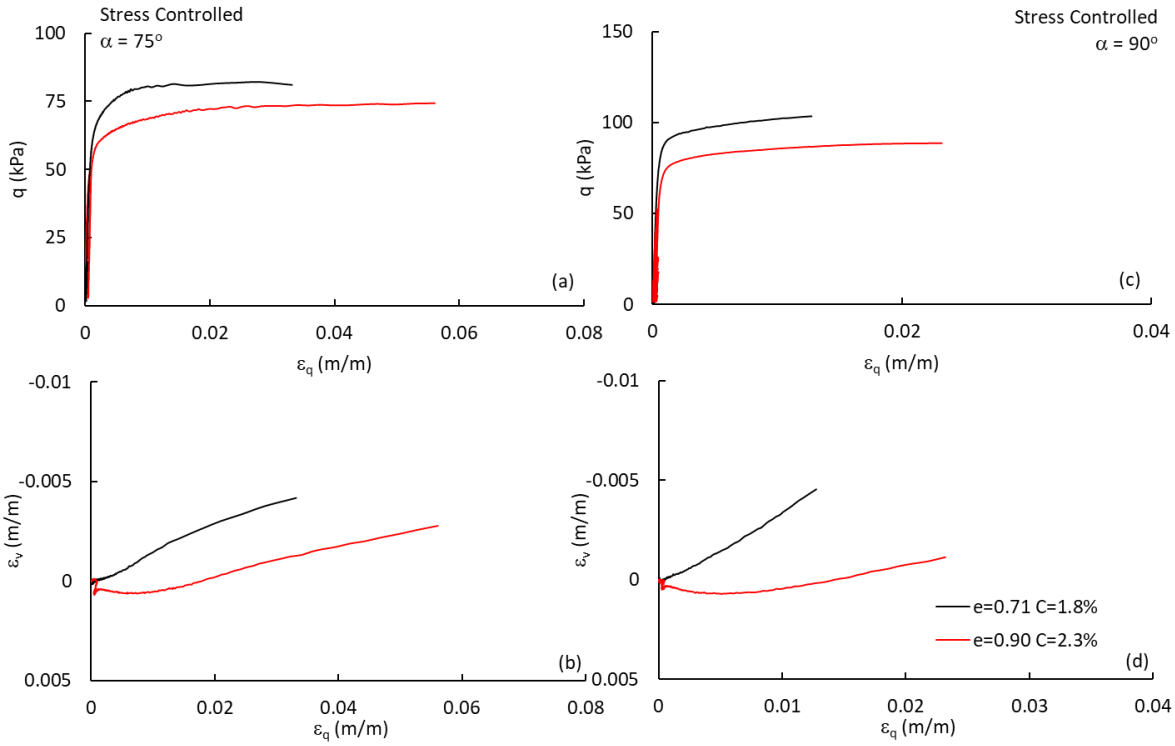


Figure 7.12 – Comparison response of tests with α = 75° and 90°

Figure 7.13 represents the maximum deviatoric stress of both sample compositions functions of the angle α for all the tests. It is observed that with the increase of α, the difference in both

sample compositions response reduces and from 45º, the results in both sets of tests are comparable.

This difference in the deviatoric strength of the tests is credited to the void ratio variation during the consolidation of the samples. While the dense sample prepared with e = 0.71 had almost no void change during consolidation phase, the loose samples with e = 0.90 presented an average of 4% reduction of the void ratio. During pure torque and toque + extension, it is noticed a similarity in the maximum deviatoric stress reached, as HC1 and HC2 were prepared with the same η/C_{iv} but with distinguishable compositions; the result is a similar peak of stress but the behaviour during the shear is different. While HC1 exhibits behaviours of a loose sand when the volume change is analysed, HC2 behaves as a dense sand.

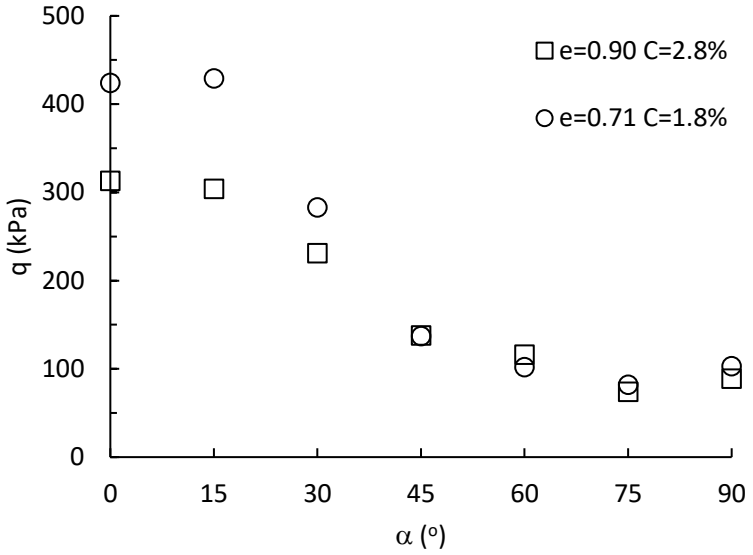


Figure 7.13 – Deviatoric stress with principal stress direction

Figures 7.14 and 7.15 present the direct comparison between both cemented samples. The strength envelope is represented with the peak readings for each test and they are normalized by $p'(\tau_{z\theta}/p' - (\sigma_z-\sigma_\theta)/2p')$ in Figure 7.15, while 7.14 presents the values that are not normalized. The difference between both envelopes is noticeable. The reduction of cement content combined to a higher void ratio on HC2 results in a bigger size envelope, especially for the compressions tests. When analysing Figure 7.14, α = 45º, 60º, 75º and 90º, the response between HC1 and HC2 is similar. The only test where the combination of HC1 higher values than HC2 was for α = 60º – when normalized.

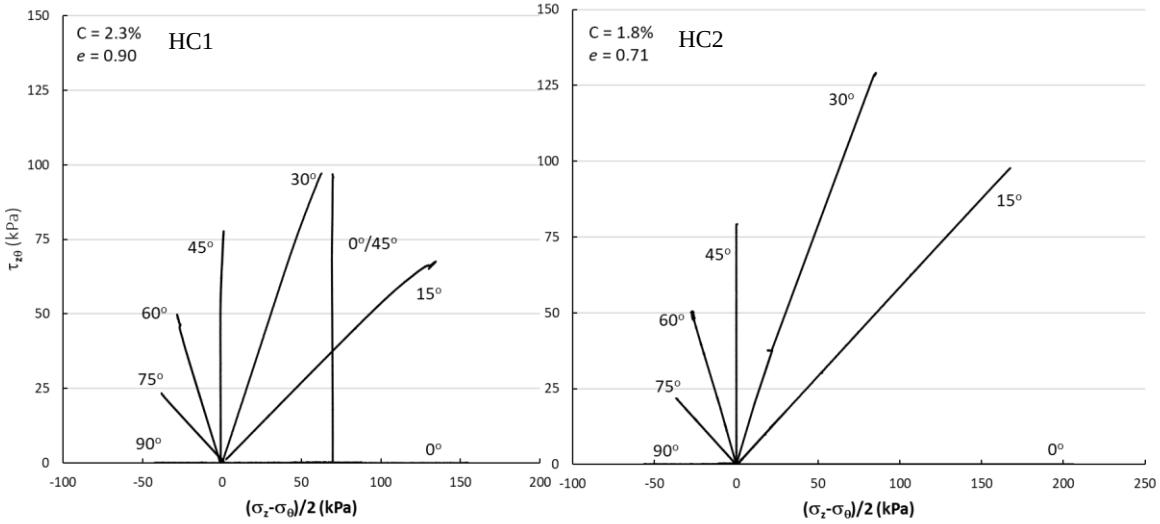


Figure 7.14 – Comparison on the rosettes of HC1 (e=0.90, C=2.3%) and HC2 (e=0.71, C=1.8%)

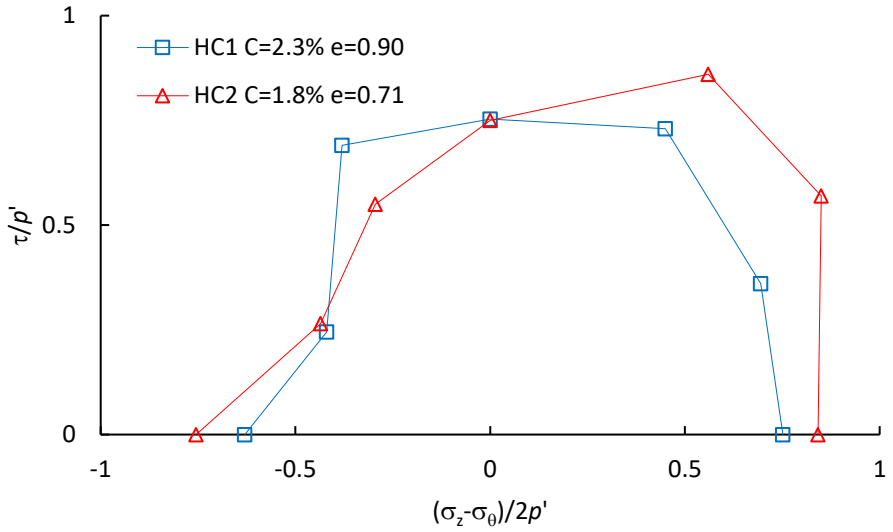
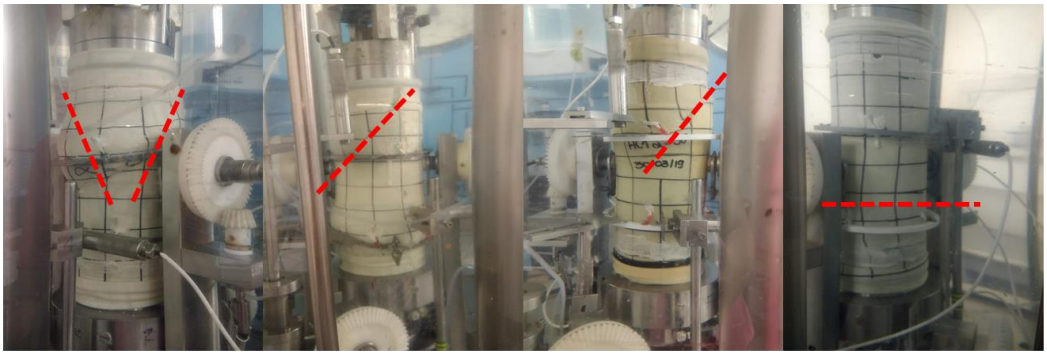
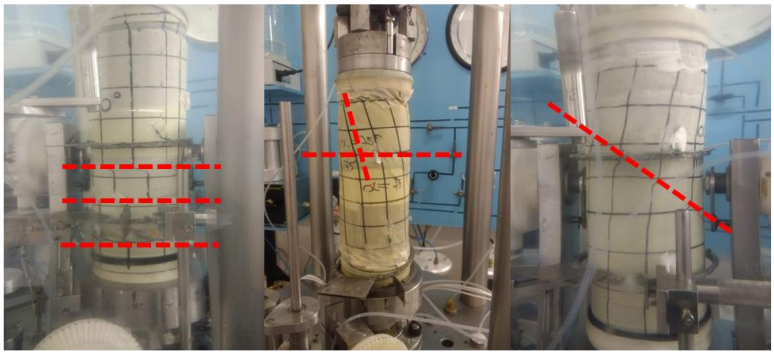


Figure 7.15 – Comparison on the rosettes normalized of HC1 (e=0.90, C=2.3%) and HC2 (e=0.71, C=1.8%)

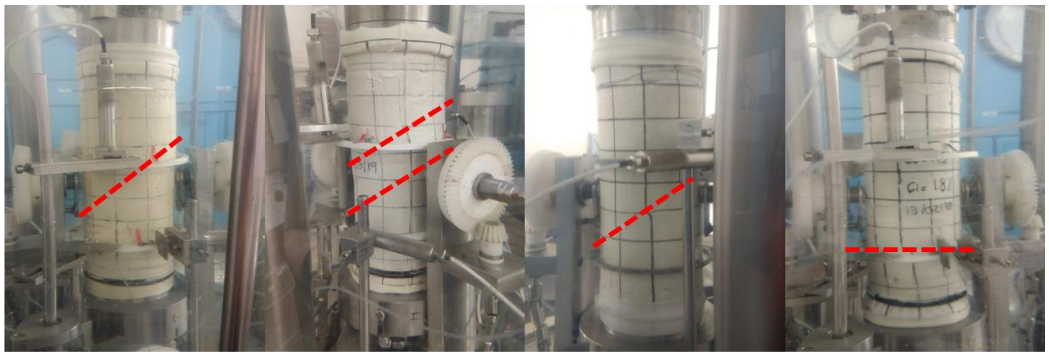
Figure 7.16 presents the samples at the end of shearing. The formation of shear bands visually observed upon failure are marked with red dashed lines in the figure.



e=0.90 C=2.3% α = 0⁰ | e=0.90 C=2.3% α = 15⁰ | e=0.90 C=2.3% α = 30⁰ | e=0.90 C=2.3% α = 45⁰



e=0.90 C=2.3% α = 60⁰ | e=0.90 C=2.3% α = 75⁰ | e=0.90 C=2.3% α = 0/45⁰



e=0.71 C=1.8% α = 0⁰ | e= 0.71 C=1.8% α = 15⁰ | e= 0.71 C=1.8% α = 30⁰ | e= 0.71 C=1.8% α = 45⁰



e= 0.71 C=1.8% α = 60⁰ | e= 0.71 C=1.8% α = 75⁰ | e= 0.71 C=1.8% α = 90⁰

Figure 7.16 – Pictures of the cemented samples at the end of shearing

7.4 FAILURE ENVELOPE

The deviatoric strength rosette for the two sets of tests on cemented sand specimens is presented in Figure 7.15 in the (τ/p'-(σ_z-σ_θ)/2p') normalised stress plane. In this case, the selected stress state corresponds with the peak values of deviatoric strain. For the sake of completeness, a range of different failure criteria has been examined such as Drucker-Prager (GAJO & WOOD, 1999), Lade (LADE & DUNCAN, 1975) and Matsuoka and Nakai (1974), finding that Matsuoka-Nakai expresses a satisfactory fit with the experimental stress state (Figure 7.17).

The Matsuoka-Nakai failure criterion (MATSUOKA & NAKAI, 1974) has been fitted to this set of tests but a unique value of friction angle was not found satisfactory to match the experimental data. For the curve presented, a friction angle is ϕ'= 33°, but it seems not to perfectly represent the results for HC1 set of results. Lade failure criterion (LADE & DUNCAN, 1975) presents a similar behaviour in comparison to the prediction from Matsuoka-Nakai and diverges when extension takes place. Drucker-Prager does not consider the anisotropy of the cemented samples, so the behaviour on extension is predicted to be similar to compression.

The analysis of Figures 7.14 and 7.15 also confirms a marked anisotropic strength for the cemented specimens. Also, the behaviour of HC1 and HC2 tends to be similar as α evolves.

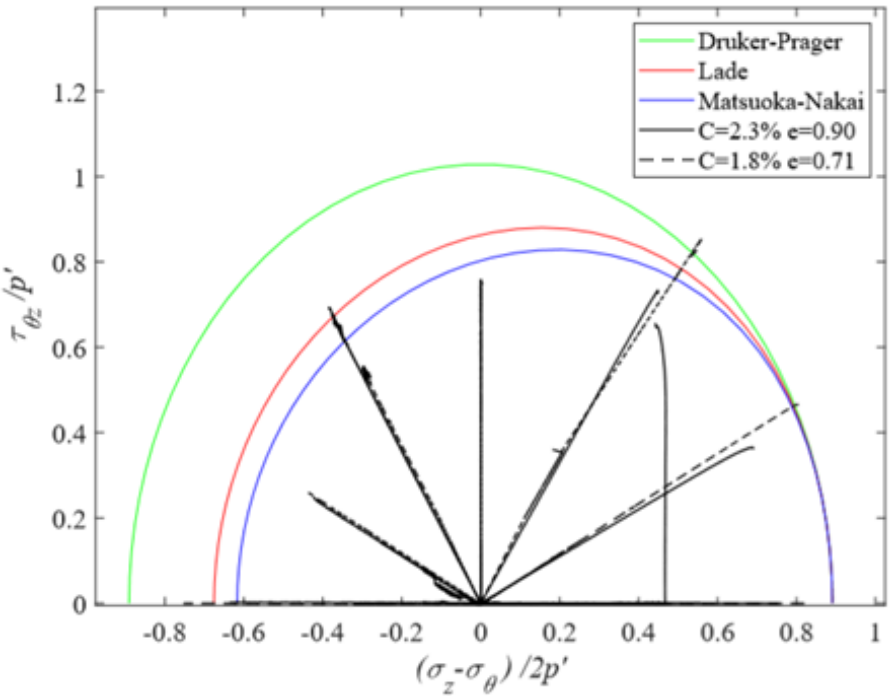


Figure 7.17 – Comparison of experimental rosette and Drucker-Prager, Lade and Matsuoka-Nakai failure criterion

7.5 SMALL STRAIN STIFFNESS

This section presents the results of the experimental programme carried out to investigate the response of the studied cemented sand under cyclic loading of small amplitude for the determination of stiffness and stiffness evolution with the stress and strain states. This testing phase focused on investigating the effect of loading direction by imposing either pure axial or torsional cyclic loading. Small strain stiffness was monitored throughout experimental tests using a local measurement system comprising six non-contact sensors able to measure strains up to 10^{-5}.

7.5.1 Compliance matrix

For a linear elastic material, the relationship between strain, $[\varepsilon^e_{ij}]$, and effective stress tensors, $[\sigma'_{kl}]$, is described by the equation $[\varepsilon^e_{ij}] = [C^e_{ijkl}]\ [\sigma'_{kl}]$, where $[C^e_{ijkl}]$ is the stress state-independent elastic compliance matrix. For a hypoelastic material, this constitutive equation is valid only in terms of stress and strain increments, and takes the form $[d\varepsilon^e_{ij}] = [(C_1)^e_{ijkl}]\ [d\sigma'_{kl}]$, where $[(C_1)^e_{ijkl}]$ is assumed to be symmetrical and independent of the effective stress increment path (provided the stress increments are sufficiently small), but dependent on stress state or stress history (IBRAIM et al., 2011).

For an isotropic material, only two elastic constants, Young's modulus (E) and Poisson's ratio (ν) are required to describe the terms of the compliance matrix. However, a general description of an anisotropic elastic material requires 36 independent parameters (Equation 7.1), which become 21 with the assumption of a symmetrical compliance matrix or 9 for orthotropic behaviour.

Many soils deposited naturally or in artificial conditions exhibit cross-anisotropic deformation properties, which are symmetrical across the vertical axis. Cross-anisotropy requires only five independent elastic parameters for the characterisation of soil properties: E_v, E_h, ν_{vh}, ν_{hh} and G_{vh}, where 'v', 'h' and G represent, respectively, the vertical direction, the horizontal directions and the shear modulus. Even for this latter model, only limited experimental data are available for the full compliance matrix $[(C_1)^e_{ijkl}]$ (BELLOTTI et al. 1996; FIORAVANTE, 2000; LINGS et al., 2000; CHAUDHARY et al., 2004; KUWANO & JARDINE, 2002; DUTTINE et al., 2007).

It is assumed that the elastic properties of soil are dependent on its mode of deposition and its stress history. A soil deposited vertically (e.g., sedimentation) and subjected to equal horizontal stresses (i.e., one-dimensional compression) over long periods of time can be expected to exhibit a vertical axis of symmetry and be cross anisotropic (or transversely isotropic) (CHAUDHARY et al., 2004). A sand specimen prepared in the laboratory by free fall gravity usually exhibits cross-anisotropy with the isotropic horizontal plane similar to natural soils (PARKIN et al., 1968; ARTHUR & MENZIES, 1972; ODA & KOISHIKAWA, 1979; FIORAVANTE & CAPOFERRI, 2001). The stress-strain relationship of a cross-anisotropic material within the elastic limit may be expressed as (LOVE, 1927):

$$\begin{bmatrix} \Delta\varepsilon_x \\ \Delta\varepsilon_y \\ \Delta\varepsilon_z \\ \Delta\gamma_{yz} \\ \Delta\gamma_{zx} \\ \Delta\gamma_{xy} \end{bmatrix} = \begin{bmatrix} \frac{1}{E_h} & -\frac{\nu_{hh}}{E_h} & -\frac{\nu_{vh}}{E_v} & 0 & 0 & 0 \\ -\frac{\nu_{hh}}{E_h} & \frac{1}{E_h} & -\frac{\nu_{vh}}{E_v} & 0 & 0 & 0 \\ -\frac{\nu_{hv}}{E_h} & -\frac{\nu_{hv}}{E_h} & \frac{1}{E_v} & 0 & 0 & 0 \\ 0 & 0 & 0 & \frac{1}{G_{vh}} & 0 & 0 \\ 0 & 0 & 0 & 0 & \frac{1}{G_{vh}} & 0 \\ 0 & 0 & 0 & 0 & 0 & \frac{1}{G_{hh}} \end{bmatrix} \begin{bmatrix} \Delta\sigma'_x \\ \Delta\sigma'_y \\ \Delta\sigma'_z \\ \Delta\tau_{yz} \\ \Delta\tau_{zx} \\ \Delta\tau_{xy} \end{bmatrix} \tag{7.1}$$

where,

E_v = Young's modulus in the vertical direction

E_h = Young's modulus in the horizontal direction

ν_{vh} = Poisson's ratio for the effect of vertical strain on horizontal strain

ν_{hv} = Poisson's ratio for the effect of horizontal strain on vertical strain

ν_{hh} = Poisson's ratio for the effect of horizontal strain on complementary horizontal strain

G_{vh} = Shear modulus in any vertical plane

G_{hh} = Shear modulus in any horizontal plane

Subscripts *x* and *y* represent orthogonal axes in the horizontal plane and the subscript *z* represents vertical axis perpendicular to the horizontal plane.

When performing a test on a Hollow Cylinder apparatus, the stress conditions imposed were presented in Figure 4.20. The torsional shear stress, $\tau_{z\theta}$, can be applied to the specimen in addition to the normal stresses: vertical stress, σ_z, circumferential stress, σ_θ, and radial stress, σ_r. They can be controlled independently by independent control of the torque, *MT*, axial load, *W*, inner cell pressure, p_i, and outer cell pressure, p_o. This allows control of the direction of the major principal stress, σ_1, at any angle from the vertical to the horizontal.

The incremental stress-strain relationship of Eq 7,1 can be rewritten in terms of cylindrical co-ordinates (*r*-θ-*z* space) for a hollow cylinder specimen as:

$$\begin{bmatrix} \Delta\varepsilon_z \\ \Delta\varepsilon_r \\ \Delta\varepsilon_\theta \\ \Delta\gamma_{z\theta} \end{bmatrix} = \begin{bmatrix} \frac{1}{E_z} & -\frac{\nu_{rz}}{E_r} & -\frac{\nu_{\theta z}}{E_\theta} & 0 \\ -\frac{\nu_{zr}}{E_z} & \frac{1}{E_r} & -\frac{\nu_{\theta r}}{E_\theta} & 0 \\ -\frac{\nu_{z\theta}}{E_z} & -\frac{\nu_{r\theta}}{E_r} & \frac{1}{E_\theta} & 0 \\ 0 & 0 & 0 & \frac{1}{G_{z\theta}} \end{bmatrix} \begin{bmatrix} \Delta\sigma'_z \\ \Delta\sigma'_r \\ \Delta\sigma'_\theta \\ \Delta\tau_{z\theta} \end{bmatrix} \tag{7.2}$$

where *x* and *y* have been replaced by *r* and θ, respectively. The *r*-θ plane represents the horizontal isotropic plane, whereas *z*-θ and *z*-r represent vertical anisotropic planes.

All the stress components in Eq. 7.2 can be applied or controlled independently, and the corresponding strains can subsequently measure. Therefore, all the five independent parameters of cross-anisotropy (E_z, E_θ, $\nu_{z\theta}$, $\nu_{\theta r}$, and $G_{z\theta}$) can be measured in the hollow cylinder apparatus. However, iun this thesis only some terms of this compliance matrix are determined.

7.5.2 Stress paths

A common test procedure for small strain and evolution of the quasi-elastic properties involves two stages. The first one is a monotonic loading which brings the specimen to a deformed stage. At the second stage, the behaviour of the specimen in the small strain domain is studied by

application of a quasi-static cyclic loading of small amplitude. These steps are then repeated up to large strains.

Each test presented in 7.1 and 7.2 had its small strain measurements performed at a different positions during the whole test. Before any loading, at the end of the consolidation, the first measurements were made. At each investigation point, unload-reload cycles of relatively low amplitudes were applied independently in both axial and torsional directions.

During the application of the torsional cycles, all the vertical, radial and circumferential stresses were maintained at a constant with the vertical stress corresponding to the current level attained at the investigation point. A similar condition was applied when axial cycles were imposed. At all investigation points, a number of 10 successive cycles were applied for each $\Delta\sigma_z$ half-cycle amplitude of ±2.5kPa, ±5kPa, and ±10kPa, followed by 10 cycles for each $\Delta\tau_{z\theta}$ half-cycle amplitude of ±2.5kPa, ±5kPa, and ±10kPa. The frequency of the small cycles was 0.1Hz.

At each stage, a creep test of 30 minutes was applied to allow all creep formations to be fully consimed. Figure 7.18 details the test stages during shearing: loading, creep and cycling. An example of the cycles applied at each stage are presented in Figure 7.19.

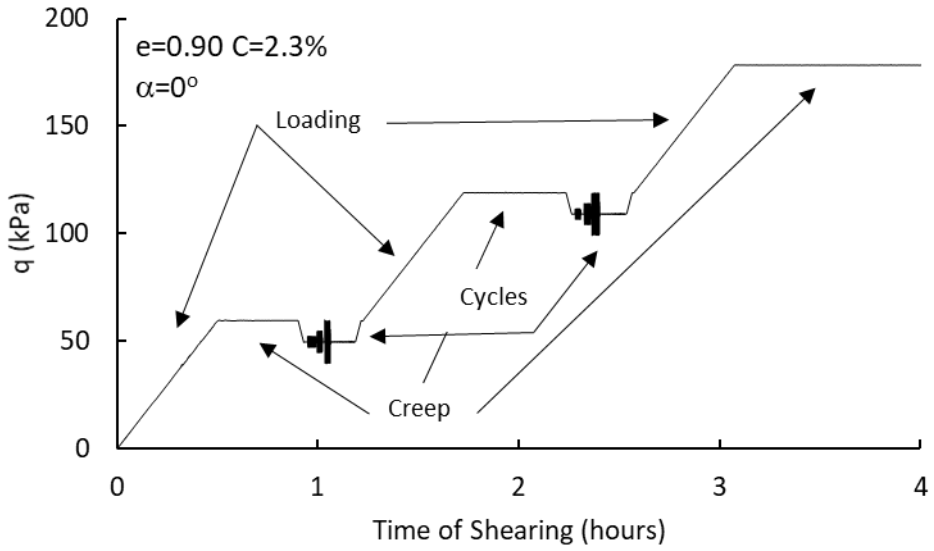


Figure 7.18 – Detailing loading stages of testing

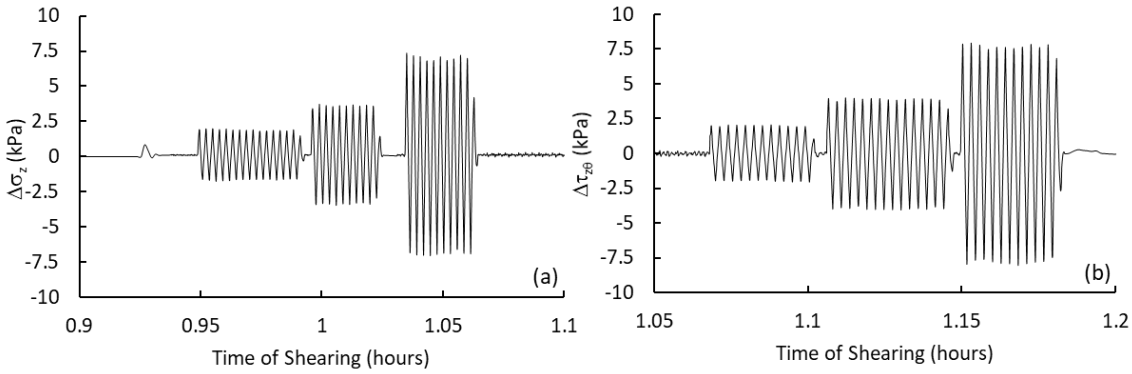


Figure 7.19 – Cyclic amplitudes imposed at each stage: (a) axial cycles and (b) torque cycles

7.5.3 Effect of the cycle's amplitude

It is clear that the region of stress or strain in which soils might be described as perfectly elastic is very small corresponding to strain levels of the order of 10^{-8}-10^{-6} m/m (JARDINE, 1992; TATSUOKA & SHIBUYA, 1992). As the strain level increases beyond the elastic zone, the soil stiffness rapidly falls off (LO PRESTI et al., 1997; CLAYTON & HEYMANN, 2001).

In order to guarantee that the measurements were correctly made in the elastic or quasi-elastic zone, three small amplitudes were imposed and analysed. The results are presented referring to the Young's moduli or shear moduli versus $(\varepsilon_z)_{sa}$ or $(\gamma_{z\theta})_{sa}$, where the subscript 'sa' means 'simple amplitude' which is taken as the half of double amplitude of quasi-static cyclic strain.

When the small cycles were applied at different investigation points, the result was three Young's moduli and three shear moduli to each stage of loading. As discussed previously, the variation of the amplitude of the cycles did not represent a significant variation of the moduli found to each point. Figure 7.20 presents the results obtained for stage (II) for the test HC2 $\alpha=0^{o}$.

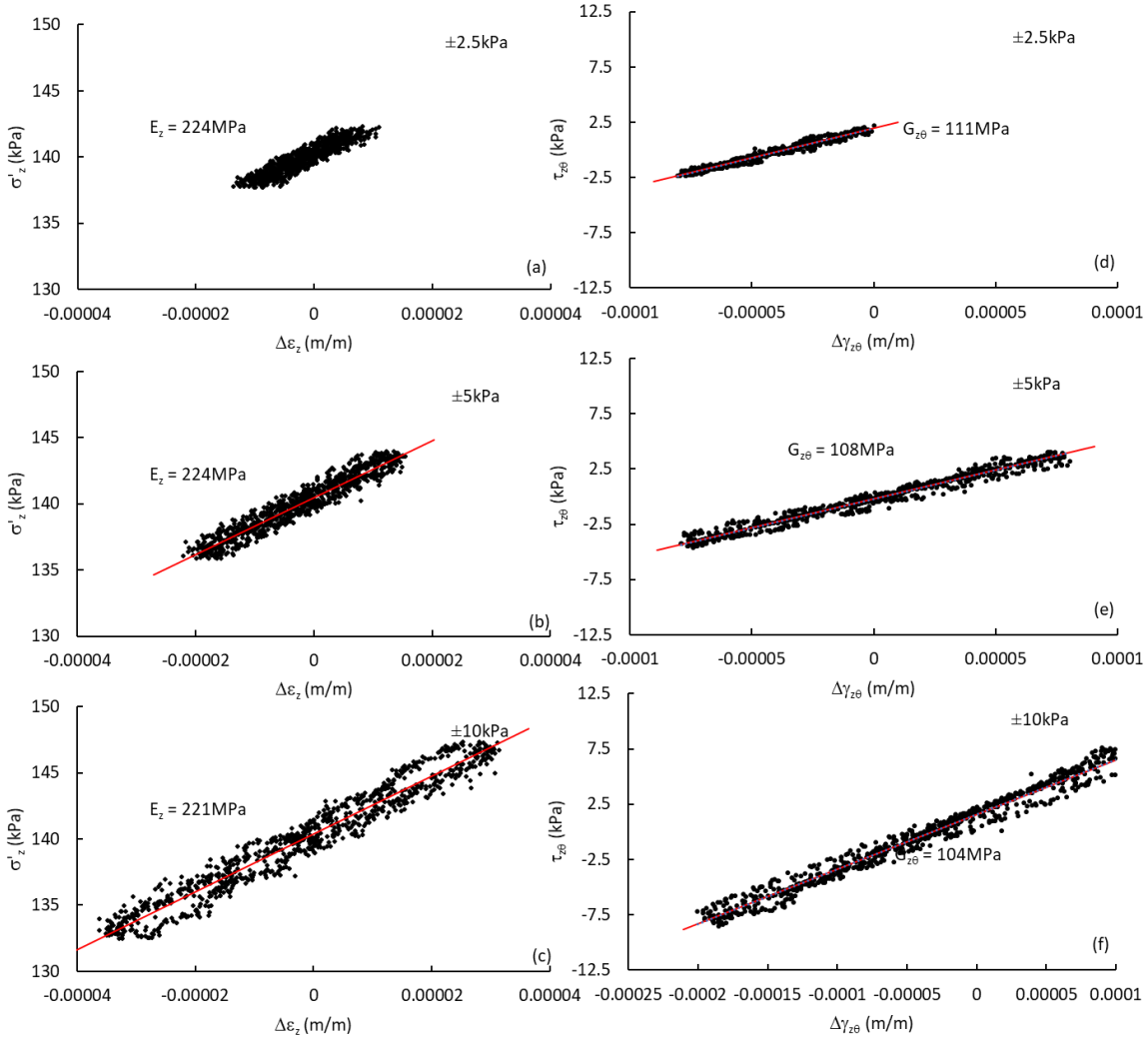


Figure 7.20 – Variation of the amplitude of cycles for (a, b, c) Young's moduli and (d, e, f) shear moduli

All the values of the Young's and shear moduli together with the stress conditions at the investigation points are presented in Table 7.1. The evolution of the Young modulus and shear modulus is analysed separately for each test, and it will be discussed later. In the next items, the results from all tests will be explored.

For this analysis, the results from tests HC1 with $\alpha = 0^o$ and 15^o, and HC2 $\alpha = 0^o$, 15^o and 45^o are presented. Figures 7.21 – 7.25 show that the amplitude variation of the small cycles leads to very small variations of the equivalent modulus obtained. Additionally, it was noticed that the influence of the amplitude causes a reduction in the modulus when higher cyclic stresses were applied to the specimens. In the following Figures, the notation with roman numbers (e.g. (II), (III)), represents each small cycle reading made at a load stage. If the cycles were axial,

the measurement obtained a Young's Modulus, represented by "E", if torque cycles were applied, the representation "G" is relative to the shear modulus obtained.

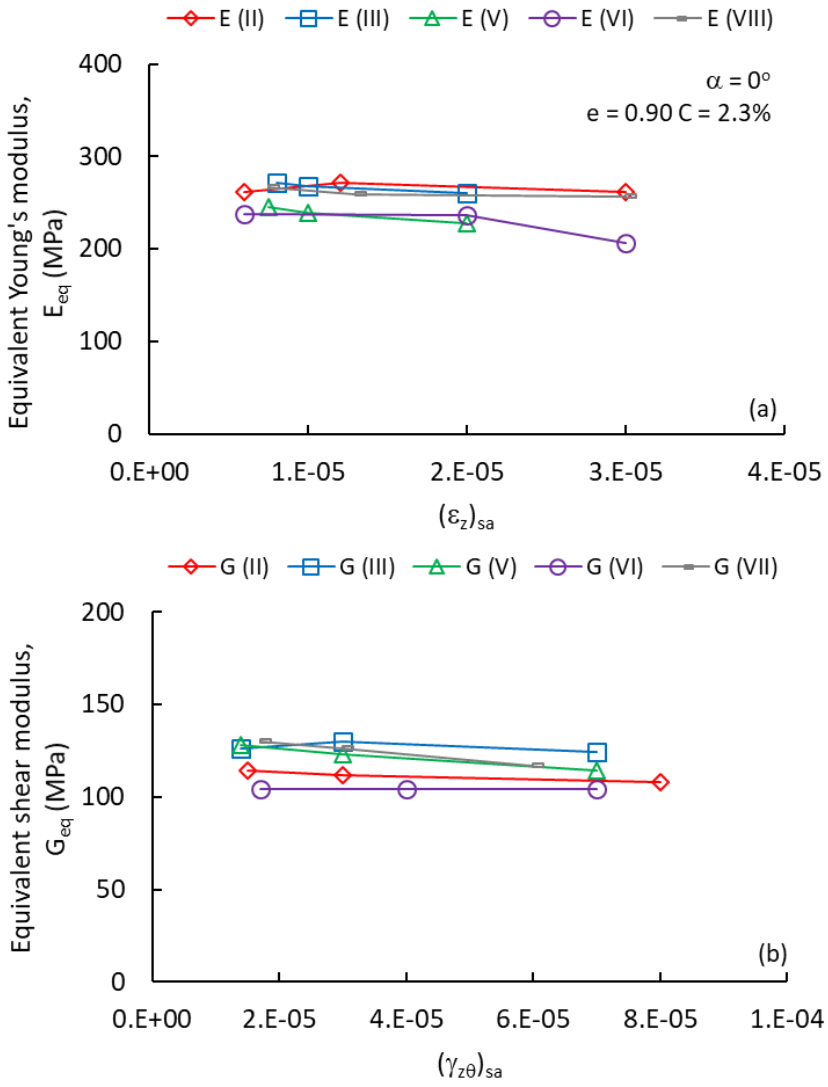


Figure 7.21 – Equivalent modulus, (a) E_{eq} and with the simple amplitude strain $(\varepsilon_z)_{sa}$ and (b) G_{eq} with $(\gamma_{z\theta})_{sa}$ – HC1 $\alpha = 0^o$

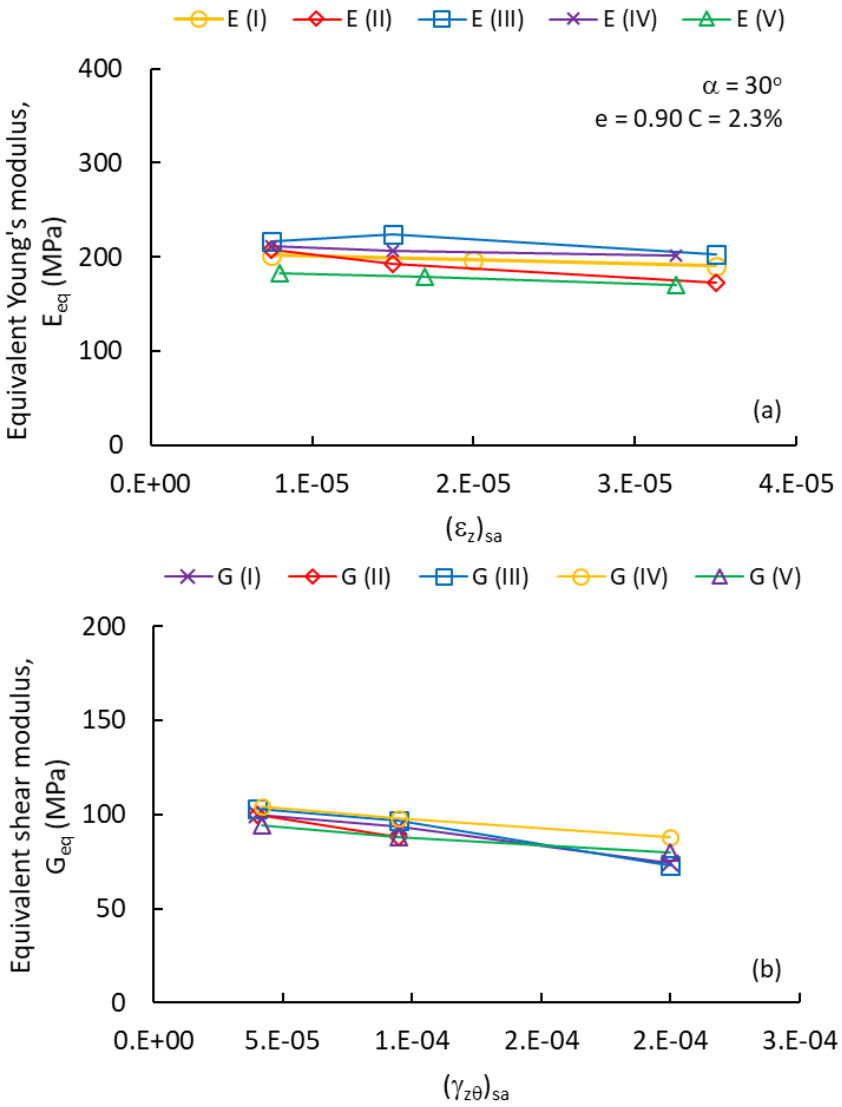


Figure 7.22 – Equivalent modulus, (a) E_{eq} and with the simple amplitude strain $(\varepsilon_z)_{sa}$ and (b) G_{eq} with $(\gamma_{z\theta})_{sa}$ – HC1 $\alpha = 30^o$

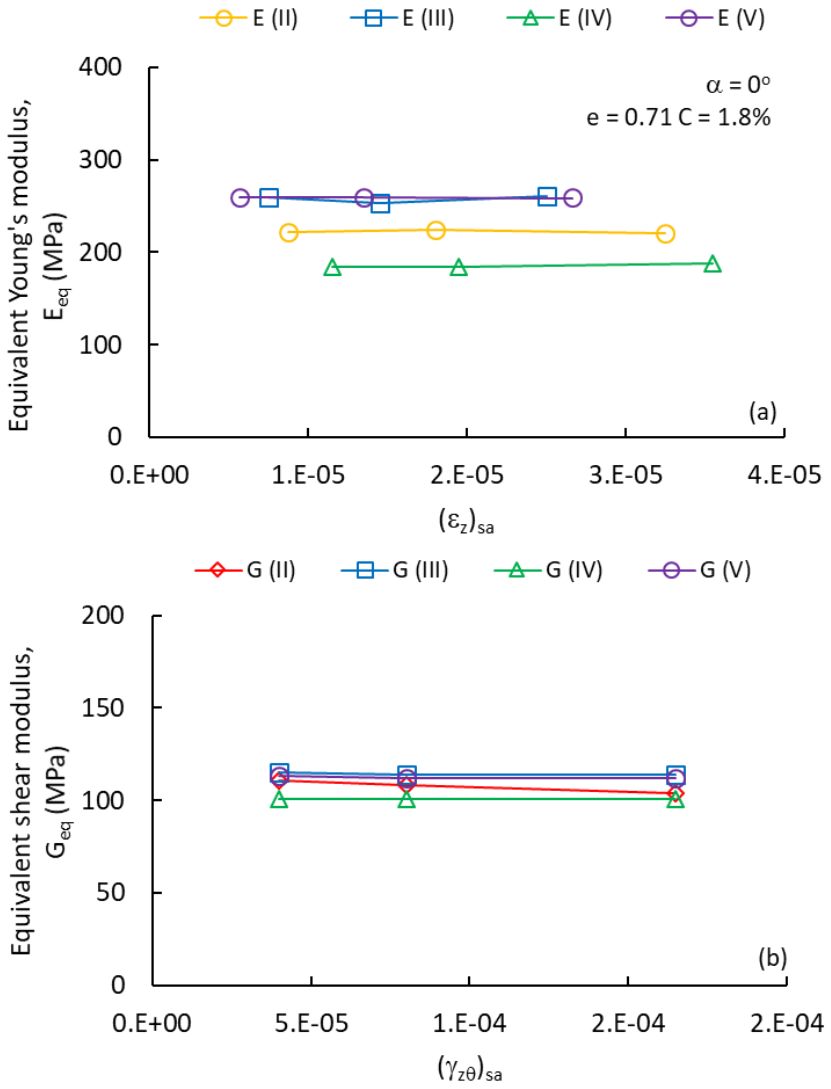


Figure 7.23 – Equivalent modulus, (a) E_{eq} and with the simple amplitude strain $(\varepsilon_z)_{sa}$ and (b) G_{eq} with $(\gamma_{z\theta})_{sa}$ – HC2 $\alpha = 0^o$

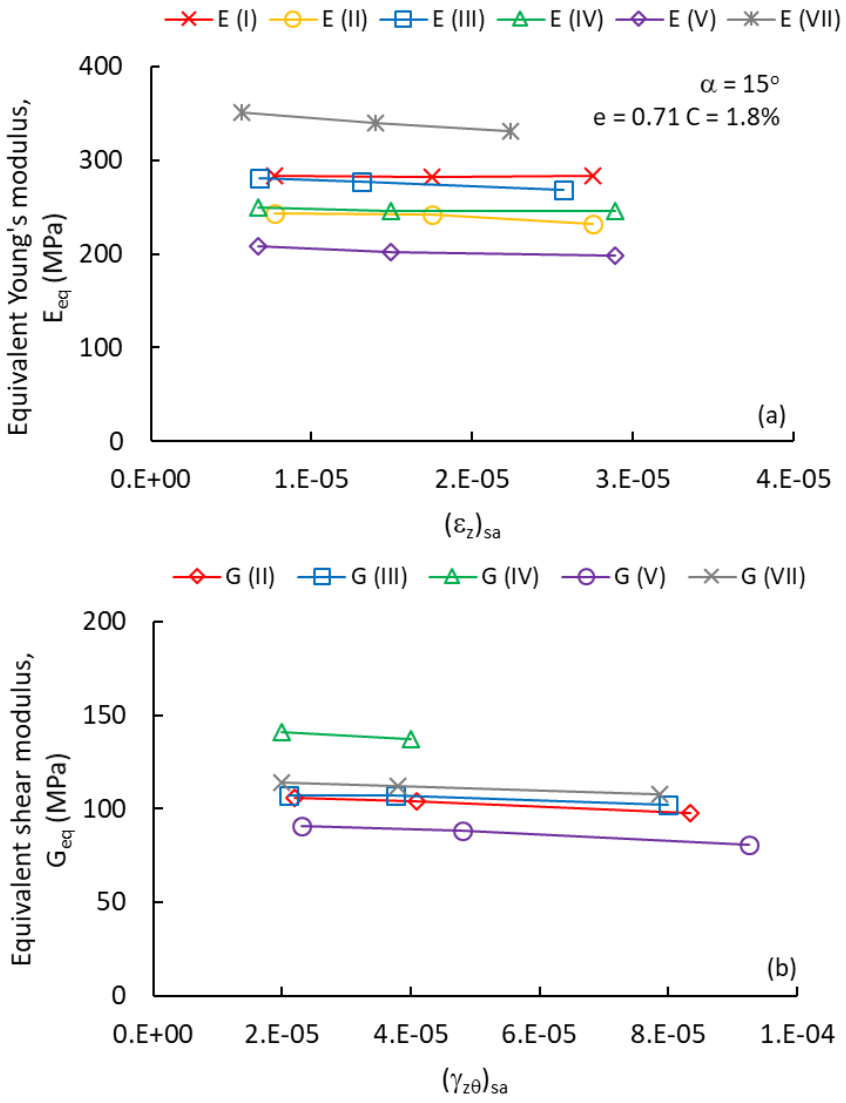


Figure 7.24 – Equivalent modulus, (a) E_{eq} and with the simple amplitude strain $(\varepsilon_z)_{sa}$ and (b) G_{eq} with $(\gamma_{z\theta})_{sa}$ – HC2 $\alpha = 15^{o}$

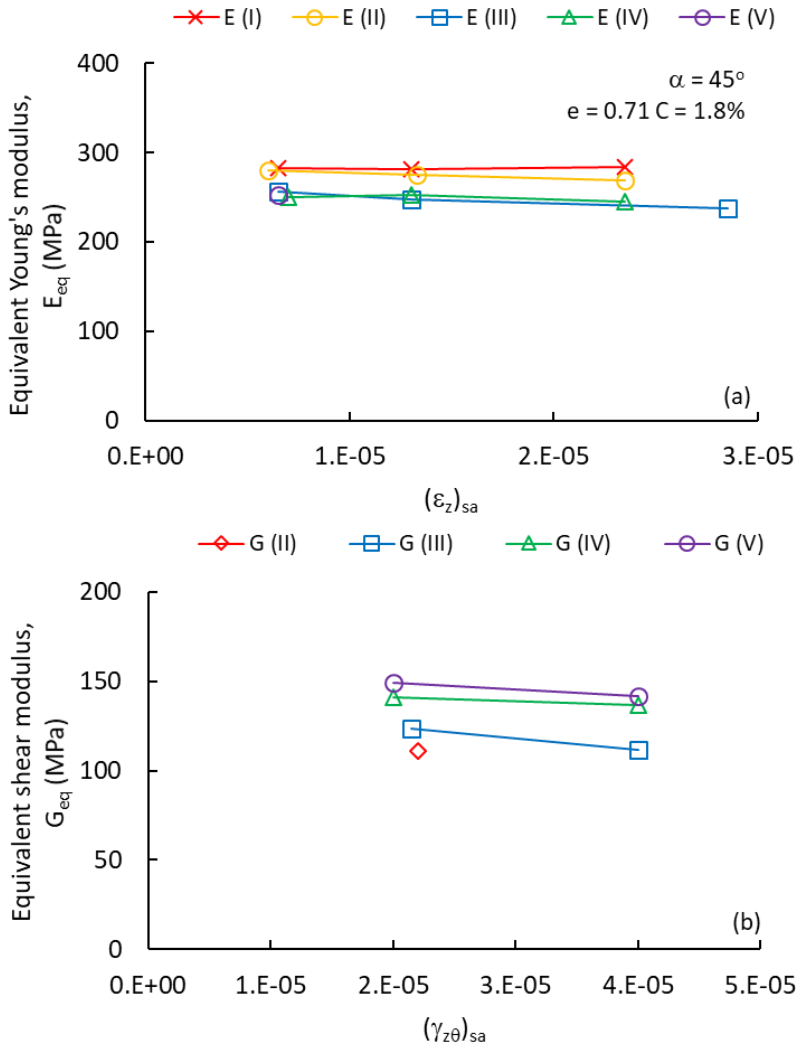


Figure 7.25 – Equivalent modulus, (a) E_{eq} and with the simple amplitude strain $(\varepsilon_z)_{sa}$ and (b) G_{eq} with $(\gamma_{z\theta})_{sa}$ – HC2 $\alpha = 45^o$

7.5.4 Effect of the stress paths

As the effect of the amplitude was not strongly pronounced on the moduli observed, the following results used the modulus obtained from the first series of cycles at each investigation point after creep with cycles of amplitude of ±2.5kPa for both axial and torque loadings.

7.5.4.1 Initial *E* and *G* analysis

The first analysis made on the small cycles corresponded to the initial starting test point, after consolidation stage. The measurement was made at the end of consolidation corresponding to a mean p'= 100 kPa. For the tests with $\alpha = 0^o$ the values correspond to the initial loading of the sample at very small strain. As for the other principal stress orientations, the values were obtained from the small cycles applied.

Figure 7.26 presents the initial moduli found in each test and the average obtained for the same sample characteristics. Figure 7.26a and 7.26b present the Young's moduli obtained for the samples HC1 and an average of the stiffness of 256MPa was recorded, while for HC2 samples this average is 260MPa. With this small variation, it can be commented that the initial Young's modulus was very similar for the same materials with identical η/C_{iv} = 47.2.

When analyzing Figure 7.26c and 7.26d, the presented shear moduli obtained for samples HC1 an average of the shear moduli of 106MPa was recorded, while for HC2 samples this average is 130MPa. The is a small variation compared with the average Young's modulus, but both still present the same order of magnitude.

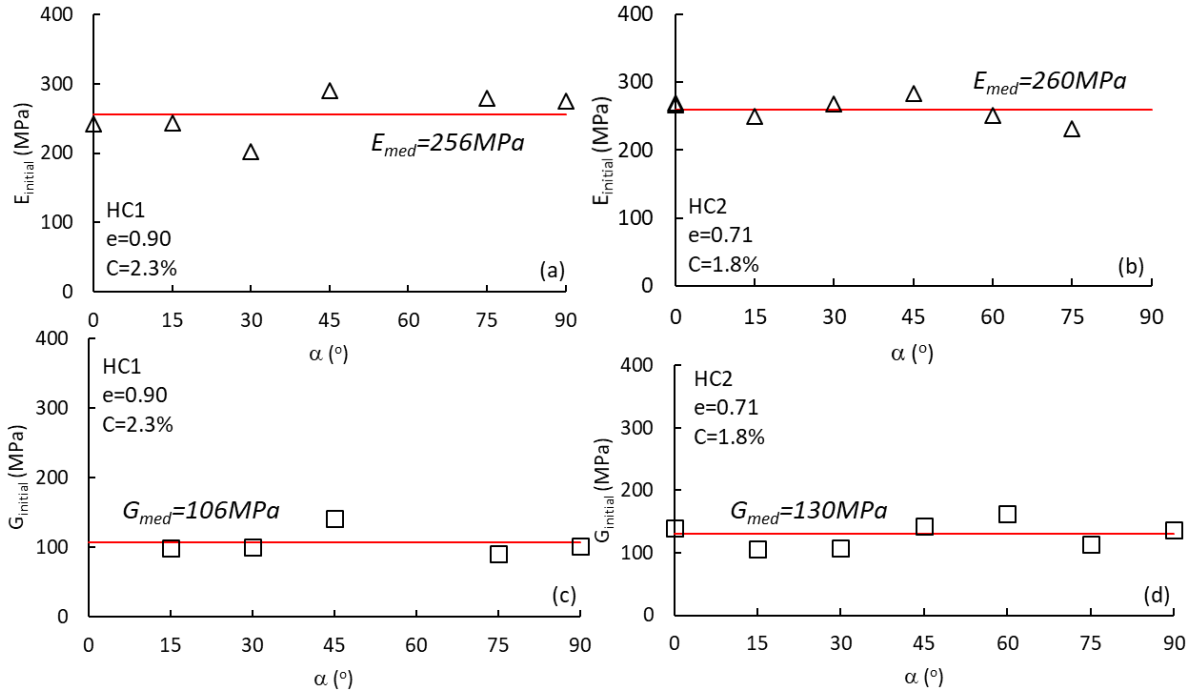


Figure 7.26- Moduli at initial *q*=0kPa: (a) Young's Moduli for HC1;
(b) Young's Moduli for HC2; (c) Shear Moduli for HC1; and
(d) Shear Moduli for HC2;

7.5.4.2 Typical test result

Figures 7.27 – 7.29 show the results from test HC2 α=0º. Each investigation point of small strain is represented with a Roman numeral in Figures 7.27 and 7.28. Figure 7.27 details each point where small cycles were measured during shearing, while Figure 7.28 depicts the test procedure over time.

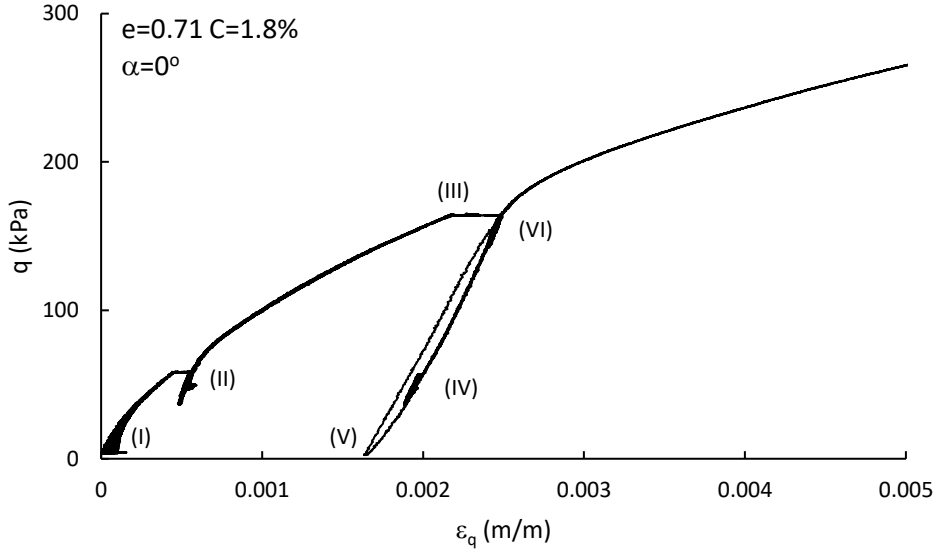


Figure 7.27 – Deviatoric stress over deviatoric strain with the points where small cycles were measured

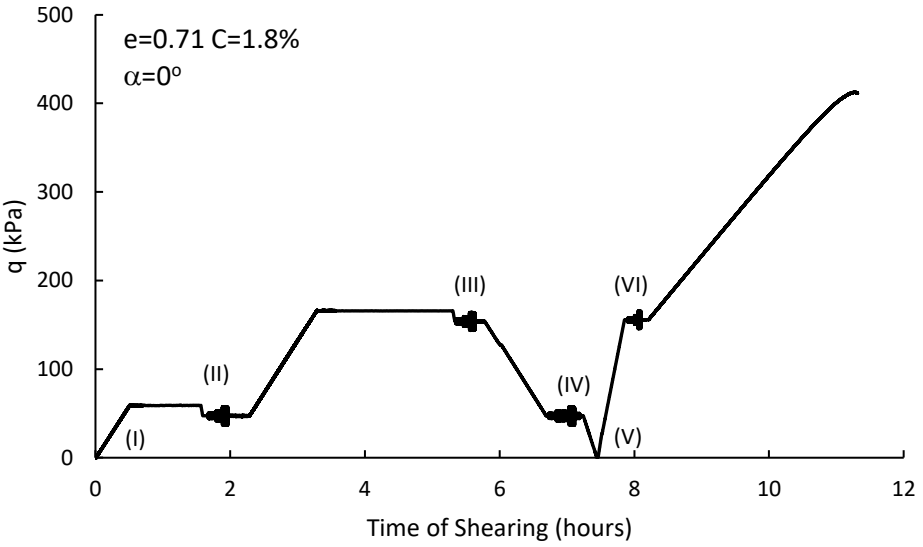


Figure 7.28 – Deviatoric stress over time with detailed small cycles imposition on the cemented sand

The estimation of the initial Young's modulus is shown is Figure 7.29 which shows the stress in "z" direction, σ'_z, plotted against the strain in this same direction, ε_z, and the initial slope of the best fit line though the stress-strain curve correspond to the modulus. The same analysis is possible when $\tau_{z\theta}$ is plotted against $\gamma_{z\theta}$.

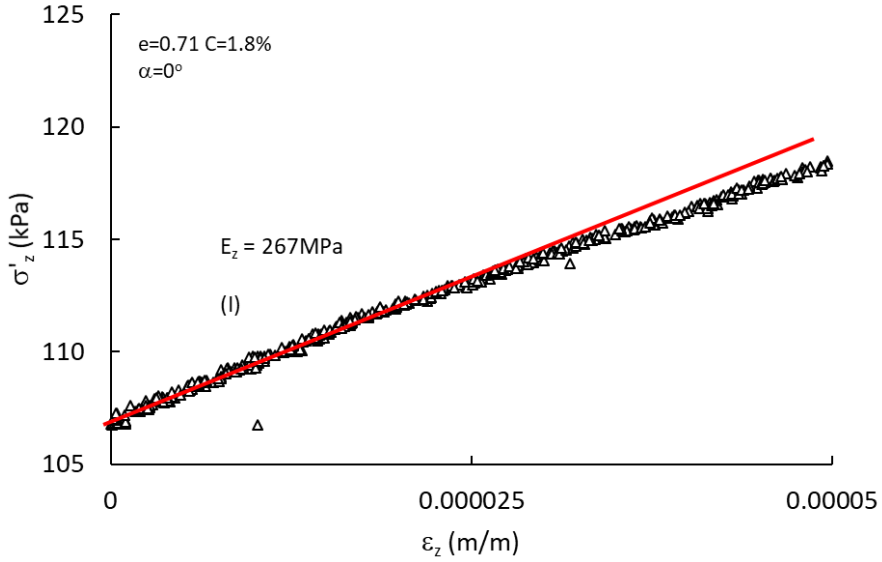


Figure 7.29 – Procedure to obtain the Young's modulus were small cycles were not performed

All the values of the Young's and shear moduli together with the stress conditions at the investigation points are presented in Table 7.1 (HC1) and Table 7.2 (HC2). The evolution of the Young modulus and shear modulus is analysed separately for each test, and it will be discussed later. In the next items, the results from all tests will be explored.

Table 7.1 – Summary of testing cycles; HC1: C=2.3%; e=0.90

	Stage	σ_z (kPa)	σ_θ (kPa)	p' (kPa)	q (kPa)	$\tau_{z\theta}$ (kPa)	E (MPa)	G (MPa)	$\sigma_z \sigma_\theta^{0.5}$
HC1 α=0	I	100	100	100	0	0	242		
	II	152	102	119	50	0	262	114	125
	III	211	102	138	109	0	271	126	147
	IV	280	102	161	178	0	284		
	V	211	102	138	49	0	245	128	147
	VI	152	102	119	49	0	238	104	124
	VII	100	100	100	0	0	235		
	VIII	275	101	160	178	0	266	130	167
HC1 α=15	I	95	95	97	0	0	243	99	95
	II	125	106	112	21	6	287	100	115
	III	146	107	120	44	12	342	111	125
	IV	124	104	110	23	6	329	106	113
	V	102	102	102	0	0	320	97	102
	VI	208	108	141	114	31		116	150
HC1 α=30	I	95	95	96	0	0	202	100	95
	II	116	94	102	23	6	208	100	105
	III	137	94	109	47	13	216	103	113
	IV	116	94	102	23	7	212	104	104
	V	94	94	95	2	0	182	94	94
	VI	201	93	130	120	32	227	114	137
HC1 α=45	I	100	100	101	0	0	291	141	100
	II	100	100	101	31	18	295	102	100
	III	99	99	100	61	35	229	83	99
	IV	99	99	100	31	18	236	96	99
	V	99	99	100	2	0	242	96	99
	VI	97	99	99	61	35	198	83	98
HC1 α=75	I	97	97	98	0	0	280	90	97
	II	76	97	91	25	6	240	73	86
	III	54	97	84	49	10	184	135	73
	IV	75	97	90	25	6	236	156	85
	V	96	96	97	3	0	253	166	96
HC1 α=90	I	97	97	97	0	0	276	102	97
	II	79	97	91	19	0	252	96	87
	III	58	97	84	39	0	217	90	75
	IV	58	97	84	39	0	214	89	75
	V	79	97	91	19	0	235	94	87
	VI	97	97	97	0	0	236	96	97
	VII	79	97	91	19	0	238	93	87

Table 7.2 – Summary of testing cycles; HC2: C=1.8%; e=0.71

	Stage	σ_z (kPa)	σ_θ (kPa)	p' (kPa)	q (kPa)	$\tau_{z\theta}$ (kPa)	E (MPa)	G (MPa)	$\sigma_z \sigma_\theta^{0.5}$
HC2 α=0	I	100	100	106	0	0	220		
	II	153	106	122	50	0	222	111	127
	III	256	106	156	155	0	259	115	165
	IV	152	105	121	50	0	182	101	126
	V	100	100	106	0	0	173		
	VI	258	105	156	155	0	260	113	165
HC2 α=15	I	101	101	100	0	0	240	106	101
	II	121	101	107	23	6	243	106	110
	III	184	100	128	95	26	279	107	136
	IV	184	100	128	96	26	250	102	136
	V	121	100	107	24	6	208	92	110
	VI	104	100	101	26	0	222	84	102
	VII	329	99	176	231		335	114	181
HC2 α=30	I	91	91	92	0	0	268	107	91
	II	108	91	97	38	16	278	100	99
	III	130	91	105	75	30	272	98	109
	IV	108	91	97	38	16	260	101	99
	V	129	91	104	75	30	284	93	108
HC2 α=45	I	99	99	99	0	0	283	143	99
	II	98	98	99	33	19	280	117	98
	III	98	98	98	66	38	256	124	98
	IV	98	98	99	34	19	250	141	98
	V	98	98	98	0	0	252	149	98
	VI	98	98	99	66	38	253	122	98
	VII	99	99	99	99	57	199	64	99
HC2 α=60	I	98	98	99	0	0	251	163	98
	II	79	98	93	37	18	200	103	88
	III	79	98	92	37	18	202	100	88
HC2 α=75	I	102	102	103	0	0	231	113	102
	II	95	102	100	15	7	200	107	98
	III	103	102	103	0	0	212	107	102
HC2 α=90	I	100	100	99	0	0	398	137	100
	II	79	100	92	20	0	327	125	89
	III	100	99	99	0	0	353	129	100
	IV	79	100	92	21	0	315	123	89

7.5.4.3 Creep characteristics of cemented Hostun sand

At certain levels in the monotonic loading, creep deformation of cemented Hostun sand was observed, as shown in Figure 7.30. Figure 7.30b shows the creep deformations and it transpires that, although the amount of creep strain was not small, the stress-strain relationship of the

further shearing after creep tests converged with the overall stress-strain curve of the monotonic shearing. This behavior was systematically observed for all tests.

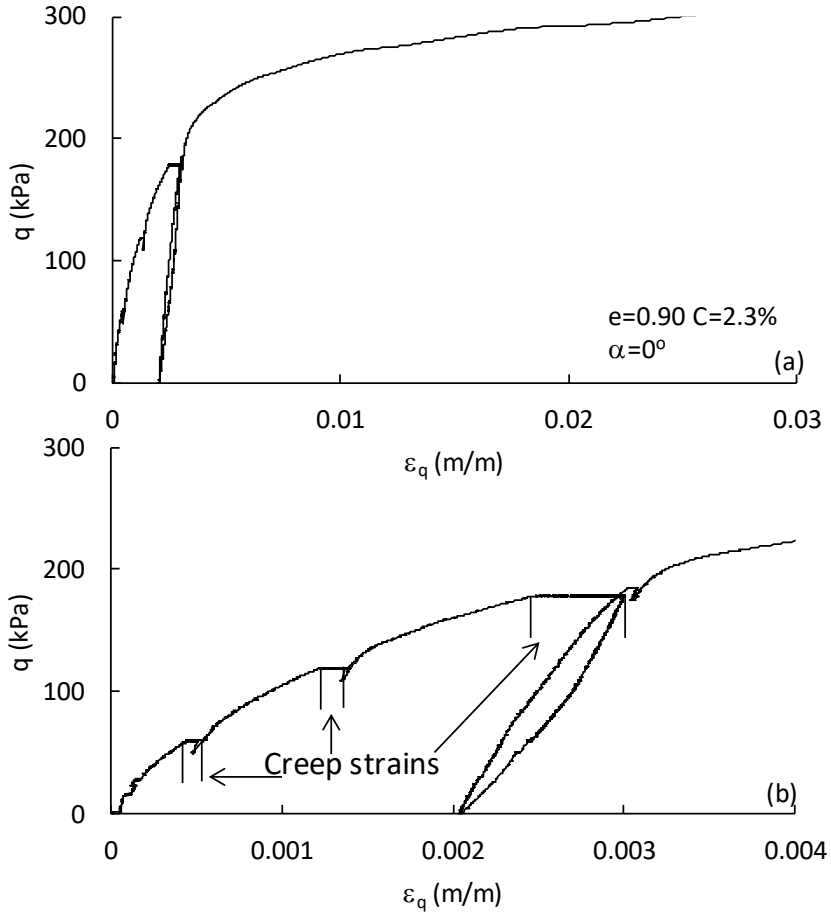


Figure 7.30 – Typical stress-strain curve in monotonic loading with creep test: HC1 $\alpha=0^o$

The 30 minutes of Creep for the test HC1 $\alpha=75^o$ was not sufficient to stop deformations. It was clear from the measurements of the small cycles applied during this test at the third point of investigation. This test had combined extension and torque, and the effect of the insufficient time on creep was observed only in the axial cycles. The effect on the cycles can be observed in Figure 7.31a and b. The Young modulus presented in Figure 7.31a was obtained through the analysis of each cycle and it was verified that they could be considered the same even with the variation of the axial strain during the application of the cycles.

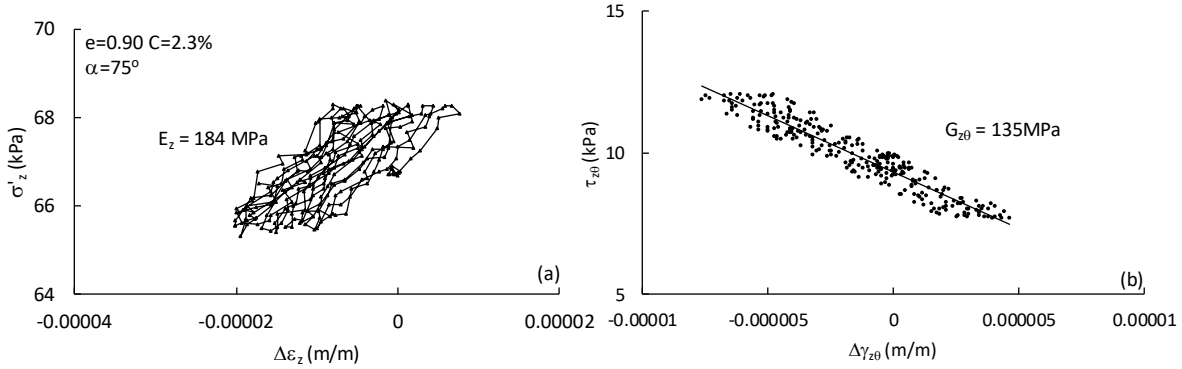


Figure 7.31 – Cycles after creep for determination of (a) E_z and (b) $G_{z\theta}$

7.5.4.4 Effect of stress level dependency of small-strain stiffness

Small-strain stiffness components E_z and $G_{z\theta}$, were measured by applying the small cyclic loads at certain stress levels in monotonic shear as well as in isotropic consolidation after the creep formation had almost terminated, as discussed in 7.5.4.3. In the results presented in this section, the analysis was made focusing on the effect of the stress level for each test performed isolation.

The effect of the stress level from both cemented samples prepared (HC1 – e=0.90 and C=2.3%; HC2 – e=0.71 and C=1.8%) showed to be similar. Firstly the results from HC2 will be presented in this section, items (a) to (g) contain the results from each α performed in this part of the research program. Items (h) to (n) present the stiffness measured from samples HC1.

The analysis of the Young's modulus is usually related to a relationship obtained between E_z or $E_z/f(e)$ expressed and modelled as a function of $\sigma_z^{'m}$ with constant power value *m*. The E_z values normalized by *f(e)* (void ratio function) is used to eliminate the effect of different void ratios among specimens. Hameury (1995) proposed the following expression of the void ratio for the Hostun RF sand:

$$f(e) = \frac{(3.01 - e)^2}{1 + e} \tag{7.1}$$

As the function of void ratio does not consider the cementation effect, the normalization was not used in this part of the analysis.

The shear modulus, $G_{z\theta}$, is expressed and modelled as a function of $(\sigma'_z\sigma'_\theta)^{0.5n}$. It is recognised that the shear modulus is mainly dependent on the normal and horizontal stresses acting on the plane of shear and independent of the stress acting normal (ROESLER, 1979).

The effect of the shear stress on the moduli will also be presented and analysed.

(a) $\alpha=0^o$: the effect of the Young's modulus of the test performed with compression monotonic loading and unloading is presented in Figure 7.32a. It is noticed that a power function was successfully related to the results and the power coefficient was m = 0.31. By analysing the points (I)-(V) and (II)-(IV), the effect of the bonding degradation during loading is clear, observed in the small cycles. This de-bonding effect is not so evident when the analysis of the shear modulus is made. When comparing (II)-(IV) from Figure 7.32b, a small variation between this two was observed, credit to a small breakage of cementation during loaging. The power observed in the shear modulus was n=0.29.

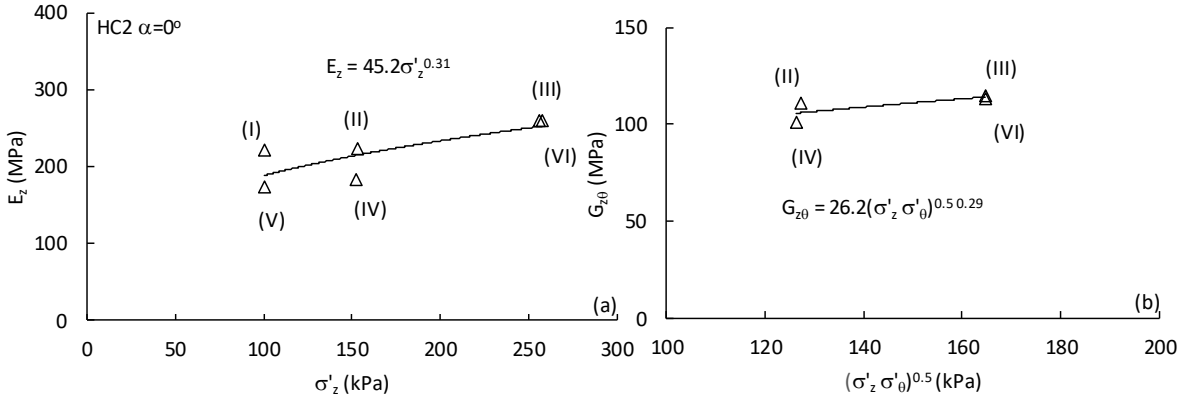


Figure 7.32 – Stress level dependency of (a) Young's moduli, E_z, and (b) shear moduli, $G_{z\theta}$; (HC2 $\alpha=0^o$)

(b) $\alpha=15^o$: Figure 7.33a presents the effect of the vertical stress level on the Young's modulus and a power law can be fitted through the experimental points with power coefficient of m=0.33. The Figure 7.33b shows the variation of the shear modulus with $(\sigma'_z\sigma'_\theta)^{0.5}$ and a power relation with a power coefficient of n=0.32 can be fitted through data too. However, comparing the loading and unloading effects on the value of the shear modulus, a degradation of the cementation is observed, expressed through a reduction of the modulus is observed.

The test with $\alpha=15^o$ has the combination of compression and torque imposed on the cemented specimen. To explore the effect of this loading condition involving fixes rotation of principal

stresses, the Young's and shear moduli are also expressed with the shear stress, $\tau_{z\theta}$. In Figure 7.33c, when observing points I, II and III, the effect of the shear stress is not considered important for the variation of the Young's moduli. The same observation can be made in Figure 7.31d: points I, II and III do not appear to be influenced by the shear stress. However, further shearing seems to induce some degradation of the moduli, both Young's and shear, with smaller values at the investigation points IV, V and VI.

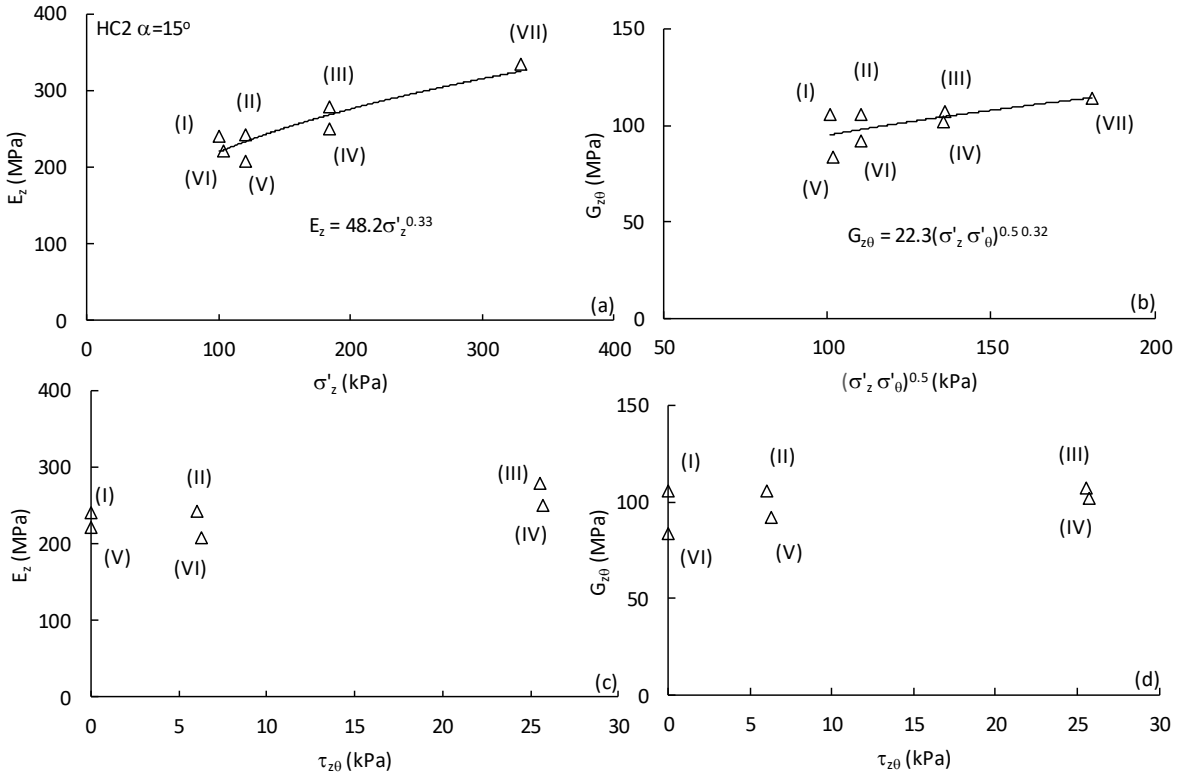


Figure 7.33 – Stress level dependency of (a) and (c) Young's moduli, E_z, and (b) and (d) shear moduli, $G_{z\theta}$, (HC2 α=15°)

(c) α=30°: this test at a fixed rotation of principal axes involves the combination of compression and torque loading; one unloading cycle was also applied as shown in point (IV) and (V) (Figure 7.34a). Figure 7.34a shows the variation of the Young's modulus with the axial stress, σ_z. Although some increase of the Young's modulus is observed, this increase looks limited and could be affected by the shear stress which may affect the soil structure during the tests. Compared with the results in Figure 7.33c, the Young's modulus variation with the shear stress shown in Figure 7.34c is much more limited. Very interestingly, as in this test the rate of the shear stress imposed is higher that for the test at α=15°, its effect is more pronounced for the shear stiffness which show steady reduction with the $(\sigma'_z\sigma'_\theta)^{0.5}$ as shown in Figure 7.34b. This

influence is directly observed in Figure 7.34d, whereas as the increase of shear stress is imposed to the sample, the degradation in the shear modulus is apparent.

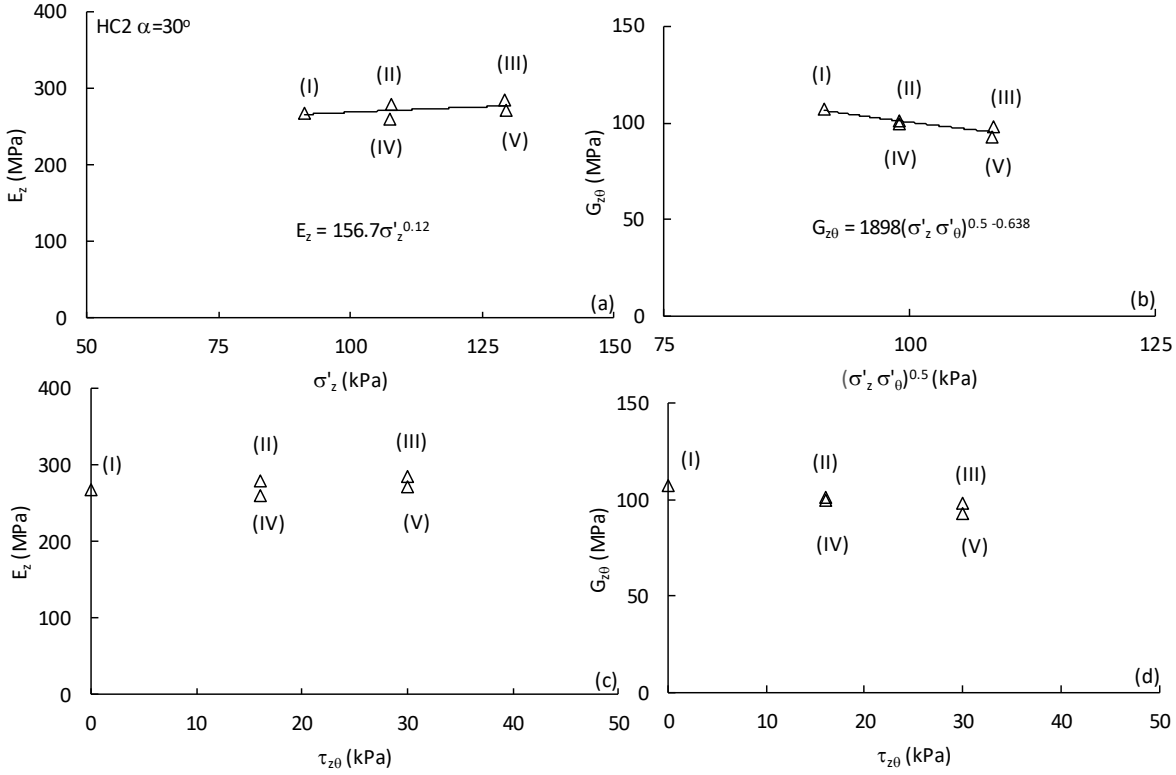


Figure 7.34 – Stress level dependency of (a) and (c) Young's moduli, E_z, and (b) and (d) shear moduli, $G_{z\theta}$, (HC2 $\alpha=30^o$)

(d) $\alpha=45^o$: Figure 7.35a and b emphasizes the clear effect of torque on the Young's and shear moduli showing a with steady degradation. During the test performed with $\alpha=45^o$, there was no variation of p', σ'_z or σ'_θ. For this reason, the analysis of the effect of the stresses imposed on the cemented sample is based on the shear stress. As loading takes place and the cycles were applied, a noticeable degradation of the cementation bonding is observed with the reduction of the Young's and shear moduli, Figure 7.35c and 7.35d respectively. It is also apparent that during unloading, from point III – IV – V – VI no more degradation was induced, but also, the loss of stiffness was not recovered. When torque was again imposed, more degradation was observed, as seen by the measurements of the moduli in the investigation points VI and VII.

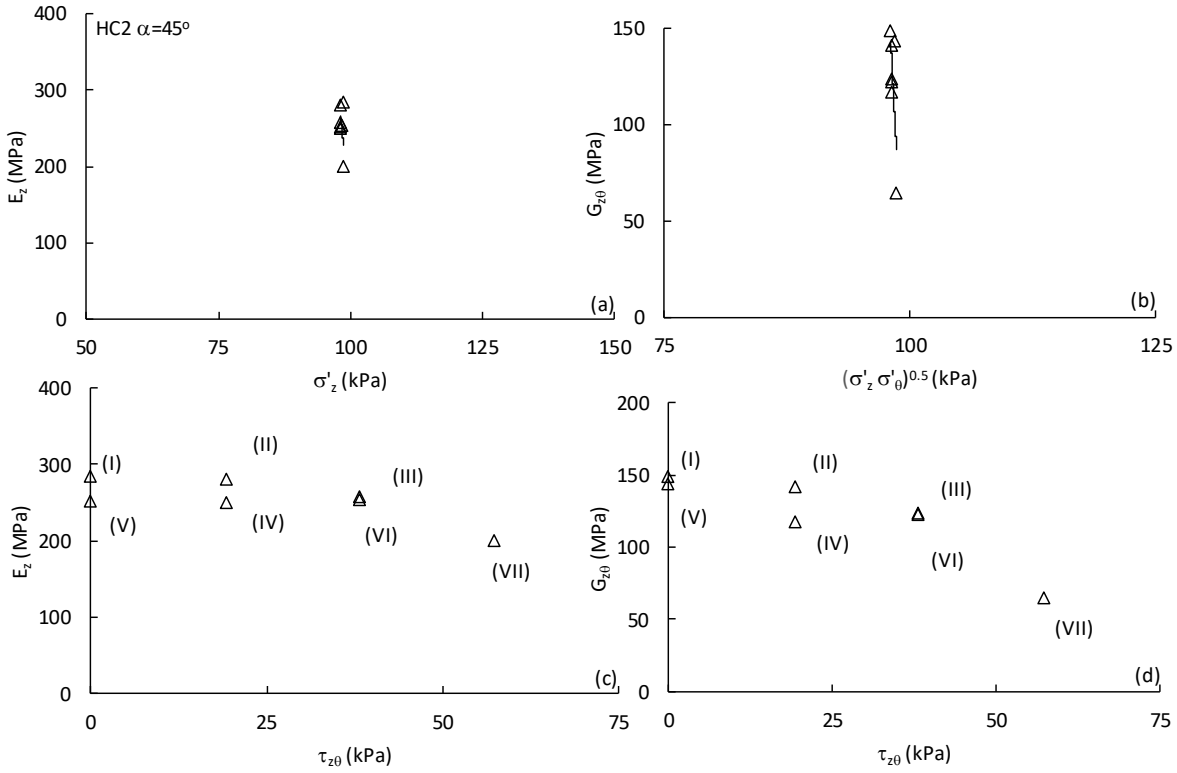


Figure 7.35 – Stress level dependency of (a) and (c) Young's moduli, E_z, and (b) and (d) shear moduli, $G_{z\theta}$, (HC2 α=45°)

(e) α=60°: the combination of torque and extension loading during this test induces a pronounced degradation on the Young's and shear moduli. This bonding breakage can be noticed in Figure 7.36b and d. The degradation on the Young modulus is presented in Figure 7.36a and c.

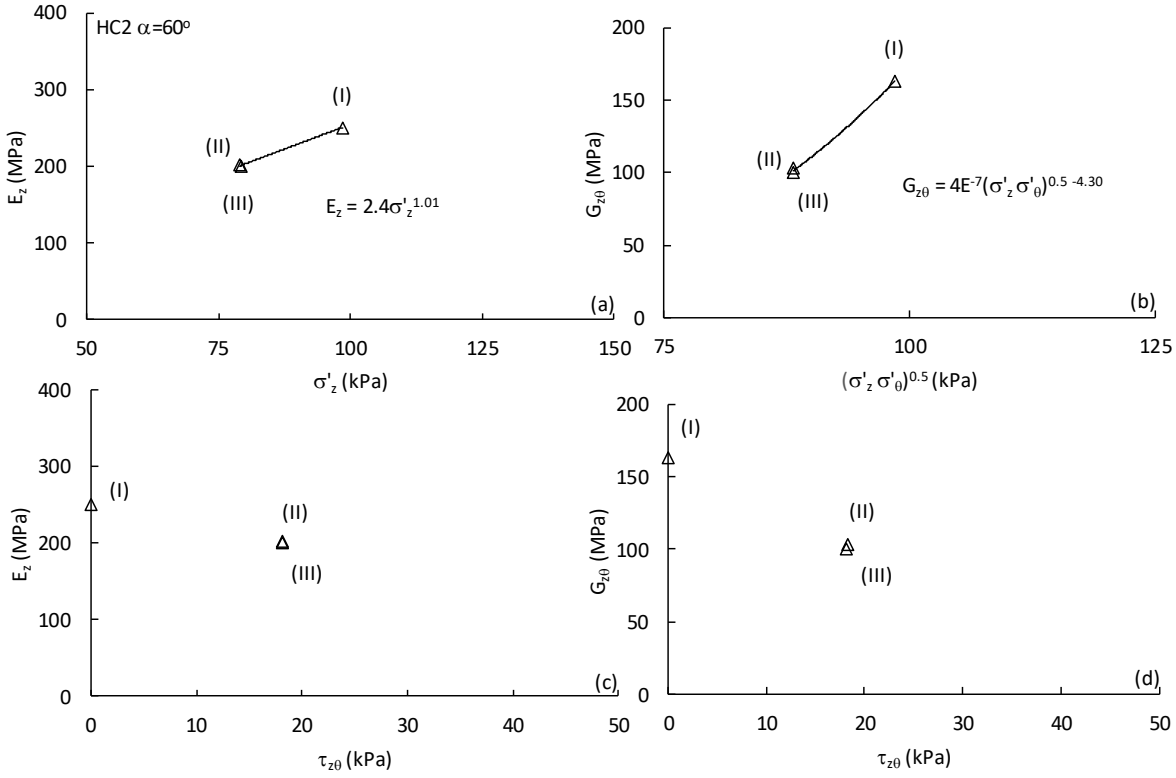


Figure 7.36 – Stress level dependency of (a) and (c) Young's moduli, E_z, and (b) and (d) shear moduli, $G_{z\theta}$, (HC2 α=60º)

(f) α=75º: this test has a lower variation of the imposed shear stress in comparison with the previous test presented with α=60º. The effect of this lower influence is noticeable in Figure 7.37c and d, where the shear stress does appear to influence in a more limited way the Young's and shear moduli measured. The effect of unloading of the material does not affect the shear modulus, as shown in Figure 7.37b. Concerning the variation of the Young's modulus with the vertical stress, a small reduction obtained, with recovery after reloading the specimen, as seen in Figure 7.37a.

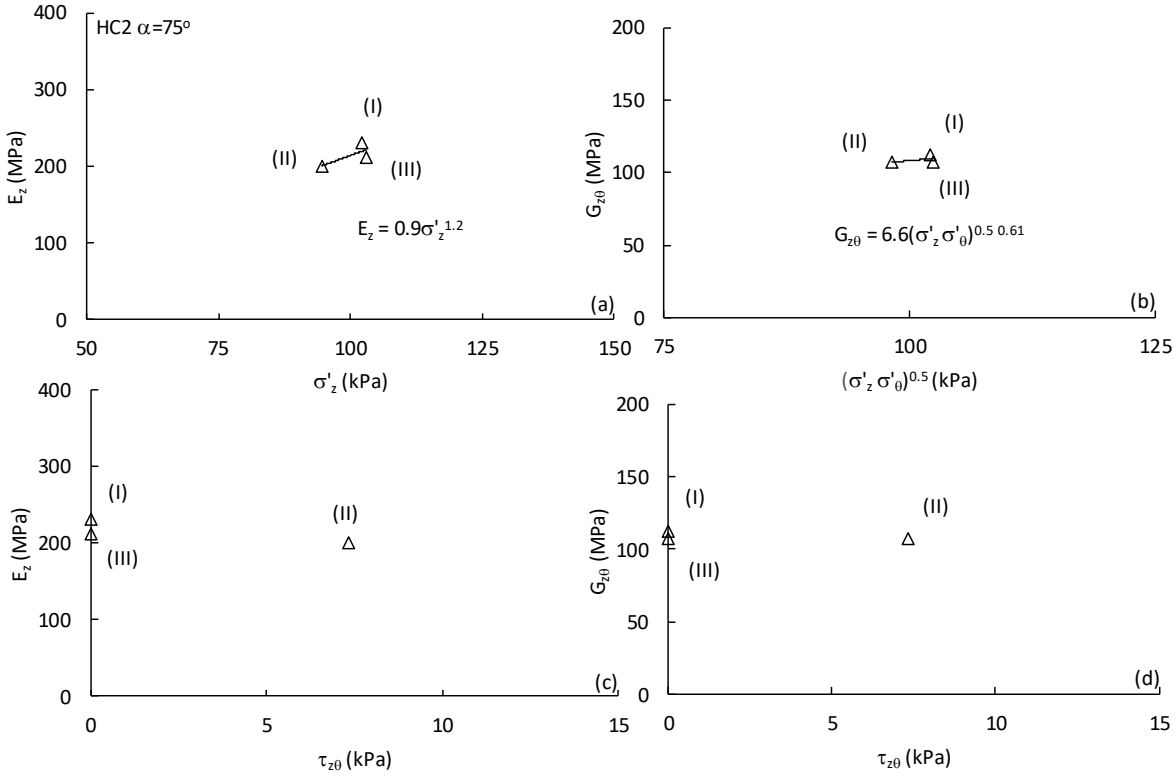


Figure 7.37 – Stress level dependency of (a) and (c) Young's moduli, E_z, and (b) and (d) shear moduli, $G_{z\theta}$; (HC2 α=75º)

(g) α=90º: the results obtained for the Young's moduli for the specimen is out of the range obtained for all the other, as showed in Figure 7.38. For this reason, Figure 7.26b did not contain the results from this test. However, the magnitude of Young's modulus is not in the range of other tests, it is observed in Figure 7.38a that the effect of unloading the specimen reduced the Young's moduli (point (I) to point (II)). When the specimen was reloaded (point (III)) the Young's modulus is not fully recovered, as points (I) and (III) are different. When the specimen is again unloaded, a similar Young's modulus obtained in point (II) is measured in point (IV). The same analysis can be made for the shear moduli, presented in Figure 7.38b.

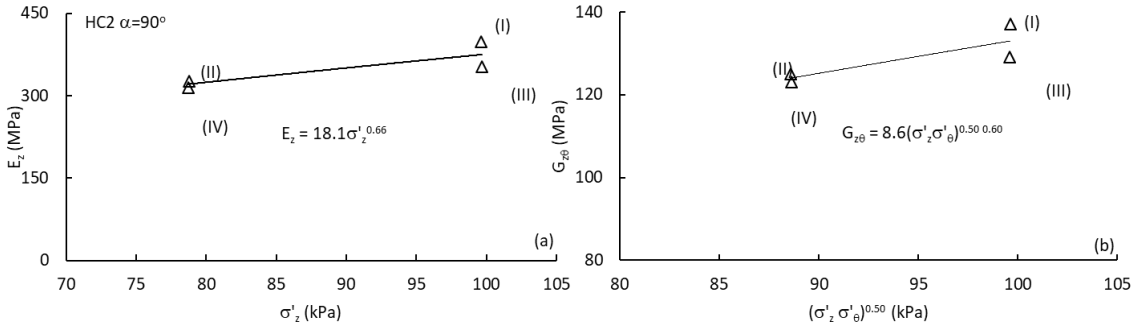


Figure 7.38 – Stress level dependency of (a) Young's moduli, E_z, and (b) shear moduli, $G_{z\theta}$; (HC2 α=90°)

(h) α=0°: Figure 7.39a shows that during loading the Young's moduli increases (points (I)-(IV)), followed by bonding degradation (points (IV)-(VII)). The results demonstrate two different trends, one observed during loading and one under, showing the unloading trend. The shear. The bonding degradation is also observed on the shear moduli, represented in Figure 7.39b. The measurements made with $(\sigma'_z\sigma'_\theta)^{0.50}$ = 125 kPa (relative to a p'=120kPa) shows a gap between points (II) and (VI), due to bond breakage. Point (V) and (III) present closer results, comparing loading and unloading stress paths.

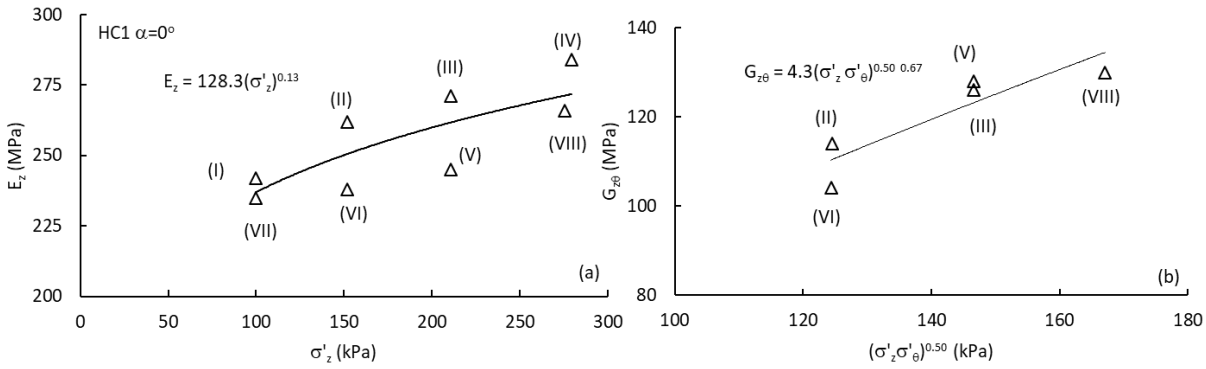


Figure 7.39 – Stress level dependency of (a) Young's moduli, E_z, and (b) shear moduli, $G_{z\theta}$; (HC1 α=0°)

(i) α=15°: Figure 7.40a presents the effect of the vertical stress level on the Young's modulus and a power law can be fitted through the experimental points with power coefficient of m=0.88. The Figure 7.40c shows the variation of the shear modulus with $(\sigma'_z\sigma'_\theta)^{0.5}$ and a power relation with a power coefficient of n=0.40 can be fitted through data too. Differently from α=0°, α=15° does not present two trends for loading and unloading, results in Figure 7.40a seems to lead to

one unique trend. This unique trend in not observed in Figure 7.40b, where the effect of the shear stress was isolated. Points I, II, III and VI present a linear trend not observed by IV and V. As for the shear moduli, the shear stress does not appear to influence the results, as points are close in Figure 7.70d.

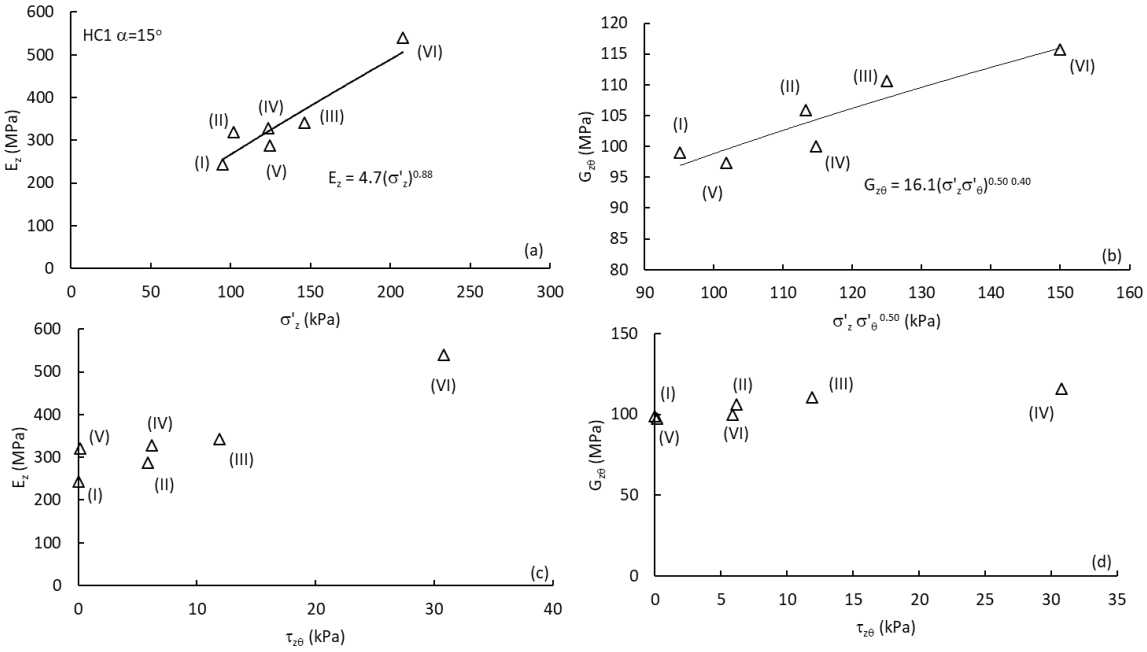


Figure 7.40 – Stress level dependency of (a) and (c) Young's moduli, E_z, and (b) and (d) shear moduli, $G_{z\theta}$; (HC1 α=15°)

(j) α=30°: Figure 7.41a shows the variation of the Young's modulus with the axial stress, σ_z. Although some increase of the Young's modulus is observed, this increase looks limited and could be affected by the shear stress which may affect the soil structure during the tests. Compared with the results in Figure 7.41c, the Young's modulus variation with the shear stress is much more limited. Figure 7.41b shows similar behaviour as presented in Figure 7.40c (α=15°). Degradation during unloading is also observed in this test, expressed in (IV) and (V). When analysing the effect of shear stress, this degradation is also observed (Figure 7.41d).

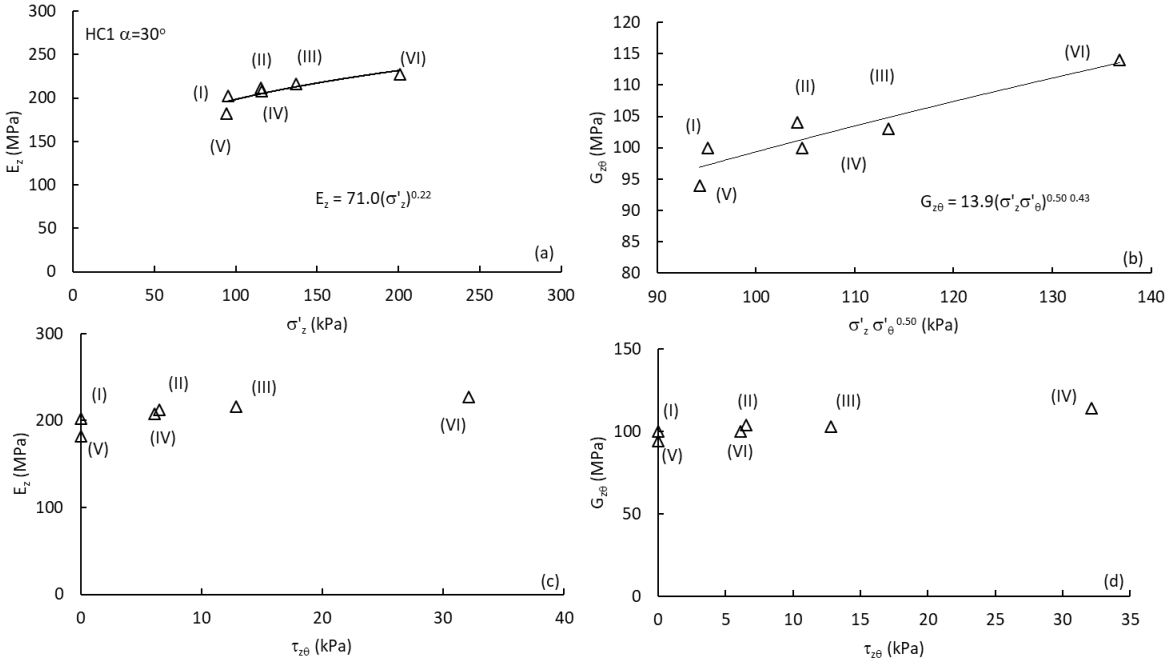


Figure 7.41 – Stress level dependency of (a) and (c) Young's moduli, E_z, and (b) and (d) shear moduli, $G_{z\theta}$; (HC1 α=30°)

(k) α=45°: Figure 7.42a and 7.42b emphasizes the clear effect of torque on the Young's and shear moduli showing a with steady degradation. As previous, during the test performed with α=45°, there was no variation of p', σ'_z or σ'_θ. Consequently, the evaluation of the effect of the stresses imposed on the cemented sample is again based on the shear stress. As loading takes place and the cycles were applied, a noticeable degradation of the cementation bonding is observed with the reduction of the Young's and shear moduli, Figure 7.42c and 7.42d respectively. It is also apparent that during unloading, from point III – IV – V – VI no more degradation was induced, but also, the loss of stiffness was not recovered.

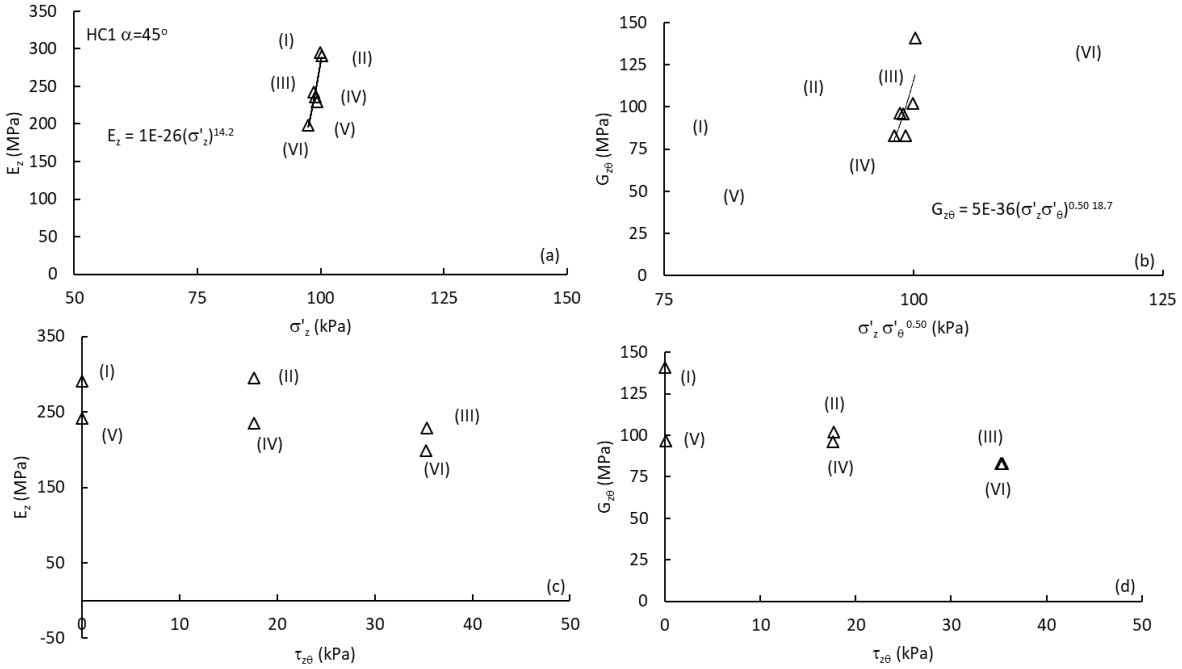


Figure 7.42 – Stress level dependency of (a) and (c) Young's moduli, E_z, and (b) and (d) shear moduli, $G_{z\theta}$, (HC1 α=45º)

(l) α=60º: at this specific test one local measurement sensor unfortunately detached from the specimen and reading could not be made.

(m) α=75º: Figure 7.43 shows the effect of unloading and reloading the specimen. The unloading expressed by the points I, II and III shows a reduction of Young's modulus (Figure 7.43a). Reloading the specimen resulted in a similar Young's moduli for IV and some unrecovered degradation in V. The degradation is also observed in 7.43c. The shear modulus presents two different behaviour, as seen in Figure 7.43b and 7.43d. The behaviour expressed by unloading from I to II is not comparable as the following strengths are imposed (III to V). The analysis of I-II presents a different trend obtained in III-V.

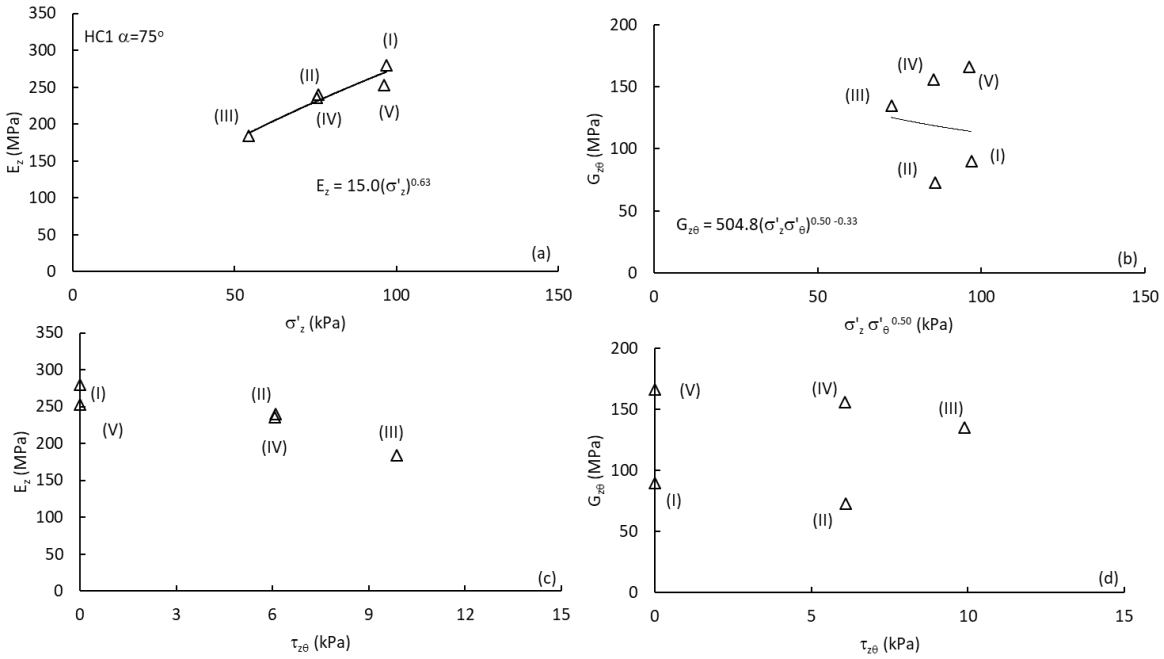


Figure 7.43 – Stress level dependency of (a) and (c) Young's moduli, E_z, and (b) and (d) shear moduli, $G_{z\theta}$, (HC1 α=75°)

(n) α=90°: the application of extension stresses to the cemented sand appear to influence the Young's modulus in a way that when the extension is removed, a recovery on the moduli was observed until a certain level, as seen in Figure 7.44a. The data at the investigation point VI shows that removing the extension loading was not enough for the full recovery of the initial Young's modulus, an indication that cementation breakages had occurred during testing. When the analysis is focused on the shear moduli (Figure 7.44b) and the influence of the extension load was applied, the variation of the modulus response to the loading condition does not present a huge influence in the shear modulus and this variation was recovered when extension loading was removed.

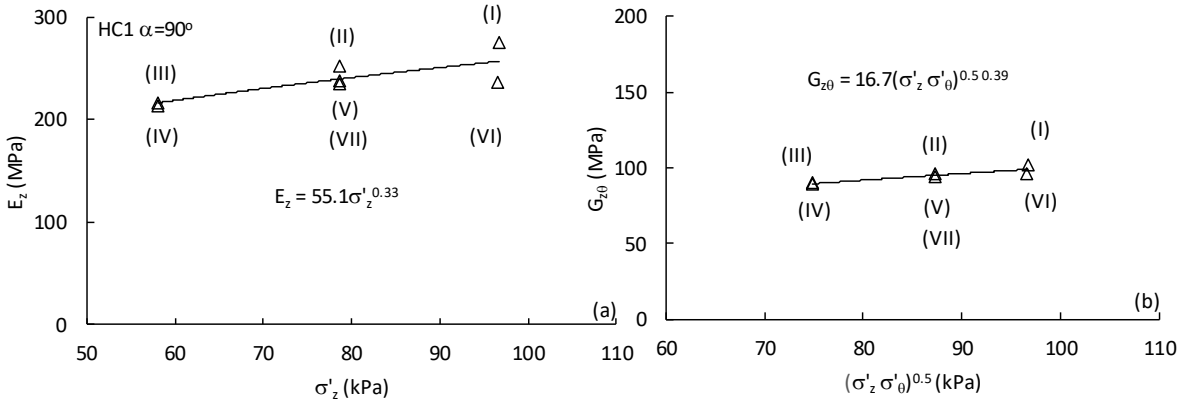


Figure 7.44 – Stress level dependency of (a) Young's moduli, E_z, and (b) shear moduli, $G_{z\theta}$; (HC1 $\alpha=90^o$)

7.5.4.5 Effect of principal stress direction

Figures 7.45 and 7.46 show the relationship between Young's and shear moduli during shearing versus the direction angle of major principal stress condition. As mentioned before, the small strain shear modulus is a function of the effective axial stress and horizontal stress. As a result, the direct comparison between each test is not possible. During shearing b, p' and α varied; for this reason, this analysis will focus on the effect of the direction into the degradation of bonds for each sample composition.

Figure 7.45 contains the results from the first rosette, with a void ratio of 0.90 and cement content of 2.3%. It is noticed that each principal stress direction leads to a stiffness degradation, and it can also be noticed that the results generally increases with the increase of the principal stress direction up to. As for the variation of the shear moduli, it is noticed that the variation of the principal stress direction did not significantly alter the shear moduli response of the cemented sample.

A similar analysis is made for the cemented samples with a void ratio of 0.71 and cement content of 1.8% (Figure 7.40). The shear modulus appears to have a slight variation with the principal stress direction.

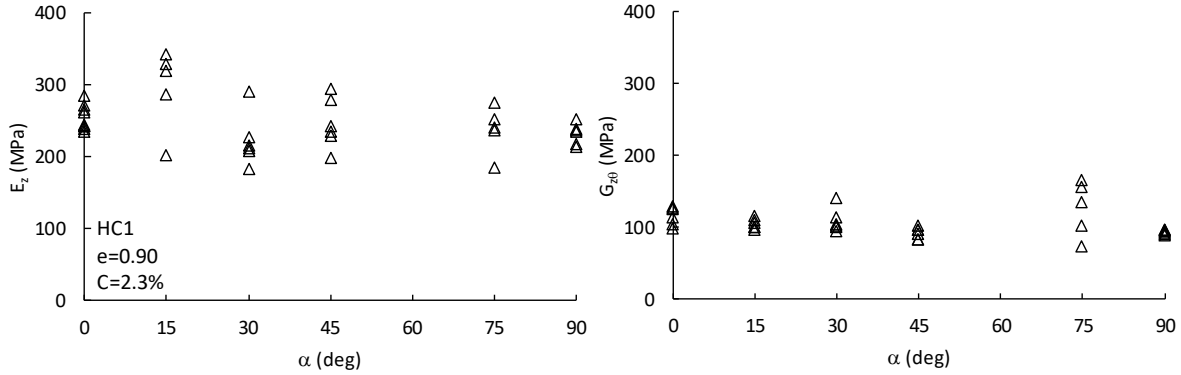


Figure 7.45 – Effect of principal stress on Young's and shear moduli; HC1 (*e*=0.90, C=2.3%)

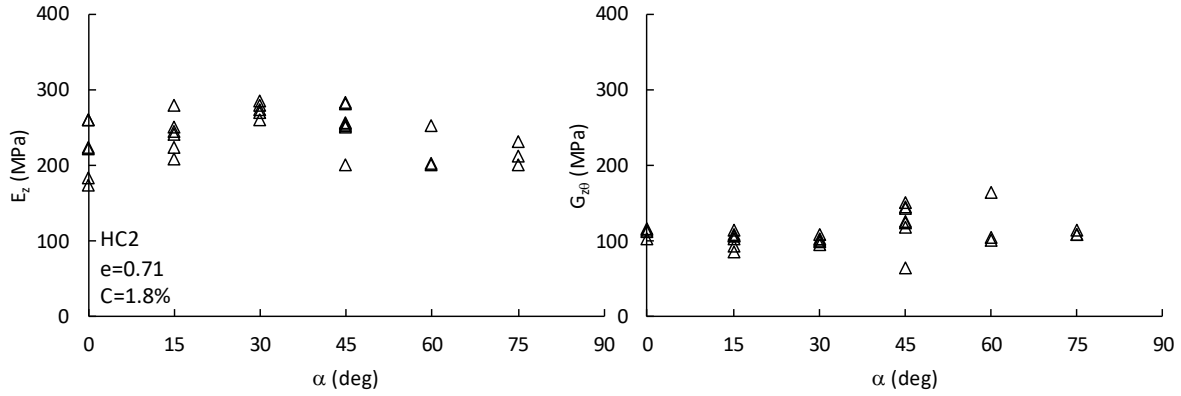


Figure 7.46 – Effect of principal stress on Young's and shear moduli; HC2 (*e*=0.71, C=1.8%)

The analysis of the effect of the principal stress direction on the Young's modulus can be made with the analysis of the *m* and *n* power constants from Section 7.5.4.4. A variation of these power coefficients is observed possibly due to damage to cemented soils structure caused by shearing at different stress paths. This is consistent with observations by Hardin (1978) that Young's modulus in a certain direction is dependent on the normal stress acting in the same direction. This was obtained for a sand, where there were no bond degradations during the application of a normal stress.

The dependency of $G_{z\theta}$ with $(\sigma'_z\ \sigma'_\theta)^{0.5}$ is consistent with the results of Roesler (1979) that the shear modulus is independent of normal stress acting on the plane of shear (σ'_r). However, since σ'_r was kept constant in this experimental program, further investigation is required to confirm the independence of $G_{z\theta}$ from σ'_r for cemented samples.

7.6 SUMMARY

The behaviour of the lightly cemented Hostun sand was analysed through the rotation of principal stresses. It was observed that the influence of the cement content and porosity was higher when the principal stress direction was 0^o, followed by 15^o and 30^o. When α was higher, both cement contents and porosities presented very similar maximum strengths.

After a detailed analysis of the tests results and condition, the variation of both specimen's maximum strength was credited to the volume change that leads to small cementation breakage during consolidation of the more porous sample (corroborated with ROTTA et al., 2003).

As for the stiffness and stiffness evolution, both specimens (HC1 and HC2) presented similar trends, with a small difference between HC1 and HC2 in the analysis of shear modulus.

8 COMPARISON OF CUBICAL CELL AND HOLLOW CYLINDER TORSIONAL TESTS REGARDING A CEMENTED SAND

The intermediate principal stress on the cemented sand presented in this research varied depending on the tests performed. On the cubical cell apparatus, values of $b = (\sigma_2-\sigma_3)/(\sigma_1-\sigma_3)$ imposed were 0, 0.5 and 1. Three-dimensional stress conditions with major principal stress inclination from 0º to 90º were imposed in the hollow cylinder and each degree presents a *b* value varying from 0 to 1. This section correlates with the results in Chapters 6 and 7 regarding the effect of the intermediate principal stress in those tests.

8.1 STRESS CONDITIONS

The stress states that were generated and applied to the cemented sand specimens in the cubical cell apparatus are presented in Figure 8.1. The specimens were assembled and tested following seven stress paths, represented by the θ angle. Each direction corresponded to a *b* value.

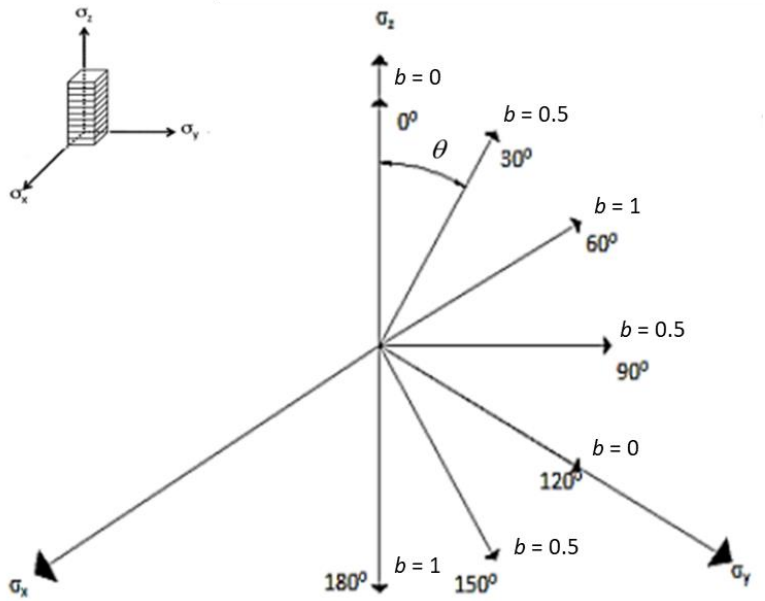


Figure 8.1 – Shear orientation on the octahedral plane

Depending on the stress path applied for a particular test, the vertical force on the hollow cylinder was either in compression or extension. When α varied from 0 to 45 degrees, compression was imposed. After 45 to 90 degrees, extension was applied, as presented in Figure 8.2. This figure also shows the b-values that each direction of the principal stress leads to.

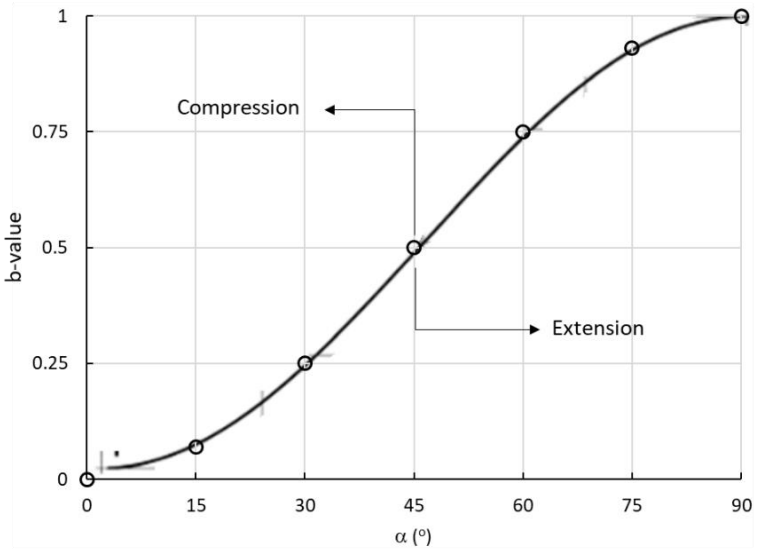


Figure 8.2 – *b*-values that each constant α-values originates

For the two rosettes performed on the cubical cell, Figure 8.3 the variation of the deviatoric stress with the evolution of θ is presented and the corresponding *b* is also identified. It is observed that, as expected, *b*=0 results in higher deviatoric stresses, followed by 0.5 and 1.

The variation of *b* is observed on both true triaxial and hollow cylinder testing. Figure 8.4 presents the deviatoric stress varying with α and the corresponding *b*. The effect of *b* is very pronounced, showing a reduction in the deviatoric stress with an increase in *b*.

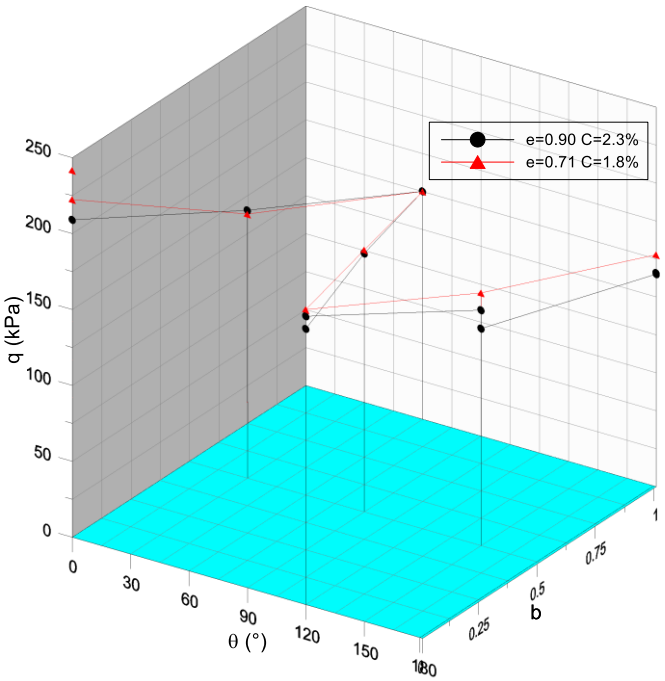


Figure 8.3 – Deviatoric stress varying with θ and b
on the cubical samples

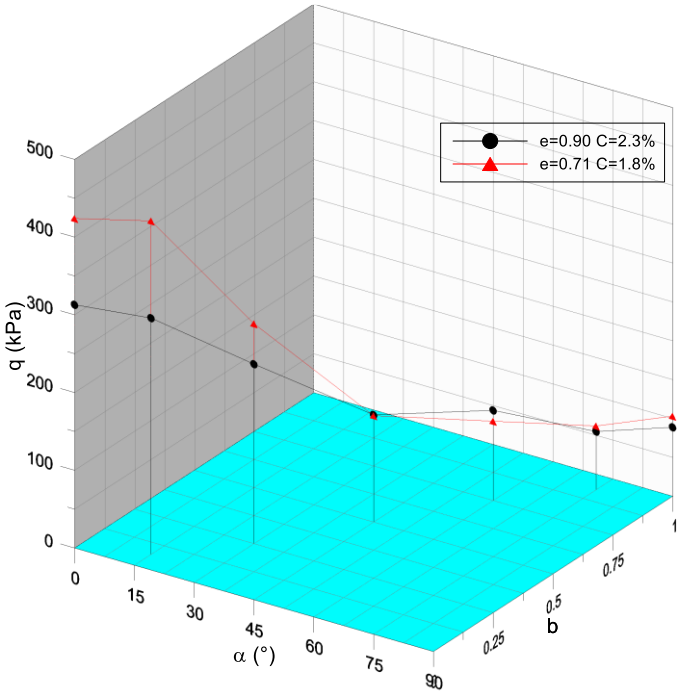


Figure 8.4 – Deviatoric stress varying with α and b o
n the hollow cylinder samples

8.2 COMPARISON

The two sets of tests presented in Section 8.1 were achieved in different apparatus performed with specific test procedures. The comparison of both results was made by combining the same *b*-values of each test. The following analysis was then performed:

a) b = 0: were analysed the tests with θ = 0º and 120 º; and α = 0º;

b) b = 0.5: were analysed the tests with θ = 30º, 90º; 150 º; and α = 45º;

c) b = 1: were analysed the tests with θ = 60º and 180 º; and α = 90º;

The tests performed on the cubical cell had the mean effective stress, *p'*, kept constant during shearing (100kPa). This procedure was not followed for the hollow cylinder tests. To consider the effect of this difference, the results presented in this section were normalized by the mean effective stress.

The first comparison presented is related to b = 0. Figure 8.5 shows the normalized deviatoric stress for each stress with the deviatoric strain observed. It is noticed that the results in the hollow cylinder present lower normalized deviatoric stress, followed by θ = 120 and 0 degrees.

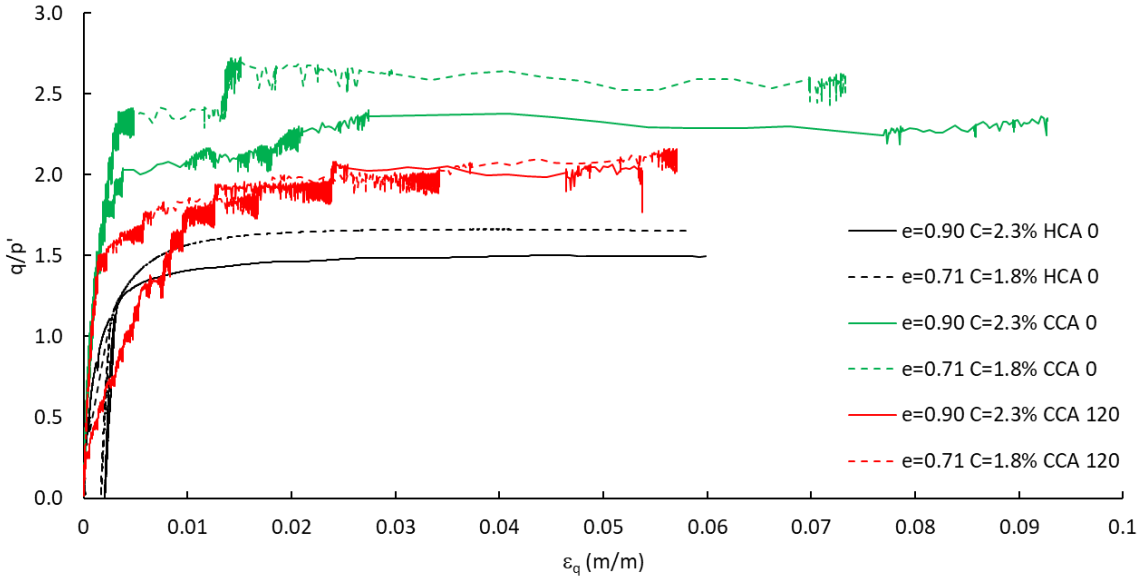


Figure 8.5 – Normalized deviatoric stress versus deviatoric strain, $b = 0$

When comparing the results with $b = 0.5$, it is observed that the results were also lower for the sample performed with pure shear in the hollow cylinder. Figure 8.6 shows that the response of the cemented sand with $\theta = 30^o$, 90^o and 150^o is very similar, while $\alpha = 45^o$ results in lower normalized deviatoric stress.

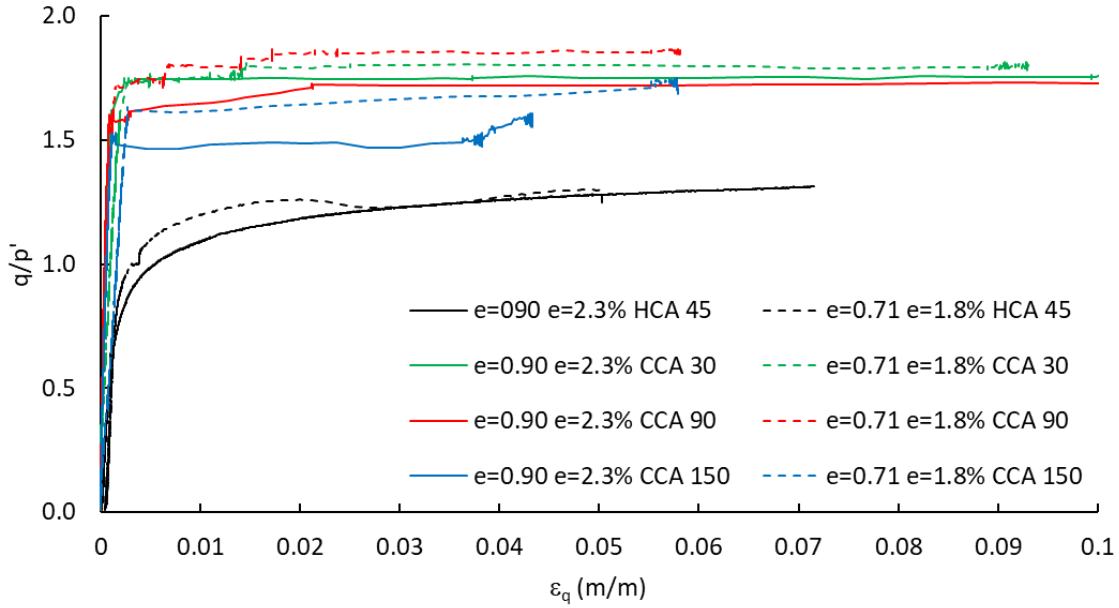


Figure 8.6 – Normalized deviatoric stress versus deviatoric strain, $b = 0.5$

The last comparison was a more severe condition, $b = 1$. On this analysis, it is observed that the results are very similar for all θ imposed and for the extension tests performed on the hollow cylinder, as shown in Figure 8.7.

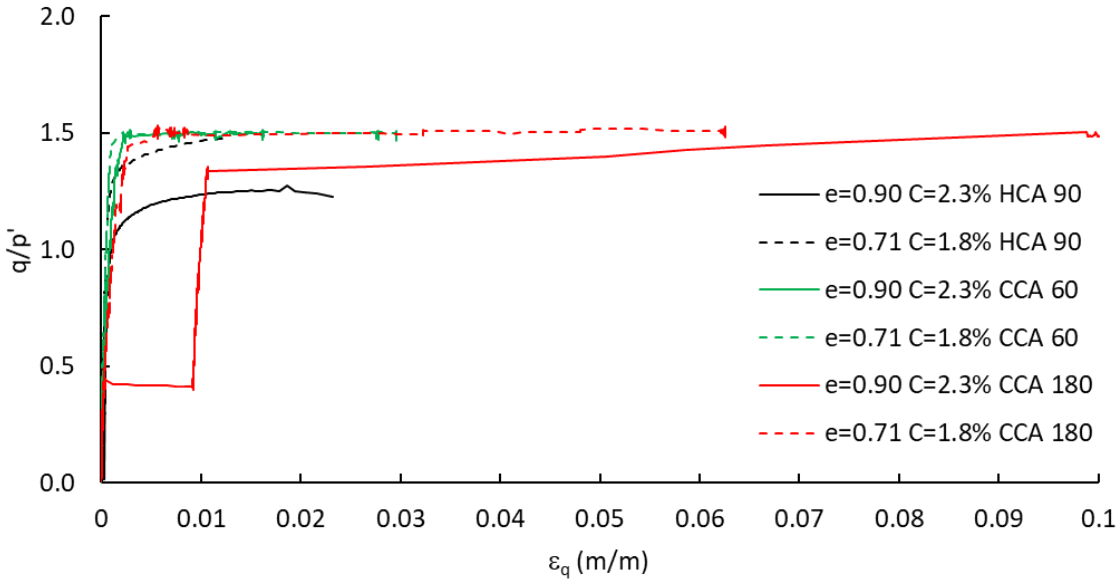


Figure 8.7 - Normalized deviatoric stress versus deviatoric strain, $b = 1$

8.3 SUMMARY

This chapter describes an experimental investigation into the response of the cemented sand on the intermediate principal stress. The cemented soil samples were weakened by the build-up of the intermediate stress. The degree of the weakening appears to not be dependent on the sample composition, presenting similar behaviour for both specimens prepared.

The parameter b was not a negligible factor for the deviatoric stress achieved during rotation of principal axes and during variation of θ. The cemented sand samples tested with b = 0 generally showed stronger resistance.

The difference in the results on the cubical cell and the hollow cylinder are principally linked to the different procedures adopted to prepare the samples; when the results are compared on the octahedral plane, it is observed that this diversion is small. The tests performed in the true triaxial had three flexible faces and three fixes faces. Although this condition exists, the variation of maximum strength on both tests is credited to the fact that specimens tests on the

Hollow Cylinder apparatus were consolidated on the sixth day of curing, while the samples tested on the true triaxial had consolidation on the seventh day, the same as shearing.

9 CONCLUSIONS

This thesis aimed to provide an experimental contribution to the understanding and investigation of the behaviour of a lightly cemented sand under multiaxial loading conditions. It also intended to elucidate the effect of the application of multiple cyclic loading, evaluating the stiffness and stiffness evolution of lightly cemented materials.

This research project involved a preliminary analysis of the unconfined strength (q_u and q_t versus η/C_{iv}) to determine the adopted dosage for the following laboratory investigation. The experimental work has been carried using bender elements, a cubical cell with a large number of displacements measurements and a hollow cylinder triaxial apparatus equipped with a very high-resolution local strain measurement system, composed of six non-contact displacement transducers which allow an accurate evaluation of the small strain stiffness sample and its evolution during cyclic loading.

A summary of conclusions drawn from the work described in earlier chapters is provided in the following sections.

9.1 SUMMARY OF MAIN CONCLUSIONS

The studied lightly cemented sand response under multiaxial loading conditions has been the focus of this thesis. Here, the main obtained conclusions are presented.

Porosity/cement ratio curves

The ratio between the amount of cement and porosity of cemented Hostun sand was observed to lead to unique curves expressing the unconfined compression strength, split tensile strength and initial shear moduli. The three curves were adjusted successfully to the same power (1.40). The ratio q_t/q_u obtained was 0.08. As for the ratio G_0/q_u, it was obtained 2465.

Also, η/C_{iv} was used to define the specimen composition to the following analysis, focusing on a lightly cemented sand with two specific void ratios and cement contents. An η/C_{iv} of 47.2 was targeted with (a) 2.3% cement and void ratio of 0.90 and (b) 1.8% cement and 0.71 void ratio.

Stiffness evolution on cement hydration

The effect of the cement hydration over time was studied with bender elements inserted on a cubic specimen. It was concluded that within the cement hydration, the difference in stiffness, caused by dumping compaction, between vertical and horizontal specimen direction reduces. This was clear for small amounts of cement added to the specimens.

Effect of variation of principal stress direction, θ

It was observed that there is an anisotropic response on the maximum strength with the variation of θ, from 0 to 180º. The effect of the intermediate stress could also be analysed with the variation of the intermediate stress parameter *b*. $b = 1$ clearly decreased the maximum strength observed in the cubical cell, followed by $b = 0.5$ and 0. Also, cementation did not prevent the anisotropic response of the cemented sand when comparing the tests with $\theta = 0^o$ and 120^o, caused by dumping compaction during specimen preparation.

Effect of variation of principal stress direction, α

It was concluded that varying the principal stress direction resulted in specific behaviour responses from the cemented sand specimen. Higher deviatoric strength was observed when the principal stress direction angle, α, was 0^o. By changing α to 15^o, an almost similar deviatoric stress was observed. Although as the angle of the principal stress direction increased, a significant reduction on the cemented soil response, *q*, was observed.

It was also concluded that the degradation imposed by torque, and torque and extension on the cemented samples, resulted on a significant reduction of the maximum deviatoric stress observed.

The analysis of the results on the stresses and shear plane, expressed by $(\sigma_z-\sigma_\theta)/2$ versus τ, shows once again that the cemented soil response is not isotropic. Once more, this anisotropic response is a consequence of sample preparation through dumping compaction in one direction.

The strength parameters obtained were $\phi' = 33^o$, and $c' = 17$ kPa for the samples with void ratio of 0.90 and cement content of 2.3%; notice that from $\alpha = 45^o$ to 90^o no cohesion intercept is observed. The same is valid for the specimen with 0.71 void ratio and 1.8% cement, where the same friction angle was observed, but the cohesion intercept for the compression and compression and torsion tests was 37 kPa.

Evaluation of the intermediate stress

The analysis of true triaxial tests showed that the *b* parameter was not a negligible factor for the maximum deviatoric stress achieved during rotational of principal axes and during variation of Lode's angle. The cemented sand samples tested with b = 0 showed higher resistance. The cemented soil samples were weakened by the build-up of the intermediate stress.

Comparison between hollow cylinder and cubical cell tests

Conditions applied in hollow cylinder and cubical cell tests were not similar. Different sample geometries and fabrication techniques seemed to have affected the behaviour of the studied cemented sand. Cubical cell tests showed slightly higher resistance than hollow cylinder tests when the results were plotted in the q_x x q_z /σ_{oct} plane. Additionally, the slight difference in the peak between both tests could be related to the consolidation on the sixth day for the hollow cylinder samples in comparison to the consolidation on the seventh day for the cubical cell tests.

Stiffness and stiffness evolution during loading

The stiffness parameter of the cemented Hostun sand was measured in the laboratory in a a hollow cylinder apparatus. The hollow cylinder was equipped with high precision non-contact sensors. With the application of small axial cycles, the Young' modulus was obtained, together with the Poisson's ratio. The Young's moduli presented degradation principally caused by the evolution of the torque, once loading occurred. The Poisson's seemed not be affected by loading. When small cycles of toque were applied to the specimen, the shear modulus was obtained. Results showed that the evolution of loading presented degradation of the moduli, especially when the combination of compression+torsional was imposed, although, for the principal direction of $\alpha = 0^o$ and 15^o an increase of the moduli response was observed as the loading occurred.

The small cycles were measured with three different amplitudes, it was observed that the increase of the amplitude did not exceed the elastic stiffness, once all amplitude resulted in similar results and degradation was only observed at higher loading points, where degradation was already expected.

The results showed that the Poisson's ratio was not affected by the direction of principal stress. Also, it was observed that both specimens blends resulted in similar Poisson's ratio.

Cemented sand response focusing on the η/C_{iv} ratio

The target η/C_{iv} was carried out on the tests with two distinguish conditions: one loose and one dense combination of lightly cemented sand. In the analysis on the cubical cell response, no visually distinguish of the results were observed. Both tests had similar peak of strength.

The response of both tests on the hollow cylinder were the same when the combination of torque and extension were imposed. The volume change had distinguished paths, but the peak strength was similar. The variation between both tests could only be observed when compression, and compression and torque were imposed to the cemented sand specimens. With these loading conditions, the sample with lower void ratio presented higher strength peak. This variation was credited to the higher volume change and associated bond breakage during consolidation of the loose sample.

When analysing the small strains, in lower strengths conditions, no significant variation of stiffness between the loose and the dense lightly cemented sand was observed. Only a small variation was observed on the analysis of the shear moduli.

9.2 FURTHER RESEARCH

A list of suggestions for further investigations which may help a better understating of the behaviour of cemented sands is proposed in this section.

Effect of variation of cement content. Although this thesis focused on a lightly cemented sand, a similar analysis with higher cement content and amplitude of void ratio would improve knowledge of the multiaxial loading response of cemented soils.

Effect of variation of consolidation pressure. It is known that the variation of the confining pressure could damage the cementation bonds. With analysis of multiple consolidation pressures, it would be possible to evaluate how this initial parameter would affect the stiffness and peak of strength of the cemented sand.

Influence of b. Analysing this non-dimensional stress parameter with a constant α will help in understanding the relevance of intermediate principal stress without the variation of α.

Small strain stiffness is a fundamental parameter to fully analyse the characterization of such anisotropic material. With the use of bender elements on the cubical cell, it would be possible to evaluate the small strain stiffness during this condition as well. The interpretation of the small strain stiffness will be conducted with the use of invariants of stress and with the inclusion of a small-strain model with consideration of inherent and stress-induced anisotropies. These will be the object of journal papers.

9.3 CLOSURE

This thesis has explored the response of a lightly cemented sand under multiaxial loading conditions using a cubical cell and a hollow cylinder apparatus. Both tests are versatile, and it is expected that the outcome from this research will be beneficial for the understanding and long-term analysis and modelling with cemented soil materials.

REFERENCES

ABBISS, C. P. Shear wave measurements of the elasticity of the ground. **Géotechnique**, v. 31 n. 1, p. 91–104, 1981. https://doi.org/10.1680/geot.1981.31.1.91

ABDULLA, A. A.; KIOUSIS, P. D. Behavior of cemented sands - II. **Modelling. International Journal for Numerical and Analytical Methods in Geomechanics**, v. 21, n. 8, p. 549–568, 1997. https://doi.org/10.1002/(SICI)1096-9853(199708)21:8<549::AID-NAG890>3.0.CO;2-7

ACAR, Y., AND EL-TAHIR, A. Low strain dynamic properties of artificially cemented sand. **Journal of Geotechnical Engineering**, ASCE, v. 112, n. 11, p. 1001–1015, 1986. https://doi.org/10.1061/(ASCE)0733-9410(1986)112:11(1001)

AIREY, D. W.; FAHEY, M. Cyclic response of calcareous soil from the North-West Shelf of Australia. **Géotechnique**, v. 41, n. 1, p. 101–121, 1991. https://doi.org/10.1680/geot.1991.41.1.101

AL-AJMI, A. M.; ZIMMERMAN, R.W. Relation between the Mogi and the Coulomb failure criteria. **International Journal of Rock Mechanics and Mining Sciences**. v. 42, n. 3, p. 431–439, 2005. https://doi.org/10.1016/j.ijrmms.2004.11.004

AMERICAN SOCIETY FOR TESTING AND MATERIALS. **ASTM D1633-17**, Standard Test Methods for Compressive Strength of Molded Soil-Cement Cylinders, ASTM International, West Conshohocken, PA, 2017, www.astm.org

ANDERSEN, K. H.; POOL, J. H.; BROWN, S. F.; ROSENBRAND, W. F. Cyclic and static laboratory tests on Drammen clay. **Journal of Geotechnical Engineering** (ASCE), v. 106, n. GT5, p. 499-529, 1981.

ARTHUR, J. R. F.; MENZIES, B. K. Inherent anisotropy in a sand. **Géotechnique**, v. 22, n. 1, p. 115–128, 1972. https://doi.org/10.1680/geot.1972.22.1.115

ARTHUR, J. R. F.; CHUA, K. S.; DUNSTAN, T. Induced anisotropy in a sand. **Géotechnique**, v. 27, n. 1, p. 13–30, 1977. https://doi.org/10.1680/geot.1985.35.4.471

ARULNATHAN, R.; BOULANGER, R. W.; RIEMER, M. F. Analysis of Bender Element Tests. **Geotechnical Testing Journal**, v. 21, n. 2, p. 120–131, 1998. https://doi.org/10.1520/GTJ10750J

ASHBY, M.; JONES, D. R. H. **Engineering Material: an Introduction to their Properties and Aplications**. New York: Pergamon Press, 1980.

ATKINSON, J. H. Non-linear soil stiffness in routine design. **Géotechnique**, v. 50, n. 5, p. 487–508, 2000. https://doi.org/10.1680/geot.2000.50.5.487

ATKINSON, J. H.; SALLFORS, G. Experimental determination of soil properties. General Report to Session 1. **Proceedings of the 10th ECSMFE**, Florence, v. 3, p. 915-956, 1991.

BAIG, S., PICORNELL, M.; NAZARIAN, S. Low strain moduli of cemented sand. **Journal of Geotechnical and Geoenvironmental Engineering**, v. 123, n. 6, p. 540–545, 1997. https://doi.org/10.1061/(ASCE)1090-0241(1997)123:6(540)

BALDI, G.; NOVA, R. Membrane Penetration Effects in Triaxial Testing. **Journal of Geotechnical Engineering**, v. 110, n. 3, p.403–420, 1984. Available at: https://doi.org/10.1061/(ASCE)0733-9410(1984)110:3(403)

BARDET, J. P. **Experimental soil mechanics**. [s.l.] Prentice Hall, 1997.

BELLOTTI, R.; JAMIOLKOWSKI, M.; LO PRESTI, D. C. F.; 0' NEILL, D. A. Anisotropy of small strain stiffness in Ticino sand, **Géotechnique**, v. 46, n. 1, p. 115-131, 1996. https://doi.org/10.1680/geot.1996.46.1.115

BISHOP, A. W. Strength of soils as engineering materials (Sixth Rankine Lecture). **Géotechnique**, v. 16, n. 2, p. 89–130, 1966. https://doi.org/10.1680/geot.1966.16.2.91

BORTOLOTTO, M. S. **Bender Elements, Ultrasonic Pulse Velocity, and Local Gauges for the Analysis of Stiffness Degradation of an Artificially Cemented Soil**. 2017. 273 p. Master thesis (MSc) – Civil Engineering Graduation Program, Department of Civil Engineering, Federal University of Rio Grande do Sul, Porto Alegre, BR-RS, 2017.

BRIGNOLI, E. G. M.; GOTTI, M.; STOKOE, K. H. Measurement of shear waves in laboratory specimens by means of piezoelectric transducers. **Geotechnical Testing Journal**, v. 19, n. 4, p. 384-397, 1996. https://doi.org/10.1520/GTJ10716J

BROMS, B. B.; CASBARIAN, A. O. Effects of rotation of the principal stress axes and of the intermediate principal stress on the shear strength. 6th International Conference on Soil Mechanics and Foundations, 1964.

BUDHU, M. **Soil mechanics and foundations**. 3rd. ed. [s.l.] John Wiley & Sons, Inc., 2011.

BURLAND, J. B. Small is beautiful: the stiffness of soil at small strains, 9th Laurits Bjerrum Memorial Lecture, **Canadian Geotechnical Journal**, v. 26, p. 499-516, 1989.

CARRARO, J. A. H. **Use of industrial residues in the stabilization of a residual soil**. 2007. 150 p. Master thesis (MSc) – Civil Engineering Graduation Program, Department of Civil Engineering, Federal University of Rio Grande do Sul, Porto Alegre, BR-RS, 2007.

CATTON, M. D. Soil-cement technology—A résumé. Research and Development Laboratories of the Portland Cement Association: **Bulletin 136**. [Reprinted from the Journal of PCA Research and Development Laboratories, v, 4, n. 1, p. 13–21, 1962.

CAZACLIU, B.; DI BENEDETTO, H. Behavior of Sand in the Small Strain Domain Observed with a Hollow Cylinder Apparatus. **Proceedings of 11thECEE**, CD-ROM, Balkema, Rotterdam, p. 10, 1998.

CHANG, T. S.; WOODS, R. D. Effect of particle contact bond on shear modulus. **Journal of Geotechnical Engineering**, v. 118, n. 8, p. 1216–1233, 1992. https://doi.org/10.1061/(ASCE)0733-9410(1992)118:8(1216)

CHAUDHARY, S. K.; KUWANO, J.; HAYANO, Y. Measurement of Quasi-Elastic Stiffness Parameters of Dense Toyoura Sand in Hollow Cylinder Apparatus and Triaxial Apparatus with Bender Elements. **Geotechnical Testing Journal**, v. 27, n. 1, p. 23–35, 2004. https://doi.org/10.1520/GTJ11267J

CHEN, M.; SHEN, S. L.; ARULRAJAH, A.; WU, H. N.; HOU, D. W.; XU, Y. S. Laboratory evaluation on the effectiveness of polypropylene fibers on the strength of fiber-reinforced and cement-stabilized Shanghai soft clay. **Geotextiles and Geomembranes**, v. 43, n. 6, p. 515–523, 2015. https://doi.org/10.1016/J.GEOTEXMEM.2015.05.004

CLARE, K. E.; POLLARD, A. E. The effect of curing temperature on the compressive strength of soil-cement mixtures, **Géotechnique**, v. 4, p. 97-107, 1954. https://doi.org/10.1680/geot.1954.4.3.97

CLAYTON, C. R. I. Stiffness at small strain: research and practice. **Géotechnique**, v. 61, n. 1, p. 5–37, 2011. https://doi:10.1680/geot.2011.61.1.5.

CLAYTON, C. R. I.; HEYMANN, G. Stiffness of geomaterials at very small strains. **Géotechnique**, v. 51, n. 3, p. 245-255, 2001. https://doi.org/10.1680/geot.2001.51.3.245

CLAYTON, C. R. I.; PRIEST, J. A.; REES, E. V. L. The effects of hydrate cement on the stiffness of some sands. **Géotechnique**, v. 60, p. 435-445, 2010. https://doi:10.1680/geot.2010.60.6.435.

CLAYTON, C. R. I.; THERON, M.; BEST, A. I. The measurement of vertical shear-wave velocity using side-mounted bender elements in the triaxial apparatus. **Géotechnique**, v. 54, n.7, p. 495-498, 2010. https://doi.org/10.1680/geot.2004.54.7.495

CLOUGH, G. W.; SITAR, N.; BACHUS, R. C. Cemented Sands Under Static Loading. **Journal of the Geotechnical Engineering Division**, v. 107, n. 6, p. 799–817, 1981.

CLOUGH, R, W.; PENZIEN, J. **Dynamic of structures**. 2nd. e.d [s.l.] McGraw-Hill, 1993.

CONSOLI, N. C. A method proposed for the assessment of failure envelopes of cemented sandy soils. **Engineering Geology**, v. 169, n. 2, p. 611-68, 2014. https://doi.org/10.1016/j.enggeo.2013.11.016

CONSOLI, N. C.; BASSANI, M. A.; FESTUGATO, L. Effect of fiber-reinforcement on the strength of cemented soils. **Geotextiles and Geomembranes**, v. 28, p. 344-351, 2010a.

https://doi.org/10.1016/j.geotexmem.2010.01.005

CONSOLI, N. C.; CRUZ, R. C.; CONSOLI, B. S.; MAGHOUS, S. Failure envelope of artificially cemented sand. **Géotechnique**, v. 62, n. 00, p. 1–5, 2012a. https://doi.org/10.1680/geot.11.P.037

CONSOLI, N. C.; CRUZ, R. C.; FLOSS, M. F.; FESTUGATO, L. Parameters controlling tensile and compressive strength of artificially cemented sand. **Journal of Geotechnical and Geoenvironmental Engineering**, v. 136, p. 759-763, 2010b. https://doi.org/10.1061/(ASCE)GT.1943-5606.0000278

CONSOLI, N. C.; da FONSECA, A. V.; SILVA, S. R.; CRUZ, R. C.; FONINI, A. Parameters controlling stiffness and strength of artificially cemented soils. **Géotechnique**, v. 62, n. 2, p. 177-183, 2012b. https://doi.org/10.1680/geot.8.P.084

CONSOLI, N. C.; da ROCHA, C. G.; SILVANI, C. Effect of Curing Temperature on the Strength of Sand, Coal Fly Ash, and Lime Blends. **Journal of Materials in Civil Engineering**, v. 26, p. 06014015, 2014. https://doi.org/10.1061/(ASCE)MT.1943-5533.0001011

CONSOLI, N. C.; DA SILVA, A. P.; NIERWINSKI, H. P.; SOSNOSKI, J. Durability, strength, and stiffness of compacted gold tailings - cement mixes. **Canadian Geotechnical Journal**, v. 55, p. 486-494, 2018b. https://doi.org/10.1139/cgj-2016-0391

CONSOLI, N. C.; DALLA ROSA, A.; CORTE M. B.; LOPES JUNIOR, L. S.; CONSOLi B. S. Porosity/cement ratio controlling strength of artificially cemented clays. **Journal of Materials in Civil Engineering**, v. 23, p. 1249-1254, 2011c. https://doi.org/10.1061/(ASCE)MT.1943-5533.0000283

CONSOLI, N. C.; FERREIRA, P. M. V.; TANG, C.; MARQUES, S.;FESTUGATO, L.; CORTE, M. B. A unique relationship determining strength of silty/clayey soils - Portland cement mixes. **Soils and foundations**, v. 56, p. 1082-1088, 2016. https://doi.org/10.1016/j.sandf.2016.11.011

CONSOLI, N. C.; FESTUGATO, L.; da ROCHA, C .G.; CRUZ, R. C. Key parameters for strength control of rammed sand-cement mixtures: Influence of types of portland cement. **Construction & Building Materials**, v. 49, p. 591-597, 2013. https://doi.org/10.1016/j.conbuildmat.2013.08.062

CONSOLI, N. C.; FESTUGATO, L.; HEINECK, K. S. Strain-hardening behaviour of fibre-reinforced sand in view of filament geometry. **Geosynthetics International**, v. 16, n. 2, p. 109-115, 2009a. https://doi.org/10.1680/gein.2009.16.2.109

CONSOLI, N. C.; FOPPA, D. Porosity/cement ratio controlling initial bulk modulus and incremental yield stress of an artificially cemented soil cured under stress. **Géotechnique Letters**, v. 4, n. 1, p. 22-26, 2014. https://doi.org/10.1680/geolett.13.00081

CONSOLI, N. C.; MORAES R. R.; FESTUGATO, L. Split tensile strength of monofilament polypropylene fiber-reinforced cemented sandy soils. **Geosynthetics International**, v. 18, p. 57-62, 2011b. https://doi.org/10.1680/gein.2011.18.2.57

CONSOLI, N. C.; PRIETTO, P. D. M.; ULBRICH, L. A. Influence of fiber and cement addition on behavior of sandy soil. **Journal of Geotechnical and Geoenvironmental Engineering**, v. 124, n. 12, p. 1211-1214, 1998. https://doi.org/10.1061/(ASCE)1090-0241(1998)124:12(1211)

CONSOLI, N. C.; QUINONEZ SAMANIEGO, R. A.; VELÁSQUEZ, L. E. G.; BITTAR MARIN, E. J.; CUISINIER, O. The impact of severe climate conditions on loss of mass, strength and stiffness of compacted fine-grained soils-Portland cement blends. **Journal of Materials in Civil Engineering**, v. 30, p. 04018174, 2018a. https://doi.org/10.1061/(ASCE)MT.1943-5533.0002392

CONSOLI, N. C.; ROTTA, G. V.; PRIETTO, P. D. M. A. Influence of curing under stress on the triaxial response of cemented soils. **Géotechnique**, v. 50, n. 1, p. 99-105, 2001. https://doi.org/10.1680/geot.2000.50.1.99

CONSOLI, N. C.; TOMASI, L. F. The impacto f dry unit weight and cement contente on the durability of sand-cement blends. **Proceedings of the Institution of Civil Engineers – Ground Improvement**, v. 171, n. 2, p. 96-102, 2018. https://doi.org/10.1680/jgrim.17.00034

CONSOLI, N. C.; VENDRUSCOLO, M. A.; FONINI, A.; DALLA ROSA, F. Fiber reinforcement effects on sand considering a wide cementation range. **Geotextiles and Geomembranes**, v. 27, n. 3, p. 196-203, 2009b. https://doi.org/10.1016/j.geotexmem.2008.11.005

CONSOLI, N. C.; VENDRUSCOLO, M. A.; PRIETTO, P. D. M. A. Behaviour of plat load tests on soil layers improved with cement and fiber. **Journal of Geotechnical and Geoenvironmental Engineering**, v. 129, n. 1, p. 96-101, 2003. https://doi.org/10.1061/(ASCE)1090-0241(2003)129:1(96)

CONSOLI, N. C.; ZORTÉA, F.; SOUZA, M.; FESTUGATO, L. Studies on the dosage of fiber-reinforced cemented soils. **Journal of Materials in Civil Engineering**, v. 23, p. 1624-1632, 2011a. https://doi.org/10.1061/(ASCE)MT.1943-5533.0000343

CONSOLI, N.C.; FOPPA, D.; FESTUGATO, L.; HEINECK, K. S. Key parameters for strength control of artificially cemented soils. **Journal of Geotechnical and Geoenvironmental Engineering**, v. 133, p. 197-205, 2007. https://doi.org/10.1061/(ASCE)1090-0241(2007)133:2(197)

CONSOLI, N.C.; NIERWINSKI, H. P.; PECCIN, A.; SOSNOSKI, J. Durability and strength of fiber-reinforced compacted gold tailings-cement blends. **Geotextiles and Geomembranes**, v. 45, p. 98-102, 2017. https://doi.org/10.1016/j.geotexmem.2017.01.001

CONSOLI, N.C.; ROTTA, G. V. ; PRIETTO, P. D. M. Yielding-compressibility-strength relationship for an artificially cemented soil cured under stress. **Géotechnique**, v. 56, n.1, p. 69-72, 2006. https://doi.org/10.1680/geot.2006.56.1.69

CONSOLI, N.C.; SCHNAID, F.; THOMÉ, A.; MANTARAS, F. M. Determination of Constitutive Parameters from Pressuremeter Tests in Lightly Cemented Soils. **In: Numerical Methods in Geomechanics**, 1997, Montreal. V NUMOG. Rotterdam: Balkema, v. 1, p. 647-651, 1997.

CONSOLI, N.C.; THOMÉ, A.; DONATO, M.; GRAHAM, J. Loading tests on compacted soil, bottom ash and lime layers. **Proceedings of the Institution of Civil Engineers**. Geotechnical Engineering, v. 161, p. 29-38, 2008. https://doi.org/10.1680/geng.2008.161.1.29

COOP, M. R.; ATKINSON, J. H. The mechanics of cemented carbonate sands. **Géotechnique**, v. 43, n. 1, p. 53-67, 1993. https://doi.org/10.1680/geot.1993.43.1.53

CRUZ, R. C. **Influence of fundamental parameters on the stiffness, strength and expansion of an artificially cemented sand**. 2008. Thesis (D.Sc.) – Civil Engineering Graduation Program, Department of Civil Engineering, Federal University of Rio Grande do Sul, Porto Alegre, BR- RS, 2008. In Portuguese.

CRUZ, R. C. **Influência de parâmetros fundamentais na rigidez, resistência e dilatância de uma areia artificialmente cimentada**. 2008. Thesis (D.Sc.) – Civil Engineering Graduation Program, Department of Civil Engineering, Federal University of Rio Grande do Sul, Porto Alegre, BR- RS, 2008. In Portuguese.

CUCCOVILLO, T.; COOP, M. R. On the mechanics of structured sands. **Géotechnique**, v. 49, n. 6, p. 741-760, 1990. https://doi.org/10.1680/geot.1999.49.6.741

CUCCOVILLO, T.; COOP, M. R. Yeldind and pre-failure deformation of structured sands. **Géotechnique**, v. 47, n. 3, p. 491-508, 1997. https://doi.org/10.1680/geot.1997.47.3.491

CUSS, R. J.; RUTTER, E. H.; HOLLOWAY, R. F. The application of critical state soil mechanics to the mechanical behaviour of porous sandstones. **International Journal of Rock Mechanics & Mining Sciences**, v. 40, p. 847–862, 2003. https://doi.org/10.1016/S1365-1609(03)00053-4

DALLA ROSA, F. **Effect of curing stress state on the behaviour of an artificially cemented sand**. 2009. 191 p. Thesis (D.Sc.) – Civil Engineering Post-Graduation Program, Department of Civil Engineering, Federal University of Rio Grande do Sul, Porto Alegre, BR-RS, 2009. In Portuguese.

DAS, B. M.; DASS, R. N. Lightly cemented sand in tension and compression. **Geotechnical and Geological Engineering**, v. 13, n. 3, p. 169–177, 1995. https://doi.org/10.1007/BF00456716

DASS, R. N.; YEN, S. C.; DAS, B. M.; PURI, V. K.; WRIGHT, M. A. Tensile stress–strain characteristics of lightly cemented sand. **Geotechnical Testing Journal**, v. 17, n. 3, p. 305–314, 1994. https://doi.org/10.1016/0148-9062(93)90011-2

DEWOOLKAR, M.; GODDERY, T.; STURE, S.; KO, H. Y. Multiaxial cubical cell apparatus for cohesive and cohesionless soils: **Description and users manual. Department of Civil**, Environmental and Architectural Engineering, University of Colorado, Boulder, 1997.

DI BENEDETTO, H.; GEOFFROY, H.,; SAUZÉAT, C.; CAZACLIU, B. Sand behaviour in very small to medium strain domains, **2nd International Symposium on Pre-failure Deformation Characteristics of Geomaterials.** Volume: Jamialkowski, Lancelotta & Lo Presti (eds), p.89-96, 1999.

DIAMBRA, A.; IBRAIM, E. Fibre-reinforced sand: interaction at the fibre and grain scale. **Géotechnique**, v. 64, n. 4, p. 296–308, 2015. https://doi.org/10.1680/geot.14.P.206

DIAMBRA, A.; IBRAIM, E.; FESTUGATO, L.; CORTE, M. B. Stiffness of artificially cemented sands: insight on characterisation through empirical power relationships, **Road Materials and Pavement Design**, 2019. https://doi.org/10.1080/14680629.2019.1705379

DIAMBRA, A.; IBRAIM, E.; MUIR WOOD, D.; RUSSELL, A. R. Fibre reinforced sands: experiments and modelling. **Geotextiles and Geomembranes**, v. 28, n. 3, p. 238–250, 2010. https://doi.org/ 10.1016/j.geotexmem.2009.09.010.

DIAMBRA, A.; IBRAIM, E.; PECCIN, A.; CONSOLI, N. C.; FESTUGATO, L. Theoretical derivation of artificially cemented granular soil strength. **Journal of Geotechnical and Geoenvironmental Engineering**, v. 143, n. 5, 04017003, 2017. https://doi.org/10.1061/(ASCE)GT.1943-5606.0001646.

DIAMBRA, A.; IBRAIM, E.; PECCIN, A.; CONSOLI, N. C.; FESTUGATO, L. Theoretical derivation of artificially cemented granular soil strength. Journal of **Geotechnical and Geoenvironmental Engineering**, v. 143, n. 5, p. 1–9, 2017. https://doi.org/10.1061/(ASCE)GT.1943-5606.0001646

DIAMBRA, A.; IBRAIM, E.; RUSSEL, A.; WOOD, D. M. Fibre reinforced sands: from experiments to modelling and beyond. **Int. J. Numer. Analyt. Methods Geomech**, v. 37, p. 2427–2455, 2013. https://doi.org/10.1002/nag.2142.

DIAMBRA, A.; IBRAIM, E.; RUSSEL, A.; WOOD, D. M. Modelling the undrained response of fibre reinforced sands. **Soils and Foundations,** v. 51, n. 4, p. 625-636, 2011. https://doi.org/10.3208/sandf.51.625

dos SANTOS, A. P. S. **Comportamento de misturas solo-cimento-fibra sob altas pressões**. 2002. Thesis (D.Sc.) – Civil Engineering Graduation Program, Department of Civil Engineering, Federal University of Rio Grande do Sul, Porto Alegre, BR- RS, 2002. In Portuguese.

DRUCKER, D. C.; PRAGER, W. Soil mechanics and plastic analysis dor limit design, **Quarterly of Applied Mathematics**, v. 10, n. 2, p. 157-165, 1952.

DUNCAN, J. M.; AND CHANG, C. Y. Nonlinear analysis of stress and strain soils. **Journal of the Soil Mechanics and Foundation Division**, v. 96, n. SM5, p. 1629-1653, 1970.

DUPAS, J.M.; PECKER, A. Static and dynamic properties of sand-cement. **Journal of the Geotechnical Engineering Division**, ASCE, v. 105, n. GT3, p. 419–435, 1979.

DUTTINE, A.; BENEDETTO, H. DI.; BANG, D. P. VAN; EZAOUI, A. Anisotropic small strain elastic properties of sands and mixture of sand-clay measured by dynamic and static methods. **Soils and Foundations**, v. 47, n. 3, p. 457–472, 2007. https://doi.org/10.3208/sandf.47.457

DYVIK, R.; MADSHUS, C. Laboratory measurements of Gmax using bender elements. **Proc. ASCE Annual Convention**: Advances in the art of testing soils under cyclic conditions, Detroit, Michigan, p. 186-197, 1985.

DYVIK, R.; OLSEN, T.S. Gmax measured in oedometer and DSS tests using bender elements. **Proceedings of the Twelfth International Conference on Soil Mechanics and Foundation Engineering**, Rio de Janeiro, v. 1, p. 39-42, 1989.

ESCRIBANO, D. L. **Evolution of stiffness and deformation of Hostun sand under drained cyclic loading**, PhD Thesis, University of Bristol. 2014

FAM, M. A.; CASCANTE, G.; DUSSEAULT, M. B. Large and Small Strain Properties of Sands Subjected to Local Void Increase, **Journal of Geotechnical and Geoenvironmental Engineering**, v. 128, n.12, p. 1018-1025, 2002. https://doi.org/10.1061/(ASCE)1090-0241(2002)128:12(1018)

FAM, M. A.; SANTAMARINA, J. C. Study of geoprocesses with complementary wave measurements in an oedometer. **Geotechnical Testing Journal**, v. 19, n. 4, p. 307–314, 1995. https://doi.org/10.1520/GTJ10999J

FARO, V. P. **Carregamento lateral em fundações profundas associadas a solos tratados: concepção, provas de carga e diretrizes**. 2014. Thesis (D.Sc.) – Civil Engineering Graduation Program, Department of Civil Engineering, Federal University of Rio Grande do Sul, Porto Alegre, BR- RS, 2017. In Portuguese.

FELT, E. J. Factors influencing physical properties of soil-cement mixtures. Research and Development Laboratories of the Portland Cement Association**: Bulletin D5**, Authorized Reprint from Bulletin 108 of the Highway Research Board, 1955.

FERNANDEZ, A. L.; SANTAMARINA, J. C. Effect of cementation on the small-strain parameters of sands. **Canadian Geotechnical Journal**, v. 38, n. 1, p. 191–199, 2001. https://doi.org/10.1139/t00-081

FERREIRA, C. **The use of seismic wave velocities in the measurement of stiffness of a residual soil**. 2008. 456 p. Thesis (D.Sc.) – Faculty of Engineerinf, University of Porto, Porto, Portugal, 2008.

FERREIRA, C.; VIANA DA FONSECA, A.; SANTOS, J. A. (2007). Comparison of simultaneous bender elements and resonant column tests on Porto residual soil, Soil Stress-Strain Behavior: Measurement, Modeling and Analysis. **A Collection of Papers of the Geotechnical Symposium in Rome**, 2006, Ling, Callisto, Leshchinsky & Koseki (Eds.). Springer. p. 523-535. https://doi.org/10.1007/978-1-4020-6146-2_34

FESTUGATO, F. **Comportamento de hidratação e Resposta Cisalhante Cíclica de Resíduos de Mineração Cimentado Reforçado com Fibras**. 2011. 221 p. Thesis (D.Sc.) – Civil Engineering Post-Graduation Program, Department of Civil Engineering, Federal University of Rio Grande do Sul, Porto Alegre, BR-RS, 2011. In Portuguese.

FESTUGATO, L.; CORTE, M. B. 2018. Discussion of Unconfined Compressive Strength of Synthetic and Natural Mine Tailings Amended with Fly Ash and Cement by Mohammad H. Gorakhki and Christopher A. Bareither. **Journal of Geotechnical and Geoenvironmental Engineering**, v. 144, p. 07018009. https://doi.org/10.1061/(ASCE)GT.1943-5606.0001879

FESTUGATO, L.; MENGER, E.; BENEZRA, F.; KIPPER, E. A.; CONSOLI, N. C. Fibre-reinforced cemented soils compressive and tensile strength assessment as a function of filament length. Geotextiles and Geomembranes, 45(1), 77–82, 2017. https://doi.org/10.1016/j.geotexmem.2016.09.001

FIORAVANTE, V. Anisotropy of small strain stiffness of Ticino and Kenya sands from seismic wave propagation measured in triaxial testing. **Soils and Foundation,** v. 40, n. 4, p. 129–142, 2000. https://doi.org/10.3208/sandf.40.4_129

FIORAVANTE, V.; CAPOFERRI, R., On the Use of Multi- Directional Piezoelectric Transducers in Triaxial Testing. **Geotechnical Testing Journal**, v. 24, n. 3, p. 243–255, 2001. https://doi.org/10.1520/GTJ11344J

FLOSS, M. F. **Parameters controlling the resistance and stiffness of artificially cemented granular soils**. 2012. Thesis (D.Sc.) – Civil Engineering Graduation Program, Department of Civil Engineering, Federal University of Rio Grande do Sul, Porto Alegre, BR- RS, 2012. In Portuguese.

FONINI, A. **Comportamento Mecânico de uma Areia Cimentada: Análise Experimental e Micromecânica**. 2012. 201 p. Thesis (D.Sc.) – Civil Engineering Post-Graduation Program, Department of Civil Engineering, Federal University of Rio Grande do Sul, Porto Alegre, BR-RS, 2012. In Portuguese.

FONSECA, A. V.; FERREIRA, C.; FAHEY, M. A Framework Interpreting Bender Element Tests, Combining Time-Domain and Frequency-Domain Methods. **Geotechnical Testing Journal**, v. 32, n. 2, p 1-17, 2009. https://doi.org/10.1520/GTJ100974

FOPPA, D. **New Method for Calculating Bearing Capacity of Footings Resting on Soil-Cement Layers**. 2016. 229 p. Thesis (D.Sc.) – Civil Engineering Graduation Program, Department of Civil Engineering, Federal University of Rio Grande do Sul, Porto Alegre, BR-RS, 2017. In Portuguese.

FRATTA, D.; SANTAMARINA, L C. Wave propagation in Soils: Muilt-Mode, Wide-Band Testing in a Waveguide Device. **Geotechnical Testing Journal**, v. 19, n. 2, p. 130-140, 1996. ttps://doi.org/10.1520/GTJ10336J

FRYDMAN, S.; ZEITLEN, J.; ALPAN, I. Membrane Effect in Triaxial Testing of Granular Soils. **Journal of Testing and Evaluation**, v. 1, n. 1, p. 37–41, 1973. https://doi.org/10.1520/JTE11599J

GAJO, A.; FEDEL, A.; MONGIOVI, L. Experimental analysis if the effects of fluid-solid coupling on the velocity of elastic waves in saturated porous media. **Géotechnique**, v. 47, n. 5, p. 993-1008, 1997. https://doi.org/10.1680/geot.1997.47.5.993

GAJO, A.; WOOD, D.M. Severn–Trent sand: a kinematic-hardening constitutive model: the q–p formulation. **Géotechnique**, v. 49, n. 5, p. 595–614, 1999. https://doi.org/10.1680/geot.1999.49.5.595.

GASPARRE, A.; HIGHT, D. W.; COOP, M. R.; RJARDINE, R. J. The laboratory measurement and interpretation of the small-strain stiffness of stiff clays. **Géotechnique**, v. 64, n. 12, p. 942-953, 2014. https://doi.org/10.1680/geot.13.P.227

GEOFFROY, H.; DI BENEDETTO, H.; DUTTINE, A.; SAUZEAT, C. Dynamic and cyclic loadings on sand: results and modelling for general stress-strain conditions. **Proc. of 3rd IS on Pre-failure Deformation Characteristics of Geomaterials**, Lyon, v. 1, p. 353-363, 2003.

GREENING, P. D.; NASH, D. F. T. Frequency domain determination of G0 using bender elements. **Geotechnical Testing Journal**, v. 27, n. 3, p. 288-296, 2004. https://doi.org/10.1520/GTJ11192

HABIB, P. Influence de la variation de la contrainte principale moyenne sur la résistance au cisaillement des sols. **Proc. Third International Conference on Soil Mechanics and Foundation Engineering**, v. 1, p. 100-105, 1953.

HAMEURY, O. (1995). **Quelques aspects du comportement des sables avec ou sand rotation des axes principauxx des petites aux grandes deformations**. PhD Thesis, ECP/ENTE France.

HERRIN, M.; MITCHELL, H. Lime-soil-mixtures. **Highway Research Board Bulletin**, Washington, n.304, p. 99-121, 1961.

HIGHT, D. W.; GENS, A.; SYMES, M. J. The development of a new hollow cylinder apparatus for investigating the effects of principal stress rotation in soils. **Géotechnique**, v. 33, n. 4, p. 355–383, 1983. https://doi.org/10.1680/geot.1983.33.4.355

HOQUE, E; TATSUOKA, F. Effects of stress ratio on small-strain stiffness during triaxial shearing. **Géotechnique**, v. 54, n. 7, p. 429–439, 2004. https://doi.org/10.1680/geot.2004.54.7.429

HUANG, J. T.; AIREY, D. W. Properties of Artificially Cemented Carbonate Sand. **Journal of the Geotechnical and Geoenvironmental. Engineering**, v. 124, n. 6, p. 492-499, 1998. http://doi.org/10.1061/(ASCE)1090-0241(1998)124:6(492)

IBRAIM, E.; CHRISTIAENS, P.; POPE, M. Development of a hollow cylinder torsional apparatus for pre-failure deformation and large strains behaviour of sand. **Geotechnical Engineering**, v. 42, n. 4, p. 58–68, 2011.

INGLES, O. G.; METCALF, J. B. **Soil stabilization—Principles and practice**, Butterworths, Australia, 1972.

ISHIHARA, K. **Soil behavior in earthquake geotechnics**. [s.l.] Clarendon Press - Oxford, 1996.

ISHIHARA, K.; YAMADA, Y. Liquefaction tests using a true triaxial apparatus. Soil Mechanics and Foundation Engineering. **Proc. 10th International Conference**, Stockholm, June 1981. v. 3, (A.A.Balkema), p. 235–238, 1981.

ISMAIL, M. A.; HOURANI, Y, An innovative facility to measure shear-wave velocity in centrifuge and 1-g models, **Proceedings of Deformation Characteristics of Geomaterials**, Lyon, France, 22-24 September, Lyon, France. Balkema, p 21-29, 2003.

ISMAIL, M. A.; JOER, H. A.; SIM, W. H.; RANDOLPH, M. F. Effect of cement type on shear behavior of cemented calcareous soil. **Journal of Geotechnical and Geoenvironmental Engineering**, v. 128, n. 6, p. 520–529, 2002. https://doi.org/10.1061/(ASCE)1090-0241(2002)128:6(520)

ISMAIL, M. A.; JOER. H. A.; SIM, W. H.; RANDOLPH, M. F. Effect of Cement Type on Shear Behavior of Cemented Calcareous Soil. **Journal of Geotechnical and Geoenvironmental Engineering**, v. 128, n. 6, p. 520-529, 2002. https://doi.org/10.1007/s10706-004-7793-1

ISMAIL, M. A.; SHARMA, S. S.; FAHEY, M. A small true triaxial apparatus with wave velocity measurement. **Geotechnical Testing Journal**, v. 28. n. 2, p. 113–122, 2005. https://doi.org/10.1520/GTJ12648

JALALI, S.; ABYANEH, M. Y.; KEEDWELL, M. J. Differential scanning calorimetry tests applied to lime-fly ash soil stabilization. **Testing soil mixed with waste or recycled materials**, STP 1275, ASTM, West Conshohocken, Pa., p. 181–191, 1997. https://doi.org/10.1520/STP15651S

JAMIOLKOWSKI, M.; LANCELLOTTA, R.; LO PRESTI, D.C.F. Remarks of the stiffness at small strains of six Italian Clays. In: **Balasubramaniam, et al.** (Eds), Developments in

Deep Foundations and Ground Improvement Schemes. Balkema, Rotterdam, p. 197–216, 1995.

JARDINE, R. J. Non-linear stiffness parameters from undrained pressuremeter tests. **Canadian Testing Journal**, v. 29, n. 3, p. 436-447, 1992. https://doi.org/10.1139/t92-048

JARDINE, R.J.; SYMES, M.J.; BURLAND, J.B. The Measurement of soil stiffness in the triaxial apparatus. **Géotechnique**, v. 34, n. 3, p. 323–340, 1984. Available at: https://doi.org/10.1680/geot.1984.34.3.323.

JOHANN, A. D. **Methodologies for predicting the mechanical behaviour of porosity of a silty soil treated with lime over long periods of curing**. 2013. Thesis (D.Sc.) – Civil Engineering Graduation Program, Department of Civil Engineering, Federal University of Rio Grande do Sul, Porto Alegre, BR- RS, 2013. In Portuguese.

JOVIČIĆ, V. Rigorous bender element testing, **Workshop on Bender Element Testing of Soils**, University College, London, 2004.

JOVIČIĆ, V. **The measurement and interpretation of small strain stiffness of soils**.1997. 181 p. Thesis (PhD) - Civil Engineering Department, City University, London, UK, 1997.

JOVIČIĆ, V.; COOP, M. R.; SIMIĆ, M. Objective criteria for determining Gmax from bender element tests. **Géotechnique**, v. 46, n. 2, p. 357–362, 1996. https://doi.org/10.1680/geot.1996.46.2.357

KAMON, M.; NONTANANANDH, S. Combining Industrial Wastes with Lime for Soil Stabilization. **Journal of Geotechnical Engineering**, v. 117, p. 1-17, 1991. https://doi.org/10.1061/(ASCE)0733-9410(1991)117:1(1)

KARASUDHI, P. **Foundations of solid mechanics: Solid Mechanics and its Applications.** Springer Science+Business Media, 1991. 3v

KIM, M. K.; LADE, P. V. Single hardening constitutive model for frictional materials. I. Plastic potential Function. **Computers and Geotechnics**, v. 5, n. 4, p. 307–324, 1988. https://doi.org/10.1016/0266-352X(88)90009-2

KO, H. Y.; SCOTT, R. F. Deformation of Sand in Shear. **Journal of the Soil Mechanics and Foundation Division**. ASCE, v. 93, SM5, p. 283-310, 1967.

KOKUSHO, T. Cyclic triaxial test of dynamic soil properties for wide strain range. **Soils and Foundations**, v. 20, n. 2, p. 45–60, 1980. https://doi.org/10.3208/sandf1972.20.2_45

KOKUSHO, T.; YOSHIOKA, Y.; ESASHI, Y. Dynamic Proper- ties of Soft Clay for Wide Strain Range. **Soils and Foundations**, v. 22, n. 4, p. 1–18, 1985. https://doi.org/10.3208/sandf1972.22.4_1

KUWANO, R.; CONNOLLY, T.M.; JARDINE, R.J. Anisotropic stiffness measurements in a stress-path triaxial cell. **Geotechnical Testing Journal**, v. 23, n. 2, p. 141–157, 2000. https://doi.org/10.1520/GTJ11039J

KUWANO, R.; JARDINE, R.J. On the applicability of cross-anisotropic elasticity to granular materials at very small strains. **Géotechnique**, v. 52, n. 10, p.727–749, 2002. Available at: https://doi.org/10.1680/geot.2002.52.10.727.

LADD, R. S. Preparing test specimens using undercompation. **Geotechnical Testing Journal**, v. 1, n. 1, p. 40–57, 1967. https://doi.org/10.1520/GTJ10364J

LADE, P. V.; DUNCAN, J. M. Cubical Triaxial Tests on Cohesionless Soil. **Journal of the Soil Mechanics and Foundation Division**. ASCE, v. 99, (SM10), p. 793–781, 1973. https://doi.org/10.1016/0148-9062(74)91579-4

LADE, P. V.; KIM, M. K. Single hardening constitutive model for frictional materials II. Yield criterion and plastic work contours. **Computers and Geotechnics,** v. 6, n. 1, p. 13-29, 1988a. https://doi.org/10.1016/0266-352X(88)90053-5

LADE, P. V.; KIM, M. K. Single hardening constitutive model for frictional materials III. Comparisons with experimental data. **Computers and Geotechnics,** v. 6,, n.1 p. 31-47, 1988b. https://doi.org/10.1016/0266-352X(88)90054-7

LADE, P. V.; OVERTON, D. D. Cementation Effects in Frictional Materials. **Journal of Geotechnical Engineering**, v. 115, n. 10, p. 1373-1387, 1989. https://doi.org/10.1061/(ASCE)0733-9410(1989)115:10(1373)

LADE, P. V.; PRABUCKI. M. J. Softening and preshearing effects in sand. **Soils and Foundations**, v. 35, n. 4, p. 93–104, 1995. https://doi.org/10.3208/sandf.35.4_93

LADE, P. V.; TRADS, N. The role of cementation in the behaviour of cemented soils. **Geotechnical Research**, v. 1, n. 4, p. 111–132, 2014. https://doi.org/10.1680/gr.14.00011

LAMBE, T. W.; WHITMAN, R. V. **Soil mechanics**, si version. [s.l.] John Wiley & Sons, Inc., 1979.

LEE, C.; TRUONG, Q. H.; LEE, J. S. Cementation and bond degradation of rubber-sand mixtures. **Canadian Geotechnical Journal**, v. 47, n. 7, p. 763–774, 2010. https://doi.org/10.1139/T09-139

LEE, J. S.; SANTAMARINA, J. C. Bender elements: Performance and signal interpretation. **Journal of Geotechnical and Geoenvironmental Engineering**, v. 131, n. 9, p. 1063–1070, 2005. https://doi.org/10.1061/(ASCE)1090-0241(2005)131:9(1063)

LEONG, E. C.; YEO, S. H.; RAHARDJO, H. Measuring shear wave velocity using bender elements. **Geotechnical Testing Journal**, v. 28, n. 5, p. 488-498, 2005. https://doi.org/10.1520/GTJ12196

LEROUEIL, S.; HIGHT, D. W. Behaviour and properties of natural soils and soft rocks. **Proceedings** Symposium on Characterization and Engineering Properties of Natural Soils, Singapore, Tan et al. (eds.). Swets e Zeitlinger, Lisse. p. 29-254, 2003.

LEROUEIL, S.; HIGHT, D.W. Behaviour and properties of natural and soft rocks. **Characterization and Engineering Properties of Natural Soils**. Eds. Tan et al., v.1, p.29-254. Swets & Zeitlinger, Lisse, 2003.

LEROUEIL, S.; VAUGHAN, P. R. The general and congruent effects of structure in natural soils and weak rocks. **Géotechnique**, v. 40, n. 3, p. 467–488, 1990. https://doi.org/10.1680/geot.1990.40.3.467

LIAO, J. J.; YANG, M. T.; HSIEH, H. Y. Direct tensile behavior of a transversely isotropic rock. I**nternational Journal of Rock Mechanics and Mining Sciences and Geomechanical**, Abstracts, v. 34, n. 5, p. 837–849, 1997.

LINGS, M. L.; GREENING, P.D. A novel bender/extender element for soil testing. **Géotechnique**, v. 51, n. 8, p. 713-717, 2001. https://doi.org/10.1680/geot.2001.51.8.713

LINGS, M. L.; PENNINGTON, D. S.; NASH, D. F. T. Anisotropic stiffness parameters and their measurement in stiff natural clay, **Géotechnique,** v. 50, n. 2, p. 109-125, 2010. https://doi.org/10.1680/geot.2000.50.2.109

LITTLE, D. N.; THOMPSON, M. R.; TERRELL, R. L.; EPPS, J. A.; BARENBERG, E. J. **Soil stabilization for roadways and airfields**. Rep. No. ESL-TR-86-19, Air Force Engineering and Services Center, Tyndall Air Force Base, Fla, 1986.

LO PRESTI, D. C. F.; JAMIOLKOWSKI, M.; PALLARA, O.; CAVALLARO, A.; PEDRON, S. Shear modulus and damping of soils. **Géotechnique**, v. 47, n. 3, p. 603-617. https://doi.org/10.1680/geot.1997.47.3.603

LOVE, A. E. H. **A Treatise on the Mathematical Theory of Elasticity**, Dover Publications, New York, 1927.

MAHER, M. H.; GRAY, D. H. Static response of sands reinforced with randomly distributed fibers. **Journal of Geotechnical Engineering**, v. 116, n. 11, p. 1661-1667, 1990. https://doi.org/10. 1061/(ASCE)0733-9410(1990)116:11(1661)

MAHER, M. H.; HO, Y. C. Behavior of fiber-reinforced cemented sand under static and cyclic loads. **Geotechnical Testing Journal**, Philadelphia, v. 16, n. 3, p. 330-338, 1993. https://doi.org/10.1520/GTJ10054J

MANDOLINi, A., 2014. **Investigation of the strength anisotropy of fibre reinforced sands under generalised condition using the HCTA**. University of Bristol. 158p Thesis (MS.) – Department of Civil Engineering, University of Bristol, UK, 2014.

MANDOLINI, A., 2018. **Change in elastic properties of sand under very large number of low amplitude multiaxial cyclic loadings**. 253p Thesis (PhD) – Department of Civil Engineering, University of Bristol, UK, 2018.

MARQUES, S. F. V. **Comportamento de uma Areia Artificialmente Cimentada até Altas Tensões de Confinamento**. 2016. 238 p. Thesis (D.Sc.) – Civil Engineering Post-Graduation Program, Department of Civil Engineering, Federal University of Rio Grande do Sul, Porto Alegre, BR-RS, 2016. In Portuguese.

Mitchell, J. K. Soil improvement—state-of-the-art report**. Proc., 10th Int. Conf. on Soil Mechanics and Foundation Engng**, v. 4, International Society of Soil Mechanics and Foundation Engineering, Stockholm, p. 509–565, 1981.

MITCHELL, J. K.; KATTI, R. K. Soil improvement. State-of-theart report. **Proc., 10th Int. Conf. on Soil Mech. and Found. Engrg**., International Society of Soil Mechanics and Foundations Engineering, London, 261–317, 1981.

MITCHELL, J. K.; SOGA, K. **Fundamentals of soil behavior**. 3rd. ed. [s.l.] John Wiley & Sons, Inc., 2005.

MOH, Z. C. Reactions of Soil Minerals with Cement and Chemicals. **Highway Research Record**, V. 86, P. 39–61, 1965.

MOLENKAMP, F.; LUGER, H.J. Modelling and minimization of membrane penetration effects in tests on granular soils. **Géotechnique**, v. 31, n. 4, p. 471-486, 1981. https://doi.org/10.1680/geot.1981.31.4.471

MOORE, R. K.; KENNEDY, T. W.; HUDSON, W. R. Factors affecting the tensile strength of cement-treated materials. **Highway Res. Rec**. v. 315, p. 64–80, 1970.

MUJAH, D. F.; AHMAD, H. H.; SAFARI, A. Evaluation of the Mechanical Properties of Recycled Glass Fibers-Derived Three Dimensional Geomaterial for Ground Improvement. **Journal of Cleaner Production**, v. 52, p. 495–203, 2013. http://doi.org/ 10.1016/j.jclepro.2013.03.035

NEWLAND, P. L.; ALLELY, B. H. Volume Changes in Drained Triaxial Tests on Granular Materials. **Géotechnique**, v. 7, n. 1, p. 17–34, 1957. https://doi.org/10.1680/geot.1957.7.1.17

ODA, M.; KOISHIKAWA, I. Effect of Strength Anisotropy on Bearing Capacity of Shallow Footing in a Dense Sand, **Soils and Foundations**, v. 19, n. 3, p. 15–28, 1979. https://doi.org/10.3208/sandf1972.19.3_15

PARKIN, A. K.; GERRARD, C. M.; WILLOUGHBY, D. R. Discussion: Deformation of Sand in Shear, **Journal of the Soil Mechanics and Foundations Division**, ASCE, v. 94, SM1, p. 336–340, 1968.

PENNINGTON, D. S.; NASH, D. F. T.; LINGS, M. L. Anisotropy of Go shear stiffness in Gault clay. **Géotechnique**, v. 47, n. 3, p. 391-398, 1997. https://doi.org/10.1680/geot.1997.47.3.391

PENNINGTON, D.S.; NASH, D.F.T.; LINGS, M. L. Horizontally-mounted bender elements for measuring anisotropic shear moduli In triaxial clay specimens. **Geotechnical Testing Journal**, ASTM, v. 24, n. 2, p. 133-144, 2001. https://doi.org/10.1520/GTJ11333J

PORBAHA, A.; TANAKA, H.; KOBAYASHI, M. State of the art in deep mixing technology. Part II: Applications. **Ground Improvement**, J. ISSMGE, v. 2, n. 2, p. 125–139, 1998. https://doi.org/10.1680/gi.1998.020303

PRIETTO, P. D. M. **Resistência e dilatância de solos reforçados com fibras submetidos a grandes deformações**. 2004. 218 p. Thesis (D.Sc.) – Civil Engineering Graduation Program, Department of Civil Engineering, Federal University of Rio Grande do Sul, Porto Alegre, BR-RS, 2004. In Portuguese.

PUPPALA, A. J.; INTHARASOMBAT, N.; VEMPATI, R. K. Experimental studies on ettringite-induced heaving in soils. **Journal of Geotechnical and Geoenvironmental Engineering**, v. 131, n. 3, p. 325–337, 2005. https://doi.org/10.1061/(ASCE)1090-0241(2005)131:3(325)

RABBI, A. T. M. Z.; KUWANO, J. Effect of curing time and confining pressure on the mechanical properties of cement-treated sand. **Geotechnical Special Publication**, 2012. https://ascelibrary.org/doi/10.1061/9780784412121.103

RAD, N. S.; CLOUGH, G. W. Influence of Cementation on the Static and Dynamic Behavior of Sands. **Report** - Stanford University, John A. Blume Earthquake Engineering Center, v. 59, 1982.

RANDOLPH, M. F., WROTH, C. P. Application of the failure state in undrained simple shear shaft capacity of driven piles. **Géotechnique**, v. 31, n. 1, p. 143–157, 1981. https://doi.org/10.1680/geot.1981.31.1.143

REDDY, K. R. **Behaviour of cemented sands under three-dimensional loadings**. 1990 Thesis (PhD) – Illinois Institute of Technology, Chicago, USA, 1990.

REDDY, K. R.; SAXENA, S. K. Effects of cementation on stress-strain and strength characteristics of sands. **Soils and Foundations**, v. 33, n. 4, p. 121–134, 1993. https://doi.org/10.3208/sandf1972.33.4_121

RINALDI, V. A. A; SANTAMARINA, J. C. C. Cemented soils: Small strain stiffness. **Deformational Characteristics of Geomaterials**, 1(December), 267–273, 2008

ROESLER, S, K. Anisotropic shear modulus due to stress anisotropy, **Journal of Geotechnical Engineering**, ASCE, v. 105, n. 7, p. 871-880, 1979.

ROTTA, G. V. **Plastificação de um solo cimentado curado sob tensão**. 2005. 198 p. Thesis (D.Sc.) – Civil Engineering Graduation Program, Department of Civil Engineering, Federal University of Rio Grande do Sul, Porto Alegre, BR- RS, 2005. In Portuguese.

ROTTA, G. V.; CONSOLI, N. C.; PRIETTO, P. D. M.; COOP, M. R.; GRAHAM, J. Isotropic yielding in an artificially cemented soil cured under stress. **Géotechnique**, v. 53, n. 5, p. 493–501, 2003. https://doi.org/10.1680/geot.2003.53.5.493

RUVER, C. A. **Estudo do arrancamento de fundações em solos tratados com cimento**. 2011. Thesis (D.Sc.) – Civil Engineering Graduation Program, Department of Civil Engineering, Federal University of Rio Grande do Sul, Porto Alegre, BR- RS, 2011. In Portuguese.

SAADA, A. S. **Elasticity, Theory and Application**, Krieger, Malabar, FL, 1983.

SADEK, T. (2006). **The multiaxial behaviour and elastic stiffness of Hostun sand**, PhD Thesis, University of Bristol, UK, 2006.

SALGADO, R. The Engineering of Foundations. **Journal of Chemical Information and Modeling**, v. 53, n. 9, p. 1689–1699, 2013. doi:10.1017/CBO9781107415324.004.

SANTAMARINA, J. C.; FAM, M. A. Interpretation of bender element tests—discussion. **Géotechnique**, v. 47, n. 4, p. 873–875, 1997. https://doi.org/10.1680/geot.1995.45.1.149

SAXENA, S. K; AVRAMIDIS, A; REDDY, K. Dynamic moduli and damping ratios for cemented sands at low strains. **Canadian Geotechnical Journal**, v. 25, n. 2, p. 353-568, 1988b. https://doi.org/10.1139/t88-036

SAXENA, S. K; LASTRICO, R. M. Static properties of lightly cemented sand. **Journal of the Soil Mechanics and Foundations Division**, ASCE, v. 104, n. 12, p. 1449–1464, 1978.

SAXENA, S. K; REDDY, K. Low strain dynamic properties of artificially cemented sand. **Journal of Geotechnical and Geoenvironmental Engineering**, v. 1, n. 2, p. 12–17, 1988a. https://doi.org/10.1061/(ASCE)0733-9410(1986)112:11(1001)

SAXENA, S. K; REDDY, K.; AVRAMIDIS, A. Liquefaction resistance of artificially cemented sand. **Journal of Geotechnical Engineering**, ASCE, v. 114, n. 12, p. 1295-1413, 1988c. https://doi.org/10.1061/(ASCE)0733-9410(1988)114:12(1395)

SAYÃO, A.; VAID, Y. P. A critical assessment of stress nonuniformities in hollow cylinder test specimens. **Soils and Foundations**, v. 31, n. 1, p. 60–72, 1991. https://doi.org/10.3208/sandf1972.31.60

SCHANZ, T. **A constitutive model for cemented sands**. In Localization and bifurcation theory for soils and rocks. Edited by T. Adachi, F. Oka, and A. Yashima. A.A. Balkema, Rotterdam, The Netherlands, p. 165–172, 1998.

SCHNAID, F.; PRIETTO, P. D. M.; CONSOLI, N. C. Characterization of cemented sand in triaxial compression. **Journal of Geotechnical and Geoenvironmental Engineering**, v. 127, n. 10, p. 857–868, 2001. https://doi.org/10.1061/(ASCE)1090-0241(2001)127:10(857)

SCHOLEY, G.; FROST, J.; LO PRESTI, D.; JAMIOLKOWSKI, M. A Review of Instrumentation for Measuring Small Strains During Triaxial Testing of Soil Specimens. **Geotechnical Testing Journal**, v. 18, n. 2, p. 137–156, 1995. Available at: https://doi.org/10.1520/GTJ10318J.

SHARMA, S. S.; FAHEY, M. Deformation characteristics of two cemented calcareous soils. **Canadian Geotechnical Journal**, v. 41, n. 6, p. 1139–1151, 2004. https://doi.org/10.1139/T04-066

SHARMA, S. S.; FAHEY, M. Degradation of stiffness of cemented calcareous soil in cyclic triaxial tests. **Journal of Geotechnical and Geoenvironmental Engineering**, v. 129, n.7, p. 619–629, 2003. https://doi.org/10.1061/(ASCE)1090-0241(2003)129:7(619)

SILVA, J.; AZENHA, A., CORREIA, A. G.; FERREIRA. C. Continuous stiffness assessment of cement-stabilised soils from early age. **Géotechnique**, v. 63, n. 16, p. 1419-1432, 2013. https://doi.org/10.1680/geot.13.P.021

SIVATHAYALAN, S.; VAID, Y.P., Truly undrained response of granular soils with no membrane-penetration effects. **Canadian Geotechnical Journal**, v. 35, n. 5, p.730–739, 1998. https://doi.org/10.1139/t98-048.

SKEMPTON, A. W. The Pore-Pressure Coefficients A and B. **Géotechnique**, v. 4, n. 4, p. 143–147, 1954. https://doi.org/10.1680/geot.1954.4.4.143.

SOUTO, A.; HARTIKAINEN, J.; OZUDOGRU, K. Measurement of dynamic parameters of road pavement materials by the bender element and resonant column tests. **Géotechnique**, v. 44, n. 3, p. 519-526, 1994. https://doi.org/10.1680/geot.1994.44.3.519

STURE, K. H.; DESAI, C.S. Fluid cushion truly triaxial or multi axial testing device. **Geotechnical Testing Journal**, ASCE, v. 2, p. 940-959, 1979. https://doi.org/10.1520/GTJ10585J

SUKOLRAT, J. (2007) **Destructuration of Bothkennar Clay**. PhD Thesis, University of Bristol, 2007.

SUN, D.; MATSUOKA, H. The Cam-clay models revised by the SMP criterion. **Soils and Foundations**, V. 39, N. 1, P. 81-95, 1999. https://doi.org/10.3208/sandf.39.81

TALESNICK M. L.; KATZ, A.; RINGEL, M. An investigation of the elastic stress–strain behavior of a banded sandstone and a sandstone-like material. **Geotechnical Testing Journal**, v. 23, n. 3, p. 257–273, 2000. https://doi.org/10.1520/GTJ11050J

TATSUOKA, F.; LO PRESTI, D.; KOHATA, Y. Deformation Characteristics of Soils and Soft Rocks under Monotonic and Cyclic Loads and Their Relationships. **In U. of Missouri--Rolla**, ed. International Conferences on Recent Advances in Geotechnical Earthquake Engineering and Soil Dynamics. St. Louis, Missouri, 1995.

TATSUOKA, F.; SHIBUYA, S. Deformation characteristics of soils and rocks from field and laboratory tests, Keynote Lecture (session No. 1), **Proc. 9th Asian Regional Conference on SMFE**, Bangkok, v. 2, p. 101-170, 1992.

TATSUOKA, F.; SONODA, S.; HARA, K.; FUKUSHIMA, S.; PRADHAN, T. E. Failure and deformation of sand in torsional shear. **Soils and Foundations**, v. 26, n. 4, p.79–97, 1986. https://doi.org/10.3208/sandf1972.26.4_79

THOMÉ, A.; CARRARO, J. A. H.; BALVEDI, D.; CONSOLI, N. C. Utilization of industrial by-products for soil stabilization and the influence of temperature in the development of pozzolanic reactions. **Proc., 3rd Int. Congr. on Envir. Geotechnics**, Balkema, Rotterdam, The Netherlands, p. 721–726, 1998.

THOMÉ, A.; DONATO, M.; CONSOLI, N. C.; GRAHAM, J. Circular footings on a cemented layer above weak foundation soil. **Canadian Geotechnical Journal,** v. 42, n. 6, p. 1569–1584, 2005. https://doi.org/10.1139/t05-069

TRHLÍKOVÁ, J.; MAŠÍN, D.; BOHÁČ, J. Small-strain behaviour of cemented soils. **Géotechnique,** v. 62, n. 10, p. 943–947, 2012. https://doi.org/10.1680/geot.9.P.100

VAID, Y. P.; SAYÃO, A.; ENHUANG, H.; NEGUSSEY, D. Generalized stress-path-dependent soil behaviour with a new hollow cylinder torsional apparatus. **Canadian Geotechnical Journal**, v. 27, n. 5, p. 601–616, 1990. https://doi.org/10.1139/t90-075

VATSALA, A.; NOVA, R.; SRINIVASA MURTHY, B. R. Elasto-plastic model for cemented soils. **Journal of Geotechnical and Geoenvironmental Engineering**, v. 127, n. 8, p. 723–815, 2001. doi:10.1061/ (ASCE)1090-0241(2001)127:8(679)

VENDRUSCOLO, M. A. **Comportamento de ensaios de placa em camadas de solo melhoradas com cimento e frbras de polipropileno**. 2003. 224 p. Thesis (D.Sc.) – Civil Engineering Graduation Program, Department of Civil Engineering, Federal University of Rio Grande do Sul, Porto Alegre, BR- RS, 2003. In Portuguese.

VENSON, G. I. 2015; **Resilience modulus and fatigue life of an artificially cemented sand.** 158 p. Dissertation (M.Sc.) – Civil Engineering Graduation Program, Department of Civil Engineering, Federal University of Rio Grande do Sul, Porto Alegre, BR- RS, 2015. In Portuguese.

VIANA DA FONSECA, A.; FERREIRA, C.; FAHEY, M. A framework interpreting bender element tests, combining time-domain and frequency-domain methods. **Geotechnical Testing Journal**, v. 32, n. 2, p. 91-107, 2009. https://doi.org/10.1520/GTJ100974

VIGGIANI, G.; ATKINSON, J. H. Stiffness of fine-grained soil at very small strains. **Géotechnique**, v. 45, n. 2, p 249-265, 1995. https://doi.org/10.1680/geot.1995.45.2.249

WILLAM, K.J., WARNKE, E. P. Constitutive models for the triaxial behaviour of concrete. **Proceeding of the International Assoc. for Bridge and Structural Engineering**, v. 19, p. 1-30, 1975.

YAMASHITA, S.; KAWAGUCHI, T.; NAKATA, Y.; MIKAMT, T.; FUJIWARA, T.; SHIBUYA, S. Interpretation of international parallel test on the measurement of Gmax using bender elements. **Soils and Foundations**, v. 49, n. 4, p. 631–650, 2009. https://doi.org/10.3208/sandf.49.631

YOON, B. S. (2005). **Commissioning of a new hollow cylinder apparatus**. University of Bristol. Thesis (MS.) – Department of Civil Engineering, University of Bristol, UK, 2005.

ZANG, A.; WONG, T. F. Elastic stiffness and stress con- centration in cemented granular material. **International Journal of Rock Mechanics and Mining Sciences & Geomechanics,** Abstracts, v. 32, n. 6, p. 563–574, 1995. doi:10.1016/0148-9062(95)00012-6.

ZENG, X.; GROLEWSKI, B. Measurement of Gmax and estimation of K0 of saturated clay using bender elements in an oedometer, **Geotechnical Testing Journal**, ASTM. 28, n. 3, p. 264-274, 2005. https://doi.org/10.1520/GTJ11318